

Electrochemical Studies

Yuanyuan Lu

St John's College

A thesis submitted for the degree of Doctor of Philosophy in

Physical and Theoretical Chemistry

Trinity Term 2022

Abstract

This thesis focuses on the electrochemical studies for two distinct purposes: one is to invent and validate an electrochemical sensor for detecting phosphate in natural aqueous solutions. The other is to develop a more comprehensive understanding of electrocatalysis at ensemble and single entity multiwalled carbon nanotubes (MWCNTs). **Chapter 1** introduces essential background knowledge about fundamental electrochemistry and the generic electrochemical techniques used in this thesis and **Chapter 2** gives a detailed description about experimental methods and materials characterization.

Chapter 3 and **4** reports a novel amperometric sensor for aqueous phosphate ions in freshwater systems: **Chapter 3** reviews previous work related to amperometric methods for phosphate analysis and uses commercial software to predict the speciation of molybdate, phosphate and their complex species both separately and in mixtures in aqueous solution as a function of concentration and pH. **Chapter 4** builds on the work in **Chapter 3** to realize the electrochemical detection of phosphate at an ammonium molybdate tetrahydrate-chitosan modified glassy carbon macro electrode in aqueous solutions. By employing cyclic voltammetry (CV) and square wave voltammetry (SWV), the electrocatalytic mechanism for quantitative detection of trace phosphate was inferred and this method was optimized and successfully applied for environmental use.

Chapter 5, 6 and 7 focus on the electrocatalytic nano-impacts of single carbon nanotubes. **Chapter 5** reports the electro-oxidation of amino-functionalized multiwalled carbon nanotubes (MWCNTs-NH_2) under acidic and neutral conditions, making comparison with pure multiwalled carbon nanotubes (MWCNTs) at ensemble and single entity level. By measuring the extent of protonation of amino groups as a function of pH reflected by the oxidative signals in CV and nano-impacts, the pK_a of the amino functionality in the MWCNTs was determined. **Chapter 6** studies the mechanism of oxygen reduction reaction (ORR) catalysed by MWCNTs

at single entity level. It reveals that the surface oxygen functionality on carbon nanotubes facilitated the reduction from oxygen to peroxide in alkaline media. Then based on this inference, we further compared the electrocatalytic performance of ORR at single MWCNT or MWCNTs-NH_2 particles in **Chapter 7**. By comparing the voltammetric behaviour on glassy carbon macro electrode modified with layers of MWCNTs or MWCNTs-NH_2 ensemble and impact signal from the collision of a single MWCNTs or MWCNTs-NH_2 particle, it was inferred that the promotion of the electrocatalytic reaction of the oxygen reduction is primarily due to the amount of surface oxygen functionality not the nitrogen content. The generic approach discussed in these three chapters gives proof of concept to the use of joint single entity and ensemble measurements for exploring electrocatalysis with scope for application to a wide range of nano-entities.

Acknowledgements

My deepest gratitude goes first and foremost to my supervisor, Prof. Richard G.Compton, for his constant encouragement and support throughout all the stages of my D.phil study. Without your consistent and illuminating instruction, I would not have such valuable opportunities and experiences in a wonderful research group over the last three years. Mostly, your extreme enthusiasm and persistency upon exploring electrochemical fundamentals will influence my attitude towards scientific research all the time.

I would also like to extend my heartfelt thanks to Dr. Xiuting Li for her great support especially providing me a suitable laboratory to continue experiments during the outbreak of COVID-19. You are always patient and gave me very helpful suggestions when I was in trouble. Another great appreciates to Dr. Danlei Li for her constructive advice and on-hand guidance in my first year of D.phil, as well as her company at each meeting. Thanks to Dr. Bertold Rasche for the teaching and instruction in theoretical calculation of complex speciation.

Big thanks to all the members of the RGC group. Thanks to Archana, Haotian and Yifei, as one of the members of 'RGC group 2019', I am so lucky to have you preparing and achieving milestones of the D.Phil. Thanks to Yuqi for your companionship and immeasurable support in the study and life. Thanks to Dr. Christopher Batchelor-McAule, Dr. Pranati Nayak, Dr. Minjun Yang, Dr. Ruochen Xie, Dr. Haonan Le, Dr. Yanjun Guo, Dr.Yuanzhe Wang, Dr. Ruiyang Miao, Joseph, Junling and many groups members of the past and present, I have been truly enjoying working with you. Special thanks to my colleges, St John's, who have provided me with a comfortable accommodation, lots of meals and generous help in many other respects.

Last but not least, I would like to thank my family for your endless love and care. Thanks to my best friend Jingtian for your positive and continuous psychological comfort. During my toughest time of life, without the encourage and support from all of you, I had no way to hold on till now. I also believe I will become stronger in the further future.

Glossary

Roman Symbols

Symbol	Meaning	Unit
A	Electroactive layer area	m^2
A_e	Electrode surface area	m^2
$[A^z]$	Bulk concentration of species A^z	mol cm^{-3}
C_d	Capacitance of the double layer per unit area	F m^{-2}
C_j	Concentration of species j	mol cm^{-3}
D	Diffusion coefficient	cm^2 s^{-1}
d	Diffusion layer thickness	cm
I	Electrical current	A
I_p	Peak current	A
I_{ss}	Steady-state current	A
J	Heterogeneous reaction flux	mol cm^{-2} s^{-1}
$J_j(x)$	Flux of species j	mol s^{-1} cm^{-2}
$J_{m,j}(x)$	Migratory flux	mol cm^{-2} s^{-1}
$[j]$	Concentration of species j	mol dm^{-3}
E	Applied potential at the electrode	V
E^0	Standard electrode potential	V
E_f^0	Formal potential	V

E_{mid}	Mid-point potential	V
$E_{1/2}$	Half-wave potential	V
ΔE_p	Pulse height in SWV	Unitless
ΔE_s	Staircase height in SWV	Unitless
ΔE_{pp}	Peak to peak separation	V
F	Faraday constant	C mol^{-1}
f	Square wave frequency	Hz
$\Delta G_c^{\dagger}$, $\Delta G_a^{\dagger}$	Standard Gibbs energy change	J mol^{-1}
k^0	Standard electrochemical rate constant	cm s^{-1}
k_c, k_a	Cathodic/Anodic rate constants	Unitless
m_i	Mass of the electroactive species	g
m_T	Mass transport coefficient	cm s^{-1}
M	Molar mass	g mol^{-1}
N_A	Avogadro constant	mol^{-1}
n	Number of electrons transferred	Unitless
P^0	Standard pressure	N m^{-2}
Q	Total electric charge	C
R	Universal gas constant	J K^{-1} mol^{-1}
R_s	Solution resistance	Ω
r_e	Radius of the microdisc electrode	cm

T	Absolute temperature	K
t_p	Single potential pulse in SWV	Dimensionless
t_s	Single potential cycle in SWV	Dimensionless
X_{DL}	Debye length	Å
z	Charge of the species	C
z_j	Ionic charge of species j	C

Greek Symbols

Symbol	Meaning	Unit
α, β	Transfer coefficient	Unitless
ρ	Density	g cm^{-3}
μ_j	Chemical potential of species j	J mol^{-1}
$\bar{\mu}_j$	Electrochemical potential	J mol^{-1}
ϕ	Electrical potential	V
γ_j	Activity coefficient of species j	Unitless
ε_0	Permittivity of free space	C^2 J^{-1} m^{-1}
v	Scan rate	Vs^{-1}
$v(x)$	Local fluid velocity	cm s^{-1}
Λ	Matsuda-Ayabe parameter	Unitless
Γ	Surface coverage of reactant at the electrode surface	mol cm^{-2}

Contents

Chapter 1 Fundamentals of Electrochemistry

1.1 Electrochemical Equilibrium....1

1.2 Electrode Kinetics....6

1.3 Electrode Processes....11

1.3.1 Electrochemical Cells....11

1.3.2 Faradaic and non-Faradaic Processes....13

1.3.3 Mass Transport....16

1.4 Electrochemical Techniques....22

1.4.1 Cyclic Voltammetry....23

1.4.2 Square Wave Voltammetry....32

1.4.3 Chronoamperometry....34

1.4.4 Nano Impacts....34

References....38

Chapter 2 Experimental

2.1 Chemicals and Reagents....42

2.2 Electrochemical Instrumentation....45

2.2.1 Preparation of Glassy Carbon Macro electrodes (GCE)....45

2.2.2 Fabrication of Cabon Fibre Microwire electrodes....45

References....46

Chapter 3 Background for the Electrochemical Detection of Phosphate

3.1 Summary of phosphate detection using electrochemical techniques 47

3.2 Species distribution of P, Mo (VI) and their containing compounds 50

References 59

Chapter 4 Amperometric Environmental Phosphate Sensor

4.1 Introduction 61

4.2 Experimental 63

4.3 Results and Discussion 66

4.4 Conclusions 85

Appendix 86

References 96

Chapter 5 Electro-Oxidation of Amino-Functionalized Multiwalled Carbon Nanotubes

5.1 Introduction 98

5.2 Experimental 102

5.3 Results and Discussion 104

5.4 Conclusions 120

Appendix 122

References 134

Chapter 6 The Oxygen Reduction Reaction at Single Entity Multiwalled Carbon Nanotubes .....

6.1 Introduction 137

6.2 Experimental 139

6.3 Results and Discussion 140

6.4 Conclusions 150

Appendix 151

References 164

Chapter 7 Does Nitrogen Doping Enhance the Electrocatalysis of the Oxygen Reduction Reaction by Multiwalled Carbon Nanotubes?

7.1 Introduction 167

7.2 Experimental 169

7.3 Results and Discussion 172

7.4 Conclusions 180

Appendix 181

References 188

Conclusions 191

Future prospects 191

Chapter 1

Fundamentals of Electrochemistry

A branch of physical chemistry, electrochemistry is concerned with the interplay between electrical and chemical effects. A large part of this field deals with the study of chemical changes due to the individual redox reactions induced by an external electric circuit and an intervening electrolyte; this is known as electrolysis. In this chapter, an overview of fundamentals of the electrochemistry and basic electrochemical techniques are introduced. Topics covered are the description of electrochemical equilibrium, electrode kinetics, electrochemical cells, *Faradaic* and *non-Faradaic* processes, mass transport and electrochemical techniques. The concepts and treatments included in this chapter will help to understand the experimental results and their interpretation in later chapters.

1.1 Electrochemical Equilibrium

In electrochemical systems, the overall electrochemical reactions occur at the interface between an electronic conductor (an *electrode*) and an ionic conductor (an *electrolyte*) when an electric potential is applied and current passes [1]. A simple one-electron transfer electrochemical equilibrium is described in Eq. (1.1). It is commonly studied at the surface of an electrode (e.g. metal) immersed in a solution consisting of a redox species A^Z and B^{Z-1}

$$\boldsymbol{A^{Z}_{(aq)} + e^{-}_{metal} \rightleftarrows B^{Z-1}_{(aq)}} \qquad (1.1)$$

where A^Z and B^{Z-1} are the oxidized and reduced forms of the redox couple in solution phase. The establishment of Eq. (1.1) implies that the rate at which A^Z acquires an electron from the electrode being reduced is exactly balanced by the rate of B^{Z-1} giving up an electron to the electrode, which are said to be 'oxidized'. Different from the normal chemical equilibrium, it can be recognized from Eq. (1.1) that a charge separation across the interface will possibly exist, leading to a potential difference that is the electrode potential established at the electrode

surface relatively to the solution phase [1, 2]. This will be clear to understand through the energy levels of relevant species involving in the potential determining equilibrium. As shown in Fig.1.1, in the electronic structure of a metal, the electrons continuously occupy the conduction 'bands' to reach an energy maximum known as the Fermi level [3]. From a thermodynamic aspect, the situation in which the Fermi level of the electrode is higher than the lowest unoccupied molecular orbital (LUMO) of A^Z in the solution phase (Figure.1.1(A)). In this case, the electrons are favourable to leave the Fermi level and help to convert A^Z to B^{Z-1}. As the electron transfer proceeds, the Fermi level of the electrode gradually becomes lower. At some point it has a lower energy level than the highest occupied molecular orbital (HOMO) of the formed B^{Z-1}, the electrons in the electrolyte solution will find a more favourable energy on the electrode to transfer in the opposite direction and B^{Z-1} is oxidized to A^Z (Figure.1.1(B)). As the reaction rate of forward and backward directions turns to be kinetically same, a situation corresponding to the dynamic equilibrium will be attained, leading to no further possible net charge. Charge separation, at this point, is established between the electrode and the solution to form the electrode potential on the metal.

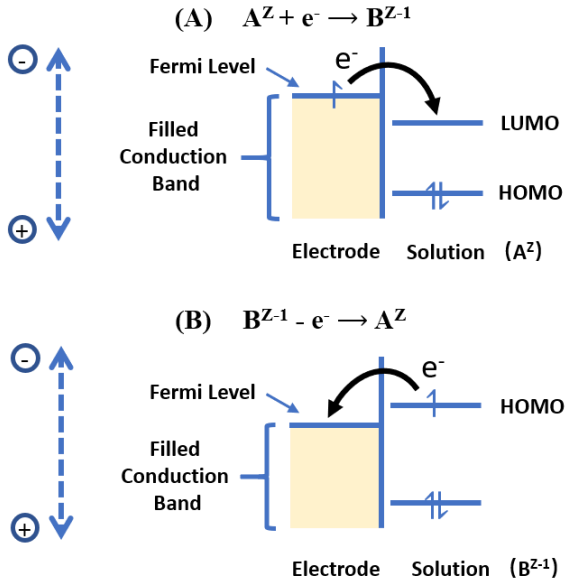


Figure.1.1 Representation of the energy levels of the ions in solution and the metallic electrode during reduction of A^Z (A) and oxidation of B^{Z-1} (B)

For the electrochemical equilibrium as listed in equation Eq. (1.1), the balance between not only the chemical energies but also the electrical energies of all the involved entities can be illustrated according to the position of the equilibrium because of two different electrical potentials, ϕ_s (solution) and ϕ_m (electrode), existed during the electron transferred between solution and electrode phase. To account for both chemical energies and electrical energies of a special species (*j*), the electrochemical potential ($\bar{\mu}_j$) is introduced [4]:

$$\bar{\mu}_j = \mu_j + Z_j F \phi \qquad (1.2)$$

where μ_j is the chemical potential (J mol^{-1}) of molecule j, Z_j is the charge of species j, F is the Faraday Constant (96485 C mol^{-1}), ϕ is the potential (V) of the solution phase (ϕ_s) or electrode phase (ϕ_m) in which species j is found. It is noted that the second term, $Z_j F \phi$, represents the the electrical energy of species j with the same units as the chemical potential (Gibbs energy *per mole*). Eq. (1.2) helps to analysis when a balance between the electrochemical potentials of the reactants and products will reach under conditions of certain temperature and pressure. Then using it to express the electrochemical potential of reaction in Eq. (1.1) at equilibrium,

$$\bar{\mu}_{A^z} + \bar{\mu}_{e^-} = \bar{\mu}_{B^{z-1}} \qquad (1.3)\ [5]$$

Applying Eq. (1.2) to transfer Eq. (1.3) to:

$$(\mu_{A^z} + ZF\phi_S) + (\mu_{e^-} - F\phi_M) = \left(\mu_{B^{z-1}} + (Z-1)F\phi_S\right) \qquad (1.4)$$

Rearranging Eq. (1.4) gives

$$F(\phi_S - \phi_M) = \mu_{B^{z-1}} - \mu_{A^z} - \mu_{e^-} \qquad (1.5)$$

Considering:

$$\mu_j = \mu_j^0 + RTln\frac{[j]}{[\ ]^0} \qquad (1.6)$$

where μ_j^0 is the standard chemical potential, R is the universal gas constant (8.314 J K^{-1} mol^{-1}), T is the absolute temperature (K), $[j]$ is the concentration of species j (mol dm^{-3}) in solution and $[\ ]^0$ is the standard concentration (1 mol dm^{-3}), the latter assuming ideality.

Substituting Eq. (1.6) into Eq. (1.5) gives:

$$\boldsymbol{\phi_M - \phi_S = \frac{\Delta\mu^0}{F} + \frac{RT}{F} \ln \left(\frac{[A^Z]}{[B^{Z-1}]}\right)} \quad (1.7)$$

where

$$\boldsymbol{\Delta\mu^0 = \mu^0_{A^z} + \mu_{e^-} + \mu^0_{B^{z-1}}} \quad (1.8)$$

Under a given temperature and pressure, which is a constant. Eq. (1.7) is the *Nernst equation* [6] to characterize the position of the electrochemical equilibrium of the A^Z / B^{Z-1} redox couple at a single electrode-solution interface. Considering the above expression Eq. (1.6) is for the chemical potentials of the species in solution, the standard concentration ($[\ ]^{\mathbf{0}}$ = 1 mol dm^{-3}) is used. As for reactions involving gases, it is used instead by a standard pressure (P^0 = ~ 10^5 N m^{-2}) for the gases. While the chemical potentials for pure solid or liquid are equal to their standard chemical potential; there is no term corresponding to concentration or pressure.

The *Nernst equation* Eq. (1.7) only applies to the ideal solutions. Therefore, in the non-ideal solution, the activity of species *j*, a_j, is introduced to modify the equation:

$$\boldsymbol{a_j = \gamma_j c_j} \quad (1.9)$$

where the 'activity coefficient' of species *j*, γ_j, considers the extent of the ion-ion and ion-solvent interactions in concentrated non-ideal solutions.

Accordingly, the Eq. (1.7) becomes:

$$\boldsymbol{\phi_M - \phi_S = \frac{\Delta\mu^0}{F} + \frac{RT}{F} \ln \left(\frac{\gamma_{A^z}[A^Z]}{\gamma_{B^{z-1}}[B^{Z-1}]}\right)} \quad (1.10)$$

Measuring an absolute value of $(\boldsymbol{\phi_M - \phi_S})$ associated with a single electrode-solution interface is impossible in experiments. Normally, a digital voltammeter used to measure the potential drop $(\boldsymbol{\phi_M - \phi_S})$ must be through the external circuit which necessarily creates a second electrode/solution interface. If a second electrode called as 'reference electrode' is introduced into the solution with a constant content [7], the measurements will become feasible

to obtain the difference ($\boldsymbol{\phi_M - \phi_S}$) between the two electrodes as follows:

$$\boldsymbol{E = (\phi_M - \phi_S)_{\,working} - (\phi_M - \phi_S)_{\,reference}} \quad (1.11)$$

where E is the change of potential difference between a 'working electrode' in voltammetric studies and the reference electrode.

so that

$$\boldsymbol{E = c_0 + \frac{RT}{F} \ln \left(\frac{\gamma_{A^z}[A^Z]}{\gamma_{B^{z-1}}[B^{Z-1}]}\right)} \quad (1.12)$$

where c_0 is a constant. It is noted that an additional term 'IR_s' should have been put in the right-hand side of Eq. (1.11) given that a limited 'conductivity' leads to certain potential drop within the solution. However, since the current pass through the external circuit connected with two electrodes is too tiny to be ignored, this part could be negligible.

Classically, and according to IUPAC definition [8, 9], the electrode potentials (E) are measured against standard hydrogen electrode (SHE) as the reference electrode. Specially, the standard electrode potential (E^0) of arbitrary redox couples (e.g. A^Z / B^{Z-1}) is measured against the SHE under conditions in which the activity ($\boldsymbol{\gamma_j}$ [$\boldsymbol{j}$]) of both species are at a unity level.

Thus, the *Nernst equation* expressed with E^0 for the two-electrode system is:

$$\boldsymbol{E = E^0 + \frac{RT}{F} \ln \left(\frac{\gamma_{A^z}[A^Z]}{\gamma_{B^{z-1}}[B^{Z-1}]}\right)} \quad (1.13)$$

Then, the formal potential E_f^0 with respect to standard potential and activity coefficient can be expressed as:

$$\boldsymbol{E_f^0 = E^0 + \frac{RT}{F} ln \left(\frac{\gamma_{A^z}}{\gamma_{B^{z-1}}}\right)} \quad (1.14)$$

So that:

$$\boldsymbol{E = E_f^0 + \frac{RT}{F} \ln \left(\frac{[A^Z]}{[B^{Z-1}]}\right)} \quad (1.15)$$

Although the formal potentials E_f^0 sometimes can approximate to the standard potentials

given correspondingly, it is restricted to the 'standard' condition of pH 0 at temperature of 298 K. Therefore, if the pH of solution under study shifts from '0' to '*m*' at 298 K, the formal potential will change by *m* times 0.059 V per pH unit assuming one-electron transfer in the electrochemical equilibrium. The above *Nernst equations* (1.15) successfully describes the relationship between potential and concentrations of the redox species. It must be stressed that the estimation of the potential at a dynamic equilibrium requires fast electrode kinetics while not applicable normally. Therefore, we will address the kinetics of electrode processes in the next section.

1.2 Electrode Kinetics

After introducing the *Nernst equation* to describe electrochemical equilibrium in section 1.1, considering it is only applicable to fast electron transfer [10], it is necessary to quantitatively measure the rate of the interfacial electrochemical reaction. Thus, we next discuss electrode kinetics in this section.

Consider the following simple electron transfer reaction in aqueous solution:

$$\boldsymbol{A_{aq}^{z} + e_{(m)}^{-} \underset{k_a}{\overset{k_c}{\rightleftharpoons}} B_{aq}^{z-1}} \qquad (1.16)$$

at an electrode of area, A_e cm^2, where the rate constants k_c and k_a illustrate the reduction of A^Z to B^{Z-1} ('cathodic') and oxidation of B^{Z-1} to A^Z ('anodic') reactions respectively. The passage of the electrical current (*I*) through the electro-solution interface results from the electron transfer between the electrode and reactant A^Z, which occurs via quantum mechanical tunnelling. Importantly, the distance between A^Z and the electrode surface should be within the distance of ca 10-20 Å since the overlap of the electron wavefunctions of A^Z and the electrode is required to avoid the significant drop of the rate of tunnelling with separation at a greater distance of separation. Therefore, for the reduction of A^Z, the redox species diffusing from the remote bulk solution to the electrode surface must arrive to within the threshold distance

required before the electron transfer at the interface can occur. Eq. (1.17) is used for expressing the relationship between the electrical current (*I*, Amps) and the flux (moles cm^{-2} s^{-1}) of reactant undergoing electrolysis:

$$\boldsymbol{I = nFA_eJ} \tag{1.17}$$

where n is the electron transfer number (equals 1 for reaction (1.16)), F is the Faraday constant (96485 C mol^{-1}), A_e is the electrode area (cm^2) and J is the heterogeneous reaction flux at the interfacial boundary (mol cm^{-2} s^{-1}):

$$\boldsymbol{J = k_c[A^z]_0 - k_a[B^{z-1}]_0} \tag{1.18}$$

where $[A^z]_0$ and $[B^{z-1}]_0$ respectively indicate the concentrations of A^Z and B^{Z-1} adjacent to the electrode rather than those in bulk solution because of the diffusion layer established. In addition, another point related to Eq. (1.18) is that the electrochemical rate constants k_c or k_a have an exponential dependence on the electrical potential between the electrode (ϕ_M) and solution (ϕ_s). To establish their mathematic relationships, the *Arrhenius Equation* [11] is first used for connecting the rate constants k_c or k_a with the Gibbs energies of activation:

$$\boldsymbol{k_c = A_c \exp\left(\frac{-\Delta G_c^{\dagger}}{RT}\right)} \tag{1.19}$$

and

$$\boldsymbol{k_a = A_a \exp\left(\frac{-\Delta G_a^{\dagger}}{RT}\right)} \tag{1.20}$$

where A_c and A_a are the pre-exponential ("frequency") factors for reduction and oxidation, respectively, representing the number of collisions per second of the electroactive species with the electrode surface. R is the universal gas constant (8.314 J mol^{-1} K^{-1}) and T is the absolute temperature (K). $\Delta G_c^{\dagger}$ and $\Delta G_a^{\dagger}$ are respectively the standard Gibbs energy change (J mol^{-1}) from the reactants ($A^Z + e^-$) or products (B^{Z-1}) to the transition state as follows:

$$\Delta G_c^{\dagger} = G_{\dagger}^{0} - G_{reactants}^{0} \tag{1.21}$$

$$\Delta G_a^{\dagger} = G_{\dagger}^{0} - G_{products}^{0} \tag{1.22}$$

where $G_{\dagger}^{0}$, $G_{reactants}^{0}$ and $G_{products}^{0}$ individually represents the standard molar Gibbs energy of transition states, reactants and products.

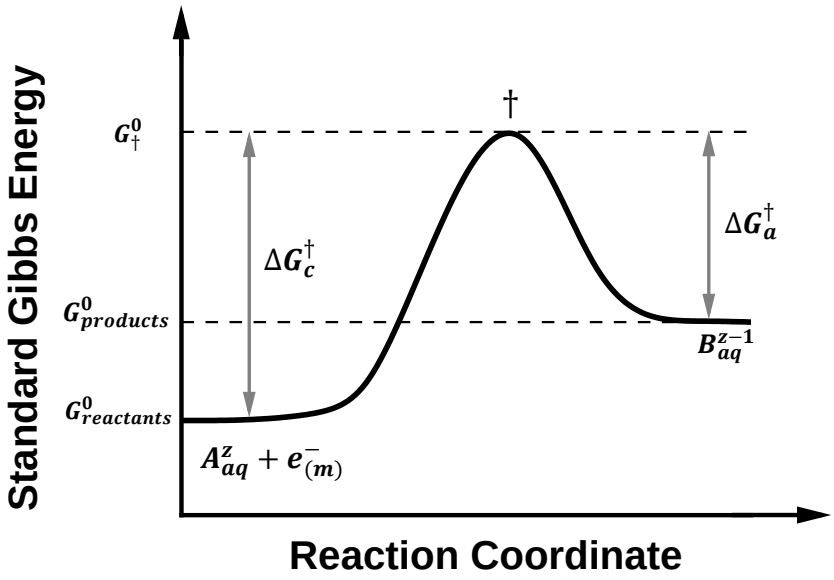


Figure.1.2 Standard Gibbs Energy profiles for an electro-reduction reaction.

The reaction profiles for the process in Eq. (1.16) is shown in Fig.1.2 which plots energy as a function of reaction coordinate. Note that the standard Gibbs energy of the reactants ($G_{reactants}^{0}$) is influenced by the potential of the electrode (ϕ_M) since the electron (e^-) is a reactant. Combining with Eq. (1.2) in Section 1.1,

$$G_{reactants}^{0} = G_{A}^{0} + G_{e^-}^{0} = c_1 + ZF\phi_s - F\phi_M \tag{1.23}$$

This leads to:

$$G_{reactants}^{0} = c_1 + (Z-1)F\phi_s - F(\phi_M - \phi_s) \tag{1.24}$$

Similarly

$$G_{products}^{0} = c_2 + (Z-1)F\phi_s \tag{1.25}$$

Assuming the standard Gibbs energy ($G_{\dagger}^{0}$) of the transition state to be in between $G_{reactants}^{0}$ and $G_{products}^{0}$ in terms of its potential dependency,

$$\boldsymbol{G_{\dagger}^{0} = c_3 + (Z-1)F\phi_s - \beta F(\phi_M - \phi_S)} \quad (1.26)$$

where c_1, c_2 and c_3 are different constants respectively. β is known as a transfer coefficient and takes a value between 0 and 1. If β is close to zero, the transition state will be the product like. On the contrary, the transition state will be reactant like if β is near unity. Defining α as another transfer coefficient:

$$\boldsymbol{\alpha = 1 - \beta} \quad (1.27)$$

Besides, the standard Gibbs energy ($G_{\dagger}^{0}$) of the transition state relates to the potential difference ($\phi_M - \phi_S$), which cannot be easily measured without a reference electrode in any complete measuring circuit. It is helpful to introduce the quantity ($E - E_f^0$):

$$\boldsymbol{E - E_f^0 = (\phi_M - \phi_s)_{working} + c_4} \quad (1.28)$$

where c_4 is a constant, ($E - E_f^0$) measures the deviation from the formal potential of the A^Z/B^{Z-1} couple of the applied potential on the working electrode, both potentials measured using the same reference electrode. Thus, the electrode energy level varies as $-F\ (E - E_f^0)$. It follows that the Gibbs energies of activation can be expressed as:

$$\boldsymbol{\Delta G_c^{\dagger} = \Delta G_{0,c}^{\dagger} + \alpha F(E - E_f^0)} \quad (1.29)$$

$$\boldsymbol{\Delta G_a^{\dagger} = \Delta G_{0,a}^{\dagger} - \beta F(E - E_f^0)} \quad (1.30)$$

Hence the electrochemical rate constants (k_c and k_a) as expressed in Eqs. (1.19) and (1.20) can be modified to be:

$$\boldsymbol{k_c = A_c \exp\left(\frac{-\Delta G_{0,c}^{\dagger} - \alpha F(E - E_f^0)}{RT}\right)} \quad (1.31)$$

$$\boldsymbol{k_a = A_a \exp\left(\frac{-\Delta G_{0,a}^{\dagger} + \beta F(E - E_f^0)}{RT}\right)} \quad (1.32)$$

Assuming there is a dynamic equilibrium where E is at the formal potential where the surface concentrations of A and B are from the *Nernst equation* equal, no net current will flow:

$$\boldsymbol{J = 0} \tag{1.33}$$

so that $k_a = k_c = k^0 = A_c exp(\frac{-\Delta G^{\dagger}_{0,c}}{RT}) = A_a exp(\frac{-\Delta G^{\dagger}_{0,a}}{RT})$, then the most convenient *Butler-Volmer* expression for the electrochemical rate constants at certain potentials is obtained:

$$\boldsymbol{k_c = k^0 exp\,[\frac{-\alpha F(E - E_f^0)}{RT}]} \tag{1.34}$$

$$\boldsymbol{k_a = k^0 exp\,[\frac{\beta F(E - E_f^0)}{RT}]} \tag{1.35}$$

The quantity k^0 represents the *standard electrochemical rate constant* with units of cm s^{-1}.

The value of α and β is often but not always ~ 0.5, in which case the transition state lies near the midpoint between the reactants and products. When the potential in the term of $(\phi_M - \phi_S)$ is changed by 1 Volt, the rate constants k_c and k_a are changed by factor of ca. 10^9 indicating the overwhelming sensitivity of the electrochemical rate constant on the electrode potential as controlling the electrode kinetics.

The combination of Eqs. (1.17), (1.18), (1.34) and (1.35) gives the important *current-potential* relation, known as the *Butler-Volmer* equation [12, 13]:

$$\boldsymbol{I = FAk^0([A^z]_0 exp\,[\frac{-\alpha F(E - E_f^0)}{RT}] - [B^{z-1}]_0 exp\,[\frac{\beta F(E - E_f^0)}{RT}])} \tag{1.36}$$

If it is assumed that $[A^z]_0$ and $[B^{z-1}]_0$ are constant over the range of the potentials studied, and only considering the reduction term in Eq (1.36), it becomes:

$$\boldsymbol{ln|I_{red}| = -\frac{\alpha FE}{RT} + c_5} \tag{1.37}$$

Similarly, for an oxidation:

$$\boldsymbol{ln|I_{ox}| = \frac{\beta FE}{RT} + c_6} \tag{1.38}$$

where I_{red} and I_{ox} are the reduction and oxidation currents respectively. c_5 and c_6 are different constants. Plots of $ln|I_{red}|$ versus E or $ln|I_{ox}|$ versus E are called Tafel plots, where the slope of the fitting line can help to acquire the transfer coefficient α or β as shown in Fig.1.3.

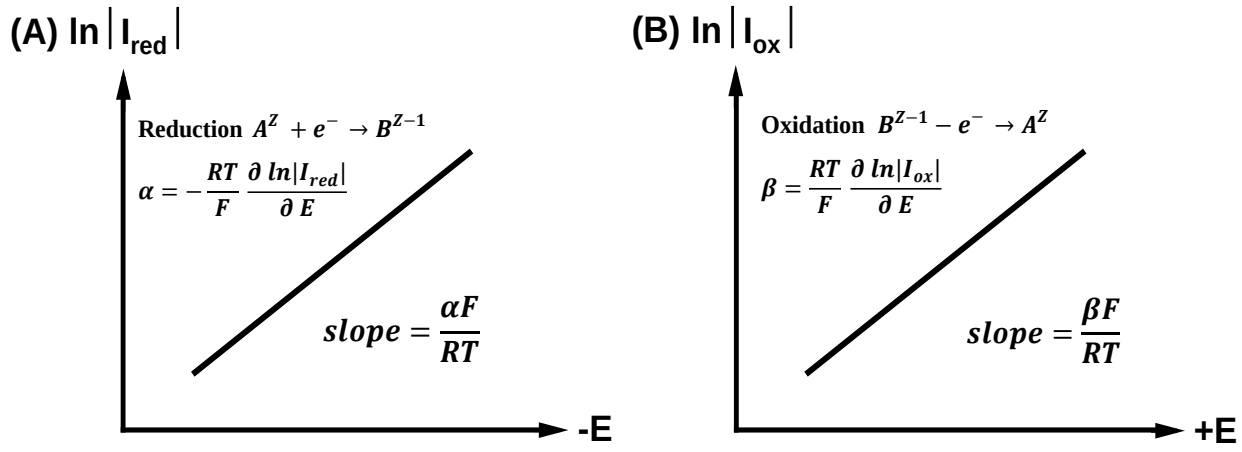


Figure.1.3 Tafel plots.

1.3 Electrode Processes

1.3.1 Electrochemical Cells

A typical electrochemical system mainly consists of three parts: an electrochemical control device known as a 'potentiostat', an electrochemical cell, and electrolyte. The electrochemical cell is basically composed of the *working electrode* (WE) as the electrode system of interest and the *reference electrode* (RE) with a fixed known potential [1]. The electrodes are immersed in the electrolyte and attached to the potentiostat. The potentiostat applies a fixed potential E between the working electrode and the reference electrode, which causes electrolysis in the cell so that current passes through the reference. Allowing for current, *I*, flow Eq (1.11) becomes:

$$\boldsymbol{E = (\phi_M - \phi_S)_{\,working} + IR_s - (\phi_M - \phi_S)_{\,reference}} \qquad (1.39)$$

where R_s is the solution resistance between the electrodes and IR_S is equal to a potential drop between the working electrode and reference electrode. When the working electrode is a microelectrode [14, 15], the passage of current (*I*) is extremely low (~ 10^{-9} A) so the *IR* term is negligible and can be neglected. Also, the tiny currents are such that the concentrations of the species fixing the potential of the reference electrode are barely perturbed so that the reference electrode maintains a fixed potential. This two-electrode with a microelectrode working electrodes cell can be used to determine the current-potential curve since changes in the applied

potential E are reflected directly in the term $(\phi_M - \phi_S)_{working}$, which is responsible for controlling the rate of the electrode reaction.

Otherwise, in experiments where the potential drop 'IR_s' may be high, part of the applied potential is 'lost' and hard to account for as the IR term is typically unknown. Further, the passage of large currents through the reference electrode significantly changes the concentrations of the species establishing the reference electrode potential so introducing a second source of uncertainty. In this situation, and typically when processes at a macro electrode are studied, a three-electrode cell (Fig.1.4) is usually preferable consisting of a *working electrode* (WE), a *reference electrode* (RE), and a *counter electrode* (CE). In this arrangement, the current is passed between the working electrode and counter electrode; no current passes through the reference electrode. Consequently, the potential of reference electrode will remain constant and equal to its open-circuit value since no electrolysis within the reference electrode occurs. Further the IR term is reduced since there is no current flowing into the reference electrode. In this way, changes in the applied potential appear directly as change in the electrochemical driving force, $(\phi_M - \phi_S)_{working}$ and quantitative measurement become possible.

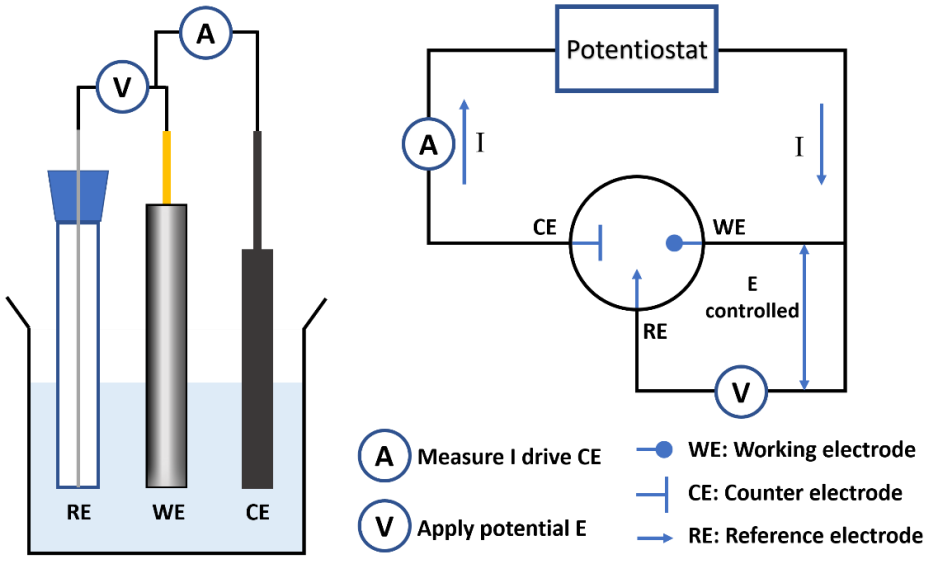


Figure.1.4 Schematic diagram of a three-electrode electrochemical cell.

1.3.2 Faradaic and non-Faradaic Processes

The current passing in an electrochemical cell as a result of applied potential can be of two basic types: *Faradaic* and *non-Faradaic* [16]. In *Faradaic* processes, in most cases the oxidation or reduction will occur through electron transfer across the electrode/electrolyte interface, from a conducting bulk phase to the electrolyte solution interface. According to Faraday's law of electrolysis [17, 18]:

$$\boldsymbol{m_i = \frac{QM}{nF}} \qquad (1.40)$$

where m_i is the mass (g) of the electroactive species produced or consumed at the electrode, Q is the total electric charge (C) transferred to or from the electrode, M is the molar mass (g mol^{-1}) of the species, n is the number of electrons transferred per species oxidised or reduced and F is the Faraday constant (96485 C mol^{-1}). It can be inferred that the moles of reactants involved in chemical reaction caused by the flow of current is proportional to the amount of electricity passed.

Instead, in *non-Faradaic* processes, there is no transfer of electrons across the electrode at all and charge is progressively stored when the current flows. This is because ions or other species are attracted to or repelled from the electrode and their arrival and departure induces the current flow which occurs without charge passing through the interface. Both *Faradaic* and *non-Faradaic* processes typically occur simultaneously during electrode reactions. Mostly we focus on investigating the *Faradaic* but so as to deconvolute the processes of interest, it is necessary to analyse the effects of the *non-Faradaic* processes on the charge transfer and related reactions.

It is found that the current-potential curves of different redox systems can be distinctly affected by the *electrical double layer,* depending on the charges of the solution-phase and adsorbed species and the concentrations of the latter along with that of any electrolyte present [19]. The driving forces for the formation of the *electrical double layer* are primarily Coulombic

but also reflect chemical interactions with the electrode surface. A schematic is depicted in Fig.1.5, the *inner layer* closest to the electrode consists of solvent molecules or sometimes other molecules or ions, often anions which have lost some of their solvating water, specifically adsorbed when applying different potentials at the electrode than that in the solution. This inner layer is also called the *compact*, *Helmholtz*, or *Stern layer* [20]. The *Inner Helmholtz Plane* (IHP) refers to the location between the electrode surface and the electrical centres of the specifically adsorbed ions where the term specific adsorption implies a strong chemical interaction of the ion with the surface. The *Outer Helmholtz Plane* (OHP) is the locus of centres of the nearest solvated ions which are not specifically adsorbed but involved in the interactions with the charged electrode only due to the long-range electrostatic forces. A *diffuse layer* extending from the OHP to the bulk solution contains both *non-specifically adsorbed* solvated anions and cations. The existence of these layers including the electrical double layer help to maintain electrical neutrality across the electrode-solution interface.

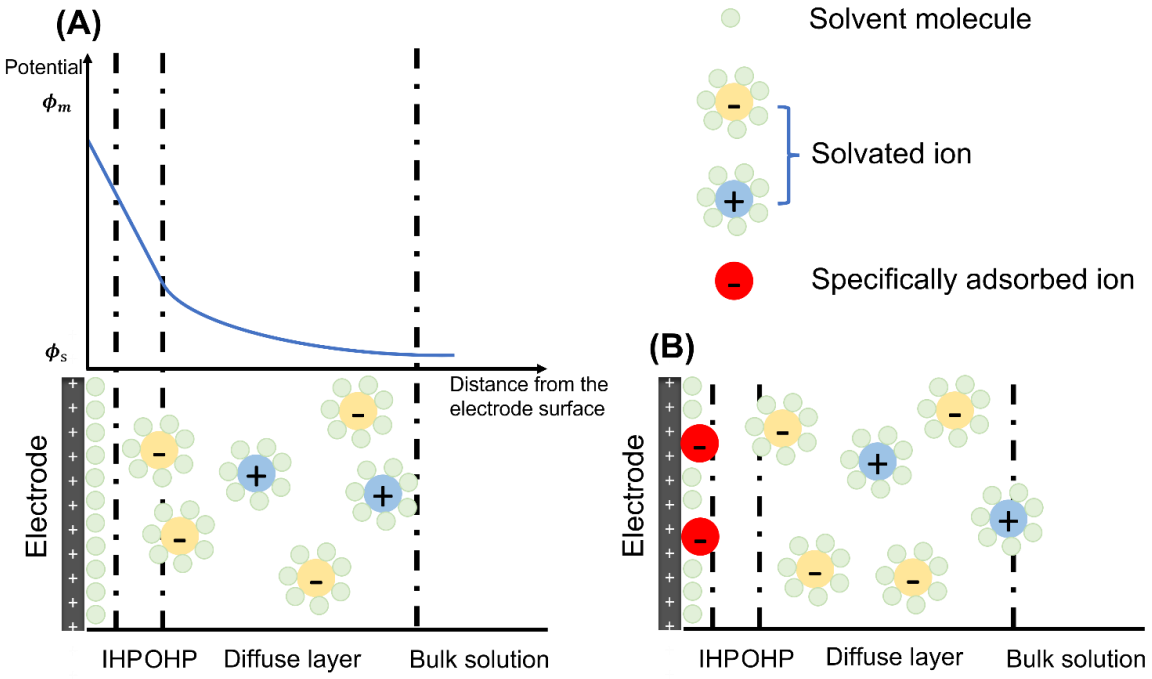


Figure.1.5 Proposed model of the double-layer region under conditions in the absence (A) and presence (B) of specific adsorption of ions. Top (A): potential profile across the double

layer under condition where anions are not specifically adsorbed.

The scale of the diffuse layer is parameterised by the *Debye length* [21]:

$$\chi_{DL} = \frac{1}{zF}\sqrt{\frac{\varepsilon_0 \varepsilon_r RT}{2C}} \tag{1.41}$$

where X_{DL} is the *Debye length* (Å), z and C are the charge and concentration of the species respectively, F is the Faraday constant (96485 C mol^{-1}), ε_0 is the permittivity of free space (8.854×10^{-12} C^2 J^{-1} m^{-1}), ε_r is the dielectric constant, R is the gas constant (8.314 J mol^{-1} K^{-1}) and T is the absolute temperature (K). The *Debye length* falls from 100 Å to 10 Å as the concentration of supporting electrolyte is increased from 1 mM to 0.1 M. Thus, in most electrochemical experiments, including voltammetry, electrolytes with high ionic concentrations are added to ensure the double layer remains within the critical range of 10-20 Å required for electron tunnelling (see above). This leads to the rapid, almost-linear drop of potential within the *compact layer* and the slow, gradual drop of potential from the *diffuse layer* to the bulk solution as shown in Fig.1.5 (A). The variation of potential profile in the presence of high electrolyte concentrations is such that across these layers that the potential drop, $\phi_M - \phi_S$, mainly occurs within the compact *Helmholtz layer* [22].

The structure of double layer can affect the currents seen when studying electrode processes, including the *non-Faradaic* current (often called the charging current or capacitive current, I_c) which arises due to the existence of the double-layer capacitance when the potential is swept in voltammetric experiments [1]:

$$I_c = \frac{dQ}{dt} = C_d A \frac{dE}{dt} = C_d A \upsilon \tag{1.42}$$

where Q is the charge (C), t is the time (s), C_d is the capacitance of the double layer per unit area (F m^{-2}), E is the applied potential (V) across the electrode/solution interface, A is the electroactive layer area (m^2) and υ is the scan rate (Vs^{-1}). Unlike real capacitors whose

capacitances are independent of the voltage across them, C_d is often a function of the potential. During electrode reactions involving very low concentrations of electroactive species, the *non-Faradaic* current can be much larger than the *Faradaic* current for the reduction or oxidation reaction and this masking provides a lower limit for the concentrations which can be probed analytically via voltammetry.

1.3.3 Mass Transport

The electrode process is a heterogeneous reaction occurring at the electrode-electrolyte interface. In section 1.2, we discussed the electrode kinetics for a given concentration of the species on the electrode surface. However, considering practical cases, the electrode reaction rate depends on not only the rate of the electron transfer as mentioned above, but also the mass transport, and various surface effects (adsorption, desorption, or crystallization), in addition to the usual kinetic variables [23]. Considering an actual overall electrode reaction for Eq. (1.16), the conversion of the dissolved oxidized species A^Z to a reduced form B^{Z-1} goes through a series of steps across the electrode-solution interface as summarized in Fig.1.6.

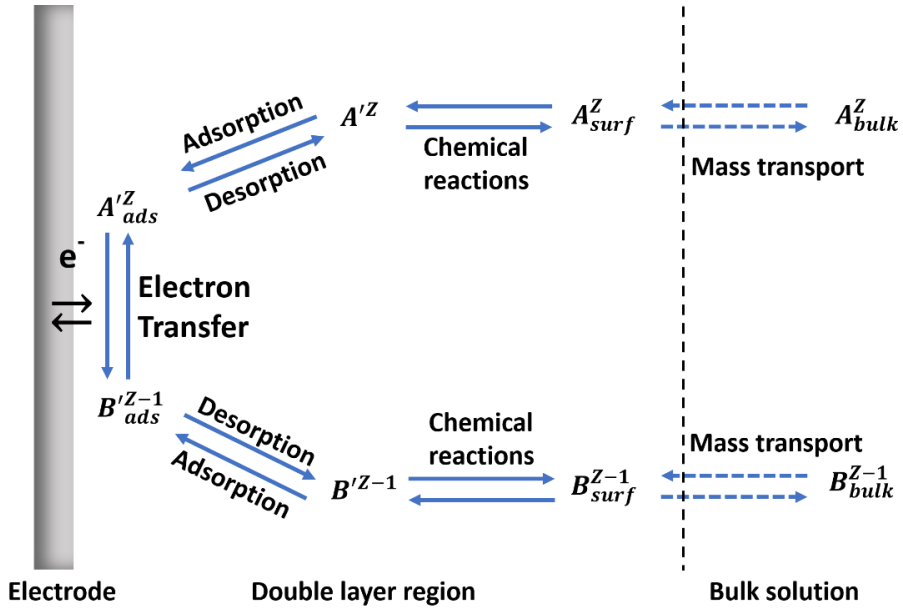


Figure.1.6 Pathway of a general electrode reaction.

In particular, if the electron transfer rate is fast, the magnitude of current is often limited

by the mass transport. The latter refers to the movement of material from one location to another in solution caused by electrical or chemical potential differences at the two locations or from mechanical disturbances. The *Nernst-Planck equation* [24] illustrates the one-dimensional mass transport along the x-axis:

$$\boldsymbol{J_j(x)} \;=\; -\boldsymbol{D_j}\frac{\boldsymbol{\partial C_j(x)}}{\boldsymbol{\partial x}} - \frac{\boldsymbol{z_j F}}{\boldsymbol{RT}}\boldsymbol{D_j C_j}\frac{\boldsymbol{\partial \phi(x)}}{\boldsymbol{\partial x}} + \boldsymbol{C_j v(x)} \qquad (1.43)$$

where $J_j(x)$ is the flux of species j (mol s^{-1} cm^{-2}) at distance x from the electrode surface, D_j is the diffusion coefficient (cm^2 s^{-1}), $\frac{\partial C_j(x)}{\partial x}$ and $\frac{\partial \phi(x)}{\partial x}$ are the concentration and potential gradients at distance x respectively, z_j and C_j are the ionic charge (dimensionless) and concentration (mol cm^{-3}) of species j, respectively, and $v(x)$ is the local fluid velocity (cm s^{-1}). The three separate terms on the right-hand side of Eq. (1.43) represents three modes of mass transport: *diffusion*, *migration* and *convection*, which will be introduced below sequentially.

Diffusion, as the most prevailing phenomenon of the three modes of mass transport, takes place spontaneously from high to low concentration. Applying a suitable potential to the electrode, the consumption of the reactant through reductive or oxidative chemistry at the electrode surface results in a concentration depletion of this species surrounding the electrode, forming a region in the vicinity of the electrode with concentration gradient between the electrode and bulk solution defined as *diffusion layer* shown in Fig.1.7 [25]. The *Nernst diffusion layer* thickness (d) is noted as the distance at which the linear concentration profile (obtained from the tangent to the concentration profile curve at the electrode surface) takes its bulk value. *Fick's 1st law* [26] of diffusion quantifies the diffusive flux down the concentration gradient in one dimension, x:

$$\boldsymbol{j} = -\boldsymbol{D}\frac{\boldsymbol{\partial c}}{\boldsymbol{\partial x}} \qquad (1.44)$$

where j is the flux (moles s^{-1} cm^{-2}) representing the number of moles of species passing through the unit area in unit time, D is the diffusion coefficient (cm^2 s^{-1}) with a typical magnitude in the

range in aqueous solution between 10^{-6} and 10^{-5} cm^2 s^{-1} and $\frac{\partial c}{\partial x}$ is the concentration gradient at distance x.

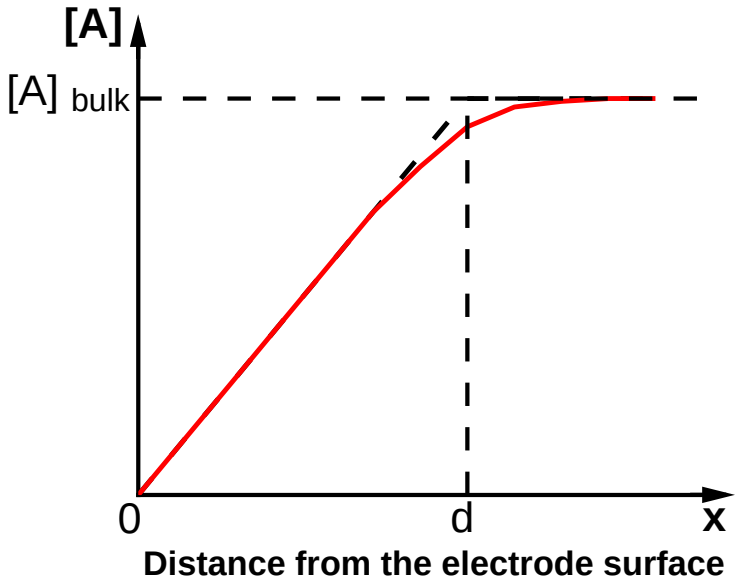


Figure.1.7 Definition of the Nerenst diffusion layer.

Taking the parameter time '*t*' into account for the variation of the concentration of species at point x, *Fick's 2nd Law* [27] is used to describe the rate of change of concentration at the point x:

$$\frac{\partial C}{\partial t} = D\frac{\partial^2 C}{\partial x^2} \qquad (1.45)$$

To appreciate its molecular basis, Fick's law in one dimension can be illustrated as shown in Fig 1.8. At a general point x on an arbitrary concentration-distance profile, a 'box' of width 2 δx is divided into two 'half boxes' of the same width δx, each of which allows molecules to move to the right or to the left inside with equal probabilities. Assuming the molecule moving a distance δx within the average time δt, the number (moles) of molecules travelling from left to right is $\frac{1}{2}C_1 A\delta x$, similarly, the number travelling from right to left is $\frac{1}{2}C_2 A\delta x$, where C_1, C_2 are the concentration of solutions separated at point x and A is the cross-section area.

Hence, the net rate of transfer through a plane positioned at *x* can be written as:

$$\boldsymbol{Rate_{net} = \frac{(C_1 - C_2)A\delta x}{2\delta t}} \quad (1.46)$$

Considering the flux (J) is expressed as:

$$\boldsymbol{J = \frac{(C_1 - C_2)\delta x}{2\delta t}} \quad (1.47)$$

The concentration gradient $\frac{\partial C}{\partial x}$ can be approximated to $-\frac{(C_1 - C_2)}{\delta x}$, so that

$$\boldsymbol{J = -\frac{(\delta x)^2}{2\delta t}\frac{\partial C}{\partial x}} \quad (1.48)$$

which is equivalent to *Fick's 1st law* (Eq. (1.44)) if

$$\boldsymbol{D = \frac{(\delta x)^2}{2\delta t}} \quad (1.49)$$

In this way, the diffusion coefficient (D) of a molecule reflects the distance of it diffuses in solution in a certain time. The root mean square displacement in time (t) leads to the *Einstein-Smoluchowski equation* [28]:

$$\boldsymbol{\sqrt{< x >^2} = \sqrt{2Dt}} \quad (1.50)$$

Eq. (1.50) plays an important role in voltammetry in estimating the thickness of the diffusion layer, d (cm) [29]. Extending the diffusion from one dimension to three dimensions, the root mean square distance is:

$$\boldsymbol{\sqrt{< x >^2 + < y >^2 + < z >^2} = \sqrt{6Dt}} \quad (1.51)$$

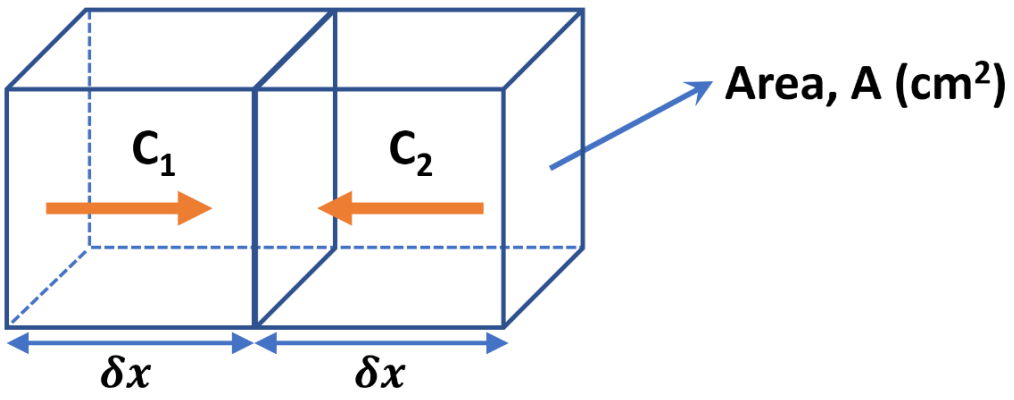


Figure.1.8 The molecular basis of Fick's 1st Law in one dimension.

Migration is the movement of charged particles in response to a local electric field and occurs predominatly in the bulk solution away from the electrode where the concentration gradients which drive diffusion are tiny. Under this condition, the total current is carried mainly by migration contributed by all charged species whether electroactive or not. For species *j* in the bulk region, the migratory flux can be determined as:

$$\boldsymbol{J_{m,j}(x) = -\frac{z_j F}{RT} D_j C_j \frac{\partial \phi(x)}{\partial x}} \qquad (1.52)$$

where $J_{m,j}(x)$ is the migratory flux (mol s^{-1} cm^{-2}), z_j is the charge of the ion *j*, C_j is the concentration of the ion (mol cm^{-3}) and $\frac{\partial \phi(x)}{\partial x}$ is the potential gradient (or electric field, V cm^{-1}).

In general, an electroactive substance near the electrode is transported by both diffusion and migration processes. The total flux (J_j) of the electroactive species *j* can be separated into the diffusive and migrational components of the flux, expressed as $J_{d,j}$ and $J_{m,j}$. Note that $J_{d,j}$ and $J_{m,j}$ may be in the same or opposite direction depending on the direction of the electric field and the charge on the electroactive species. For cationic species reacting at cathodes or anionic species reacting at anodes, $J_{d,j}$ and $J_{m,j}$ are always in the same directions; for cations are oxidized at anodes or anions are reduced at cathodes, $J_{d,j}$ and $J_{m,j}$ are in the opposite directions. Detailed examples of different directions of migratory flux in a reduction process are shown in Fig.1.9.

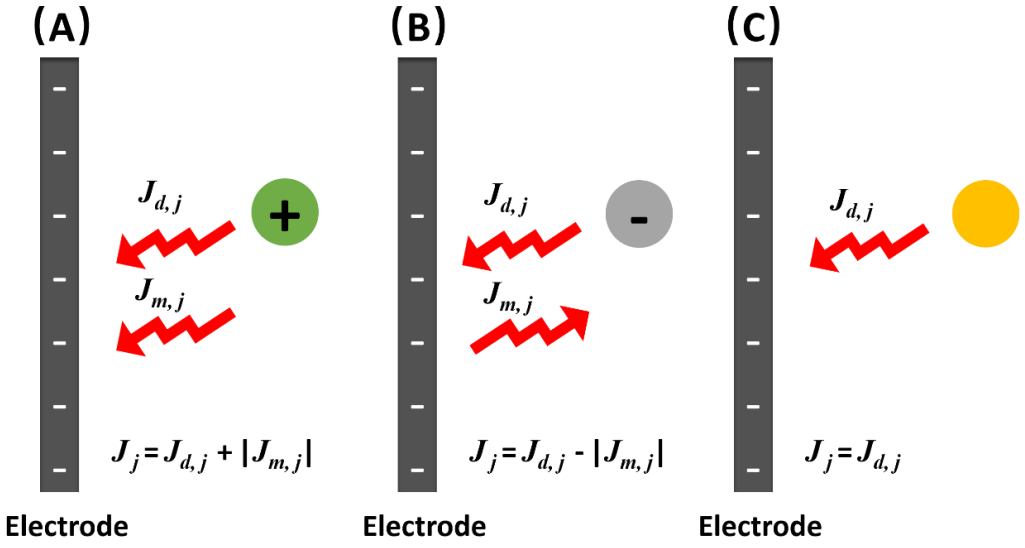


Figure.1.9 Examples of a reduction process with different directions of migratory flux: (A) postively charged reactant; (B) negatively charged reactant; (C) uncharged reactant.

Since the majority of analytical theory in electrochemistry assumes diffusion-only conditions, the presence of migration effects can make the experimental data complicate to analyze and have to be eliminated from the mass transport of solution phase species. Thus, a supporting electrolyte containing non-electroactive ions at a higher concentration level than that of the electroactive substances is usually added to an electrochemical experiment, for the main purpose of confining the differences of potential to a narrow region close to the electrode where most of the electroactive ions can diffuse to the electrode surface to react [30]. This is, as also emphasised above, essential to ensure the double layer within 10-20 Å serving for the electron transfer by mechanical quantum tunnelling and the migratory flux with the term $\frac{\partial \phi(x)}{\partial x}$ is hence reduced to negligible levels. In addition, the presence of supporting electrolyte reduces the solution resistance and helps to further minimize the resistance drop between the working and reference electrode (see Section 1.3.1), consequently improves the accuracy of controlling or measuring the working electrode potential. A uniform and high ionic strength throughout the solution is vital to ensure the consistent activity of the redox couple and facilitate the use of formal potentials (see Section 1.1), even when ions are produced or consumed at the electrodes.

Finally, *Convection*, a phenomenon resulting from an imbalance of forces on the solution, can be distinguished into two types [31]: natural convection and forced convection. Natural convection arises from density differences and arises from concentration or thermal gradients brought about either by the electrolysis itself or by imperfect thermostatting of the electrolyte. In most electrochemical experiments, e.g. cyclic voltammetry (CV) or chronoamperometry (CA), where a heterogeneous reaction perturbs the local concentration and density profiles, the mass transport by natural convection is rendered negligible by way of using a suitable orientation of the electrode, replacing macroelectrodes by the microelectrodes or performing measurements only at short times [32]. As for forced convection, it usually arises from some motion deliberately introduced by the experimenter, for example, the mechanical agitation in solution via stirring, electrode rotation, bubbling gas or pumping. Such actions yield irreproducible results unless careful attention is paid to the geometry of the system and to ensure control of the imparted motion via for example rotating disks [33, 34] or channel electrodes [35, 36]. so-called hydrodynamic methods [37] often involving measurements at steady state where double-layer charging is avoided.

Henceforth in this thesis, we only consider the influence from diffusion this kind of mass transport on the voltammetric behaviour; migration and convection are minimised and hence neglected in all experiments reported.

1.4 Electrochemical Techniques

The above sections described theoretical concepts in electrochemistry. Next, we will introduce four practical electrochemical techniques utilized in the latter experimental chapters: cyclic voltammetry, square wave voltammetry, chronoamperometry and nano-impacts. Among those methods, the measurement of the current is conducted as a function of time or potential via pre-setting the working electrode potential to be either constant or changed with time.

1.4.1 Cyclic Voltammetry

Cyclic voltammetry (CV) is the most important and most widely utilized electrochemical technique in the entire field of voltammetry [38]. In cyclic voltammetry, the current flowing through the working electrode is recorded as a function of applied potential varied with a triangular waveform over time. As shown in Fig 1.10, the scan begins at a potential (E_1) usually chosen where no oxidation or reduction of the analyte of interest occurs, then sweeps linearly at a constant scan rate ($\boldsymbol{\upsilon}= \frac{\partial E}{\partial t}$, Vs^{-1}) to a predetermined potential (E_2), at which point the oxidation or reduction process is fully driven. After that, the direction of scan is reversed and the working electrode potential is usually swept back to its original value (E_1). Fig. 10 shows that the 'linear' ramp is typically performed digitally consisting of multiple small potential steps ('staircase'). The current is successively recorded at a constant position within each potential step. The '*voltammogram*' is a display of current *I* (vertical axis) versus potential *E* (horizontal axis).

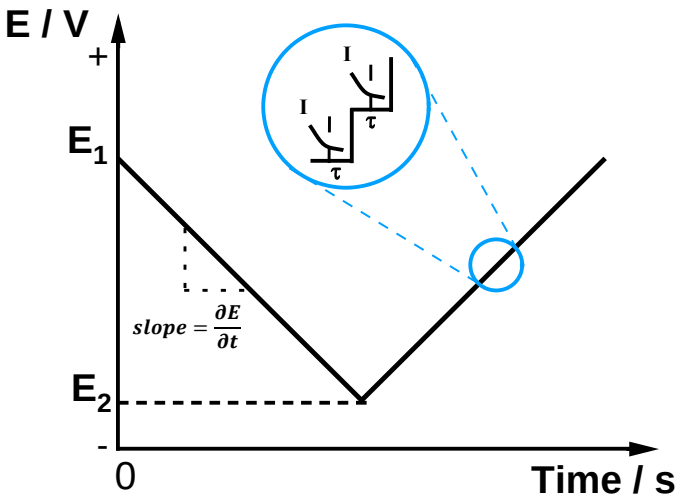


Figure.1.10 The potential-time of a cyclic voltammogram for a reduction. The inset expands the steps at each of which current is recorded at t =τ measured from the start of eah step.

The shape of a voltammogram is determined by the absolute and relative rates of electron transfer and mass transport. Based on these factors, we will discuss the cyclic voltammetric

features for a one-electron transfer reduction process observed at two types of working electrodes: macroelectrodes and microelectrodes, characterized according to their size. Macroelectrodes have a dimension on a scale of millimetres or centimetres while a microelectrode has its dimension on the scale of micrometres [15]. One of the key differences between them is demonstrated in diffusion patterns, as shown in Fig 1.11. Macroelectrodes have a much larger radius than the thickness of diffusion layer ($r_e \gg d$), so that linear diffusion occurs during the electrolysis (Fig 1.11 (A)) leading to a planar diffusion layer in shape and, in the cyclic voltammetry, a peak shaped response. In contrast significant convergent diffusion ('edge effects') occurs at microelectrodes (Fig 1.11(B) and (C)) due to a smaller or comparable radius of microelectrodes relative to the thickness of diffusion layer ($r_e \ll d$), resulting in an approximately hemispherical shaped diffusion layer, enhanced rates of mass transport and the disappearance of characteristic 'peak' which is replaced by a steady-state limit (Fig 1.11 (B)). In addition, the small dimensions of microelectrodes help to reduce capacitance and since, they draw only tiny currents, minimise ohmic drop (Section 1.2). Because microelectrodes have efficient form of mass transport in comparison with macroelectrodes, the utilization of microdisc electrodes is more suitable for the measurement of faster electrode kinetics [39]. Meanwhile, microwire electrodes are also commonly used for electrochemical characterization of carbon nanotubes in this thesis where the electrode has one macro-dimension (length) and one micro-diemnsion (radius) so presenting a compromise of much larger surface area than a microdisc electrode so allowing for more collisions of the tubes with the electrode and the reasonably high mass transport rate conferred by the micro-dimension. For such electrodes a quasi-steady state is observed in the voltammetric current in contrast to the true steady state seen at a microdisc electrode. In practice, the microwire electrode is made from a cylindrical carbon fibre with a length of around 1 mm and a diameter around 7 μm (the detailed preparation process is described in Chapter 2). The mass transport towards the cylindrical microwire

electrode are demonstrated in a combination mode: linear diffusion at the side and convergent diffusion at the end (Fig 1.11(C)).

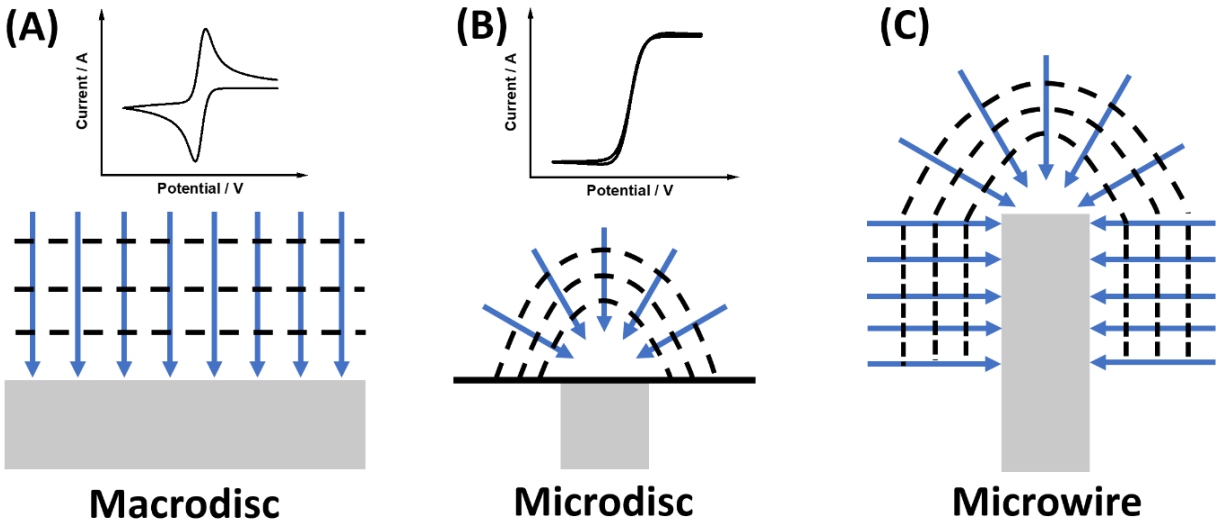


Figure.1.11 Diffusion at a macrodisc (A), microdisc (B) and microwire (C) electrodes. Arrows: diffusion of electroactive species. Dashed line : the diffusion layers. Top (A) and (B) are the typical cyclic voltammograms of macrodisc and microdisc electrodes respectively.

For a simple electron transfer process, the standard electrochemical rate constant k^0 introduced in Section 1.2 can have 'large' or 'small' values leading to voltammetry with the labels 'electrochemically reversible' or 'electrochemically irreversible' respectively, corresponding to 'fast' and 'slow' electrode kinetics where fats and slow is relative to the rate of mass transport as described in the next section. Considering Eq. (1.1) $A^{Z}_{(aq)} + e^{-}_{metal} \rightleftarrows B^{Z-1}_{(aq)}$, where both A^{Z} and B^{Z-1} are solution phase species, the cyclic voltammetry for different levels of reversibility of this redox process on a macrodisc electrode (Fig 1.12 (A)) and a microdisc electrode (Fig 1.12 (B)) can be compared by scanning the potential from positive (E_1) to negative (E_2), then reversed to E_1. In Fig 1.12 (A) for macroelectrodes, it is found that from the green curve (*electrochemically reversible*) to red curve (*electrochemically quasi-reversible)* finally to blue curve (*electrochemically irreversible*), the peak-to-peak separation of the forward (reductive) and back (oxidative) peak ($\Delta E_{pp} = |E_p(anodic) - E_p(cathodic)|$)

gradually increases with the decrease of both peak currents (I_p). As for Fig 1.12 (B) for microelectrodes, the half-wave potential ($E_{1/2}$, V) representing the potential in which the current is half of the steady-state current ($I = \frac{I_{ss}}{2}$, A) is noticed to shift more negatively as the curve from electrochemically reversible (green) to quasi-reversible (red) and irreversible (blue) with a slower current increase with voltage. The reversibility for macroelectrodes and microelectrodes will be further discussed separately in the next subsections

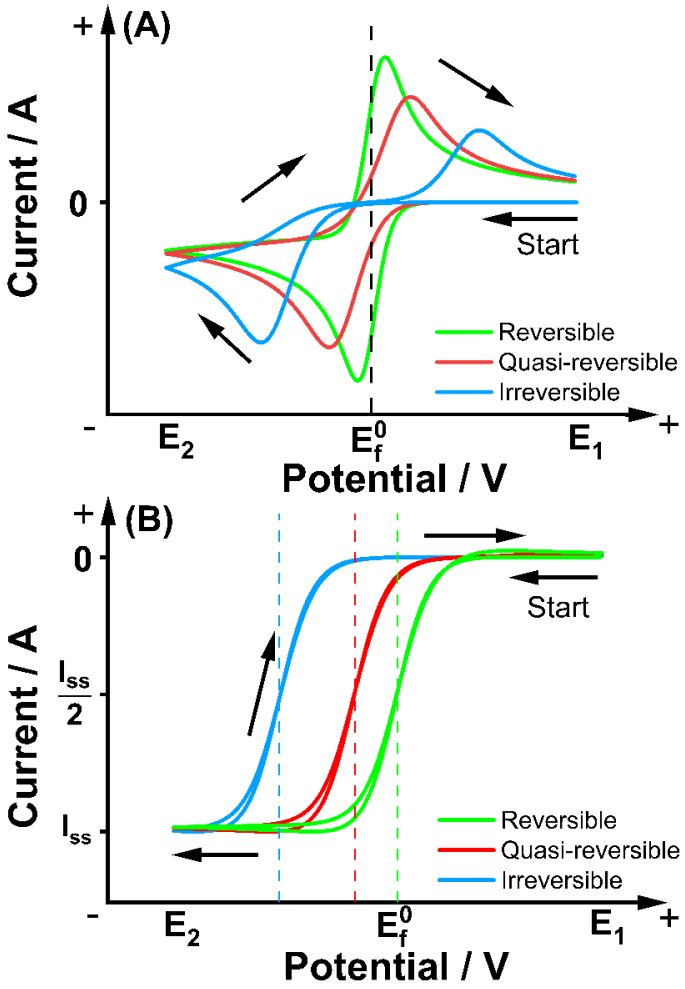


Figure.1.12 Voltammetric scans for the reversible, quasi-reversible and irreversible reduction of diffusive species at (A) macrodisc electrodes and (B) microdisc electrodes. Arrows show the starting point and scan direction. Vertical dashed lines in (B) represents the half-wave potential at each system with different reversibility. All the voltammograms were simulated by FreeSim electrochemical reaction simulator V1.0 [42]**.**

1. Voltammetry at macroelectrodes

To define the distinction between fast and slow electrode kinetics (namely electrochemically reversible, quasi-reversible and irreversible process) at macroelectrodes, we usually compare the standard electrochemical rate constant, k^0, with the mass transport coefficient, m_T (cm s^{-1}),

where

$$\boldsymbol{m_T = \frac{D}{d}} \tag{1.53}$$

D is the diffusion coefficient of the species (cm^2 s^{-1}) and d is the diffusion layer thickness (cm). According to Eq. (1.50), the latter depends on time (*t*) which can be related to the scan rate (v):

$$\boldsymbol{t \propto \frac{RT}{Fv}} \tag{1.54}$$

so that m_T can be estimated

$$\boldsymbol{m_T \propto \sqrt{\frac{FDv}{RT}}} \tag{1.55}$$

By introducing the *Matsuda and Ayabe parameter*, Λ, the limits of reversibility can be evaluated [40, 41]:

$$\boldsymbol{\Lambda = \frac{k^0}{\sqrt{\frac{FDv}{RT}}}} \tag{1.56}$$

The following ranges for three different classifications at macroelectrodes were inferred:

Reversible

$$\Lambda \geq 15, k^0 \geq 0.3\sqrt{v}\ cm\ s^{-1}$$

Quasi-reversible

$$15 > \Lambda > 10^{-3}, 0.3\sqrt{v} > k^0 > 2 \times 10^{-5}\sqrt{v}\ cm\ s^{-1}$$

Irreversible

$$\Lambda < 10^{-3}, k^0 \leq 2 \times 10^{-5}\sqrt{v}\ cm\ s^{-1}$$

where *T*, *D* relate to 298 K and 1×10^{-5} cm^2 s^{-1} and α is assumed ~ 0.5.

In principle, all electrochemical processes can appear to be electrochemically irreversible at sufficiently fast scan rates according to the *Matuda-Ayabe* conditions.

It is insightful to analyze the variation of the peak current (I_p) and peak potentials (E_p) as a function of scan rate. Returning to Fig 1.12 (A), at the initial E_1 to relatively positive potentials, no current flows because the potential is insufficient negative in comparison with the reduction potential from A^Z to B^{Z-1}. For an electrochemically reversible system (green curve), the reductive current starts to flow at potentials around the formal potential (E_f^0) of the A^Z-B^{Z-1} couple and the concentration of A^Z and B^{Z-1} at the electrode surface are related by the *Nernst Equation*. In the irreversible case (blue curve), the electrode kinetics are so 'slow' (relative to the rate of mass transport). Following the *Butler-Volmer* equation, with increasing potential, the peak corresponding to the reduction of A^Z is achieved when the electron transfer rate is balanced by the diffusion rate of A^Z. As the potential continues moving more negatively, the current decreases because the diffusion rate of A^Z is not sufficient to replenish the material depleted at the electrode surface. Then in the reverse scan, the accumulation of high-concentration B^{Z-1} in the electrode's vicinity drives the electrochemical balance towards the reconversion of B^{Z-1} to A^Z, leading to an anodic current from the oxidation of B^{Z-1} and a similar peak shape with the forward scan for the same essential reasons.

To summarize, three diagnostics can identify the reversible and irreversible voltammetry for a one-electron transfer process at macroelectrodes:

1) Peak to peak separation, ΔE_{pp}

It is clear from Fig 1.12 (A) that the increasing irreversibility leads to the greater ΔE_{pp}. In a fully reversible system, ΔE_{pp} is independent of scan rate and has a value of 57.4 mV at 298 K. In contrast under quasi- and irreversible systems, ΔE_{pp} is a function of scan rate [43].

2) Mid-point potential of the forward and back peak, E_{mid}

The mid-point potential ($E_{mid} = \frac{E_{p,forward}+E_{p,reverse}}{2}$) can be expressed with the formal potential (E_f^0) in the reversible and irreversible limit:

Reversible:

$$\boldsymbol{E_{mid} = E_f^0 + \frac{RT}{2F} ln (\frac{D_{B^{z-1}}}{D_{A^z}})} \quad (1.57)$$

Irreversible, assuming α = β = 0.5:

$$\boldsymbol{E_{mid} = E_f^0 + \frac{RT}{F} ln (\frac{D_{B^{z-1}}}{D_{A^z}})} \quad (1.58)$$

When the diffusion coefficient of A and B are equal ($D_{A^z} = D_{B^{z-1}}$), $E_{mid} = E_f^0$.

3) Peak current, I_p

According to *Randles-Sevcik* equations [44], for a one electron transfer process involving freely diffusing species A^z under reversible and irreversible conditions, I_p (A) is respectively given by:

Reversible $$\boldsymbol{I_p = 0.446FA_e[A^Z]_{bulk}\sqrt{\frac{FD_{A^z}v}{RT}}} \quad (1.59)$$

Irreversible $$\boldsymbol{I_p = 0.496\sqrt{\alpha}FA_e[A^Z]_{bulk}\sqrt{\frac{FD_{A^z}v}{RT}}} \quad (1.60)$$

where A_e is the surface area of electrode (cm^2), $[A^Z]$ and D_{A^z} are the bulk concentration (mol cm^{-3}) and the diffusion coefficient ($cm^2\ s^{-1}$) of species A^Z, v is the scan rate (Vs^{-1}), α is the transfer coefficient.

In the case above all species participating in the electrode process are present in the solution phase. Another common phenomenon is that the reactant and product adsorb on the surface of electrode and a distinctive voltammetry is obtained relative to that of the diffusive species [45]. Supposing that both surface-bound species A and B undergo the following redox process:

$$\boldsymbol{A}\,(\boldsymbol{ads}) + \boldsymbol{e}^{-} \rightarrow \boldsymbol{B}\,(\boldsymbol{ads}) \qquad (1.61)$$

Fig 1.13 shows the ideal shapes of the associated voltammograms undergoing a reversible and irreversible process. The current falls to zero at potentials beyond the peak due to the finite quantity of electroactive species adsorbed on the electrode surface, which makes the peak shape dependent solely on the rate of electron transfer. The forward and back current response from reversible voltammetric wave are symmetric about the zero-current axis (green curve).

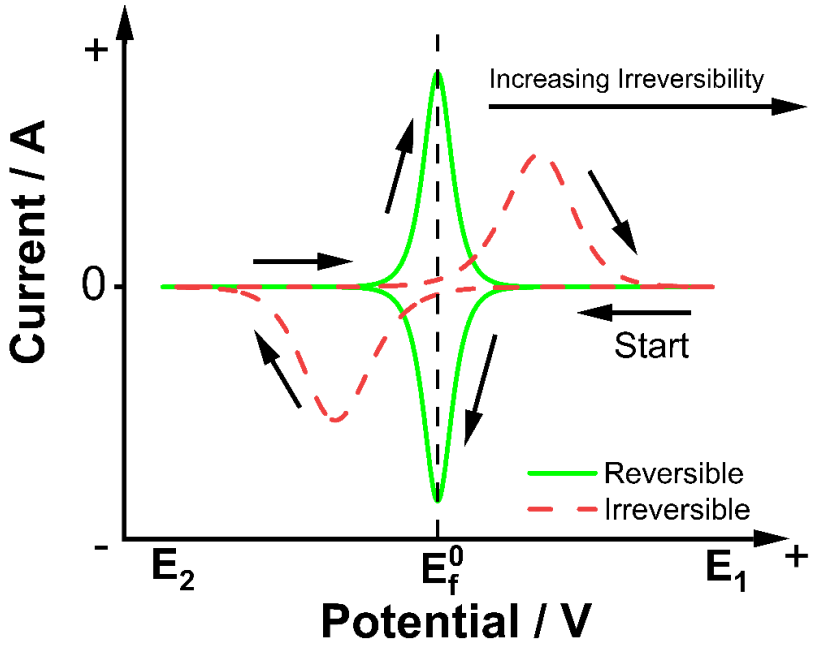


Figure.1.13 Typical cyclic voltammogram for a reversible or irreversible process for surface bound species generated by FreeSim electrochemical simulator [42]**.**

The formal potential is the potential location of two identical peaks in the forward and back scan respectively. In the irreversible case, the voltammetric feature is distorted and a pair of asymmetric waves shift to either side of the formal potential (red curve) with the greater ΔE_{pp} and decreasing peak following the slow electron transfer kinetics. For an electrode-adsorbed species, the current response is described by [46]:

Reversible $$\boldsymbol{I_p = \frac{F^2}{4RT} v A_e \Gamma_A^0}$$ (1.62)

Irreversible $$\boldsymbol{I_p = \frac{\alpha F^2}{2.718RT} v A_e \Gamma_A^0}$$ (1.63)

where Γ_A^0 is the surface coverage of reactant at the electrode surface (mol cm^{-2}). Other terms have been defined in previous sections. In contrast to the case of solution phase voltammetry where it scales with the square root of the scan rate, I_p in adsorption-controlled voltammetry is directly proportional to the voltage scan rate.

2. Voltammetry at microelectrodes

The cyclic voltammetry seen using microelectrodes differs significantly from that at macroelectrodes. At sufficiently low scan rates, steady-state behaviour is achieved since the convergent diffusion at microelectrodes provides a constant replenishment of electroactive species from bulk solution to electrode surface. The steady-state current at a micro-disc electrode, I_{ss} (A) can be expressed by:

$$\boldsymbol{I_{ss} = 4nFD_{A^z}[A^Z]_{bulk} r_e} \quad (1.64)$$

where r_e is the radius of the micro-disc electrode (cm).

Fig 1.12 (B) shows the three kinetic limits corresponding to various voltammetric behaviour at a micro-disc electrode. These have increasing irreversibility from the green curve to the blue curve as quantified using a parameter κ_0:

$$\boldsymbol{\kappa_0 = \frac{r_e k^0}{D}} \quad (1.65)$$

where r_e is the radius of the electrode (cm), k^0 is the standard electrochemical rate constant (cm s^{-1}) and D is the diffusion coefficient (cm^2 s^{-1}). The boundaries of the three kinetic zones at microelectrodes are [47]:

Reversible $\kappa_0 > 10$

Quasi-reversible $10 \geq \kappa_0 \geq 10^{-2\alpha}$

Irreversible $\kappa_0 \leq 10^{-2\alpha}$

Note α is the transfer coefficient.

The reversibility of voltammetry is also identified by the half-wave potential ($E_{1/2}$) where half of the steady-state current ($I = \frac{I_{ss}}{2}$) is observed. $E_{1/2}$ can be related to E_f^0 in the reversible and irreversible limits:

Reversible: $$\boldsymbol{E_{1/2} = E_f^0 + \frac{RT}{F} ln(\frac{D_{B^{z-1}}}{D_{A^z}})} \quad (1.66)$$

Irreversible: $$\boldsymbol{E_{1/2} = E_f^0 + \frac{RT}{\alpha F} ln(\frac{r_e k^0}{D_{A^z}})} \quad (1.67)$$

When $D_{A^z} = D_{B^{z-1}}$, $E_{1/2} = E_f^0$ for the reversible process as shown by the green curve from Fig 1.12 (B). As for the irreversible process, the $E_{1/2}$ for redox couple A^Z/B^{Z-1} is dependent on the electrochemical rate constant.

1.4.2 Square Wave Voltammetry

Square wave voltammetry (SWV) is a powerful electrochemical technique suitable for mechanistic study of electrode processes in solution-phase and surface-confined redox systems but most often applied analytically because of its higher sensitivity over CV. The typical potential modulation used in SWV consists of a staircase potential ramp modified with square-shaped potential pulses (Fig 1.14(B)). At each step of the staircase ramp, two equal in height and oppositely directed potential pulses are imposed to drive both anodic and cathodic electrode reactions (Fig 1.14 (A)) [48].

The duration of single potential cycle (t_s) or equivalently the duration of a single potential pulse ($t_p = \frac{1}{2} t_s$) can be altered in terms of the square wave *frequency*, $f = \frac{1}{t_s}$ *or* $\frac{1}{2t_p}$. As the waveform is characterised by a pulse height (ΔE_p), the staircase height (ΔE_s) and square wave frequency (f), the overall potential modulation can be related to the scan rate ($\boldsymbol{\upsilon}$) defined as [49]:

$$v = \frac{\Delta E_s}{2t_p} = f\Delta E_s \qquad (1.68)$$

Note that ΔE_p controls the resolution of voltammetric features because of its much larger value relative to ΔE_s in practical experiments.

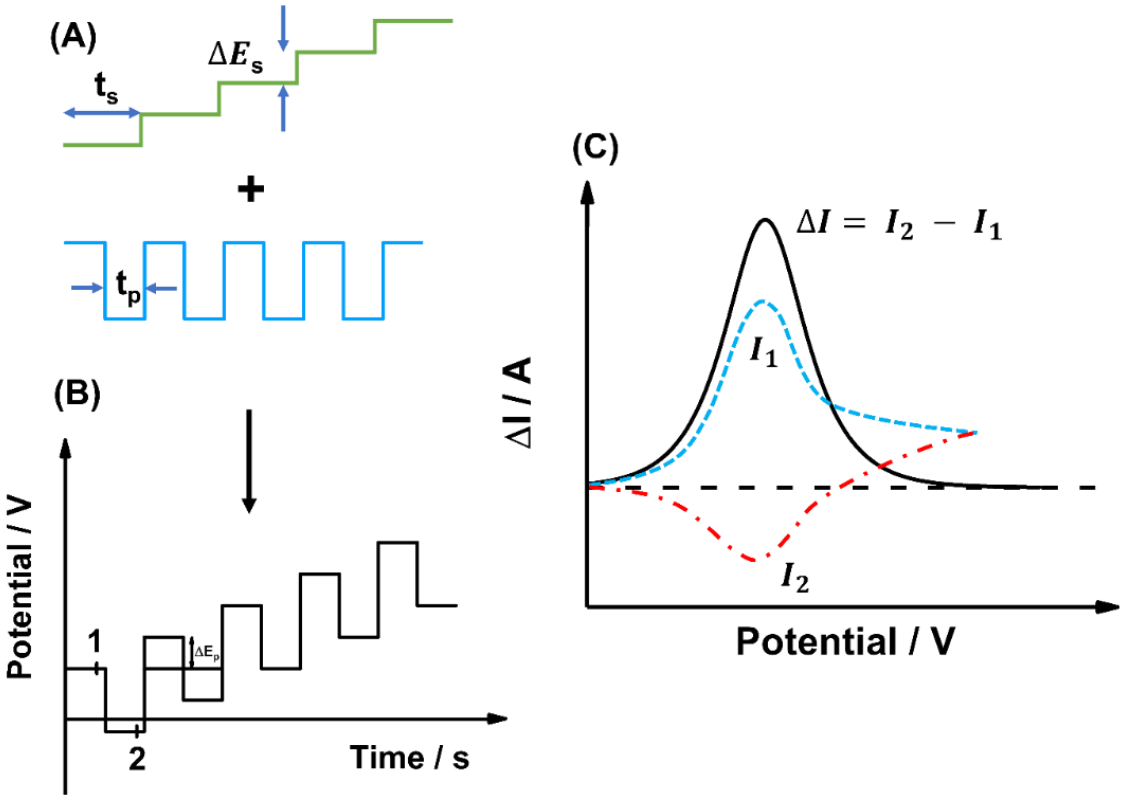


Figure.1.14 Illustration of potential cycles (A) and waveform (B) for SWV; (C) voltammetric profiles obtained from a SWV scan.

During each square wave cycle, two current values are assigned as I_1 and I_2 at the end of forward and reverse potential pulse respectively. The difference between I_1 and I_2 ($\Delta I = I_2 - I_1$) is plotted against the stair-case potential to create the square wave voltammogram (black curve in Fig 1.14 (C), blue and red dashed curves describe I_1 and I_2 as a function of the staircase potential). This subtraction procedure of the forward and backward currents contributes further in cancelling out the double layer charge current as mentioned in Section 1.3.2 enhancing the sensitivity of measuring Faradaic current. The application of SWV in improving the sensitivity of electrochemical sensors is reported in Chapter 4.

1.4.3 Chronoamperometry

Chronoamperometry is a technique frequently used in electroanalysis [50]. Specifically, it is initiated by stepping the potential E_1 where usually no electrolysis occurs to E_2 at which electrolysis of interest proceeds (Fig.1.15 (A)), then the resulting current versus time is observed. At the onset of potential step, no Faradaic current but only background current arises from bulk solution to the electrode surface. When the potential is stepped to E_2, the redox reaction of the electrochemically active species in interest takes place leading instantly to a significant current response. If the reaction of the electrochemically species at the electrode surface is diffusion limited, this Faradaic current near the electrode surface decays to zero (for a macroelectrode under linear-diffusion control) or to a steady-state value (for a microelectrode under convergent diffusion) over time due to the continuous consumption of the reactants in the vicinity of electrode surface [51], as shown in the Fig.1.15 (B) and (C) below.

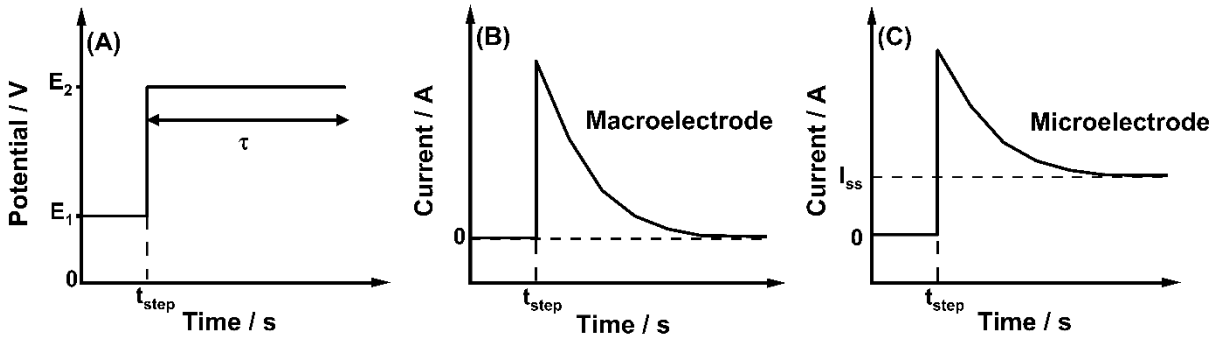


Figure.1.15 (A) The potential-time profile for a single step chronoamperometry. The chroamperometic current as a function of time at (B) a macroelectrode and (C) a microelectrode.

1.4.4 Nano Impacts

A nanomaterial refers to a material with at least one nanoscale (1-100 nm) dimension according to the guidelines of IUPAC (International Union of Pure and Applied Chemistry) [52]. Nanomaterials are widely applied in the field of electrocatalysis, electrochemical sensing and

other fundamental electron transfer studies [53] owing to their controllable structure-dependent properties such as large specific surface area, good electronic conductivity, high density of active sites and diversity of functionalization [54]. Carbon nanotubes (CNTs) as a representative type of carbon-based nanomaterials have aroused considerable interest in both fundamental and applied electrochemistry[55, 56]. The factors explaining the electrochemistry of CNTs includes their structure (e.g. 'edge-like' defects in CNT walls [57]) and the presence of surface oxygen-containing groups [58], which will be further investigated in this thesis.

Most electrochemical studies in investigating the electrochemical performance and applications of nanomaterials are on the basis of ensembles, the voltammetric behaviour of which on the electrode depends upon not only the chemical and physical characteristics of single entities but also the size and morphology of nanoparticle and the interparticle separation with the nanoparticle surface coverage reflecting size, polydispersity, particle orientation and agglomeration. Ensemble electrochemistry may be difficult to interpret due to irregular drop-cast technique and other influences. Therefore, single entity electrochemistry (aka 'nano impacts') is helpful to solve the difficulty in clarifying the functional features on the electrochemical reactions from the nanomaterial itself. Moreover, it provides an understanding of the connection between the properties of individual particles and their ensembles to obtain the more accurate kinetics of associated electrochemical reactions [59].

In the nano-impact experiment, random collisions of the nanoparticles in a suspension with the electrode held at a suitable potential allows electrochemical reactions to occur for the duration of the impact whilst the particle is in electrical contact with the electrode. Current-time traces ('chronoamperometry') are recorded as a function of the potential. and impacts are revealed by the appearance of spikes and steps on the current [60-62]. Impact events have been categorized into two types: '*direct*' nano-impacts and '*mediated*' nano-impacts [62]. In the case of a *'direct'* Faradaic impact, the colliding analyte is itself either oxidized or reduced, and

consequently may dissolve under some conditions. As illustrated in Fig.1.16 (A), a characteristic 'spike-like' current response is observed for a direct Faradaic impact. The particle is oxidized (or reduced) when it reaches the electrode from bulk solution by virtue of its Brownian motion and subsequently either dissolves at the electrode as a result of electron transfer for becoming converted into an insoluble product. Thus, in some cases oxidative impacts of silver nanoparticles lead to dissolution as Ag^+ [64] but in some halide media form insoluble silver halides on the surface of the particle [65]. Typical *'direct'* nano-impacts are demonstrated from a host of different nanoparticle materials including metals [66, 67], metal oxides [68], organic nanoparticles [69] and so on. In contrast to the *'direct'* nano-impacts, '*mediated*' nano-impacts, also known as a catalytically amplified impacts, occur in the presence of a redox active couple in the solution phase. For these types of impact, the electrocatalytic processes cannot be observed until nanoparticles collide with an inert electrode and electron transfer is mediated through the nanoparticle to the electrocatalytic surface of the nanoparticle at which a further electron transfer occurs. Fig.1.16 (B) and (C) shows two current features in shape of spike or step respectively reflecting either a short or long residence time that the catalytic nanoparticle is in contact with the electrode. A current spike response usually appears in the chronoamperometric curve (Fig.1.16 (B)) when the nanoparticle desorbs or deactivates at a faster speed relative to the measurement time. Characteristic 'steps' reflect sustained consumption of the solution-phase electroactive species (Fig.1.16 (C)). Example of *'mediated'* nano-impacts has been seen and studied for a variety of systems including platinum for hydrogen peroxide reduction [70], iridium oxide for electrocatalytic water oxidation [71], carbon nanotubes [72] and graphene oxide particles [73] for hydrogen oxidation and reduction (HOR/HER) and to probe the electron transfer kinetics on the surface of individual nanoparticles.

It is noted that nano-impacts experiments are normally performed at a microelectrode even though the collision of nanoparticles can also take place at a macroelectrode. Due to the large

electrode area of the latter leading to high frequencies of collision and overwhelming background signals and the large capacitive response seen with impacts which masks the Faradic impacts, it is very challenging to determine the individual collision event from a single nanoparticle. While the adoption of microelectrodes whilst lowering the frequency of collision effectively minimizes baseline noise and reduces the capacitive responses of the impacts permitting the analyse of single impact events.

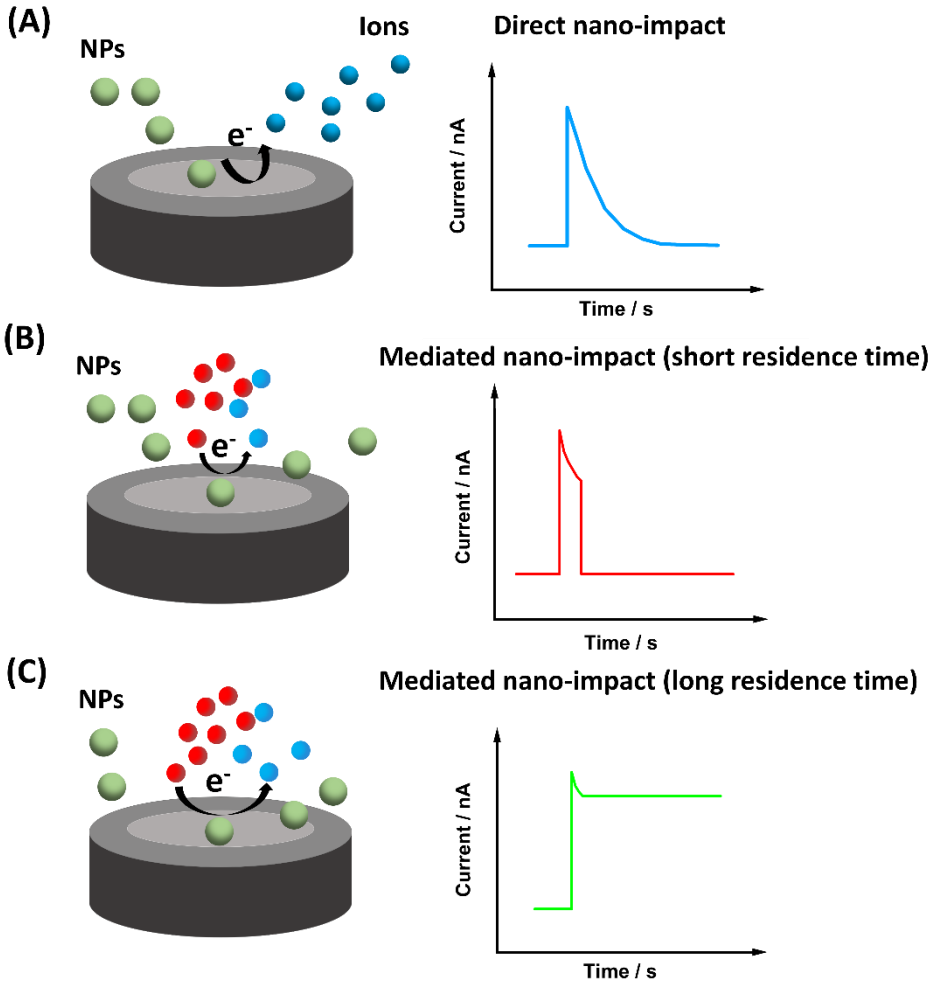


Figure.1.16 Three main scenarios of impact experiments and related current responses from (A)direct nano-impact, (B) mediated nano-impact with short residence time and (C) mediated nano-impact with long residence time.

In this thesis, we employ nano-impact technique to study the electrochemical characteristics (Chapter 5) and the catalytic mechanism (Chapter 6 and Chapter 7) for the

oxygen reduction reaction at two types of multiwalled carbon nanotubes (MWCNTs). They are either bamboo-type CNTs or the same with with amino functionalization. Comparison is made with the voltammetric responses seen at macroelectrodes modified with ensemble of carbon nanotubes.

References

1. A. J. Bard and L. R. Faulkner, *Electrochemical Methods: Fundamentals and Applications 2nd Edition*, 2001.
2. R. G. Compton and C. E. Banks, *Understanding voltammetry, third edition*, World Scientific, 2018.
3. H. Reiss, *The Journal of Physical Chemistry*, 1985, **89**, 3783-3791.
4. F. J. Vidal-Iglesias, J. Solla-Gullón, E. Herrero, A. Rodes and A. Aldaz, *Electrocatalysis*, 2013, **4**, 1-9.
5. A. Arevalo and G. Pastor, *Journal of Chemical Education*, 1985, **62**, 882.
6. F. J. Vidal-Iglesias, J. Solla-Gullón, A. Rodes, E. Herrero and A. Aldaz, *Journal of Chemical Education*, 2012, **89**, 936-939.
7. J. R. Runo and D. G. Peters, *Journal of chemical education*, 1993, **70**, 708.
8. H. P. Lehmann, X. Fuentes-Arderiu and L. F. Bertello, *Pure and Applied Chemistry*, 1996, **68**, 957-1000.
9. T. Renner, *Quantities, units and symbols in physical chemistry*, Royal Society of Chemistry, 2007.
10. C. Puente and I. López, in *Direct Synthesis of Metal Complexes*, Elsevier, 2018, pp. 87-141.
11. S. Logan, *Journal of Chemical Education*, 1982, **59**, 279.
12. M. R. Deakin, R. Wightman and C. Amatore, *Journal of electroanalytical chemistry and interfacial electrochemistry*, 1986, **215**, 49-61.
13. E. J. F. Dickinson and A. J. Wain, *Journal of Electroanalytical Chemistry*, 2020, **872**.
14. R. C. Engstrom, M. Weber, D. J. Wunder, R. Burgess and S. Winquist, *Analytical Chemistry*, 1986, **58**, 844-848.
15. R. J. Forster, *Chemical Society Reviews*, 1994, **23**, 289-297.
16. P. Biesheuvel, S. Porada and J. Dykstra, *arXiv preprint arXiv:1809.02930*, 2018.
17. F. C. Strong, *Journal of Chemical Education*, 1961, **38**, 98.
18. W. Sleator, *American Journal of Physics*, 1941, **9**, 166-168.

19. Z. Stojek, in *Electroanalytical methods*, Springer, 2010, pp. 3-9.
20. D. Pavlov, in *Lead-Acid Batteries: Science and Technology (Second Edition)*, ed., 2017, 621-662.
21. E. J. F. Dickinson and R. G. Compton, *Journal of Electroanalytical Chemistry*, 2011, **661**, 198-212.
22. B. Conway, J. M. Bockris and I. Ammar, *Transactions of the Faraday Society*, 1951, **47**, 756-766.
23. K. B. Oldham and C. G. Zoski, in *Comprehensive Chemical Kinetics*, eds. C. H. Bamford and R. G. Compton, Elsevier, 1986, vol. 26, pp. 79-143.
24. E. Lee, in *Interface Science and Technology*, ed. E. Lee, Elsevier, 2019, vol. 26, pp. 3-45.
25. N. Ibl, *Pure and Applied Chemistry*, 1981, **53**, 1827-1840.
26. A. Fick, *Annalen der Physik*, 1855, **170**, 59-86.
27. A. Fick, *The London, Edinburgh, and Dublin Philosophical Magazine and Journal of Science*, 1855, **10**, 30-39.
28. M. Islam, *Physica Scripta*, 2004, **70**, 120.
29. A. J. Samin, *AIP Advances*, 2016, **6**, 055101.
30. G. H. Sanders and R. G. Compton, *Electrode potentials*, Oxford University Press, 1996.
31. J. Newman, *Electroanalytical Chemistry*, 1973, **6**, 187-352.
32. J. K. Novev and R. G. Compton, *Current Opinion in Electrochemistry*, 2018, **7**, 118-129.
33. M. I. Khan, *International Communications in Heat and Mass Transfer*, 2021, **122**, 105177.
34. C. Hagan and L. A. Coury, *Analytical Chemistry*, 1994, **66**, 399-405.
35. R. G. Compton, A. C. Fisher, R. G. Wellington, P. J. Dobson and P. A. Leigh, *The Journal of Physical Chemistry*, 1993, **97**, 10410-10415.
36. K. Aoki, K. Tokuda and H. Matsuda, *Journal of Electroanalytical Chemistry and Interfacial Electrochemistry*, 1977, **76**, 217-233.
37. B. Miller and S. Bruckenstein, *Journal of The Electrochemical Society*, 1970, **117**, 1032.
38. P. T. Kissinger and W. R. Heineman, *Journal of Chemical Education*, 1983, **60**, 702.
39. O. Tutty, *Journal of Electroanalytical Chemistry*, 1994, **377**, 39-51.
40. M. Hiroaki and A. Yuzo, *Bulletin of the Chemical Society of Japan*, 1955, **28**, 422-428.
41. H. Matsuda and Y. Ayabe, *Zeitschrift für Elektrochemie, Berichte der Bunsengesellschaft für physikalische Chemie*, 1955, **59**, 494-503.
42. H. Chen, FreeSim Electrochemical Simulator, 2022, can be found at https://github.com/nmerovingian/FreeSim.

43. R. S. Nicholson and I. Shain, *Analytical chemistry*, 1964, **36**, 706-723.
44. P. Zanello, C. Nervi and F. F. De Biani, *Inorganic electrochemistry: theory, practice and application*, Royal Society of Chemistry, 2019.
45. C. Batchelor-McAuley, B. R. Kozub, D. Menshykau and R. G. Compton, *The Journal of Physical Chemistry C*, 2011, **115**, 714-718.
46. E. E. Tanner and R. G. Compton, *Electroanalysis*, 2018, **30**, 1336-1341.
47. R. G. Compton and G. H. W. Sanders, *Electrode potentials*, Oxford University Press, Oxford, 2009.
48. V. Mirceski, R. Gulaboski, M. Lovric, I. Bogeski, R. Kappl and M. Hoth, *Electroanalysis*, 2013, **25**, 2411-2422.
49. J. G. Osteryoung and R. A. Osteryoung, *Analytical chemistry*, 1985, **57**, 101-110.
50. D. J. Chesney, *ACS Publications*, 1996.
51. W. Schwarz and I. Shain, *The Journal of Physical Chemistry*, 1965, **69**, 30-40.
52. M. Vert, Y. Doi, K. H. Hellwich, M. Hess, P. Hodge, P. Kubisa, M. Rinaudo and F. Schué, *Pure and Applied Chemistry*, 2012, **84**, 377-410.
53. L. Lu, *Microchimica Acta*, 2019, **186**, 664.
54. Q. Wu, W. Miao, Y. Zhang, H. Gao and D. Hui, *Nanotechnology Reviews*, 2020, **9**, 259-273.
55. J. J. Gooding, *Electrochimica Acta*, 2005, **50**, 3049-3060.
56. K. Gong, Y. Yan, M. Zhang, L. Su, S. Xiong and L. Mao, *Analytical sciences*, 2005, **21**, 1383-1393.
57. C. E. Banks and R. G. Compton, *Analyst*, 2006, **131**, 15-21.
58. M. Pumera, *Chemistry – A European Journal*, 2009, **15**, 4970-4978.
59. W. Cheng and R. G. Compton, *TrAC Trends in Analytical Chemistry*, 2014, **58**, 79-89.
60. N. V. Rees, *Electrochemistry Communications*, 2014, **43**, 83-86.
61. W. Cheng and R. G. Compton, *TrAC Trends in Analytical Chemistry*, 2014, **58**, 79-89.
62. P. H. Robbs and N. V. Rees, *Physical Chemistry Chemical Physics*, 2016, **18**, 24812-24819.
63. S. V. Sokolov, S. Eloul, E. Kätelhön, C. Batchelor-McAuley and R. G. Compton, *Physical Chemistry Chemical Physics*, 2017, **19**, 28-43.
64. Y.G. Zhou, B. Haddou, N. V. Rees and R. G. Compton, *Physical Chemistry Chemical Physics*, 2012, **14**, 14354-14357.
65. E. E. L. Tanner, C. Batchelor-McAuley and R. G. Compton, *The Journal of Physical Chemistry C*, 2016, **120**, 1959-1965.

66. Y. G. Zhou, N. V. Rees and R. G. Compton, *Angewandte Chemie International Edition*, 2011, **50**, 4219-4221.
67. D. Qiu, S. Wang, Y. Zheng and Z. Deng, *Nanotechnology*, 2013, **24**, 505707.
68. Y.G. Zhou, N. V. Rees and R. G. Compton, *Physical Chemistry Chemical Physics*, 2013, **15**, 761-763.
69. W. Cheng, X. F. Zhou and R. G. Compton, *Angewandte Chemie*, 2013, **125**, 13218-13220.
70. X. Xiao and A. J. Bard, *Journal of the American Chemical Society*, 2007, **129**, 9610-9612.
71. S. J. Kwon, F.R. F. Fan and A. J. Bard, *Journal of the American Chemical Society*, 2010, **132**, 13165-13167.
72. X. Li, C. Batchelor-McAuley, S. A. I. Whitby, K. Tschulik, L. Shao and R. G. Compton, *Angewandte Chemie International Edition*, 2016, **55**, 4296-4299.
73. R. Miao, L. Chen, L. Shao, B. Zhang and R. G. Compton, *Angewandte Chemie International Edition*, 2019, **58**, 12549-12552.

Chapter 2

Experimental

This chapter details the experimental details including chemical reagents and electrochemical instrumentation used in the experiments reported in this thesis. Specific descriptions of each experiment can be found in the experimental parts of each chapter (**Chapter 4-7**).

2.1 Chemicals and Reagents

All chemicals and reagents involved in the experimental chapters in this thesis were of analytical grade and were used as received without any further purification as listed in Table 2.1. All solutions were prepared in ultra-pure water at a resistivity of 18.2 MΩ cm at 298K (Millipore, MA, USA).

Table 2.1 List of chemicals and reagents involved in this thesis

Chemical	Formula	Purity	Supplier
Ammonium molybdate tetrahydrate	$(NH_4)_6Mo_7O_{24} \cdot 4H_2O$	99%	Alfa Aesar
Potassium phosphate monobasic	KH_2PO_4	99.5%	Macklin
Chitosan	$C_{6n}H_{11n}NO_{4n}$	MW=100,000	Macklin
Acetic acid	CH_3COOH	100.5 %	Sigma-Aldrich
Sulphuric acid	H_2SO_4	95.0% - 97.0%	Sigma-Aldrich
Potassium sulfate	K_2SO_4	≥ 99.0%	Sigma-Aldrich
Potassium chloride	KCl	≥ 99.0%	Sigma-Aldrich
Potassium nitrate	KNO_3	99.99%	Sigma-Aldrich
Potassium hydroxide	KOH	85%	Sigma-Aldrich
Nitric acid	HNO_3	70%	Sigma-Aldrich
Ethanol	CH_3CH_2OH	≥ 99.8%	Sigma-Aldrich

Bamboo-like multiwalled carbon nanotubes	MWCNTs	>95%	Nanolab
Amino multiwalled carbon nanotubes	MWCNTs-NH_2	>95%	Nanjing XFNANO

MWCNTs-NH_2 (amino ratio: ~0.45 wt%) were purchased from Nanjing XFNANO Materials Tech Co., Ltd. (Nanjing, China) after synthesis via the following procedure of three steps: i) The introduction of carboxylic acid groups at defects (tube ends, vacancies, etc) in the MWCNTs made by chemical vapor deposition (CVD) to form MWCNTs-COOH; ii) The reaction of the -COOH groups to form -CO-NH_2 groups via chemical reaction with liquid ammonia[1]; iii) Decarbonylation to remove the carbonyl group, so that the amino groups become directly linked with carbon atoms in the MWCNTs to obtain the final product MWCNTs-NH_2, the structure is shown schematically in Fig.2.1 with the NH_2 group attached to an aromatic ring.

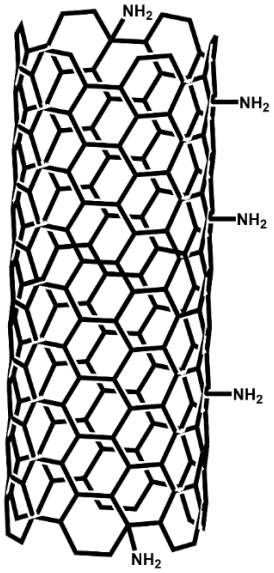


Figure.2.1 Schematic structure of the single layer of MWCNTs-NH_2.

Bamboo-like MWCNTs were purchased from Nanolab ((Brighton, MA, USA). The transmission electron microscopy (TEM) and FTIR characterization of its sample are shown in Fig.2.2 and 2.3 supplied by NanoLab [2]. XPS data [3] analysis of MWCNTs indicated that this sample contains 98.9 atomic% carbon, 1.0 atomic% oxygen, 0.1 atomic% iron, and trace (< 0.1 atomic%) copper and sulphur. The MWCNTs and MWCNTs-NH_2 were used for comparative

experiments as described in Chapter 5 and Chapter 7. Their dimensions are compared in Table 2.2 and it is noticed that the external surface area of the two different types of individual carbon nanotubes are similar (~2×10^{-12} m^2) so permitting comparisons made in the experiments. Meanwhile Fourier-transform infrared (FTIR) spectroscopy [2] for MWCNTs observed the -OH stretching, CNT Backbone and two unassigned peaks (1375 cm^{-1} and 1000 cm^{-1}). For MWCNTs-NH_2, the FTIR spectroscopy for the functional groups attached to the MWCNTs-NH_2 exhibited peaks corresponding to the amino group (-NH_2), MWCNT back bone and C-N bond stretch vibration [5].

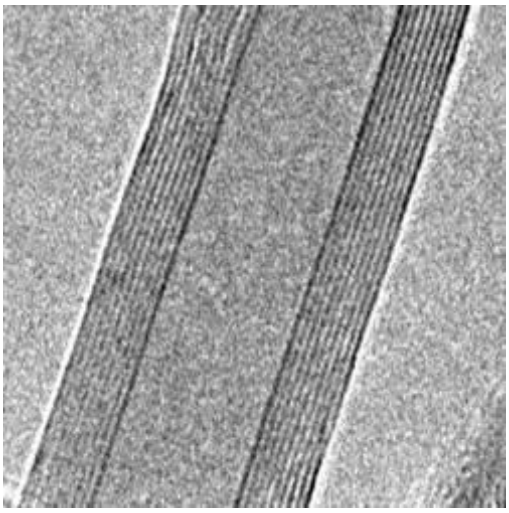


Figure.2.2 The transmission electron microscope (TEM) image of a typical single MWCNT supplied by NanoLab [2].

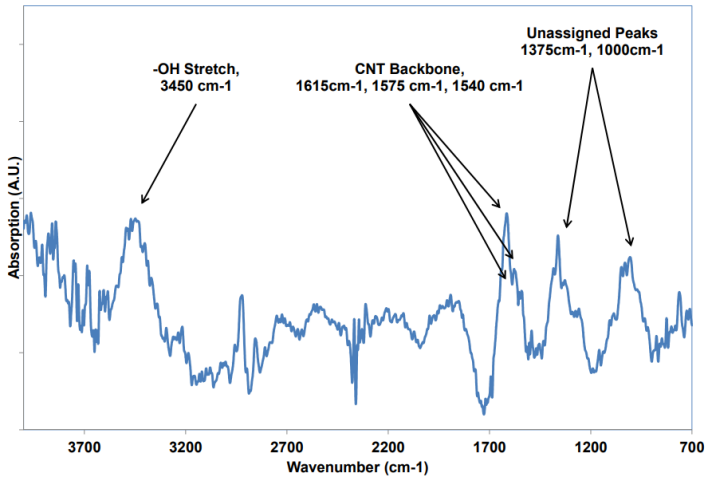


Figure.2.3 Fourier-transform infrared spectroscopy (FTIR) of MWCNTs supplied by NanoLab [2].

Table 2.2 The dimensions of MWCNTs and MWCNTs-NH_2

	MWCNTs	MWCNTs-NH_2
Diameter	30 nm	15 nm
Length	20 μm	50 μm
External surface area	1.9×10^{-12} m^2	2.3×10^{-12} m^2
Number of concentric tubes	9	6

2.2 Electrochemical Instrumentation

All electrochemical experiments were conducted in a Faraday cage at 298 ± 0.5 K using an EC-Lab potentiostat (SP-200 with an ultra-low current module, Biologic Science Instruments, France). A conventional three-electrode system was operated with a saturated calomel electrode (SCE, ALS distributed by BASi Inc., Japan) or a Ag/AgCl electrode (in 3.5 M KCl solution) used as the reference electrode, a graphite rod as the counter electrode and a working electrode. The details of specific working electrodes will be discussed corresponding to each experiment reported in different chapters.

2.2.1 Preparation of Glassy Carbon Macro electrodes (GCE)

Prior to both modification via drop-casting and all electrochemical measurements on a bare glassy carbon macro electrode (GCE), it was polished carefully using alumina with decreasing particle sizes of 1.0, 0.3 and 0.05 μm (Buehler, IL, UK) in turn on soft lapping pads (Buehler, UK), followed by rinsing with ultra-pure water and drying with nitrogen (99.998%, BOC Gases plc). The different surface drop-casting methods onto the polished electrode will be introduced in the relevant chapters.

2.2.2 Fabrication of Cabon Fibre Microwire electrodes

For nano-impact experiment, chronoamperometry was conducted using a carbon fibre micro-wire electrode of 7 μm diameter and 1 mm in length as the working electrode respectively.

The in-house fabrication of carbon fibre microwire electrodes was according to the literature reported by Ellison et al. [4]. First, a 7 μm diameter carbon fibre (GoodFellow Ltd., Huntingdon, UK) was connected to a conducting copper wire by using silver explosive (RS Components Ltd.), followed by a 15-min heating in the oven at ca.358 K. This connection was then threaded through a plastic pipette tip to let only the carbon fibre extended out of the end. The interstice between the carbon fibre/copper wire and the plastic tip was sealed using cyanoacrylate adhesive, thus preventing electrical leakage. After that, the fabricated electrode was put in the oven at 358 K overnight for the adhesive complete drying. Every time before the utilization of a fresh carbon fibre microwire electrodes in the nano-impact experiments, the length of each is to cut to ca. 1mm.

References

1. R. M. Lanigan and T. D. Sheppard, *European Journal of Organic Chemistry*, 2013, **2013**, 7453-7465.
2. N. Inc., Multiwall Carbon Nanotubes, Bamboo Structure, can be found at *https://www.nano-lab.com/bamboopowderd30l520.html*.
3. C. E. Banks, A. Crossley, C. Salter, S. J. Wilkins and R. G. Compton, *Angewandte Chemie International Edition*, 2006, **45**, 2533-2537.
4. J. Ellison, C. Batchelor-McAuley, K. Tschulik and R. G. Compton, *Sensors and Actuators B: Chemical*, 2014, **200**, 47-52.
5 F. T. Patrice, K. Qiu, L.J. Zhao, E. Kouadio Fodjo, D.W. Li and Y.T. Long, *ACS Applied Nano Materials*, 2018, **1**, 2069-2075.

Chapter 3

Background for the Electrochemical Detection of Phosphate

Chapters 3 - 4 demonstrate a novel amperometric sensor for aqueous phosphate ions in freshwater systems. Chapter 3 first introduces the prior art of phosphate detection describing a wide range of electrochemical techniques and, in particular, summarizes amperometric methods for phosphate analysis from literature. Moreover, through the theoretical calculations using Hydra/Medusa software [1], the speciation of molybdate (Mo (VI)), phosphate (P) and related species in aqueous solution as a function of concentration and pH are ascertained, providing significant help in the subsequent understanding of the electrochemical signals with respect to speciation of Mo/P complexes in **Chapter 4**.

3.1 Summary of Phosphate Detection Using Electrochemical Techniques

Phosphate anions are one essential constituent of living systems, which not only play an important role in biological systems but also cause detrimental effects in aquatic ecosystems [2, 3]. Excessive inorganic phosphate anions created from unscientific fertilization in farmland soil pass into local water systems through surface and underground runoff, resulting in eutrophication causing widespread water-quality problems, now widely recognised [4, 5]. The US Environmental Protection Agency (EPA) has reported the Federal criteria limit[6] for phosphate of 0.1 ppm, 0.05 ppm and 0.025 ppm in rivers, streams entering lakes and lakes/reservoirs respectively. Therefore, developing simple, sensitive and cost-effective approaches for phosphate analysis in aqueous solutions meets a need.

In principle potentiometric sensing should be a simple electrochemical approach and ion selective sensors (ISEs) have been developed [7-10]. However, the realization of high sensitivity within the operable concentration detection range of the phosphate anions is problematic since a triply charge anion shows one third of the Nernstian sensitivity of that of a singly charged

anion and, furthermore, the response of phosphate ISEs is strongly pH dependent as the speciation within the solution changes with the formation of $H_2PO_4^-$ and HPO_4^{2-} as well as PO_4^{3-}. Moreover, the hydrophilicity and the size of the phosphate anion make it challenging to design a phosphate selective membrane, which precludes the use of size-exclusion principles for increased selectivity[11]. As a result, few phosphate sensors have become commercially available and attention has shifted to voltammetric (amperometric) sensing. Many reported electrochemical methods for phosphate detection are based on the electrochemical reaction of a phosphomolybdic complex created in situ by using screen-printed electrodes modified with preloaded reagents or even enzymatic systems (shown in Table 3.1). These detection strategies are usually coupled with complicated and costly preparation procedures, limited electrode lifetimes and high detection limits. The development of a facile, cheap, sensitive electrochemical methodology for the detection of phosphate remains a significant and worthwhile challenge.

Table 3.1Summary of phosphate detection methods using amperometric techniques

(A) Electrode	Reagent	LOD μM	Linear Range μM	Sensitivity	Interferents	Ref
GOD–MP–MR biosensor	0.1M Citrate buffer pH 6.0	1	1-50	50 μA/mM	/	[12]
Cobalt phthalocyanine SPCE	0.05 M MOPS pH 7.3	2.3	2.5-50	0.5 μA/mM	/	[13]
PPy–PNP–XOD–Fe $(CN)_6^{4-}$-Pt Electrode	0.05M Tris–HCl	100	100-1000	6 μA/mM	Uric acid, ascorbic acid, glycine	[14]
PB-GCE (Used in Brazilian biodiesel)	0.5 M KCl	38.3	500-5000	0.2 μA/mM	$LiNO_3$, $NaNO_3$, KNO_3, $Mg(NO_3)_2$, $Ca(NO_3)_2$, $Sr(NO_3)_2$, $Ba(NO_3)_2$	[15]

ZnO-PyO-FET biosensor	0.02 M HEPES buffer (pH 7.0)	0.05	0.1-7000	80 μA/mM cm^2	K^+, SO_4^{2-}, Ca^{2+}, TPP, HCO_3^-	[16]

Note: GOD–MP–MR: glucose oxidase-maltose phosphorylase-mutarotase; MOPS：3-(n-morpholino) propanesulphonic acid; SPCE: screen printed carbon electrode; PPy–PNP–XOD: Purine nucleoside phosphorylase- xanthine oxidase-polypyrrole; PB: Prussian Blue; ZnO-PyO-FET:ZnO-pyruvate oxidase-field-effect transistor; HEPES: N-2-Hydroxyethylpiperazine-N'-2-ethanesulfonic acid；TPP：thiamine pyrophosphate chloride.

Table 3.2 Summary of phosphate detection methods using amperometric electrochemical reduction of phosphomolybdates.

Electrode	Reagent	LOD μM	Linear Range μM	Sensitivity μA/μM	Interferents	Ref
PMo_{12} carbon paste electrode	0.5 M H_2SO_4	0.42	4-260	0.28	Na^+, K^+, SO_4^{2-}, NO_3^-, Cu^{2+}, Cd^{2+}, SiO_4^{2-}, BO_3^-, AsO_4^{3-}, TeO_4^{3-}, Pb^{2+}	[17]
PSS/PEDOT/IL/Mo/PSS/PEDOT/Chit/Mo-GCE	Tris buffer pH=7.2	0.79	0.79-3.96	3.06	Cl^-, NO_3^-, As (V)	[18]
CBNPs-SPE	1 mM Mo/ 0.1 M H_2SO_4/0.1 M KCL	0.10	0.5-100	0.45	SiO_4^{2-}	[19]
SPE	640 ppm Mo+H_2SO_4 (pH=1)	0.002	0.003-0.115	5.92	Cl^-, HCO_3^-, NO_3^-, NO_2^-	[20]
Carbon paste microelectrode	2 mM $Mo_7O_{24}^{6-}$ / 0.2 M HNO_3	0.5	0.5-20	0.00009	SiO_4^{2-}	[21]
Mo-gold electrode	NaCl (pH=4.5)	0.10	0.25-4	0.013	$Si(OH)_4$.	[22]

Gold electrode	20 mM MoO_4^{2-} in pH 1.0 artificial seawater	0.12	0.33–3.20	0.27	SiO_4^{2-}	[23]

Note: PSS / PEDOT/IL: Poly stryrenesulphonate/Poly (3,4-ethylene dioxythiophene)/ ionic liquid; CBNPs-SPE: Carbon black nanoparticles-screen printed electrode.

3.2 Species Distribution of P, Mo (VI) and Their Containing Compounds

From Table.3.2, it is found that most amperometric method of detecting phosphate is based on the monitoring of an electroactive complex obtained by the reaction between phosphate anions and Mo (VI) (Eq. (3.1)), due to the electrochemically inactivity of phosphate.

$$\mathbf{7}H_3PO_4 + \mathbf{12}Mo_7O_{24}^{6-} + \mathbf{51}H^+ \rightarrow \mathbf{7}PMo_{12}O_{40}^{3-} + \mathbf{36}H_2O \qquad (3.1)$$

while the Keggin anion $PMo_{12}O_{40}^{3-}$ is the best known phosphomolybdate complex first identified in 1934 and which appears in very acidic aqueous solutions [24]. In the experiments indicated in Chapter 4, on the basis of this chemical equilibrium, we develop the electrochemical detection of phosphate in aqueous solutions at an ammonium molybdate tetrahydrate (AMT)-chitosan modified glassy carbon macro electrode (AMT-CS-GCE) using cyclic voltammetry (CV) and square wave voltammetry (SWV). Therefore, it is a necessary preliminary to find out the specific species distribution for molybdenum, phosphate and molybdophosphate complexes in aqueous solution before investigating the electrochemical detection mechanism for phosphate.

3.2.1 Theoretical calculations of speciation

The distribution diagrams for molybdenumn (VI) (Mo (VI)) were obtained in the pH range 0 to 7 and for total Mo concentrations of 1 mM and 8 mM using Hydra/Medusa software [1] based on the formation conditions of different Mo (VI) complexes H_2MoO_4, $H_3MoO_4^+$, $HMoO_4^-$, MoO_4^{2-}, $Mo_7O_{24}^{6-}$. The distribution diagrams for orthophosphate were similarly obtained in the

pH range 0 to 8 again using Hydra/Medusa to identify the relevant concentrations of PO_4^{3-}, HPO_4^{2-}, $H_2PO_4^-$ and H_3PO_4.

Last, based on the equilibria and associated equilibrium constants reported for the formation of the various molybdophosphate complexes [25] from Mo (VI) complexes and orthophosphate species, the speciation in solutions containing both Mo (VI) and phosphates was modelled for different total concentrations of uncomplexed phosphate (0.01 mM to 10.0 mM) for total Mo (VI) concentrations of 8mM using Hydra/Medusa. In all cases, the distribution diagrams of Mo (VI) or P containing species were generated as a function of pH.

3.2.2 Speciation of Mo (VI) in aqueous solution.

The equilibration of molybdenum (VI) in aqueous solution involves reactions between MoO_4^{2-} and hydrogen ions and depends on the molybdenum concentration which controls the extent of condensation reactions to form species containing more than one Mo atom. Molybdate and protons were produced by decomposition of $Mo_7O_{24}^{6-}$ utilized as the analyte in this work; the electrolyte solutions studied were prepared according to the following reaction Eq. (3.2):

$$\boldsymbol{Mo_7O_{24}^{6-} + 4H_2O \rightleftharpoons 7MoO_4^{2-} + 8H^+} \qquad (3.2)$$

Fig.3.1 shows the distribution diagrams of the different Mo (VI) species which exist in monomeric forms for a given total amount of Mo (VI) of 1mM and 8mM as a function of pH, respectively. At pH $\leq$ 2 hexavalent molybdenum exists primarily as monomeric species, $Mo_7O_{24}^{6-}$ was substantially decomposed in the most acidic region but remained predominant in the range 3 < pH < 5, MoO_4^{2-} with a tetrahedral shape[26] prevailed in solutions at pH > 7. However, when the concentration of Mo (VI) was decreased from 8 mM to 1 mM, $Mo_7O_{24}^{6-}$ was almost totally decomposed in the acidic region. Meanwhile as the proportion of $HMoO_4^-$ rose to be the dominant monomeric species in the range 3 < pH < 5, the percentage of the other two kinds of molybdate (H_2MoO_4 and $H_3MoO_4^+$) gradually decreased to zero in this acidic region.

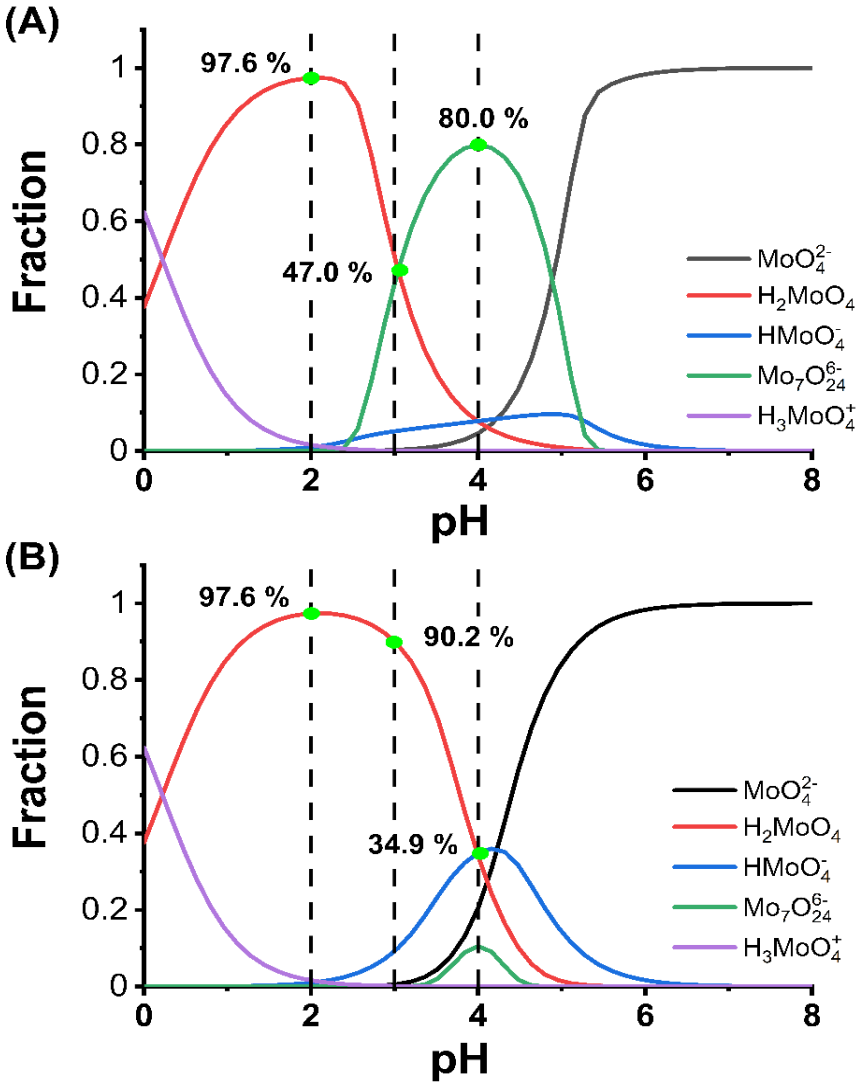


Figure.3.1 Species distribution diagram of major molybdenum chemical species when [Mo (VI)] = 1 mM or 8 mM calculated using Hydra/Medusa [1].

3.2.3 Speciation of phosphate as a function of pH.

Using the known chemical equilibrium constants of the various phosphate species[27], the distribution diagram of orthophosphate as a function of pH (0-8) was calculated using Hydra/Medusa (Fig.3.2). The speciation of phosphate among various species in aqueous solution was strongly dependent on solution pH but $H_2PO_4^-$ was the major species when the pH range was within $2.1 \leq pH \leq 7.2$, while H_3PO_4 and HPO_4^{2-} were predominant at pH below 2.1 and above 7.2 respectively.

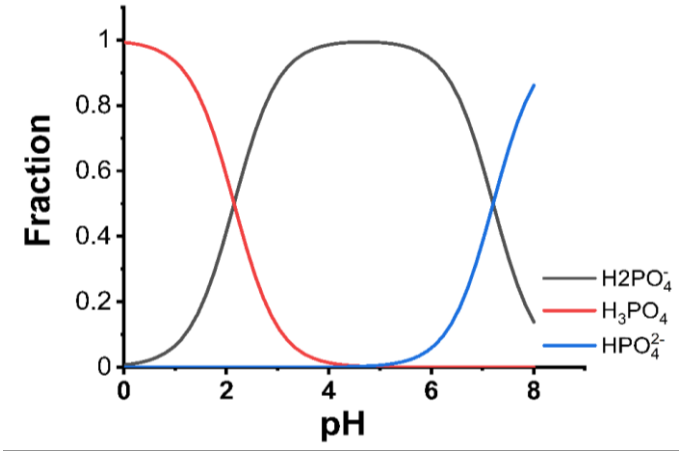


Figure.3.2 Speciation of orthophosphate chemical species in solution as a function of pH calculated using Hydra/Medusa [1].

3.2.4 Species distribution of Mo (VI) and P containing compounds

In order to clarify the speciation in solutions of Mo (VI) and phosphate, the distribution diagrams of Mo (VI) and P containing compounds as a function of pH from 0 to 7 were generated respectively when $[Mo\ (VI)]_{Total}$ = 8 mM while varying the total phosphate concentration $[PO_4^{3-}]_{TOT}$ from 0.1 μM to 0.01, 0.1, 1.0 and 10.0 mM. Note all the thermodynamic calculations were under ideal condition without considering any kinetic barriers.

As illustrated in Fig.3.3(A)-(D), the Mo (VI) containing speciation diagrams show the effects of total phosphate concentrations as well as pH on the identity of the most stable form, which have the following features in comparison with the speciation described above for pure phosphate and pure Mo (VI) solutions. The following equilibria (Eqs. (3.3) - (3.6)) and associated equilibrium constants [25] were considered：

$$2PO_4^{3-} + 5MoO_4^{2-} + 10\,H^+ \overset{K_1}{\rightarrow} P_2Mo_5O_{23}^{6-} + 5H_2O \qquad \textbf{Log } K_1\textbf{=86.6} \qquad (3.3)$$

$$2PO_4^{3-} + 18MoO_4^{2-} + 36\,H^+ \overset{K_2}{\rightarrow} P_2Mo_{18}O_{62}^{6-} + 18H_2O \qquad \textbf{Log } K_2\textbf{=242.5} \qquad (3.4)$$

$$PO_4^{3-} + 11MoO_4^{2-} + 18\,H^+ \overset{K_3}{\rightarrow} PMo_{11}O_{39}^{7-} + 9H_2O \qquad \textbf{Log } K_3\textbf{=131.0} \qquad (3.5)$$

$$PO_4^{3-} + 12MoO_4^{2-} + 24\,H^+ \overset{K_4}{\rightarrow} PMo_{12}O_{40}^{3-} + 12H_2O \qquad \textbf{Log } K_4\textbf{=152.0} \qquad (3.6)$$

First when $[PO_4^{3-}]_{TOT}$ = 0.01 or 0.1 mM, H_2MoO_4 and $Mo_7O_{24}^{6-}$ predominate separately in the conditions of pH at 0.2 - 3.1 and 3.1 - 4.8. But on increasing $[PO_4^{3-}]_{TOT}$ from 0.01 to 0.1mM, the molybdophosphate anions $PMo_{12}O_{40}^{3-}$ and $PMo_{11}O_{39}^{7-}$ appeared in the pH region of 0 - 3.0 and 2.3 - 5.6, respectively. Second when $[PO_4^{3-}]_{TOT}$ =1.0 or 10.0 mM, $P_2Mo_{18}O_{62}^{6-}$ became the dominant species in the pH range of 0-3.0. However, if the concentration of PO_4^{3-} was increased to 10.0 mM, the major species in the pH region (3.0-5.5) was no longer $PMo_{11}O_{39}^{7-}$ ($[PO_4^{3-}]_{TOT}$ =1.0 mM) but changed to be $PMo_{11}O_{39}^{7-}$ (pH 3.1-3.8) and $P_2Mo_5O_{23}^{6-}$ (pH 3.8 - 5.5) individually. Third for pH above 5.5, MoO_4^{2-} prevailed within all the PO_4^{3-} concentration as seen when only Mo (VI) was present.

Fig.3.4, presents the speciation diagrams for P-containing species. The phosphate anion $H_2PO_4^-$ was not the major species in solutions until pH > 5.5 when $[PO_4^{3-}]_{TOT}$ = 0.01, 0.1 and 1.0 mM. This reflected in part the pK_a value of 2.2 (298 K) for the acid-base pair $H_3PO_4/H_2PO_4^-$. At PO_4^{3-} concentrations of 0.01 and 0.1 mM, $PMo_{12}O_{40}^{3-}$ and $PMo_{11}O_{39}^{7-}$ were predominant in the range 0 < pH < 2.6 and 2.6 < pH < 5.5 respectively. However, when the concentration of PO_4^{3-} was increased from 0.1 to 1.0 mM, the proportion of $P_2Mo_{18}O_{62}^{6-}$ rose to be the dominant species in the acidic region (pH 0 - 3.0) instead of $PMo_{12}O_{40}^{3-}$, the fraction of which gradually descended to zero as pH increases to 2.5. The species $PMo_{11}O_{39}^{7-}$ predominated in the pH range pH 3.0 to 5.1. Meanwhile the range of existence in acid of $P_2Mo_5O_{23}^{6-}$ was observed to extend and reach the range of pH from 3.0 to 6.0 with a maximum presence of ca 62.0% in the pH of 5.1 - 5.6 at a $[PO_4^{3-}]_{TOT}$ of 1.0 mM. After the concentration of PO_4^{3-} was increased to 10.0 mM, uncomplexed phosphate species were prevalent as in the speciation of phosphate in the absence of Mo (VI) over the whole pH range from 0 to 7.

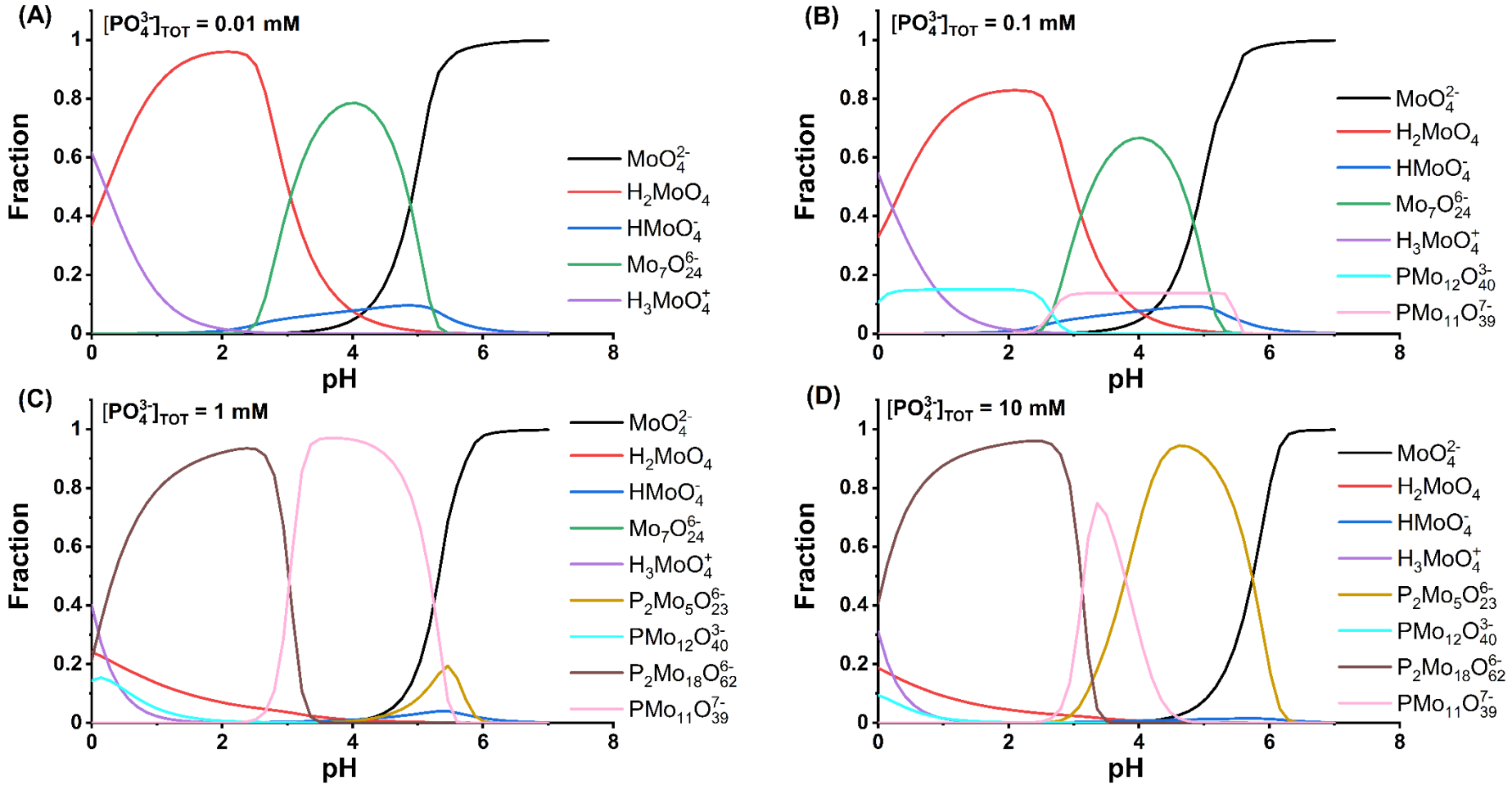


Figure.3.3 Species distribution diagram of Mo (VI) containing compounds for a total Mo (VI) concentration of 8mM when $[PO_4^{3-}]_{TOT}$ = 0.01 mM (A), 0.1 mM (B), 1.0 mM (C), 10.0 mM (D) calculated using Hydra/Medusa [1].

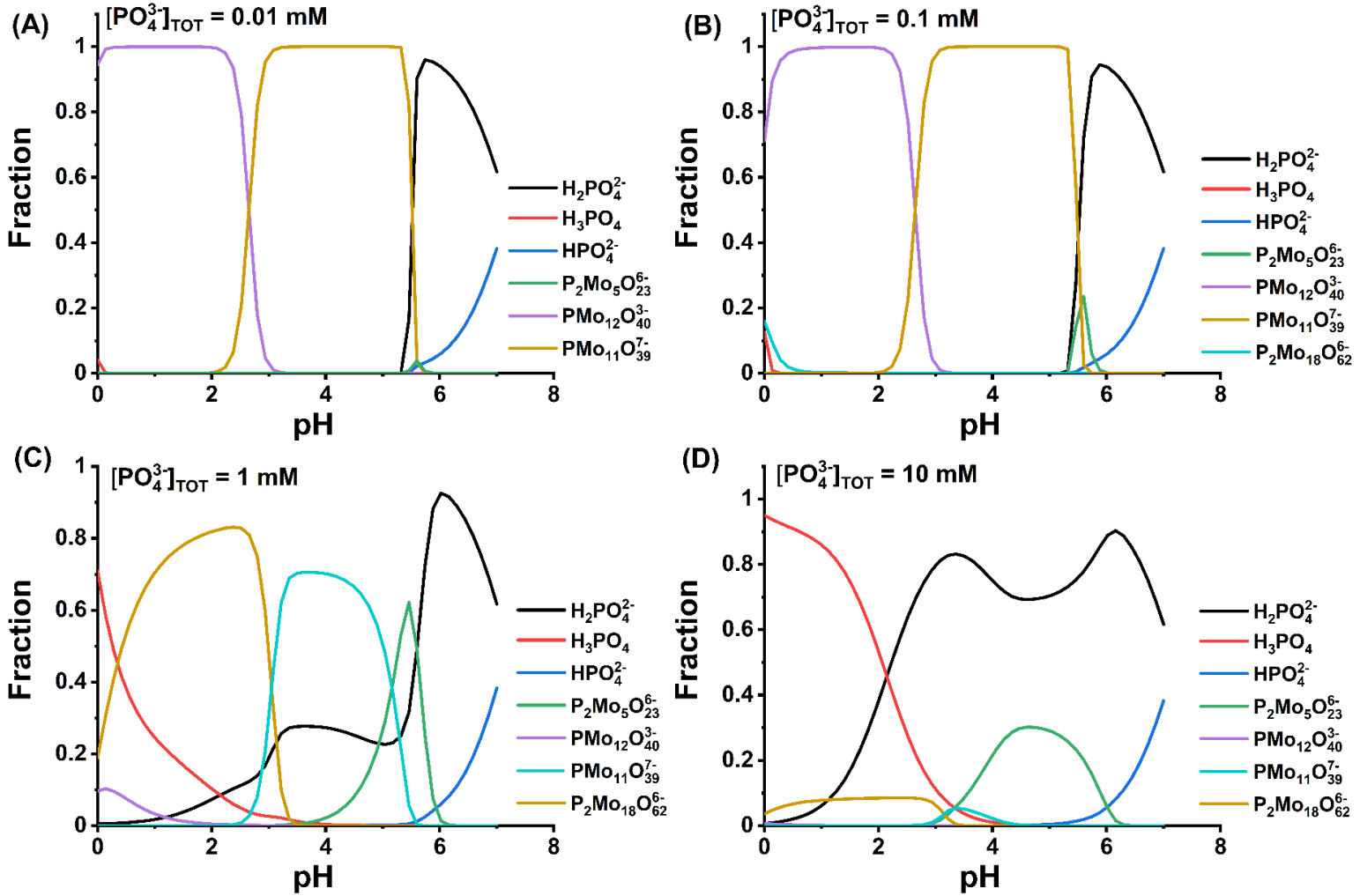


Figure.3.4 Species distribution diagram of P containing compounds for a total Mo(VI) concentration of 8 mM when the total phosphate concentration is 0.01 mM (A), 0.1 mM (B), 1.0 mM (C), or 10.0 mM (D) calculated using Hydra/Medusa [1].

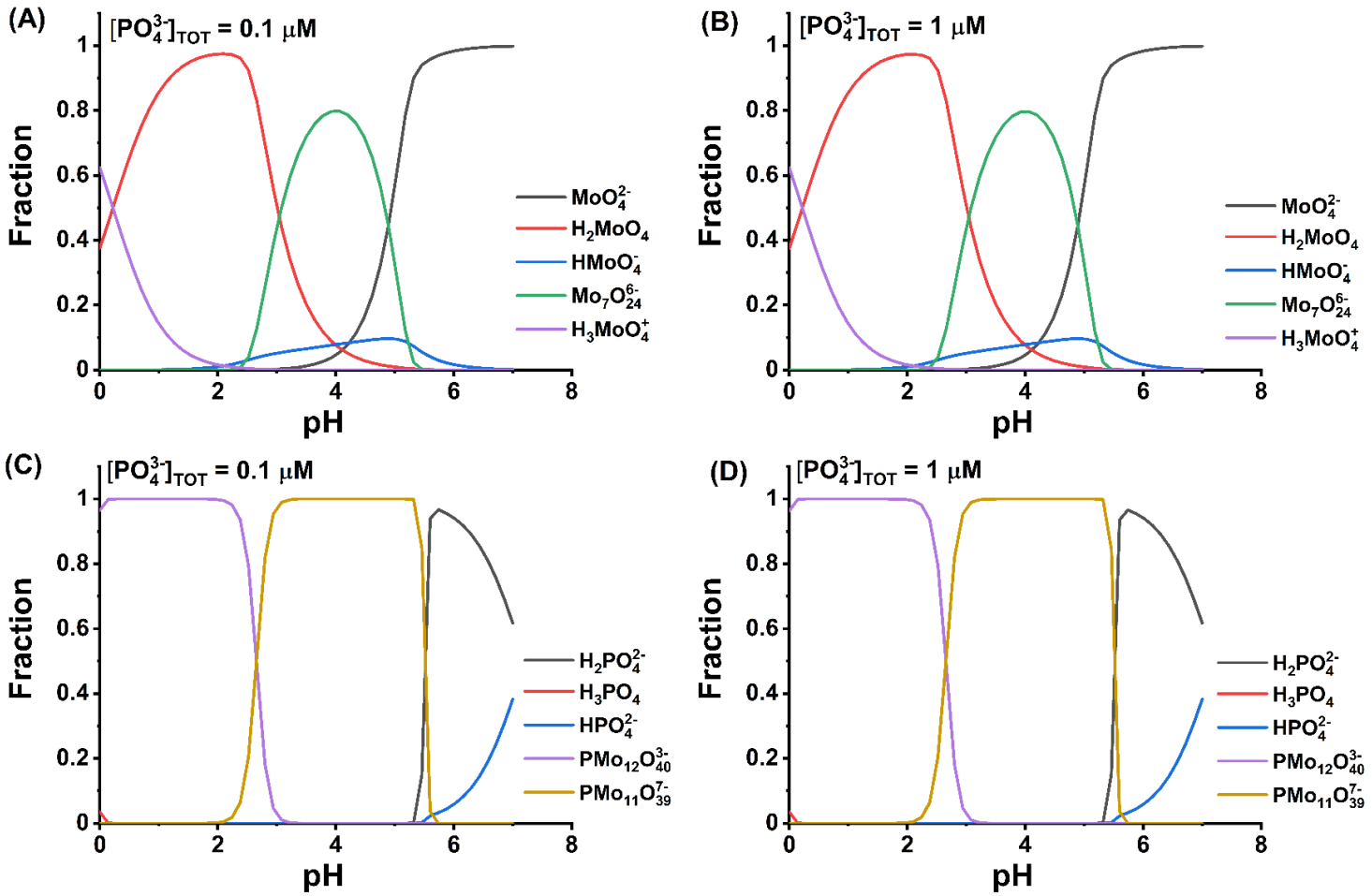


Figure.3.5 Species distribution diagram of Mo (VI) containing compounds for a total Mo (VI) concentration of 8mM when $[PO_4^{3-}]_{TOT}$ = 0.1 µM (A) and 1.0 µM (B); Species distribution diagram of P containing compounds for a total Mo(VI) concentration of 8mM when $[PO_4^{3-}]_{TOT}$ = 0.1 µM (C) and 1.0 µM (D) using Hydra/Medusa [1].

It was noted that the distribution diagrams were unchanged for total phosphate concentrations $[PO_4^{3-}]_{TOT}$ equal or below 1 μM as shown in Fig.3.5. By way of summary, Table 3.3 shows the changing composition of an 8 mM Mo solution as the amount of phosphate was altered based on the fraction distribution of Mo containing species (Fig.3.3) and P containing species (Fig.3.4) at pH=2 with a [Mo (VI)] total concentration of 8 mM when $[PO_4^{3-}]_{TOT}$ was changed from 0.01 mM to 0.1, 1 and 10 mM. The conditions under which individual concentrations of key species are maximal are given in Table 3.4. The distribution of Mo (VI) and P containing complexes are very sensitive to the Mo (VI)/P concentration ratio and are strongly pH dependent.

Table 3.3 Concentrations of molybdate, phosphate and Mo (VI)-P complexes as a function of $[PO_4^{3-}]_{TOT}$ when [Mo(VI)]= 8 mM at pH=2.

$[PO_4^{3-}]_{ToT}$ /mM	0	0.01	0.1	1	10
H_2MoO_4	7.65	7.65	6.60	0.60	0.41
$H_3MoO_4^+$	0.14	0.14	0.12	0.01	0.006
$HMoO_4^-$	0.08	0.08	0.06	0.005	0.004
$H_2PO_4^-$	/	/	/	0.08	3.90
H_3PO_4	/	/	/	0.1	5.26
$PMo_{12}O_{40}^{3-}$	/	0.01	0.10	0.0076	0.001
$P_2Mo_{18}O_{62}^{6-}$	/	/	/	0.4	0.45

Table 3.4 Maximal concentration of molybdate, phosphate and Mo (VI)-P complexes at a certain $[PO_4^{3-}]_{TOT}$ and pH when [Mo(VI)]= 8 mM.

Species	$[PO_4^{3-}]_{ToT}$ /mM	pH	Maximal Concentration /mM
H_2MoO_4	0	pH = 2.1	7.80
$Mo_7O_{24}^{6-}$	0	pH = 4.0	6.30
$PMo_{12}O_{40}^{3-}$	0.1	pH 0.8-2.0	0.10
$PMo_{11}O_{39}^{7-}$	10	pH = 3.7	0.5
$P_2Mo_5O_{23}^{6-}$	10	pH = 4.6	3.02
$P_2Mo_{18}O_{62}^{6-}$	10	pH = 2.5	0.86
$H_2PO_4^-$	10	pH = 6.1	9.05
H_3PO_4	10	pH = 0	9.51

The sections above include the essential background for the electrochemical detection of phosphate. Most of all, the distribution of Mo/P species based on the Hydra/Medusa program and database can help to correlate electrochemical signals with the speciation and hence assign voltammetric peaks as reported in Chapter 4. Specific experimental methodology and results will be discussed in the next chapter.

References

1. I. Puigdomenech, *KTH Royal Institute of Technology*, 2004.
2. D. J. Currie and J. Kalff, *Limnology and Oceanography*, 1984, **29**, 311-321.
3. S. Berchmans, T. B. Issa and P. Singh, *Analytica chimica acta*, 2012, **729**, 7-20.
4. R. Chitrakar, S. Tezuka, A. Sonoda, K. Sakane, K. Ooi and T. Hirotsu, *Journal of colloid and interface science*, 2006, **298**, 602-608.
5. W. Yao and F. J. Millero, *Environmental Science & Technology*, 1996, **30**, 536-541.
6. US Environmental Protection Agency, *Water quality standards handbook*, Office of Water Regulations and Standards, 1983.

7. W. R. Heineman, H. J. Wieck and A. M. Yacynych, *Analytical Chemistry*, 1980, **52**, 345-346.
8. R. De Marco, *Talanta*, 2003, **60**, 1215-1221.
9. L. Zhu, X. Zhou and H. Shi, *Frontiers of Environmental Science & Engineering*, 2013, **8**, 945-951.
10. R. Zeitoun and A. Biswas, *Electroanalysis*, 2020, **33**, 421-430.
11. H.J. Kim, J. W. Hummel, S. J. Birrell and K. A. Sudduth, *ASAE Annual Meeting*, American Society of Agricultural and Biological Engineers, 2005..
12. C. Mousty, S. Cosnier, D. Shan and S. Mu, *Analytica chimica acta*, 2001, **443**, 1-8.
13. L. Gilbert, A. T. A. Jenkins, S. Browning and J. P. Hart, *Sensors and Actuators B: Chemical*, 2011, **160**, 1322-1327.
14. A. T. Lawal and S. B. Adeloju, *Biosens Bioelectron*, 2013, **40**, 377-384.
15. L. Torrezani, A. A. Saczk, M. Firmino de Oliveira, N. R. Stradiotto and L. L. Okumura, *Electroanalysis*, 2011, **23**, 2456-2461.
16. R. Ahmad, M. S. Ahn and Y. B. Hahn, *J Colloid Interface Sci*, 2017, **498**, 292-297.
17. L. Guanghan, W. Xiaogang, L. Yanhua and Y. Shenlai, *Talanta*, 1999, **49**, 511-515.
18. S. Berchmans, R. Karthikeyan, S. Gupta, G. E. J. Poinern, T. B. Issa and P. Singh, *Sensors and Actuators B: Chemical*, 2011, **160**, 1224-1231.
19. D. Talarico, F. Arduini, A. Amine, D. Moscone and G. Palleschi, *Talanta*, 2015, **141**, 267-272.
20. A. V. Kolliopoulos, D. K. Kampouris and C. E. Banks, *Analytical chemistry*, 2015, **87**, 4269-4274.
21. J. C. Quintana, L. Idrissi, G. Palleschi, P. Albertano, A. Amine, M. El Rhazi and D. Moscone, *Talanta*, 2004, **63**, 567-574.
22. C. Barus, I. Romanytsia, N. Striebig and V. Garçon, *Talanta*, 2016, **160**, 417-424.
23. J. Jonca, V. Leon Fernandez, D. Thouron, A. Paulmier, M. Graco and V. Garcon, *Talanta*, 2011, **87**, 161-167.
24. J. F. Keggin, *Proceedings of the Royal Society of London*, 1934, **144**, 75-100.
25. L. Pettersson, I. Andersson and L. O. Oehman, *Inorganic Chemistry*, 1986, **25**, 4726-4733.
26. K. Matsumoto, A. Kobayashi and Y. Sasaki, *Bulletin of the Chemical Society of Japan*, 1975, **48**, 1009-1013.
27. R. Parsons, *Standard Electrode Potentials, Units, Conventions, and Methods of Determination*, 2017.

Chapter 4

Amperometric Environmental Phosphate Sensor

After clarifying the specific distribution of Mo/P species in aqueous solution as a function of concentration and pH in **Chapter 3**, the electrochemical detection of phosphate in aqueous solutions at an ammonium molybdate tetrahydrate (AMT)-chitosan modified glassy carbon macro electrode (AMT-CS-GCE) using cyclic voltammetry (CV) and square wave voltammetry (SWV) are investigated in **Chapter 4**. This practical amperometric phosphate sensor was based on the immobilization of Molybdate (VI) anions within a chitosan matrix deposited on a glassy carbon electrode and the electrochemical reduction from Mo (VI) to Mo (V) together with square wave voltammetry. Quantitative detection of trace phosphate with a high sensitivity (4.4 ± 0.1 μA/μM) and a LOD of 0.15 μM was realized in model systems. Analytical measurements were successfully made in authentic samples of tap and pond water.

The work of **Chapter 3** and **4** has been published in the journal *ACS Sensors*, and was carried out under the supervision of Prof. Richard G.Compton (University of Oxford) and in collaboration with Dr. Xiuting Li (Shenzhen University) and Dr. Danlei Li (University of Oxford) who helped with the interpretation of the experimental results.

4.1 Introduction

The major issue for the amperometric detection of phosphate results from the structure of the orthophosphate ion [1]. To be specific, it has been suggested the central P atom covalently bonded to four oxygen atoms creates a hydrophilic sphere around the anion and results in a high enthalpy of hydration, which makes it electrochemically inactive to reduction and hence difficult to be detected [2] whilst the oxidation state of the P atom makes it inert to oxidation. Thus, in order to be detectable a chemical derivatisation of phosphate is typically required. It was in 1934 that Keggin proposed the structures of a range of 12-heteropoly acids [3]. This

Keggin species $[XM_{12}O_{40}]^{n-}$ (X = B, P, Si, etc; M = Mo and W) have been frequently incorporated into diverse transition metals and organic ligands, for example, the molybdenum blue (MB) reaction is commonly used in the standard determination of inorganic phosphate through two stages; the first stage involves the formation of a Keggin anion around the analyte anion and the second stage entails the reduction of this heteropoly acid to form a deeply blue-coloured product ($[H_4PMo(VI)_8Mo(V)_4\,O_{40}]^{3-}$) [4].

In this work, we present the electrochemical detection of phosphate in aqueous solutions at an ammonium molybdate tetrahydrate (AMT)-chitosan modified glassy carbon macro electrode (AMT-CS-GCE) using cyclic voltammetry (CV) and square wave voltammetry (SWV). A schematic for the proposed analytical procedure of this phosphate sensor is shown in Fig.4.1 (A), accompanied with the structures of the chitosan and AMT in Fig 4.1 (B) and (C) respectively, Chitosan is known to show good adhesion to electrodes and excellent film forming ability [5, 6]. Besides, the amino groups in chitosan have a pKa value of ~ 6.5 at 298K[7] and they are protonated at acidic pH. The protonated amino groups are known to bind anions [8,9] and in the present study are using to immobilise the molybdate species.

The reductive behaviour of solution-phase molybdate (VI) anions and phosphate was first investigated via CV. For phosphate detection, we used the enhancement of the observed Mo reduction peaks seen in the presence of phosphate for which an electrocatalytic mechanism is suggested. For the creation of a practical sensor, chitosan was adopted to immobilize the probe molybdate anions onto an electrode surface. The electrochemical response of the sensor was investigated via CV and SWV respectively, and it was found that SWV showed a significantly improved detection sensitivity compared with CV by reducing the effect of capacitive background currents [10]. The method was optimized for detection at pH 2 after simple sample acidification but also shown to be valuable as a reagent free sensor for environmental use at

around pH 7, where an application of the optimized sensor for quantifying phosphate concentration in real environmental water samples was developed.

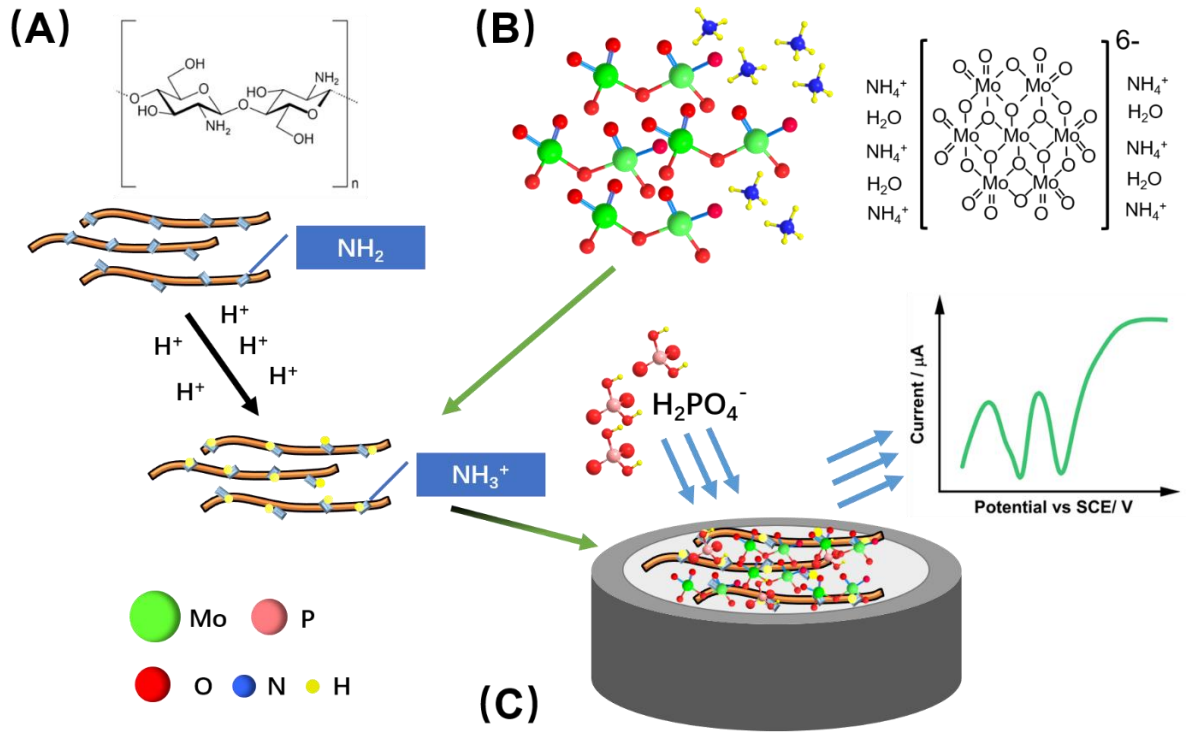


Figure.4.1 The chemical structure of Chitosan [7](A) and ammonium molybdate (VI) tetrahydrate (B); (C) A scheme for the amperometric detection of phosphate using AMT-CS-GCE.

4.2 Experimental

Details of the chemicals and reagents were listed in Section 2.1.

Electrochemical Apparatus

All electrochemical experiments were carried out in a Faraday cage at 298K using an EC-lab potentiostat (SP-200 with an ultra-low current module, Biologic Science Instruments, France). The CV and SWV measurements were performed using a standard three-electrode system with a glassy carbon macro electrode (GCE) as the working electrode (diameter of 3.02 ± 0.005 mm). A saturated calomel electrode (SCE, SH Xianren Inc., China) was used as the reference electrode and a graphite rod as the counter electrode.

Preparation of ammonium molybdate (VI) tetrahydrate-Chitosan modified electrode (AMT-CS-GCE)

For voltammetric experiments to detect phosphate, a novel ammonium molybdate (VI) tetrahydrate-Chitosan modified electrode (AMT-CS-GCE) was fabricated. The drop-cast suspension was prepared by dissolving 0.05 g chitosan in 10 mL 0.1M acetic acid then slowly mixing with 4.0 g ammonium molybdate (VI) tetrahydrate followed by constant stirring for 12 hours. The freshly polished GCE was modified by drop casting 2 μL of ammonium molybdate (VI) tetrahydrate-Chitosan suspension, and the modified electrode was then dried under vacuum.

Voltammetric Analysis of Phosphate at AMT-CS-GCE

KH_2PO_4 stock solutions of 1.0 mM were prepared with 0.05M K_2SO_4 and standard working solutions at different KH_2PO_4 concentrations of 0.01, 0.05, 0.1, 0.2, 0.3, 0.4, 0.6, 0.8, 1.0, 2.0 and 5.0 μM were then obtained by diluting the stock solution with 0.05 M K_2SO_4 solution (pH=2, adjusted by H_2SO_4), 0.05 M K_2SO_4 solution (pH=5.8, without acid or alkali addition) or 0.05 M K_2SO_4 solution (pH=7.8, adjusted by KOH) respectively.

For the CV experiments on the study of Mo (VI) reduction in the absence and presence of phosphate, the GCE was first placed in 0.05M K_2SO_4 solution (pH =2, adjusted by small additions of 0.5M H_2SO_4) containing 0, 50 and 100 μM KH_2PO_4 and 8 mM ammonium molybdate (VI) tetrahydrate. Prior to the measurements, the solutions were bubbled with N_2 to remove the dissolved oxygen. The potential window was chosen to be 0.5 to −1.0 V and 0.5 to −0.1 V respectively, the voltammograms were recorded at different scan rates (25, 50, 100, 200, 400 mVs^{-1}).

To investigate the electrochemical response to aqueous phosphate of different concentrations, CVs were performed by immersing an AMT-CS-GCE in degassed solutions containing 5, 10, 20, 40 and 80 μM KH_2PO_4 in 0.05M K_2SO_4 (pH=2) from 0.5 V to - 0.1 V at

a scan rate of 100 mV s^{-1}. The effect of pH was also investigated experimentally: CVs at an AMT-CS-GCE were obtained at a scan rate of 0.1 V s^{-1} in a solution containing 10 μM KH_2PO_4 in 0.05M K_2SO_4 at different pH values (1.5 to 5.5) which were adjusted using different concentrations of H_2SO_4 and the potential window was adjusted to accommodate the shift in potential to observe the oxidation and reduction peaks.

The phosphate detection was realized using SWV where the AMT-CS-GCE was immersed in solutions containing 0, 0.3, 0.6, 1 and 2 μM KH_2PO_4 in 0.05M K_2SO_4 (pH=2) and solutions containing 0, 0.05, 0.1, 0.2, 0.4, 0.6 and 0.8 μM KH_2PO_4 in 0.05M K_2SO_4 (pH=5.8, without acid or alkali addition) respectively under degassed conditions as above. An oxidizing pulse was first applied at a potential of 0.6 V for 10 s to generate hydrogen ions via electrolysis of water to make the electrode environment more acidic, then SWV experiments were carried out from 0.6 V to - 0.1 V at a scan rate of 25 mVs^{-1}, with a pulse height of 25 mV and an accumulation time of 3 minutes.

Real Sample Analysis

The authentic water samples used in this work were either laboratory tap water or natural pond water from Wenshan lake. Both located sources were in Shenzhen University, China (113.93 °E, 22.54 °N). Pond water samples were filtered using filter paper (pore size: 1 μm) to remove solid impurities before further analysis.

Tap water was directly used as the solvent to prepare a 0.05 M K_2SO_4 solution (pH=2). The pond water was diluted 10 times with a 0.05 M K_2SO_4 solution (pH=2). The AMT-CS-GCEs were used in the real sample solutions for SWV analysis at a scan rate of 25 mV s^{-1} with a pulse height of 25 mV and an accumulation time of 3 minutes. The potential was stepped from 0.6 V to -0.1 V and an oxidizing pulse was first applied at a potential of 0.6 V for 10 s before the SWV was conducted. The concentrations of phosphate were determined by the standard addition method and the accuracy was assessed by a recovery test.

4.3 Results and Discussion

We first investigated the cyclic voltammetry at GC macro electrodes in acidified molybdate (VI) solutions in the absence or presence of phosphate and a detection mechanism for phosphate involving an electrochemical catalytic process was proposed. Second, the analytical responses using CV and SWV for the detection of phosphate at AMT-CS-GCEs were studied. Finally, as a proof of concept, we applied AMT-CS-GCEs to quantify phosphate concentrations in real samples of water.

4.3.1 The electrochemical study of Mo (VI) in the absence of phosphate

Cyclic voltammograms were scanned from 0.5 V to -0.1 V at bare GCEs in 0.05 M K_2SO_4 (pH=2, see Experimental section) in the presence of 8 mM Mo (VI) or not at 400 mVs^{-1}. As depicted in Fig.4.2, there were two reduction peaks observed at 0.20 V and 0.05 V only in the presence of Mo (VI) into 0.05 M K_2SO_4 (pH=2). These reduction peaks were labelled as $Peak_1$ and $Peak_2$ and the areas (charge) were the same for both cathodic and anodic peaks, the origins of which were discussed below.

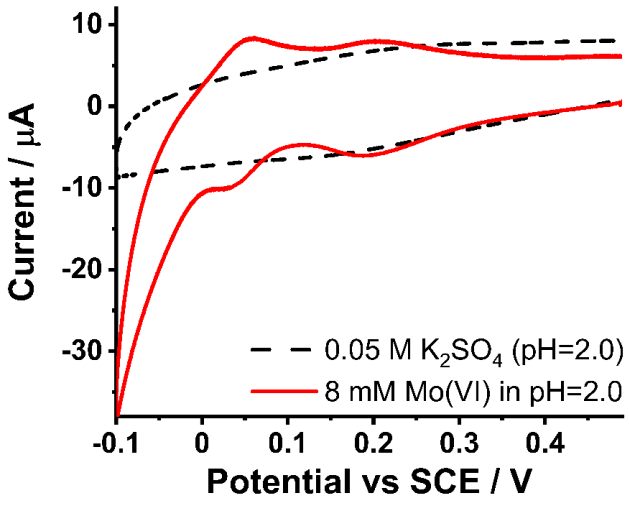


Figure.4.2 Electrochemical characterization of solution phase Mo (VI) in 0.05 M K_2SO_4 solution (pH = 2.0) under degassed conditions: cyclic voltammograms of bare GCE of background (black dashed line) and 8 mM Mo (VI) (red solid line) in the potential window from 0.5 V to -0.1 V at a scan rate of 400 mVs^{-1}.

Cyclic voltammograms were recorded at scan rates in the range of 25–400 mVs^{-1} in 8mM Mo (VI)/0.05 M K_2SO_4 (pH = 2) (Fig.4.3). As shown in inlay of Fig.4.3, the currents of $peak_1$ and $peak_2$ scaled linearly with the scan rate from 25 to 400 mVs^{-1} indicating the electrochemistry of surface bound Mo species. The peak to peak separation ($\Delta E_{pp}=|E_{p(anodic)}-E_{p(cathodic)}|$) for $peak_1$ and $peak_2$ were calculated to be 0.015 ± 0.002 V and 0.023 ± 0.003 V respectively which were close to the ideal value of zero for a reversible surface process and also roughly constant at different scan rates from 25 mV s^{-1} to 400 mV s^{-1}, indicating the reduction of Mo (VI) occurring at $Peak_1$ and $Peak_2$ were both electrochemically reversible processes. The formal potentials for each redox process were obtained to be 0.200 ± 0.002V ($peak_1$) and 0.047 ± 0.003V ($peak_2$) from the midpoint potential ($E_{formal} = \frac{E_{p(anodic)}+E_{p(cathodic)}}{2}$). The surface coverages (Γ) were obtained via:

$$\boldsymbol{\Gamma = \frac{Q}{nFA_e}} \qquad (4.1)$$

where Q is the charge passed ($Q = \frac{S_{peak\ area}}{v}$, C), n is the number of electrons transferred (n=1), F is the Faraday constant (96485 C mol^{-1}), A_e is the electrode area (7.1×10^{-2} cm^2). The raw cyclic voltammograms were background corrected prior to calculation of the coverage as shown in the Section A 4.1. Accordingly, in 0.05 M K_2SO_4 (pH=2), based on the one-electron reduction of Mo (VI) to Mo (V), the average surface coverage of $Peak_1$ and $Peak_2$ were estimated to be $(7.6\pm1.8) \times 10^{-10}$ mol cm^{-2} and $(2.1\pm1.3) \times 10^{-11}$ mol cm^{-2}, respectively. Comparing the average estimated distance between the particles (~ (10^{-8}-10^{-7}) cm/per particle) and $Mo_7O_{24}^{6-}$ ion particle size (~9×10^{-8} cm)[11], the Mo (VI) adsorption is considered to be approximately monolayer coverage.

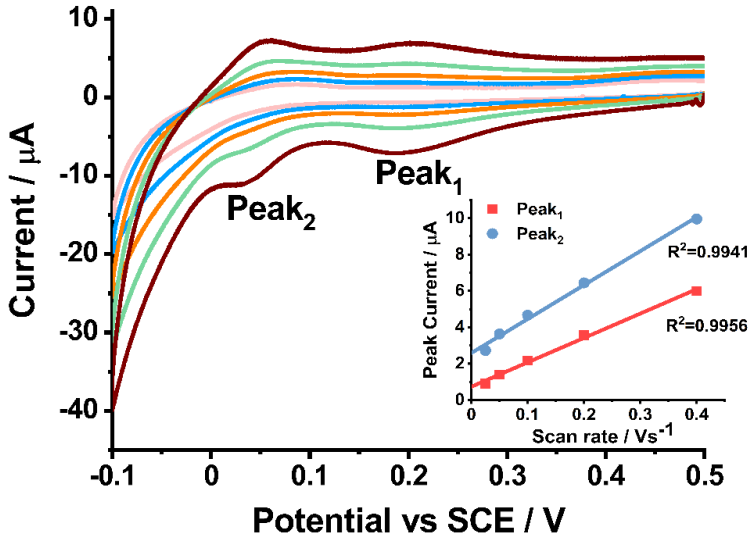


Figure.4.3 Cyclic voltammograms of bare GCE in 0.05 M K_2SO_4 solution (pH 2.0) under degassed conditions with 8.0 mM Mo (VI) in the potential window from 0.5 V to -0.1 V at variable scan rates of 25 (pink), 50 (blue), 100 (orange), 200 (green) and 400 (brown) mV s^{-1} (Inlay: plot of peak current of $Peak_1$ (red) or $Peak_2$ (blue) as a function of scan rate).

Having reported the voltammetry of 8 mM Mo (VI) occurring at bare GCEs in the potential window from 0.5 V to -0.1 V, we next investigated the electroreduction process of 8 mM Mo (VI) in 0.05 M K_2SO_4 (pH 2.0) across the full potential ranges from 0.5 V to -1.0 V (shown in Fig.4.4). Fig.4.4 (A) shows the response with (red line) or without (black line) the Molybdenum species at a scan rate of 100 mV s^{-1}. Four reduction peaks were observed at 0.20 V, 0.03 V, -0.31 V and -0.47 V marked as $Peak_1$, $Peak_2$, $Peak_3$ and $Peak_4$. The electrochemical behavior of $Peak_1$ and $Peak_2$ have been revealed as surface bound features in Fig.4.3 and the discussion thereof above, while the peak currents of reduction $Peak_3$ at -0.31 V and $Peak_4$ at -0.47 V were found to exhibit a linear relationship with the square root of scan rates from 25 to 400 mVs^{-1} (Inlay of Fig.4.4 (B)) respectively, suggesting $Peak_3$ and $Peak_4$ are diffusion-controlled. The reverse voltammetric scan showed a peak ($Peak'_4$) at -0.34 V which is related to $Peak_4$. The peak-to-peak separation for Peaks 4 and '4 was scan rate dependent and in the potential range of 0.1 - 0.2 V suggesting a Peaks 4 and '4 relate to a solution phase electrochemically quasi-reversible process.

The valence states of the Mo based redox couples involved in $Peak_1$, $Peak_2$, $Peak_3$ and $Peak_4$ were assigned based on literature reports. X-ray photoelectron spectroscopy (XPS) [12] identified Mo (V) as the electrochemical reduction product for both $Peak_1$ and $Peak_2$, which were believed to arise due to reduction of two different forms (or adsorption sites) of adsorbed Mo (VI) species. The presence of reverse peaks in the anodic scan shown in Fig.4.3 suggested that the species were retained on the surface after reduction. By studying cyclic voltammetric behaviour of Mo (VI) at GCE in the potential range from 0.5 V to -1.0 V, K.Chandarasekara Pillai et.al [13] also suggested that the electron transfer process corresponding to $Peak_4$ in Mo (VI) had a solution phase diffusion-controlled mechanism but the $Peak_3$ was influenced by reactant adsorption especially at high scan rates. In summary, the same authors proposed that all four peaks were all attributable to the Mo (VI) reduction to Mo (V) in 0.1M H_2SO_4 but in four different chemical and/or adsorbed forms. We suggest that $Peak_3$ lying at -0.31 V was likely to be an adsorptive pre-wave of $Peak_4$ and most Mo (VI) in solution phase could be postulated to take part in the reduction reaction at $Peak_4$ following a one-electron electrochemically quasi-reversible step. The whole process can be represented as Eqs. (4.2) -(4.5):

$Peak_1$ $\quad (Mo\ (VI)_A)_{ads} + e^- \rightarrow Mo\ (V)_{ads}$ (4.2)

$Peak_2$ $\quad (Mo\ (VI)_B)_{ads} + e^- \rightarrow Mo\ (V)_{ads}$ (4.3)

$Peak_3$ $\quad (Mo\ (VI)_C)_{sol} + e^- \rightarrow (Mo\ (V)_C)_{sol}$ (4.4)

$Peak_4$ $\quad (Mo\ (VI)_D)_{sol} + e^- \rightarrow (Mo\ (V)_D)_{sol}$ (4.5)

Note that the subscript 'ads' means that the species is adsorbed and that different adsorption sites are speculated to apply to Peaks 1, 2 and 3.

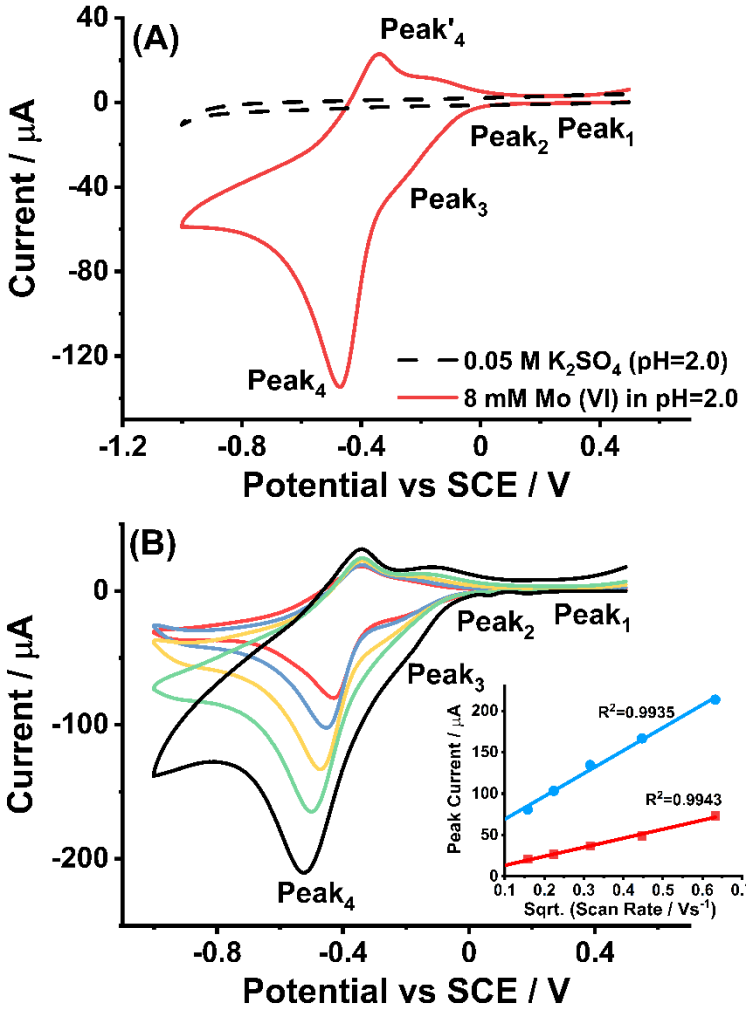


Figure.4.4 Electrochemical characterization of solution phase Mo (VI) in 0.05 M K_2SO_4 solution (pH 2.0) under degassed conditions in the potential window from 0.5 V to -1.0 V: cyclic voltammograms at GCE of (A) background (black line) and 8 mM Mo (VI) (red line) at a scan rate of 100 mV s^{-1} ; (B) 8.0 mM Mo (VI) at varying scan rates of 25 (red), 50 (blue), 100 (yellow), 200 (green) and 400 (black) mVs^{-1} (Inlay: plot of peak current of $Peak_3$ (red) or $Peak_4$ (blue) as a function of scan rate). All the voltammograms were after baseline correction as shown in Section A 4.1.

4.3.2 Electrochemical behaviour of Mo (VI) reduction in the presence of phosphate studied via cyclic voltammetry

The electro-reduction of Mo (VI) across the full potential ranges of interest was investigated by scanning voltammograms between 0.5 V to -1.0 V in 8mM Mo (VI)/0.05 M

K_2SO_4 (pH 2.0) in the presence of 0, 50 and 100 μM KH_2PO_4. As can be seen in Fig. 4.5, five peaks were observed at 0.20 V, 0.03 V, -0.31 V, -0.47 V and -0.82 V labelled $Peak_1$, $Peak_2$, $Peak_3$, $Peak_4$ and $Peak_5$ in the presence of KH_2PO_4. It was noted that the first four peaks ($Peak_{1-4}$) appeared at similar potentials as those in the absence of KH_2PO_4 while $Peak_5$ was observed only in the presence of 0.05 and 0.1 mM KH_2PO_4. It was also found that currents of $Peak_1$, $Peak_2$, $Peak_3$ and $Peak_5$ increased but the $peak_4$ current decreased with the continuous addition of KH_2PO_4.

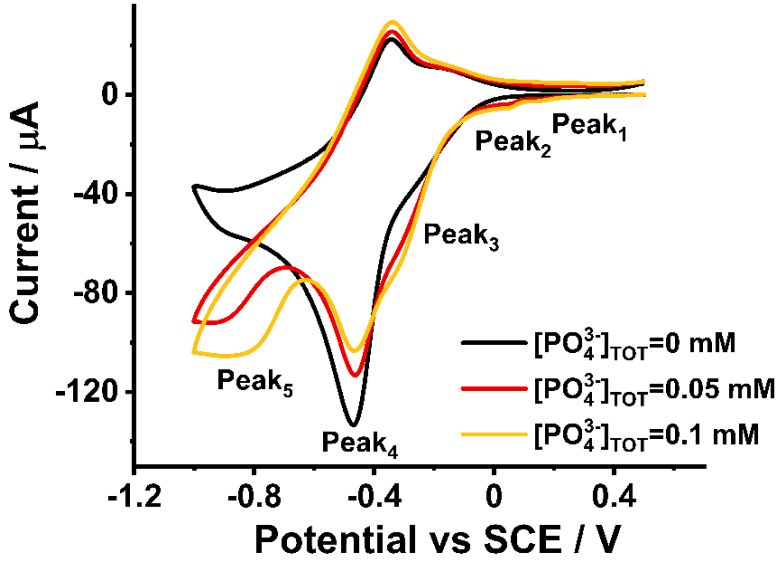


Figure.4.5 Cyclic voltammograms of 0, 0.05 and 0.1 mM KH_2PO_4 from 0.5 V to -1.0 V at a scan rate of 100 mVs^{-1} at a bare GC macroelectrode in 8 mM Mo (VI)/0.05 M K_2SO_4 solution (pH = 2.0) under degassed conditions. ***All the voltammograms were after baseline correction as shown in Section A 4.1.***

Fig.4.6(A) showed the CV response over the narrower potential range of 0.5 V to -0.1 V for concentrations of KH_2PO_4 of 0, 0.05, 0.1, 0.2, 0.5 and 1.0 mM. $Peak_1$ was only slightly influenced by the addition of KH_2PO_4 (see Fig.4.6(B)) but $Peak_2$ was seen to develop a shoulder (labelled $Peak^*_2$) and the overall $Peak_2$ + $Peak^*_2$ feature grew in size developing a current plateau rather than a peak at higher scan rates. These features signaled a possible catalytic process and probably also an enhanced adsorption. It was noted that the current of $Peak_2$ and

Peak*$_2$ increased linearly with increasing KH_2PO_4 concentration over the range studied (Fig.4.6(B)) and Peak*$_2$ assigned as a pre-peak of Peak$_2$ gradually disappeared as the scan rate was increased to 200 mV s^{-1} (Fig.4.6 (C)). Meanwhile the current values of Peak$_1$ and Peak$_2$ had a linear relationship with the scan rate from 25 mV s^{-1} to 400 mV s^{-1} respectively again suggesting their surface bound nature (Fig.4.6(D)). The enhancement of both forward and reverse peaks 1 and 2 in the presence of phosphate suggested that there was a chemical reaction of the phosphate with the Mo (VI) species, leading to the formation of species which showed enhanced adsorption especially in the case of Peak$_1$. The possible species included $PMo_{12}O_{40}^{3-}$ and $P_2Mo_{18}O_{62}^{6-}$ which were significant at pH = 2 when [PO_4^{3-}] was in the range from 0.01 to 1 mM according to the speciation distribution diagram (Fig.3.3 in Chapter 3). The catalytic reaction probably involved Mo(V) reacting with either the phosphate or with Mo-P species via a reaction[14] such as Eqs (4.6) and (4.7):

$$\boldsymbol{(Mo\ (V))_{ads} + PMo_{12}(VI)O_{40}^{3-} \rightarrow Mo\ (VI) + PMo_2(V)\ Mo_{10}(VI)O_{40}^{3-}} \quad (4.6)$$

$$\boldsymbol{(Mo\ (V))_{ads} + P_2Mo_{18}(VI)O_{62}^{6-} \rightarrow Mo\ (VI) + P_2Mo_2(V)\ Mo_{16}(VI)O_{62}^{6-}} \quad (4.7)$$

The increase of Peak$_3$ currents with the addition of KH_2PO_4 also suggested a possible surface catalytic (EC') process such as:

$$\boldsymbol{(Mo(V)_C)_{ads} + PMo_2(V)Mo_{10}(VI)O_{40}^{3-} \rightarrow (Mo\ (VI)_C)_{sol} + PMo_4(V)\ Mo_8(VI)O_{40}^{3-}} \quad (4.8)$$

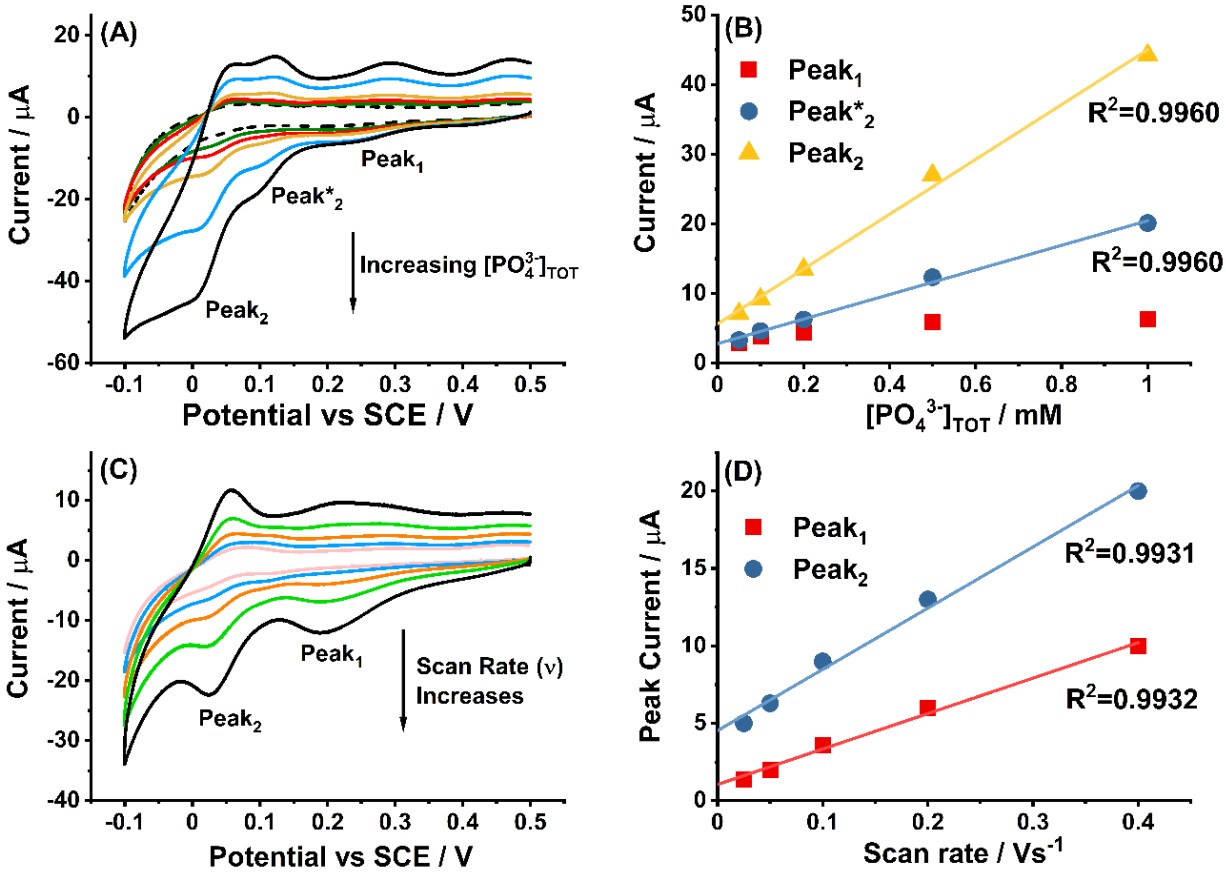


Figure.4.6 CV of KH_2PO_4 in 8mM Mo (VI)/0.05 M K_2SO_4 solution (pH = 2.0) from 0.5 V to -0.1 V under degassed conditions: (A) cyclic voltammograms of a bare GC macroelectrode with 0 mM, 0.05 mM, 0.1 mM, 0.2mM, 0.5mM and 1.0 mM of KH_2PO_4 at a scan rate of 100 mV/s; (B) calibration curve plot showing the peak currents of $Peak_1$, $Peak^*_2$ and $Peak_2$ versus total phosphate concentration at a scan rate of 100 mVs^{-1} ;(C) cyclic voltammograms of 0.1 mM KH_2PO_4 at a bare GC macroelectrode at varying scan rates from 25 mVs^{-1} to 400 mVs^{-1}; (D) the plot of $Peak_1$ and $Peak_2$ current as a function of the scan rate.

In order to clarify the origins of the Peaks 1-5, Fig.4.7 shows the speciation of Mo (VI) containing compounds over the range of phosphate studied from 0.05 to 1.0 mM, it can be seen that the concentrations of all mono Molybdate species (MoO_4^-, $H_3MoO_4^+$, H_2MoO_4 and $HMoO_4^-$) gradually decreased when [PO_4^{3-}] was increased from 0.05 mM to 1.0 mM. In contrast, the concentrations of $PMo_{12}O_{40}^{3-}$ and $PMo_{11}O_{39}^{7-}$ stayed stable when [PO_4^{3-}] was lower than 0.7 mM and then started to decrease slightly. In contrast the concentration of $P_2Mo_{18}O_{62}^{6-}$ increased

over the whole range of phosphate. In particular it can be seen from Fig.4.8 (A) and (B) that the peak currents associated with $Peak_4$ and new $Peak_5$ seen in the presence of KH_2PO_4 correlated with the calculated trends in H_2MoO_4 and $PMo_{12}O_{40}^{3-}$ concentration respectively when the $[PO_4^{3-}]_{TOT}$ was set to be 0, 0.05, 0.07 and 0.10 mM, suggesting that the electroreduction of H_2MoO_4 was observed at $Peak_4$ and electron-reduction product of $PMo_{12}O_{40}^{3-}$ was responsible for this diffusion controlled electroreduction $Peak_5$ (Fig.4.8 (C)).

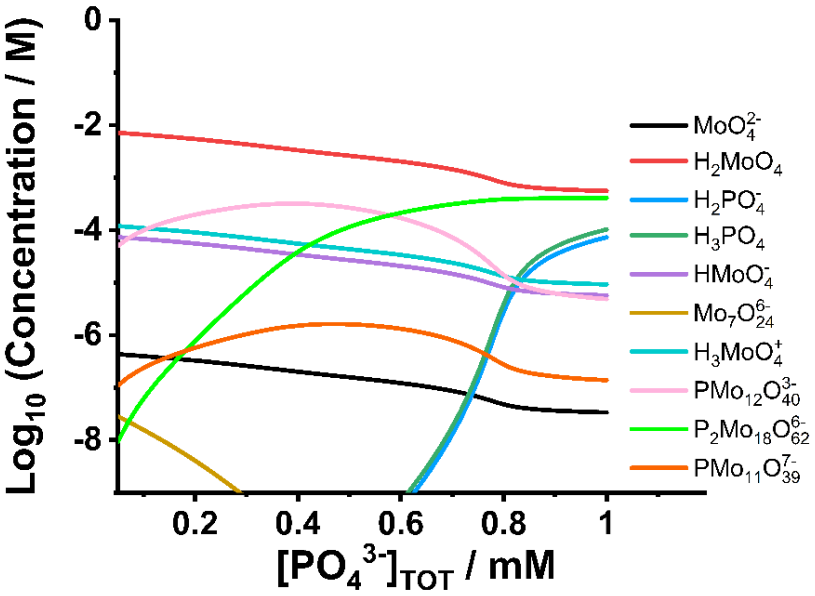


Figure.4.7 Plot of Log_{10}.Concentration of each species (including Mo(VI) and P containing compounds) versus total phosphate concentration, $[PO_4^{3-}]_{TOT}$ from 0.05 mM to 1 mM in the presence of 8 mM Mo(VI) when pH is 2.0.

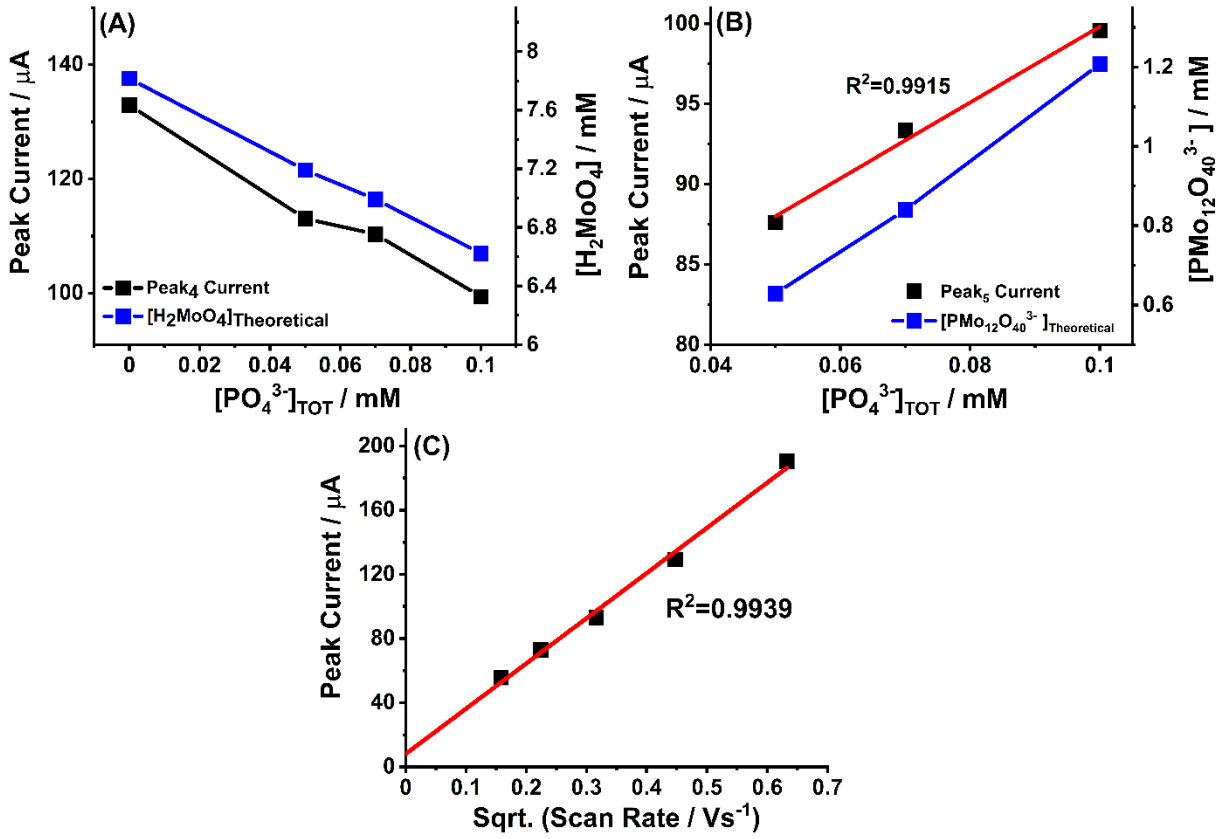


Figure.4.8 (A) Peak$_4$ current (Left Y-axis) and H_2MoO_4 theoretical concentration (Right Y-axis) as $[PO_4^{3-}]_{TOT}$ changes from 0 mM to 0.1 mM; (B) Correlation of Peak$_5$ current (Left Y-axis) and the concentration of $PMo_{12}O_{40}^{3-}$ inferred from modelling as in Chapter 3 (Right Y-axis) as a function of concentration of $[PO_4^{3-}]_{TOT}$ changes from 0.05 mM to 0.1 mM;(C) Linear peak current of Peak$_5$ behaviour at various scan rates.

In the following we sought to build on the observations above that peaks 1 and, especially, 2 were responsive to the solution phosphate concentration. We noted that these involved adsorbed Mo (VI) and that on a GCE surface the extent of adsorption was strictly limited and constrained by the geometric area of the electrode. In order to increase the amount of Mo (VI) available for detection of phosphate, we sought to immobilize the Mo (VI) species in a matrix of chitosan. As described above, the amino groups in chitosan have a pK_a value of ~ 6.5 at 298K [7] so they are protonated at acidic pH and the resulting cationic groups in principle can bind anions of Mo (VI).

Molybdate (VI) was immobilized on GC macroelectrodes by drop casting a certain amount of a chitosan-ammonium molybdate (VI) tetrahydrate (AMT) suspension dissolved in 0.1M acetic acid to create a Mo (VI)-chitosan modified electrode (AMT-CS-GCE). Then to explore the electrochemical response of AMT-CS-GCE, three GC electrodes after different treatments were compared: 1) an unmodified GCE after polishing, 2) chitosan immobilized on a bare GCE; and 3) an AMT-CS-GCE as described in the Experimental section. These were separately placed in 0.05 M K_2SO_4 (pH = 2.0) in the absence and presence of 0.01 mM KH_2PO_4. After N_2 bubbling as above to remove oxygen, the cyclic voltammograms were recorded in the sweep potential range from 0.50 V to – 0.1 V at a scan rate of 100 mV s^{-1}. As shown in Fig.4.9 (A), in the absence of KH_2PO_4, two reduction peaks were observed at 0.15 V ($Peak_1$) and 0.03 V ($Peak_2$) in 0.05 M K_2SO_4 (pH = 2.0) at AMT-CS-GCE (orange curve). The peak-to-peak separations of $Peak_1$ and $Peak_2$ ($\Delta Epp=|E_{p(anodic)}-E_{p(cathodic)}|$) were calculated to be 0.014 $\pm$ 0.003 V and 0.005 $\pm$ 0.000 V respectively which were close to the ideal value of zero for a reversible surface process, indicating that both peaks 1 and 2 seen at the AMT-CS-GCE were electrochemically reversible processes. Formal potentials were obtained from the midpoint between the reduction and oxidation peak potentials and the values of 0.158 ± 0.006V ($Peak_1$) and 0.027 ± 0.003V ($Peak_2$) were obtained. The average charge passed at $Peak_1$ and $Peak_2$ were calculated to be 1.7(±0.3) $\times10^{-6}$ C and 9.3(±3.5) $\times10^{-7}$ C, which were both substantially higher than the charge passed on the surface of only Mo(VI) modified GCE ($Peak_1$: 5.1(±1.2) $\times10^{-7}$ C and $Peak_2$: 4.7(±1.2) $\times10^{-7}$ C) suggesting there were more electroactive Mo(VI) ions adsorbed on the surface probably due to the Mo(VI) anions bound electrostatically to the $–NH_2$ groups of the chitosan which were protonated at the pH values used. Then the number of Mo (VI) containing molecules on the surface of AMT-CS-GCE of 1.2 (±0.3) $\times10^9$ ($Peak_1$) and 6.1 (±2.6) $\times10^8$ ($Peak_2$) were estimated by using the average charge passed, which was smaller compared to the number of NH_2- groups in the deposited chitosan (~1.5×10^{13}). All above indicated that the

molybdate had been successfully immobilized by chitosan on the surface of GCE and behaved in a similar way as in the solution phase.

We next turned to the analytical response of phosphate at AMT-CS-GCEs by using CV in 0.05 M K_2SO_4 (pH=2.0). The voltammogram recorded by bare GCE (green curve in Fig.4.9 (A)) and chitosan modified GCE (blue curve in Fig.4.9 (A)) containing 0.01 mM KH_2PO_4 showed no reduction peak; Only exposing the modified AMT-CS-GCE to 0.01 mM KH_2PO_4 (black curve in Fig.4.9 (A)), both reduction $Peak_1$ and $Peak_2$ became more apparent at the same potential location compared with those in the absence of KH_2PO_4. It was clear that chitosan trapped the molybdate species and provided the required acidic environment for the electrochemical reactions to occur but had no substantive effect on the response to phosphate.

To achieve the best detection sensitivity, several parameters in the cyclic voltammetric behaviour were optimized (Fig.4.10). The effect of chitosan mass concentration in the modification suspension was studied with a fixed 40 g L^{-1} AMT/10 mL 0.1M acetic acid setting the modification volume for drop-casting to be 2 μL. As shown in Fig. A4.3 (A), in the presence of 5.0 μM KH_2PO_4, the response increased initially upon raising the chitosan concentration to 5 g L^{-1} due to the presence of chitosan which was inferred to have effectively promoted the stabilization of AMT adsorbed on the surface. However, this effect began to decrease at concentrations higher than 5 g L^{-1} probably because excess chitosan lowered the electrical conductivity of the film. Therefore, the chitosan mass concentration of 5 g L^{-1} was used for subsequent electrode preparation. Further, when 2 μL of the AMT/chitosan suspension was used for modification, the current of $Peak_2$ in the resulting AMT-CS-GCE was the highest (Fig.A4.3(B)). The thickness of the modified AMT-chitosan layer was estimated to be 1.4 μm (see Section A4.3).

The effect of pH on the performance of AMT-CS-GCEs in respect of the cyclic voltammetric behaviour of phosphate was investigated in 10.0 μM KH_2PO_4/0.05M K_2SO_4

(Fig.A 4.3(C)-(D)). In the pH range from 1.5 to 5.0, the reduction peaks, $Peak_1$ and $Peak_2$ were seen to shift in the cathodic direction to lower potential values with increasing pH of the electrolyte solution. Further, above pH 2 there was a gradual decrease in the peak sizes which was consistent with the species distribution diagram (Fig.3.1 in Chapter 3) where the monomeric forms ($HMoO_4^-$, H_2MoO_4 and $H_3MoO_4^+$) gradually disappeared in the range 3<pH<5, and which were likely the dominant species of Mo (VI) in electrochemical reduction processes. This might limit the sensitivity of AMT-CS-GCEs in low acidic condition.

Next, cyclic voltammograms with respect to phosphate concentration at AMT-CS-GCEs were further conducted in 0.05 M K_2SO_4 (pH=2.0). Fig.4.9 (B) depicted the cyclic voltammetric response as a function of increasing concentration of KH_2PO_4 with the concentration in the range of 5.0–80.0 μM. The plot of peak height versus phosphate concentration obtained using CV showed a linear relationship in the mentioned range (Inlay of Fig.4.10 (B)). The calibration curves are: $Peak_1$: $I_p(\mu A) = 0.027[PO_4^{3-}]_{TOT}$ (μM) + 2.2 (μA), R^2=0.9685; $Peak_2$: I_p (μA) = $0.093[PO_4^{3-}]_{TOT}$ (μM) +3.6 (μA), R^2=0.9974. The limit of detection (LOD) was found equal to 0.7 μM, calculated as $3\sigma_b/m$ using 10 measurements of the blank (n=10), where σ_b is standard deviation of results obtained in blank solution, m is the slope of calibration curve.

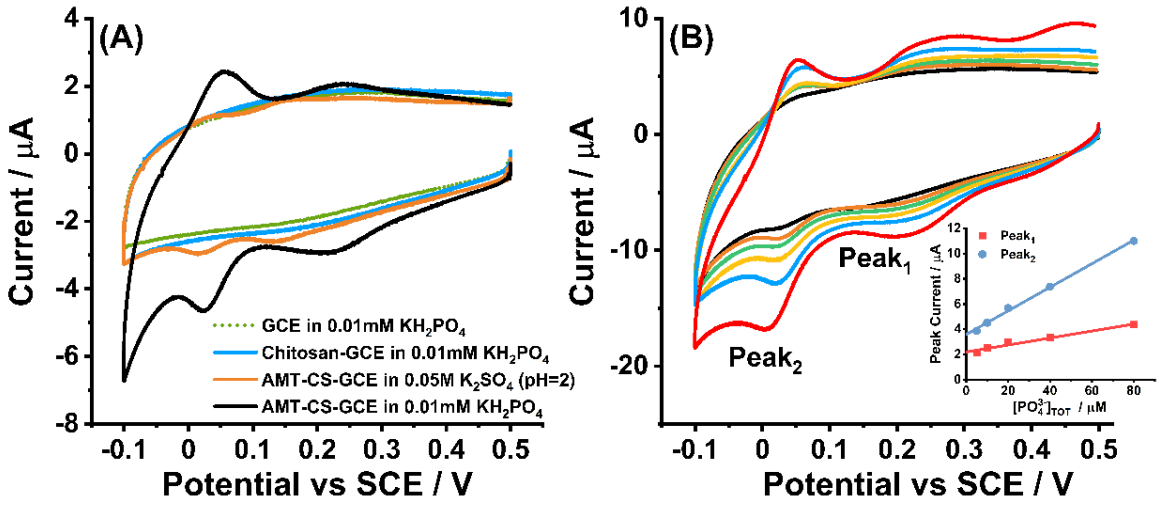


Figure.4.9 (A) Electrochemical study of KH_2PO_4 at GC macroelectrodes at a scan rate of 100 mV s^{-1} under degassed condition: cyclic voltammograms of modified and unmodified GC

macroelectrodes; (B) cyclic voltammetric responses of increasing concentration from 5.0–80.0 μM of KH_2PO_4 at AMT-CS-GCEs in 0.05 M K_2SO_4 (pH=2.0) (Inlay: calibration curve of peak current versus total phosphate concentration).

The above demonstrated that the AMT-CS-GCE had the capability to detect the lower concentrations of phosphate in aqueous solutions by CV in respect to the bare GCE, also suggested that the electrochemical reduction of Mo (VI) to Mo (V) happened on the modified electrode were more effectively promoted by catalysing phosphate reduction. However, to further meet the requirements of trace phosphate analysis in real samples and find out the possibility of reagent-less detection of phosphate at neutral pH, we employed square wave voltammetry (SWV) to reduce the effect of capacitive background current and improve the detection sensitivity in the following.

4.3.3 The sensitivity performance of the modified electrode assessed using square wave voltammetry

Before investigating the detection of phosphate by SWV, the analytical and voltammetric parameters such as accumulation time, scan rate and pulse height were optimized as described in the Section A4.4.

Next the SWV curves in varying concentrations of KH_2PO_4 and an AMT-CS-GCE were studied in 0.05M K_2SO_4 to determine the lower detectable level under two pH conditions (pH=2.0 and pH=5.8) separately (Fig.4.10). When the 0.05M K_2SO_4 solution pH was adjusted to 2.0, the peak heights of $Peak_1$ and $Peak_2$ at potentials of 0.20 V and 0.05V obtained at freshly prepared AMT-CS-GCEs within the detection range of 0.3-2.0 μM (Fig.4.10(A)) showed 'memory effects' since the adsorption of phosphate on the surface of modified electrode was almost fully irreversible with only slow desorption observed over very long timescales (Fig. A4.5). The linear relationships between $Peak_2$ current and phosphate concentration were described in Fig.4.10(B) by the following equation: $I_p(\mu A) = 4.38(\pm 0.12)\ [PO_4^{3-}]_{TOT}\ (\mu M)$ +

5.59(±0.01) (μA), R^2=0.9977. The limit of detection (LOD) for KH_2PO_4 was found to be 0.15 μM ($3\sigma_b/m$, n=10) with a sensitivity of 4.4(±0.1) μA/μM, signals were significantly amplified in SWV compared to CV. While concentrations exceeding 2.0 μM KH_2PO_4, the electrochemical signal in SWV started to level out as the adsorption sites on the surface of modified electrode and tended to saturate with KH_2PO_4 (Fig.A4.6(A)).

SWV by using AMT-CS-GCE was then conducted of KH_2PO_4 with the concentration in the range of 0.05–0.8 μM in 0.05M K_2SO_4 (measured pH=5.8) with three separate measurements for each concentration. Fig.4.10 (C) showed the SWV response as a function of increasing concentration of KH_2PO_4. The plot of peak height of $Peak_2$ versus KH_2PO_4 concentration (Fig.4.10 (D)) also indicated a linear relationship in the concentration range of 0.05–0.8 μM which could be depicted by a calibration curve I_p(μA) = 6.53(±0.28) $[PO_4^{3-}]_{TOT}$ (μM) + 2.53(±0.06) (μA), R^2=0.9908. The LOD was calculated to be 0.17 μM ($3\sigma_b/m$, n=10) of the blank by with a sensitivity of 6.5(±0.3) μA/μM. This result provides experimental validation for the practicality of AMT-CS-GCE to detect the concentration of KH_2PO_4 sensitively with SWV technique under neutral condition. As displayed in Fig.A4.6(B), when the concentration of KH_2PO_4 was increased to 1.0 μM in 0.05M K_2SO_4 (pH = 5.8), the linear relationship between $[PO_4^{3-}]_{TOT}$ and peak height of $Peak_2$ started to level out.

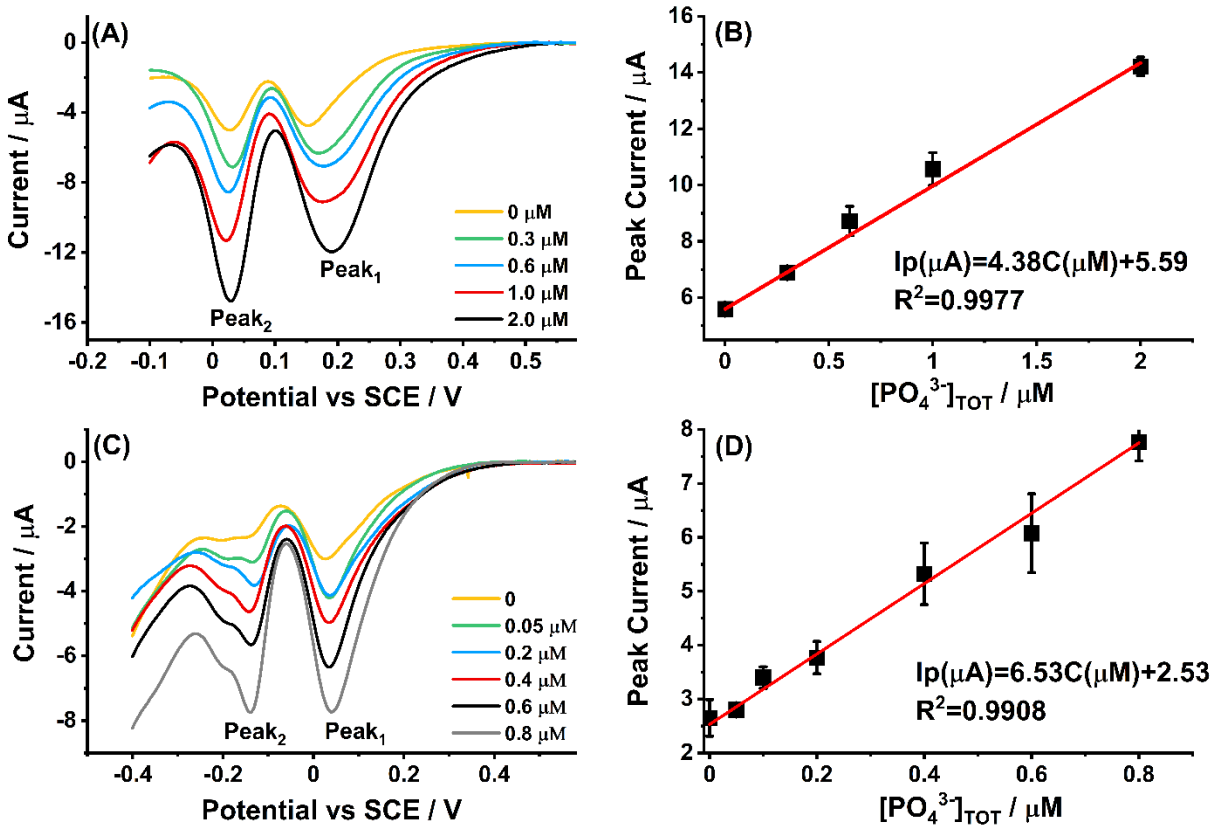


Figure.4.10 (A) Square wave voltammograms of AMT-CS-GCEs in 0.05M K_2SO_4 (pH=2) with varying concentrations of KH_2PO_4 from 0 μM to 2.0 μM and (B) calibration curve of peak$_2$ current versus total phosphate concentration; (C) Square wave voltammograms of AMT-CS-GCEs in 0.05M K_2SO_4 (pH=5.8) with varying concentration of KH_2PO_4 from 0 μM to 0.8 μM and (D) calibration curve of peak$_2$ current versus total phosphate concentration, scan rate =25 mVs^{-1}.

4.3.4 Interference testing and detection in real samples

Before applying AMT-CS-GCE for the detection of phosphate in real samples, the selectivity of the AMT-CS-GCE to phosphate was evaluated in the presence of Cl^- and NO_3^- separately (Fig. A4.7) since PO_4^{3-}, Cl^- and NO_3^- co-exist in most water environments[15, 16]. The SWV response of AMT-CS-GCE were first scanned in 0.05M K_2SO_4 (pH = 2) in the presence of 0, 0.1 and 1 mM Cl^- or NO_3^- respectively in varying concentrations of KH_2PO_4 from 0 to 2.0 μM. The plot of current value of Peak$_2$ versus KH_2PO_4 concentration in the presence of 0, 0.1

and 1 mM Cl^- or NO_3^- visible in Fig.A4.7 (A) and Fig.A4.7 (B) respectively showed that the linear response to phosphate was unchanged to within 12% and 13% for concentrations of either chloride or nitrate of less than 1 mM which was markedly above the levels necessary for environmental analysis[17, 18]

Having investigated the inference from NO_3^- and Cl^- to the detection of KH_2PO_4 at AMT-CS-GCE, we next employed the SWV for the quantification of phosphate in real samples. The concentration of phosphate varies from 25 μg L^{-1} to 1.6 mg L^{-1} (0.26 μM to 16.8 μM) in natural and waste waters[19, 20]. WHO in 1980 concluded that there was no nutritional basis for the regulation of phosphorus levels in the drinking water supplies [21]. However, to control eutrophication, US EPA made the recommendation of a total phosphate concentration, $[PO_4^{3-}]_{TOT} < 0.025$ mg L^{-1} (0.26 μM) in reservoirs and a maximum permissible concentration of orthophosphate in river water is 0.1 mg L^{-1} (1.05 μM) [22]. Based on these conditions and recommended safety limits for phosphate in the water, it is suggested that the LOD of AMT-CS-GCE (0.15 μM) meets the requirements of analysing the concentration of phosphate in authentic samples, as next confirmed experimentally.

After simple filtering to remove any particulate matter, samples of tap water and 10-fold diluted pond water solution were analysed directly after the addition of 0.05M K_2SO_4 (pH=2). SWV was then performed under the experimental parameters reported. The $peak_2$ heights were measured from square wave voltammograms of AMT-CS-GCEs in solution with tap water or 10-fold diluted pond water using the standard addition method as described in the Experimental section and employing a simple background correction to the voltammetry (Fig.4.11). The accuracy of the electrochemical measurement was validated by a "recovery" test where known concentration (0.05, 0.15 and 0.35 μM) KH_2PO_4 standard solutions were used to add into tested electrolyte 0.05M K_2SO_4 (pH=2) prepared by the tap water and 10-fold diluted pond water

solution respectively prior to square wave voltammetric measurements. Values close to 100% were attained as shown in Table 4.1.

To investigate the applicability of AMT-CS-GCEs in raw, undiluted samples, the detection of inorganic phosphate in pond water was conducted by exposing the AMT-CS-GCEs to neat pond water. SWV performed according to optimized experimental parameters and the square wave voltammetric response in original sample (pH=7.8) was first obtained, then spiked with 0.05, 0.08, 0.10 and 0.15 μM KH_2PO_4. The possible interference by chloride at similar pH were investigated first in 0.05M K_2SO_4 (pH=7.8) at AMT-CS-GCEs in the presence of 0, 0.1 and 1 mM Cl^- in variable concentrations of KH_2PO_4 from 0 to 0.2 μM (shown in Section A4.8), the results of which showed a good resilience towards chloride at a pH value similar to the neat pond water. Meanwhile, the concentration of chloride in the neat pond water was obtained to be 10.2 mg L^{-1} (0.29 mM) by a Ag^+ standard titration method [23], confirming a concentration compatible with the analysis of phosphate at AMT-CS-GCEs. As shown in Fig.4.12 (A), the electrochemical signal $Peak_1$ and $Peak_2$ from SWV can be observed at 0.0 and -0.2 V. The linear relationships between $Peak_2$ current and added KH_2PO_4 concentration in pond water was described in Fig.4.12 (B) by Eq. (4.9), confirming the application of AMT-CS-GCEs for environmental monitoring.

$$\boldsymbol{I_p(\mu A) = 28.71(\pm 2.53)\,[PO_4^{3-}]_{TOT}\,(\mu M) + 2.89(\pm 0.22)\,(\mu A),\ R^2 = 0.9772} \qquad (4.9)$$

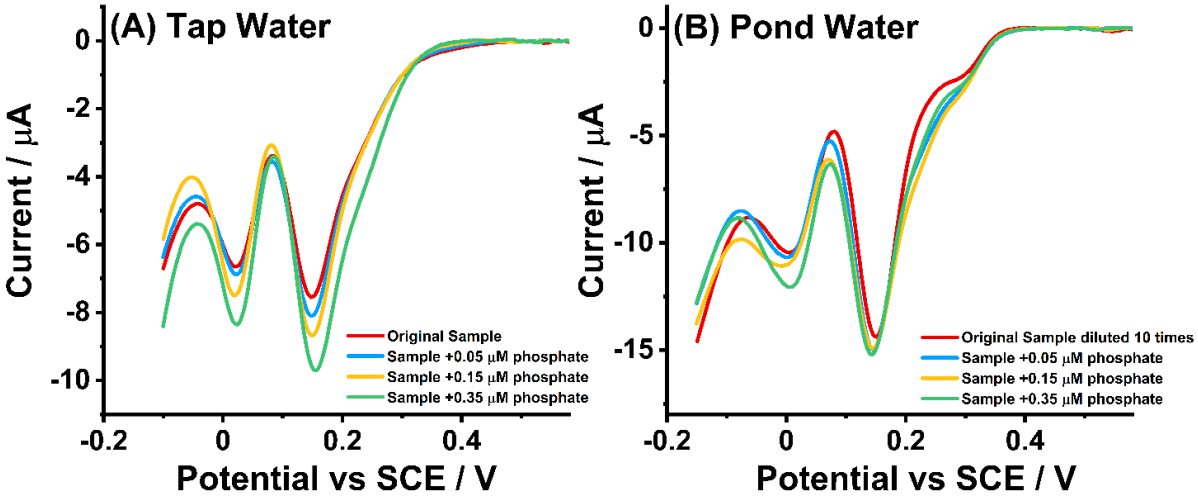


Figure.4.11 Square wave voltammograms of AMT-CS-GCEs in 0.05M K_2SO_4 (pH=2) solution prepared by (A) tap water and (B)10 times-diluted pond water with the addition of 0, 0.05,0.15 and 0.35 μM KH_2PO_4 standard solution, scan rate =25 mVs^{-1}.

Table 4.1 Concentrations analyzed by calibration curves in Fig.4.10 (B) of detected phosphate in tap water and pond water with standard solutions and the corresponding recoveries.

Solution	Measured Concentration using SWV /μM	Recovery/%
Tap water		
Original Sample	0.22 ± 0.02	/
Sample+0.05 μM KH_2PO_4	0.28 ± 0.01	110
Sample+0.15 μM KH_2PO_4	0.37 ± 0.07	91
Sample+0.35 μM KH_2PO_4	0.57 ± 0.04	100
Pond water		
Original Sample after diluted 10 times	1.11 ± 0.01	/
Sample+0.05 μM KH_2PO_4	1.17 ± 0.01	116
Sample+0.15 μM KH_2PO_4	1.26 ± 0.02	92
Sample+0.35 μM KH_2PO_4	1.47 ± 0.01	107

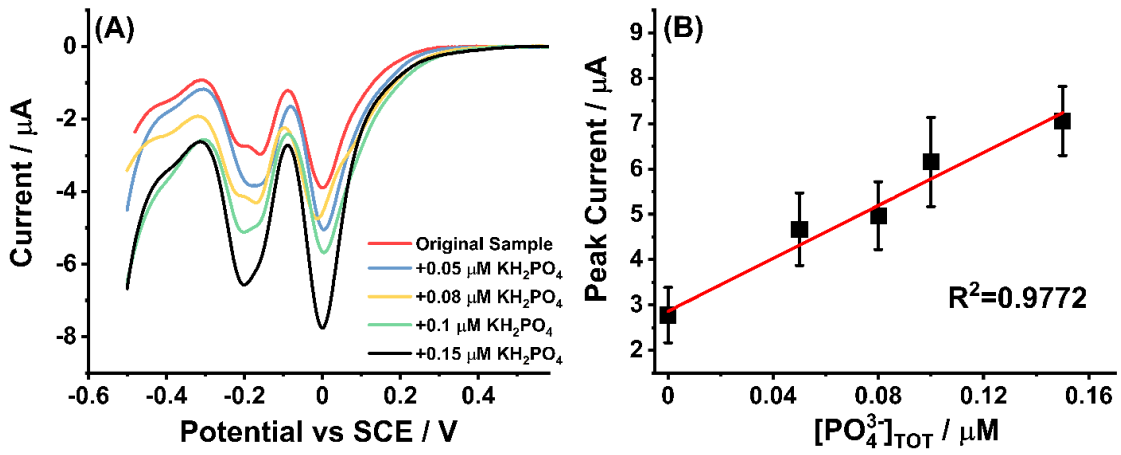


Figure.4.12 (A)Square wave voltammograms of AMT-CS-GCEs in pond water without any pre-treatment with varying concentrations of KH_2PO_4 from 0 μM to 0.15 μM and (B) calibration curve of $Peak_2$ current versus total phosphate concentration, scan rate=25 mVs^{-1}

4.4 Conclusions

The developed AMT-CS-GCE sensor realised a low detection limit for phosphate using cyclic voltammetry (CV) and square wave voltammetry (SWV), showing a high sensitivity of 4.4 ± 0.1 μA/μM and selectivity in standard solutions and real samples. This type of amperometric sensor is promising and practical for trace detection of inorganic phosphate in water environments in respect of the safety limits in drinking water and natural water set by US EPA. Preliminary experiments with the Mo/P system explored in this chapter were discouraging in certain respects notably the limit of detection range and severe 'memory effects' due to the irreversibility of phosphate adsorption on the surface of modified electrode. The sensitivity of a phosphate sensors in which protonated amino groups are used to anchor anionic mediators reflects in part the quantity of material which can be so immobilised. This, in turn, is limited ion in the case of chitosan by the electronic conductivity of the drop casted film. Consideration was thus given the use of amino-functionalised multiwalled carbon nanotubes. Nevertheless, interesting electrochemical data on the nanotube themselves stimulated the work presented in the next chapter.

Appendix

Section A4.1: Calculation of surface coverage and particle average separation

In order to determination the charge passed in the voltammetric signals from surface bound redox couples the following procedure was used in which the charge passed (Q / C) was calculated via $Q = \frac{S_{peak\ area}}{v}$, where $S_{peak\ area}$ is the peak area (A·V) and v is the scan rate (V s^{-1}). The peak area was found using OriginPro 2017 after background correction of the raw cyclic voltammograms. This is illustrated by way of a first example using a simple cyclic voltammogram with single peak as shown in Fig.A4.1. A baseline spline was fitted between the potentials at which the surface bound voltammetric wave was judged to have started and ended, then subtracted from the peak and the peak area was calculated by numerical integration.

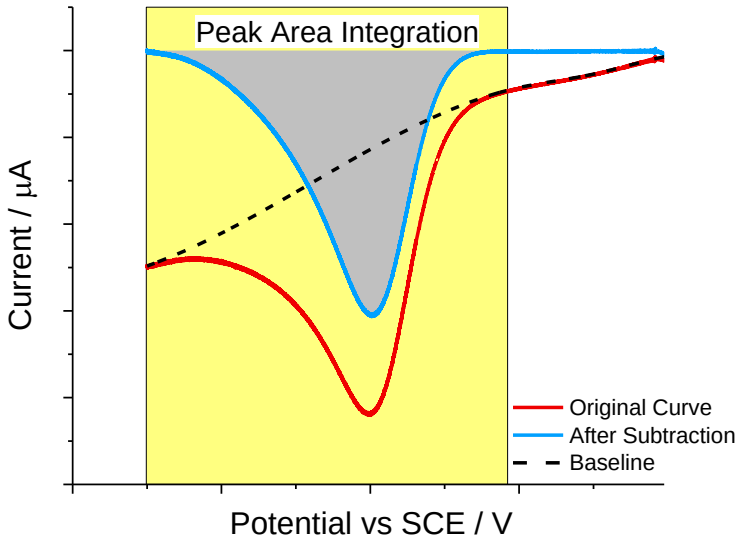


Figure.A4.1 The calculation for estimation of the single peak area in cyclic voltammograms including the original curve (red line), subtracted curve (blue line) and baseline (black line).

In a second example in which there were overlapping peaks the procedure was illustrated using the cyclic voltammogram measured at a bare GC macroelectrode in 8 mM Mo (VI)/ 0.05 M K_2SO_4 solution (pH 2.0) at a scan rate of 400 mVs^{-1} shown in Fig.A4.2 (A) where peaks 1 and 2 overlapped markedly. Fig. A4.2 illustrated the procedure: the raw cyclic voltammogram

curve was again referenced to a baseline spline drawn between the potentials at which the combine feature was judged to have started and finished. In order to deconvolute the charge into separate contributions form peaks 1 and 2, the peak fitting function (Y=0 as baseline, Peak finding method: 2nd Derivative (search Hidden peaks), Smooth derivative method: Quadratic Savitzky-Golay, Peak filtering by number (n=2)) in OriginPro 2017 was used to separate peaks 1 and 2 (Fig.A4.2(B)). The peak areas of $Peak_1$ and $Peak_2$ were then found by numerical integration (Fig. A4.2 (C) and Fig. A4.2 (D)) respectively. Next, the surface coverage (Γ, mol cm^{-2}) can be obtained via $\Gamma = \frac{Q}{nFA}$, where n is the number of electrons transfer (n=1), F is the Faraday constant (96485 C mol^{-1}), A is the electrode area (7.1×10^{-2} cm^2). Finally, the average adsorbate-adsorbate separation(d) was obtained via $d = \sqrt{\frac{1}{N_A\times\Gamma}}$, where N_A is the Avogadro constant (6.02×10^{23} mol^{-1})

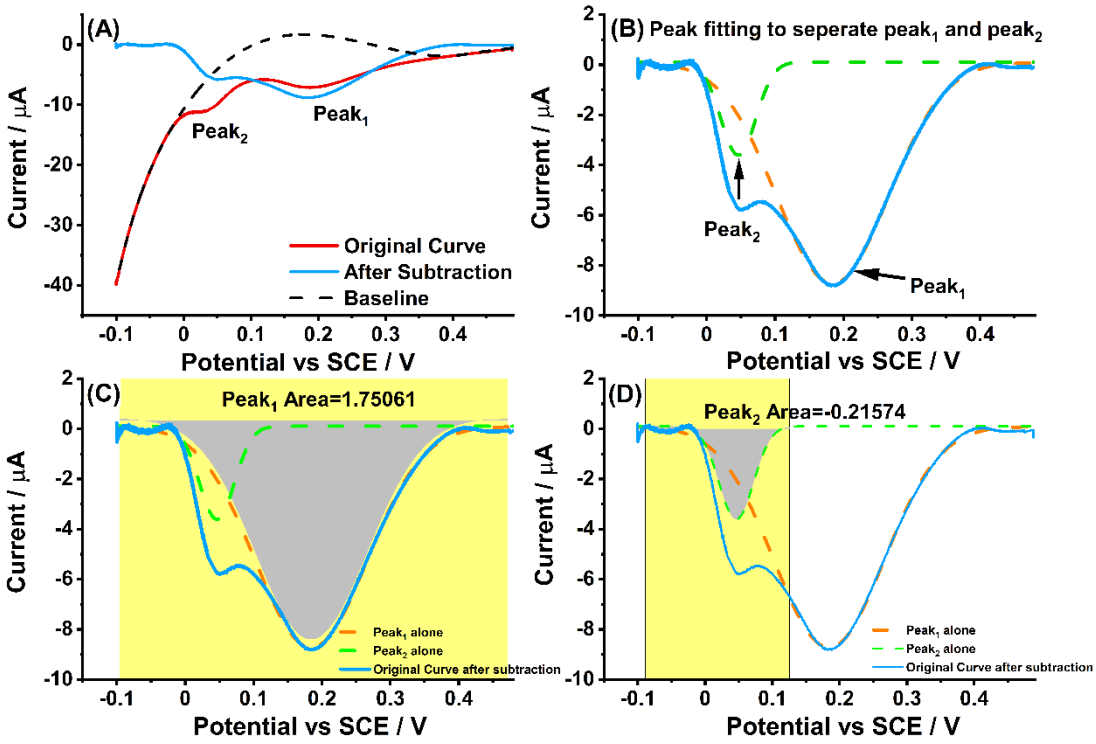


Figure.A4.2 Schematic for the estimation of the peak area in cyclic voltammograms recorded at a GC macroelectrode in 8 mM Mo (VI)/ 0.05 M K_2SO_4 solution (pH 2.0) at a scan rate of 400 mVs^{-1}: (A) The background correction to the original cyclic voltammogram: the

original curve (red line), the baseline (black line) and subtracted curve (blue line); (B) The peak fitting to separate Peak$_1$ and Peak$_2$: the subtracted curve (blue line), separate Peak$_1$(orange line) and Peak$_2$ (green line); (C) The peak area integration of Peak$_1$; (D) The peak area integration of Peak$_2$.

The charge passed (Q), surface coverage (Γ) and average adsorbate molecular separation (d) for each reduction peak (Peak$_1$ and Peak$_2$) at different scan rates (100, 200 and 400 mVs^{-1}) are listed in Table A4.1.

Table A4.1 The average surface coverage given by the average value of Q (n = 3) calculated from peak areas at scan rates (100, 200 and 400 mVs^{-1}) after background correction and the average molecular adsorbate separation of Peak$_1$ and Peak$_2$

	Scan rate / mVs^{-1}	Q / C	Surface coverage / mol cm^{-2}	Particle Distance /cm
Peak$_1$	100	6.6×10^{-6}	9.7×10^{-10}	4.1×10^{-8}
	200	4.6×10^{-6}	6.7×10^{-10}	5.0×10^{-8}
	400	4.4×10^{-6}	6.4×10^{-10}	5.1×10^{-8}
	Average	5.2×10^{-6}	$(7.6\pm1.8)\times10^{-10}$	$(4.7\pm0.5)\times10^{-8}$
Peak$_2$	100	4.2×10^{-7}	6.1×10^{-12}	5.2×10^{-7}
	200	8.5×10^{-7}	2.5×10^{-11}	2.6×10^{-7}
	400	5.5×10^{-7}	3.2×10^{-11}	2.3×10^{-7}
	Average	6.1×10^{-7}	$(2.1\pm1.3)\times10^{-11}$	$(3.4\pm1.6)\times10^{-7}$

Section A4.2: Optimization of CV parameters

As shown in Fig. A4.3 (A), in the presence of 5.0 μM KH_2PO_4, the response increased initially upon raising the chitosan concentration to 5 g L^{-1} due to the presence of chitosan which was inferred to have effectively promoted the stabilization of AMT adsorbed on the surface. However, this effect began to decrease at concentrations higher than 5 g L^{-1} probably because excess chitosan lowered the electrical conductivity of the film. Therefore, the chitosan mass

concentration of 5 g L^{-1} was used for subsequent electrode preparation. Further, when 2 µL of the AMT/chitosan suspension was used for modification, the current of $Peak_2$ in the resulting AMT-CS-GCE was the highest (Fig.A4.3(B)).

The effect of pH on the performance of AMT-CS-GCEs in respect of the cyclic voltammetric behavior of phosphate was investigated in 10.0 µM KH_2PO_4/0.05M K_2SO_4 (Fig.A 4.3(C)-(D)). In the pH range from 1.5 to 5.0, the reduction peaks, $Peak_1$ and $Peak_2$ were seen to shift in the cathodic direction to lower potential values with increasing pH of the electrolyte solution. Further, above pH 2 there was a gradual decrease in the peak sizes.

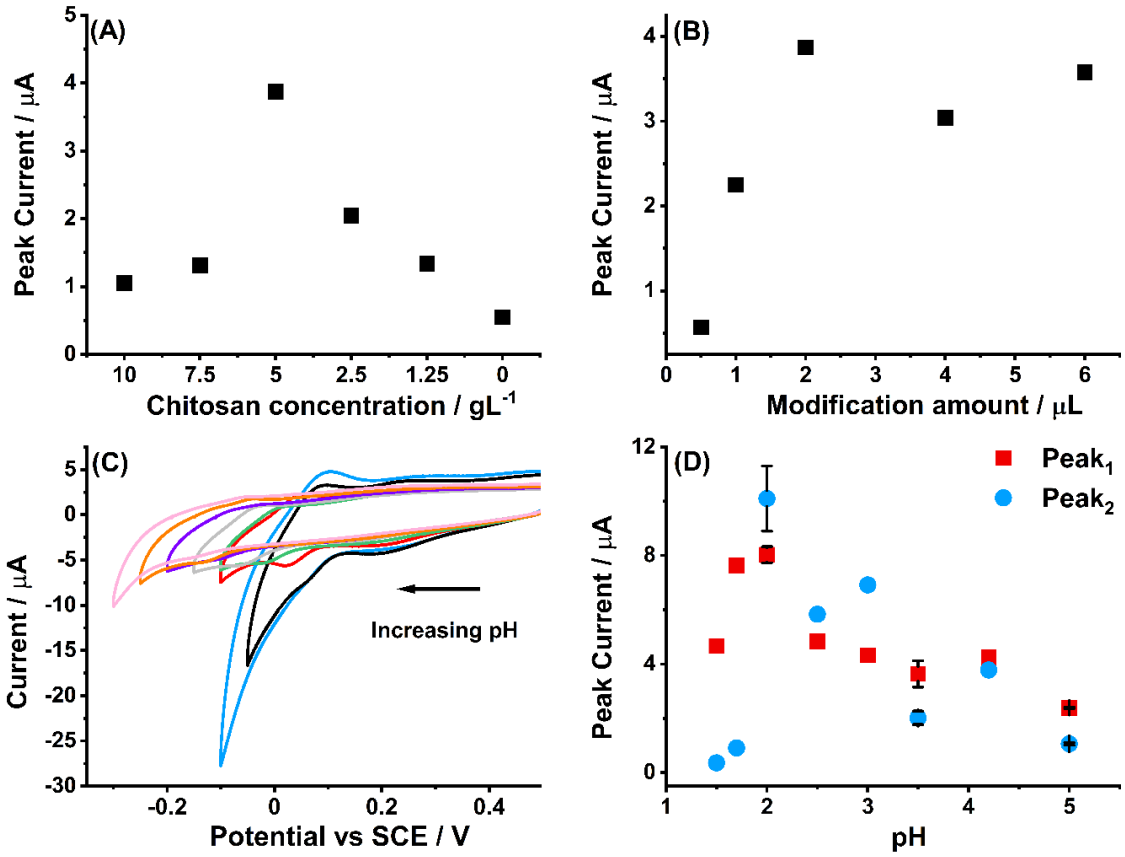


Figure.A4.3 Effect of (A) the concentration of chitosan in 40 g L^{-1} AMT/10 mL 0.1M acetic acid suspension and (B) modification amount on the $Peak_2$ current response of AMT-CS-GCEs in 5.0 µM KH_2PO_4/0.05M K_2SO_4 (pH=2.0); (C) Cyclic voltammetric responses of AMT-CS-GCEs measured in 10.0 µM KH_2PO_4/0.05M K_2SO_4 at different pH under degassed condition, Scan rate = 100 mVs^{-1}.

Section A4.3: Estimation of thickness of the chitosan layer

2 μL of AMT-chitosan (400:5g /L) stock mixture was drop-cast on the GC electrode and the film dry thickness can be determined as follows:

Mass of 2μL chitosan in suspension is m=5g/L×2×10^{-6} L=10^{-5} g

The density of dry chitosan is relevant to its storage and drying conditions and in this case the dry density of chitosan $\rho_{\text{DryChitosan}}$=1.0 g cm^{-3} [15]

Therefore, the dry volume of Chitosan is

$$V=\frac{m}{\rho_{\text{DryChitosan}}}=\frac{10^{-5}\ g}{1\ g/cm^3}=10^{-5}\ cm^3$$

The diameter of GC electrode is 3.02 ± 0.005 mm, hence the area is $A=\frac{\pi D^2}{4}$=7.07×10^{-6} m^2

The dry thickness for 2 μL of AMT-Chitosan thin film on the GC electrode is

$$h=\frac{V}{A}=\frac{10^{-11}\ m^3}{7.07\times10^{-6}\ m^2}=1.4\ \mu m$$

Section A4.4: Optimization of SWV parameters

To optimise the SWV parameters, AMT-CS-GCEs were immersed in 0.05M K_2SO_4 (pH=2) containing 1.0 μM KH_2PO_4 (shown in Fig.A4.4). First, the effect of accumulation time on the current intensity was examined at a range from 30 to 600s, while maintaining all other parameters constant (preliminary selection of a scan rate of 25 mVs^{-1} and a pulse height of 25 mV). As shown in Fig. A4.4 (A), the peak current increased up to a value of 180s and subsequently decreased at longer accumulation time possibly because of leaching. Hence, 180s was selected as the optimal accumulation time for KH_2PO_4 detection. Second, the effect of scan rate on the AMT-CS-GCE sensitivity was evaluated at different values of 2.5, 5, 10, 25, 50 and 100 mVs^{-1} maintaining an optimal accumulation time of 180s and a preliminarily selected pulse height of 25 mV. As shown in Fig. A4.4 (B), the optimal scan rate of 25 mVs^{-1} was found for KH_2PO_4 detection which help to achieve the max electrochemical current signal. Finally, the

pulse height was re-assessed for SWV maintaining all other optimum parameters constant, peak currents of $Peak_1$ and $Peak_2$ increased upon increase of the pulse height up to 25 mV and gradually kept steady in the range from 25 to 40 mV (Fig. A4.4 (C)), therefore, 25 mV was selected as the optimum pulse height. In summary, optimal parameters for the detection of KH_2PO_4 using SWV selected to be at an accumulation time of 180s, a scan rate of 25 mVs^{-1} and a pulse height of 25 mV for all subsequent experiments.

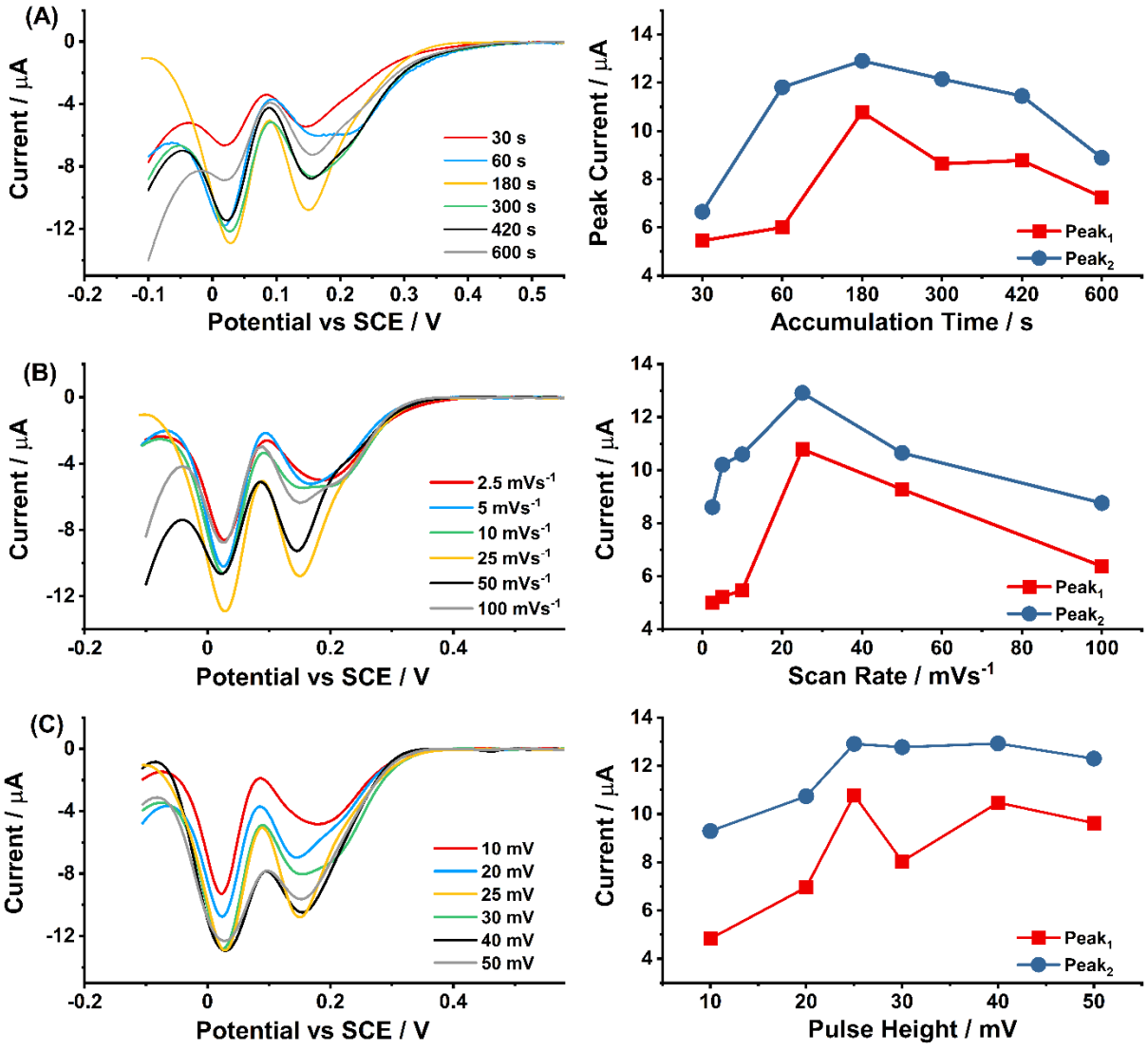


Figure.A4.4 The effect of (A) accumulation time, (B) scan rate and (C) pulse height on the peak currents of $Peak_1$ and $Peak_2$ using SWV at AMT-CS-GCEs in 0.05M K_2SO_4 (pH=2) containing 1.0 µM KH_2PO_4.

Section A4.5: Memory effects in AMT-CS-GCE

A freshly prepared AMT-CS-GCE was first immersed in 0.05M K_2SO_4 solution (pH = 2.0, adjusted by a small amount of 0.5 M H_2SO_4) in the presence of 1 µM KH_2PO_4. After obtaining the peak heights of $Peak_1$ and $Peak_2$ at 0.20 V and 0.05 V by employing SWV, this used AMT-CS-GCEs was transferred into another 0.05 M K_2SO_4 solution with absence of KH_2PO_4. Extending the waiting time gradually from 1min to 4, 9 ,20 ,40 ,80 ,140 ,200 ,260 and 320 mins, the square wave voltammograms were scanned in succession at those time points. Fig.A4.5 (A) demonstrates the significantly enhanced peak heights especially for $Peak_2$ at the first time of scanning in blank solution as compared with that obtained from a freshly prepared AMT-CS-GCE in solution containing 1 µM KH_2PO_4. Then with the prolonged waiting time, the peak current of $Peak_2$ indicated a slow decay and remained close to the first response value until the duration time is over 300 mins (Fig.A4.5(B)). This showed 'memory effects' since the adsorption of phosphate on the surface of modified electrode was almost fully irreversible with only slow desorption observed over very long timescales.

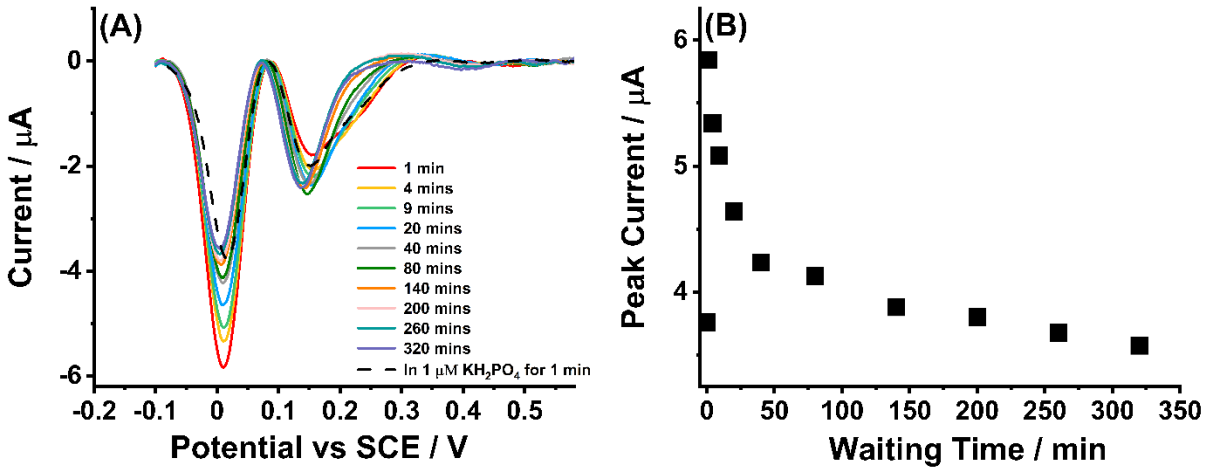


Figure.A4.5 Square wave voltammograms of AMT-CS-GCEs in 0.05M K_2SO_4 (pH=2) in the absence of KH_2PO_4 as waiting time extended after scanned in the presence of 1µM KH_2PO_4 for 1 min (A) and plot of peak current of $Peak_2$ versus waiting time (B).

Section A4.6: The upper detection limit of AMT-CS-GCE in 0.05M K_2SO_4 (pH=2 and 5.8)

To find out the upper detection limit of AMT-CS-GCE in 0.05 M K_2SO_4 of pH = 2 and pH = 5.8 respectively, SWV curves were studied using freshly prepared AMT-CS-GCEs with varing concentrations of KP_2SO_4. Under pH = 2.0 condition, when concentrations of KH_2PO_4 exceeded 2.0 μM, the electrochemical signal in SWV started to level out and tended to saturate with KH_2PO_4 (Fig.A4.6(A)). As for pH 5.8, the linear relationship between $[PO_4^{3-}]_{TOT}$ and peak height of $Peak_2$ started to level out when the concentration of KH_2PO_4 was increased to 1.0 μM (Fig.A4.6(B)).

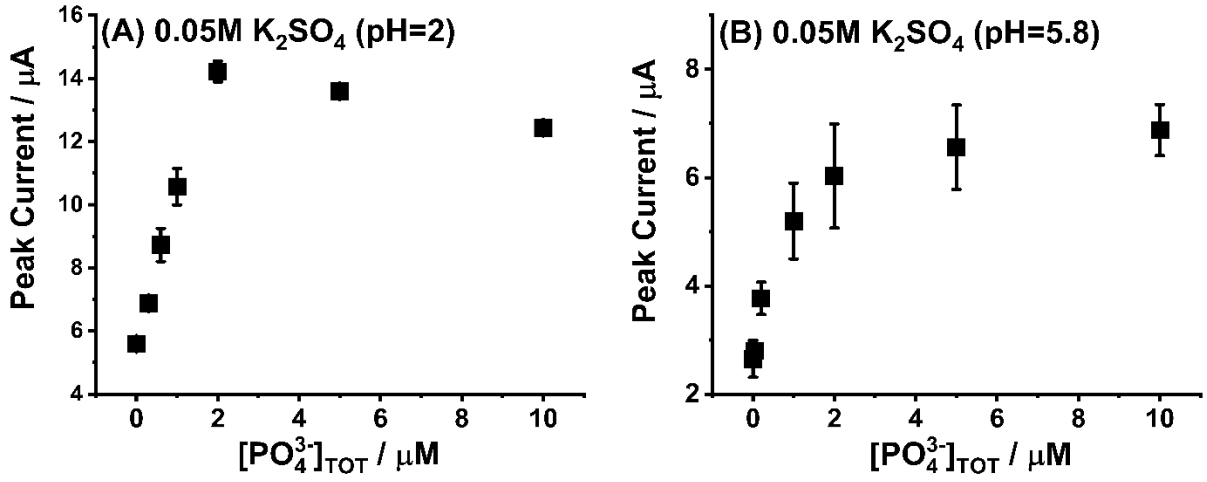


Figure.A4.6 Plot of peak current of $Peak_2$ versus the concentration of total phosphate concentration in the range from 0 to 10.0 μM at AMT-CS-GCE in (A) 0.05M K_2SO_4 (pH=2) and (B) 0.05M K_2SO_4 (pH=5.8).

Section A4.7: Interference tests in the presence of NO_3^- and Cl^-

To investigate possible interference by chloride or nitrate, amperometric detection of KH_2PO_4 with different concentration (0-0.8 μM) in the presence of 0, 0.1 and 1 mM Cl^- or NO_3^- were carried out in 0.05M K_2SO_4 (pH=5.8) at AMT-CS-GCEs. As detailed in Fig.A4.7 (C) and (D), $Peak_2$ increased in size slightly in the presence of either chloride or nitrate but linear correlations between the $Peak_2$ current and KH_2PO_4 concentration in the presence of excess Cl^- or NO_3^- for concentration of chloride below 0.1 mM and nitrate below 0.1 mM were observed

validating the standard addition method. For concentrations of either anion in excess of 100 times that of the analyte necessary linearity was absent signalling the need for sample pre-treatment in these cases.

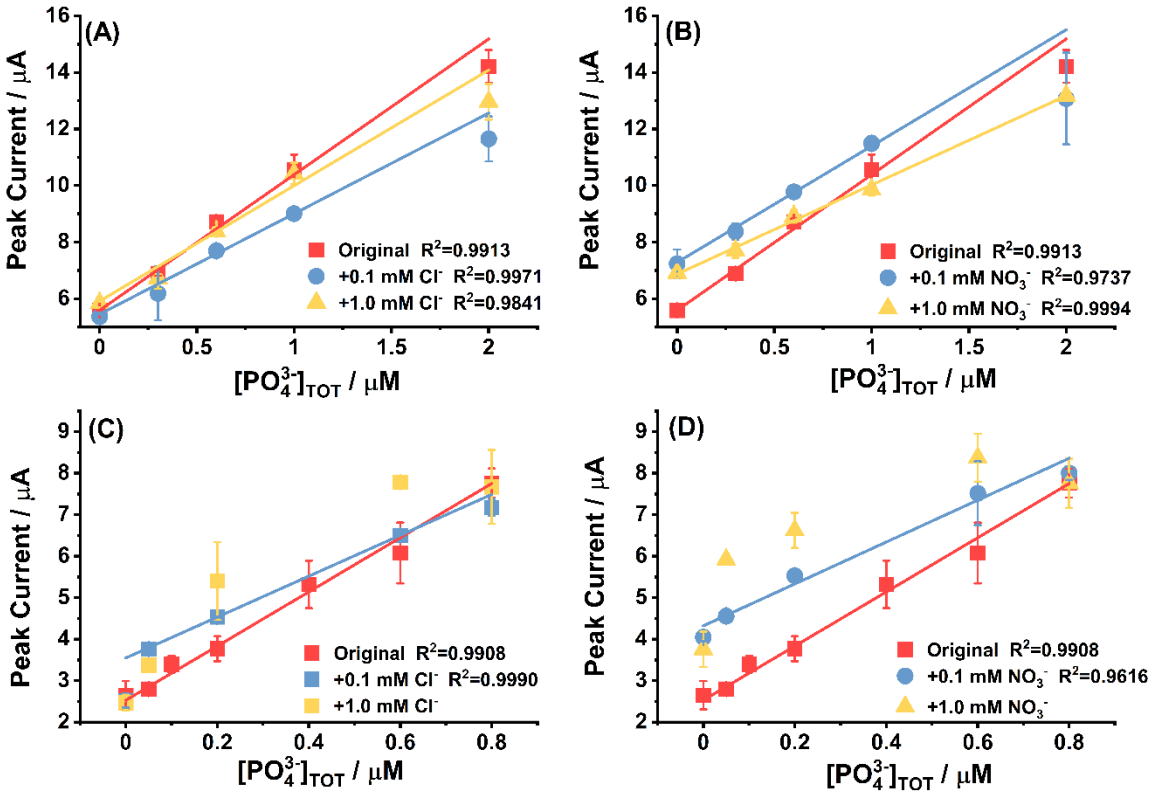


Figure.A4.7 Plots of peak$_2$ current versus KH_2PO_4 concentration in the presence of 0, 0.1,1 mM Cl^- (A) and NO_3^- (B) respectively in 0.05M K_2SO_4 (pH=2), scan rate = 25 mVs^{-1}; Plots of peak$_2$ current versus total phosphate concentration in the presence of 0, 0.1,1 mM Cl^- (C) and NO_3^- (D) respectively in 0.05 M K_2SO_4 (pH=5.8), scan rate = 25 mVs^{-1}.

Section A4.8: The applicability of AMT-CS-GCE in 0.05M K_2SO_4 (pH=7.8)

SWV at AMT-CS-GCEs was then conducted for KH_2PO_4 of concentrations in the range of 0 - 0.2 μM in 0.05M K_2SO_4 (measured pH=7.8) with three separate measurements for each concentration. Fig.A4.7 (A) shows the SWV response as a function of increasing concentration of KH_2PO_4. The inlay plot of peak height of Peak$_2$ versus KH_2PO_4 concentration (Fig.A4.8(A)) indicates a linear relationship in the concentration range of 0 - 0.2 μM which was quantified by the linear calibration $I_p(\mu A) = 57.1(\pm 4.5)\ [PO_4^{3-}]_{TOT}\ (\mu M) + 1.36(\pm 0.18)\ (\mu A)$, $R^2=0.9816$. The

LOD was calculated to be 0.006 µM ($3\sigma_b/m$, n=10). As displayed in Fig.A4.8(B), when the concentration of KH_2PO_4 was increased to 0.2 µM in 0.05M K_2SO_4 (pH=7.8), the linear relationship between $[PO_4^{3-}]_{TOT}$ and peak height of $Peak_2$ started to level out.

The possible interference by chloride at the same pH condition were investigated first in 0.05M K_2SO_4 (pH=7.8) at AMT-CS-GCEs in the presence of 0, 0.1 and 1 mM Cl^- in variable concentrations of KH_2PO_4 from 0 to 0.2 µM (Fig A4.9 (A) and (B)), the results of which showed a good resilience towards chloride at a pH value similar to the neat pond water (Fig.A4.9 (C)).

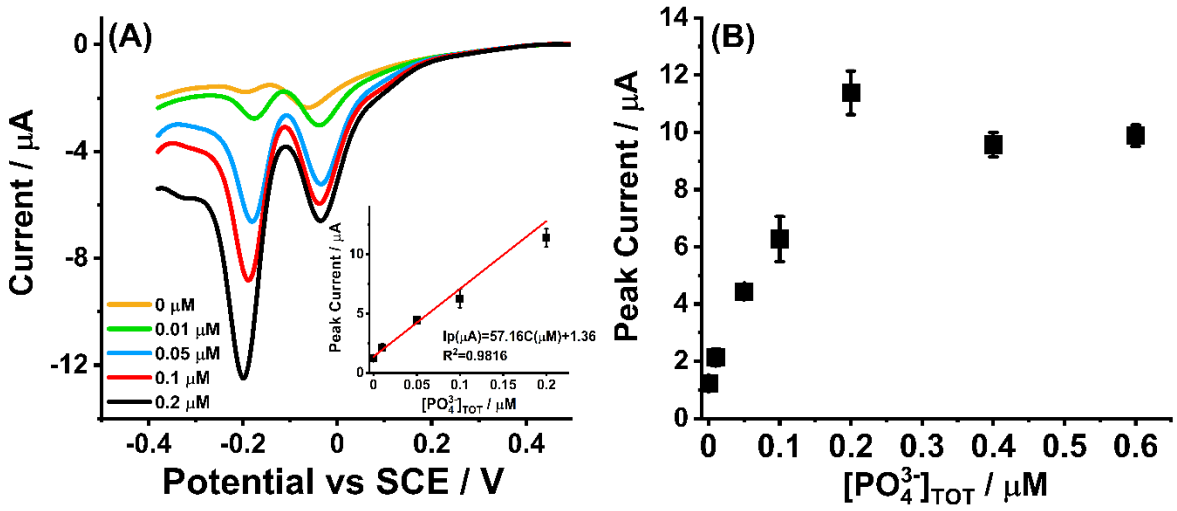


Figure.A4.8 (A) Square wave voltammograms of AMT-CS-GCEs in 0.05M K_2SO_4 (pH=7.8) with varying concentrations of KH_2PO_4 from 0 µM to 0.2 µM (Inlay: calibration curve of $peak_2$ current versus total phosphate concentration); (B) Plot of peak current of $Peak_2$ versus the concentration of total phosphate concentration in the range from 0 to 0.6 µM at AMT-CS-GCEs in 0.05 M K_2SO_4 (pH=7.8).

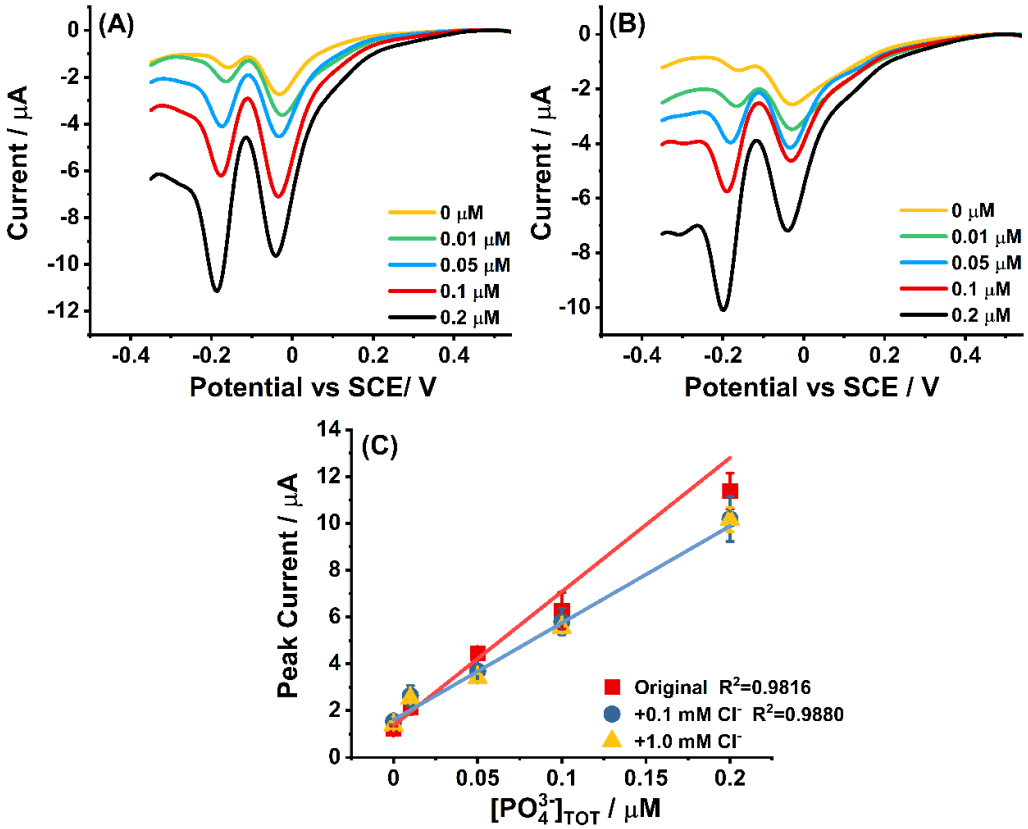


Figure.A4.9 (A) Square wave voltammograms of AMT-CS-GCEs in 0.05M K_2SO_4 (pH=7.8) with varying concentrations of KH_2PO_4 from 0 µM to 0.2 µM in the presence of 0.1 mM Cl^-; (B) Square wave voltammograms of AMT-CS-GCEs in 0.05M K_2SO_4 (pH=7.8) with varying concentrations of KH_2PO_4 from 0 µM to 0.2 µM in the presence of 1 mM Cl^- (C)Plots of peak$_2$ current versus KH_2PO_4 concentration in the presence of 0, 0.1,1 mM Cl^- in 0.05 M K_2SO_4 (pH=7.8), scan rate = 25 mVs^{-1}.

References

1. M. G. Cacace, E. M. Landau and J. J. Ramsden, *Quarterly Reviews of Biophysics*, 1997, **30**, 241.
2. M. Cacace, E. Landau and J. Ramsden, *Quarterly reviews of biophysics*, 1997, **30**, 241-277.
3. J. F. Keggin, *Proceedings of the Royal Society of London*, 1934, **144**, 75-100.

4. E. A. Nagul, I. D. McKelvie, P. Worsfold and S. D. Kolev, *Anal Chim Acta*, 2015, **890**, 60-82.
5. M. Rinaudo, G. Pavlov and J. Desbrieres, *Polymer*, 1999, **40**, 7029-7032.
6. G. Congur, E. Eksin and A. Erdem, *Sensing and Bio-Sensing Research*, 2019, **22**, 100255.
7. E. S. de Alvarenga, *Biotechnology of biopolymers*, 2011, **91**, 48-53.
8. G. A. Roberts, *Chitin chemistry*, Macmillan International Higher Education, 1992.
9. B. An, *Processes*, 2020, **8**, 1194.
10. V. Mirceski, S. Skrzypek and L. Stojanov, *ChemTexts*, 2018, **4**, 1-14.
11. H. T. Evans, B. M. Gatehouse and P. Leverett, *Journal of the Chemical Society, Dalton Transactions*, 1975, 505-514.
12. G. Ilangovan and K. C. Pillai, *Journal of Solid State Electrochemistry*, 1999, **3**, 357-360.
13. K. C. Pillai and G. Ilangovan, *Bulletin of Electrochemistry*, 1993, **9**, 592-595.
14. K. Unoura and N. Tanaka, *Inorganic Chemistry*, 1983, **22**, 2963-2964.
15. S. H. Ewaid and S. A. Abed, *The Egyptian Journal of Aquatic Research*, 2017, **43**, 117-122.
16. S. Bahroun and W. Chaib, *Journal of Water and Land Development*, 2017.
17. D. Ozoko and C. Onyeabor, *International Journal of Science and Research*, 2017, **6**, 833-838.
18. R. Adejumo, T. Adagunodo, H. Bility, A. Lukman and P. O. Isibor, *International Journal of Civil Engineering and Technology (IJCIET)*, 2018, **8**, 887-903.
19. S. Berchmans, T. B. Issa and P. Singh, *Analytica chimica acta*, 2012, **729**, 7-20.
20. J. Bartram, N. Thyssen and A. Gowers, *Water and health in Europe: a joint report from the European Environment Agency and the WHO Regional Office for Europe*, WHO Regional Office Europe, 2002.
21. F. Edition, *WHO chronicle*, 2011, **38**, 104-108.
22. U. S. EPA, *Water quality standards handbook*, Office of Water Regulations and Standards, 1983.
23. W. E. Federation and A. Association, *American Public Health Association (APHA): Washington, DC, USA*, 2005.

Chapter 5

Electro-Oxidation of Amino-Functionalized Multiwalled Carbon Nanotubes

Chapter 5 reports the electrochemistry of amino-functionalized multiwalled carbon nanotubes (MWCNTs-NH_2) in the pH range from 0.3 to 6.4 using quantitative cyclic voltammetry (CV) and single entity electrochemistry measurements, making comparison with non-functionalized MWCNTs. CV showed the latter to both catalyse the solvent (water) decomposition and to undergo irreversible electro-oxidation forming oxygen containing surface functionality. The MWCNTs-NH_2 additionally undergo an irreversible oxidation to an extent which is dependent on the pH of the solution, reflecting the variable amount of deprotonated amino groups present as a function of pH. Nano-impact experiments conducted at the single particle level confirmed the oxidation of both types of MWCNTs, showing agreement with the CV. The pK_a of the amino groups in MWCNTs was determined via both electrochemical methods giving consistent values of ca 2.5.

The work of **Chapter 5** has been published in the journal *Chemical Science* [1], and was carried out under the supervision of Prof. Richard G.Compton (University of Oxford) and in collaboration with Dr. Xiuting Li (Shenzhen University) who helped with the interpretation of the experimental results.

5.1 Introduction

The exceptional physical properties,[2] including excellent electrical conductivity[3], high porosity [4] and specific surface area,[5] of multiwall carbon nanotubes (MWCNTs) have led to their widespread use for example in nanodevices like transistors[6] and nanosensors[7, 8], for composite reinforcement[9], in metal (ion) nanocomposites[10] and especially as catalyst supports in both chemical and electrochemical reactions[11]. However, the application of pure MWCNTs

is limited especially in detection devices such as electrochemical detectors and biosensors with immobilized biomolecules due to their hydrophobic nature and low dispersibility[12]. That said, functional groups, notably -COOH, -OH and -NH_2, either generated on or covalently attached to the carbon surface[13] usefully confer a more hydrophilic character allowing much better compatibility with certain solvents, especially water [14, 15].

Amino-functionalized MWCNTs (MWCNTs-NH_2) have aroused considerable interest since the amino groups attached to the CNTs allows a diversity of further chemical functionalization as well as showing valuable properties in themselves[16] notably as absorbents for metal ions[17, 18], acting as supports for the preparation of electrocatalysts[19, 20] and facilitating the fabrication of (bio) sensors [21, 22]. The formation of MWCNTs-NH_2 have been realized by different approaches. Generally, the first step is the oxidation of MWCNTs by treatment with concentrated acids (sulfuric acid or nitric acid) or other oxidative protocols to generate carboxylated MWCNTs (MWCNT-COOH) [22, 23]. These oxidized CNTs are subsequently linked to amines to form various amides or esters through different chemical reactions for example with ethylenediamine[17] or diethylenetriamine [24]. Finally, decarbonylation is performed to remove the other carbonyl group linked between the MWCNT and the N atom in the amide so creating amino groups attached directly to carbon atoms in the CNT.

The amino groups in MWCNTs-NH_2 are basic and become protonated in acidic solution. Thus, the acid-base characteristics of the $–NH_2$/$-NH_3^+$ pair underpins all MWCNTs-NH_2 chemistry in aqueous solution. In this chapter, we focus first on the electrochemistry of MWCNTs-NH_2 comparing it with that of MWCNTs and second on measuring the acid dissociation constant (pK_a) of the amino groups bonded to single, isolated MWCNTs and in ensembles of the latter. We note that in principle, the pK_a of functional groups attached to the surface of CNTs may differ very significantly from the pK_a of the same groups in small molecules in solution, since the hydrophobic/hydrophilic nature of the CNT surface may

markedly influence the thermodynamics of the acid-base reaction, for example by altering the local water structure. Quantitative information about these differences is rather limited but, for instance, the pK_a of formic acid is 3.7[25] at 298K whilst the corresponding pK_a for the carboxylic acid group within MWCNTs has been measured to range from 3.6[26] to 6.3[27] according to the extent of oxidation of the surface. Similar effects have been noted for carboxylic acid groups on glassy carbon surfaces[28], while the pK_a of water, alcohols and phenols are 15.7 [29], 15.9 [30] and 9.9 [31] respectively compared to hydroxyl group on the functionalized MWCNTs with a pK_a estimated to be below 10.0 [27].

Knowledge of the pK_a of MWCNTs-NH_2 is essential in their utilization most notably in terms of controlling the uptake of metal ions and in exploiting the chemical reactivity of the amino-groups as well as being of fundamental. We note that significant difference between the pK_a values of amino groups in molecules and bound covalently to the surface of graphite has been noted by Abiman *et al*.[32] In the work reported below, two electrochemical techniques are used to estimate the pK_a of MWCNTs-NH_2 so as to probe their acid/base behaviour either as ensembles of many CNTs drop-casted on an electrode surface or as single CNTs in solution. The first method utilizes cyclic voltammetry (CV) at a glassy carbon macroelectrode (GCE) modified with MWCNTs-NH_2, and for comparison with MWCNTs, in a solution electrolyte at different pH values. Both types of nanotube are seen to catalyse the solvent decomposition and to undergo chemically irreversible surface modification leading to the introduction of oxygen functionality. In addition, the MWCNTs-NH_2 show additional current at suitably high pH due to oxidation of unprotonated -NH_2 groups. In contrast to the conventional voltammetric method for solution phase molecules, based on peak potential shifts upon addition of acid[33], the pK_a of the MWCNTs-NH_2 is obtained by estimating the amount of free -NH_2 groups on the surface via electro-oxidation on the assumption that the protonated amino groups are electro-inactive in

contrast to the unprotonated groups. This allows the estimation of the pK_a of the CNTs in the drop-casted ensemble.

The second method corresponds to a nano-impact experiment of single MWCNTs-NH_2 particles using a carbon microelectrode in the electrolyte solution containing a suspension of MWCNTs-NH_2. In the nano-impact experiment, the random collisions of the particles in the suspension with the electrode held at a suitable potential allows electrochemical reactions to occur for the duration of the impact whilst the particle is in electrical contact with the electrode. Current - time traces ('chronoamperometry') are recorded as a function of the potential and impacts are revealed by the appearance of spikes and steps on the current [34-36]. Both MWCNTs and MWCNTs-NH_2 show impact signals consistent with the voltammetry and, in the case of the impact spikes, additional charge assigned to oxidation of unprotonated -NH_2 groups which was measured as a function of the solution pH. In this way, the integrated current – time spikes give the charge partly associated with the oxidation of the –NH_2 groups and hence the amount of free –NH_2 groups present as a function of pH. Thus, a larger charge is seen for higher pH (>4) where the groups are essentially all unprotonated, whilst for pH < 2 a smaller but not negligible current is seen since the electro-inactive –NH_3^+ groups dominate to reduce the magnitude of the current; the origin of the remaining current is explored by comparison with analogous measurements on MWCNTs which do not contain amino groups.

In this way, the pK_a of single MWCNTs-NH_2 can be found and compared with the value obtained for ensembles via cyclic voltammetry. The origin of the smaller current spikes seen on the non-functionalized MWCNTs and the steps on both types of CNTs are attributed in part to the oxidation of the carbon tubes themselves with the formation of quinone groups and other oxygen functionality as previously reported from cyclic voltammetry measurements allied to spectroscopic analysis [37, 38] in addition to enhanced (catalysed) solvent decomposition. Below

we report the first application of single entity electrochemistry (aka 'nano-impacts') to the electro-oxidation of single MWCNTs.

5.2 Experimental

Details of the characterisation of the MWCNTs-NH_2 and MWCNTs were presented in Section 2.1.

Cyclic Voltammetry of MWCNTs and MWCNTs-NH_2 Modified GCEs

A suspension of 0.1 g L^{-1} MWCNTs-NH_2 was prepared by adding 1.0 mg of MWCNTs-NH_2 to 10 mL ethanol. The suspension was then sonicated for 30 min in a Fisher Scientific FB15050 ultrasonic bath to get a well-dispersed solution. A freshly polished GCE was modified by drop-casting a 2 μL (0.2 μg of MWCNTs-NH_2) suspension of MWCNTs-NH_2 and left to dry under vacuum. A conventional three-electrode system was operated with a MWCNTs-NH_2 modified GCE as the working electrode, a saturated calomel electrode (SCE, ALS distributed by BASi Inc., Japan) used as the reference electrode and a graphite rod as the counter electrode. Based on the same procedure as above, MWCNTs modified GCEs were prepared again with 0.2 μg of MWCNTs via drop casting and studied voltammetrically in an analogous way to the MWCNTs-NH_2 modified GCEs.

To investigate the electrochemical oxidative peak current obtained by MWCNTs and MWCNTs-NH_2 modified GCEs at variable pH, CVs were conducted by immersing a freshly prepared MWCNTs modified GCE or MWCNTs-NH_2 modified GCE respectively in a 1.0 M HNO_3 (pH = 0.3), 0.1 M HNO_3 (pH = 1.0) and 0.1 M KNO_3 solution at different pH values of 2.0, 2.5, 3.0, 3.5, 4.0, 5.0 and 6.4 by changing the addition amount of 0.1 M HNO_3 or 0.1 M KOH under degassed conditions as above. The potential window was chosen as + 0.1 V to + 2.0 V vs SCE. The voltammograms were recorded at a scan rate of 50 mVs^{-1}. A control experiment was also performed in the same solution but on a bare GCE.

To determine the voltammetric signals from the oxidation of MWCNTs and MWCNTs-NH_2 quantitively, the peak current was found using OriginPro 2020 after background correction of the raw cyclic voltammograms. This is illustrated in Figure.A5.1 (Section A5.1), where a baseline spline is fitted between the potentials at which the voltammetric wave is judged to have started and ended, then subtracted from the peak to obtain the actual peak height.

To investigate possible surface functional group formation on electro-oxidation voltammetry, CV was conducted using MWCNTs or MWCNTs-NH_2 modified GCE in 0.1 M KNO_3 (pH=6.4) by first sweeping from 0.10 V to 1.78 V then applying a fixed potential of 1.78 V for 0 s, 50 s, 100 s and 200 s respectively. After that, the potential was swept from 1.78 V to -1.50 V and back to 1.0 V under degassed conditions as above. The voltammograms were recorded at a scan rate of 50 mVs^{-1}.

Nano-impact Experiments of MWCNTs and MWCNTs-NH_2

Nano-impact experimental measurements were performed using an EC-Lab Biologic potentiostat where the charge passed during the impact events was conserved. A carbon micro-disc electrode of nominally 33 μm diameter (IJ Cambria Scientific Ltd., U.K.) was used as the working electrode. Before each experiment, it was polished carefully using alumina with decreasing particle sizes of 1.0, 0.3 and 0.05 μm in turn on soft lapping pads, followed by rinsing with ultra-pure water and drying with nitrogen. Pure MWCNTs was separately dispersed into 0.1 M HNO_3 (pH = 1.0) and 0.1 M KNO_3 (pH=6.4) to form a uniform suspension (0.1 mg /10 mL) after 30-minute sonication. Then the measurements of current at various potentials in the range from 1.4 V to 2.0 V vs SCE ("chronoamperometry") were performed on the 0.1 M KNO_3 (pH=6.4) solution containing dispersed MWCNTs after bubbling with nitrogen for 10 minutes. An atmosphere of nitrogen was maintained during the experiments. Control experiments were conducted in the presence of 0.01 gL^{-1} MWCNTs-NH_2 suspension. The effect of pH condition on the chronoamperometric current spikes and steps produced was investigated

by placing the freshly polished carbon micro-disc electrode into 1.0 M HNO_3 (pH = 0.3), 0.1 M HNO_3 (pH = 1.0) and 0.1 M KNO_3 solution at different pH values of 0.3, 1.0, 1.8, 2.4, 2.7, 3.6, 4.1, 5.3 and 6.4 (adjusted by a small addition of 0.1 M HNO_3 or 0.5 M KOH) containing 0.01 g L^{-1} MWCNTs-NH_2 suspension or not. The data analysis program "Signal Counter" (Centre for Marine and Environmental Research, Zagreb, Croatia)[39] was employed for making impact spike identification and individual spike charge determination. Counting and analysis of the impact step signals were performed in OriginPro 2020.

5.3 Results and Discussion

This section reports the electro-oxidation of MWCNTs and MWCNTs-NH_2 using both cyclic voltammetry and nano-impact experiments in the pH range of 0.3 to 6.4. The oxidative peak currents seen in cyclic voltammetry of MWCNTs and MWCNTs-NH_2 modified GCEs are compared with the average charge of the current spikes and/or steps seen in nano impact experiments from MWCNTs and MWCNTs-NH_2 particles, allowing the contributions from the electro-oxidation of the CNTs to be distinguished from the oxidation of the amino groups, if present. The pH dependency of the latter is used to infer the pK_a of the amino groups. First the electro-oxidation of MWCNTs ensembles without functionalization are investigated using cyclic voltammetry. Then to further confirm the oxidation process, MWCNT particle impact experiments are conducted.

5.3.1 Cyclic Voltammetry (CV) of MWCNTs

To investigate the electrochemical oxidation of MWCNTs, cyclic voltammograms at bare and MWCNTs modified GCEs were first recorded in 0.1 M KNO_3 (pH adjusted to 6.4) in the potential range from 0.1 V to 2.0 V vs SCE at a scan rate of 50 mVs^{-1}. As depicted in Fig. 5.1(A), there is a single chemically irreversible oxidation peak observed at 1.68 V for the MWCNTs modified GCE. The magnitude of the peak current increased linearly with the

amount of MWCNTs dropcast (Fig.5.1(B)) and was assigned in part (see below) to the electro-oxidation of the MWCNTs based on its reported FTIR characterization [40] indicating the existence of -OH group bonded to MWCNTs (Fig.2.3 in Chapter 2) and previous reports [41, 42]. Notably, previous work using CV and X-Ray Photoelectron Spectroscopy (XPS) analysis [37, 38] has associated the electrochemical oxidation of MWCNTs with increased oxygen content and assigned the oxidative peak to the formation of quinoidal and ketone functional groups at the surface of carbon nanotubes. The formation of functional groups after electrochemical oxidation of the MWCNTs is also evident on the basis of voltammetry. Fig.5.1(C) shows the cyclic voltammograms of MWCNTs modified GCE in 0.1 M KNO_3 (pH = 6.4) in which a potential scan from 1.0 V to -1.5 V with a return scan to 1.0 V is held for different times (0, 50, 100, 200 seconds) at +1.78V in the middle of the scan, corresponding to a potential after the oxidative peak attributed to the immobilized CNTs. Two reduction peaks (c_1 and c_2) appeared at -0.34 ± 0.14 V and -0.75 ± 0.16 V which increased in size in proportion to the length of time held at +1.78V. The voltammetric reduction peaks c_1 and c_2 are similar to the behaviour observed from the quinone/hydroquinone system in acid solution[43]. The requirement however to hold the potential at an oxidizing value for a period of up to 200 seconds in order to see a voltammetric signal suggests that the formation of oxygenated species is not the dominant process in the CV peak. Rather it is likely that the peak represents a catalysis by the CNTs of the solvent oxidation possibly further catalysed by the simultaneously introduced oxygen functionality. This is consistent with the enhanced currents in the second anodic scans shown in Fig. 5.1(C). However, we return to this issue below after nano impact measurements are reported.

The pH variation of the oxidative peak at MWCNTs modified GCEs was studied by recording CVs in the pH range 1.0 to 6.4 (Fig.5.1(D)) as described in the experimental section. The potential of the oxidative peak was pH independent with an average value of 1.71 ± 0.03

V. The peak current data obtained in MWCNTs modified GCEs after background subtraction were plotted against the corresponding solution pH value (Inlay of Fig.5.1(D)) again indicating independence of the electro-oxidation of MWCNTs on pH in the range studied. This suggests that the rate limiting step for the oxidation of the CNTs leading to the introduction of oxygen functionality is slow electron transfer prior to any proton release.

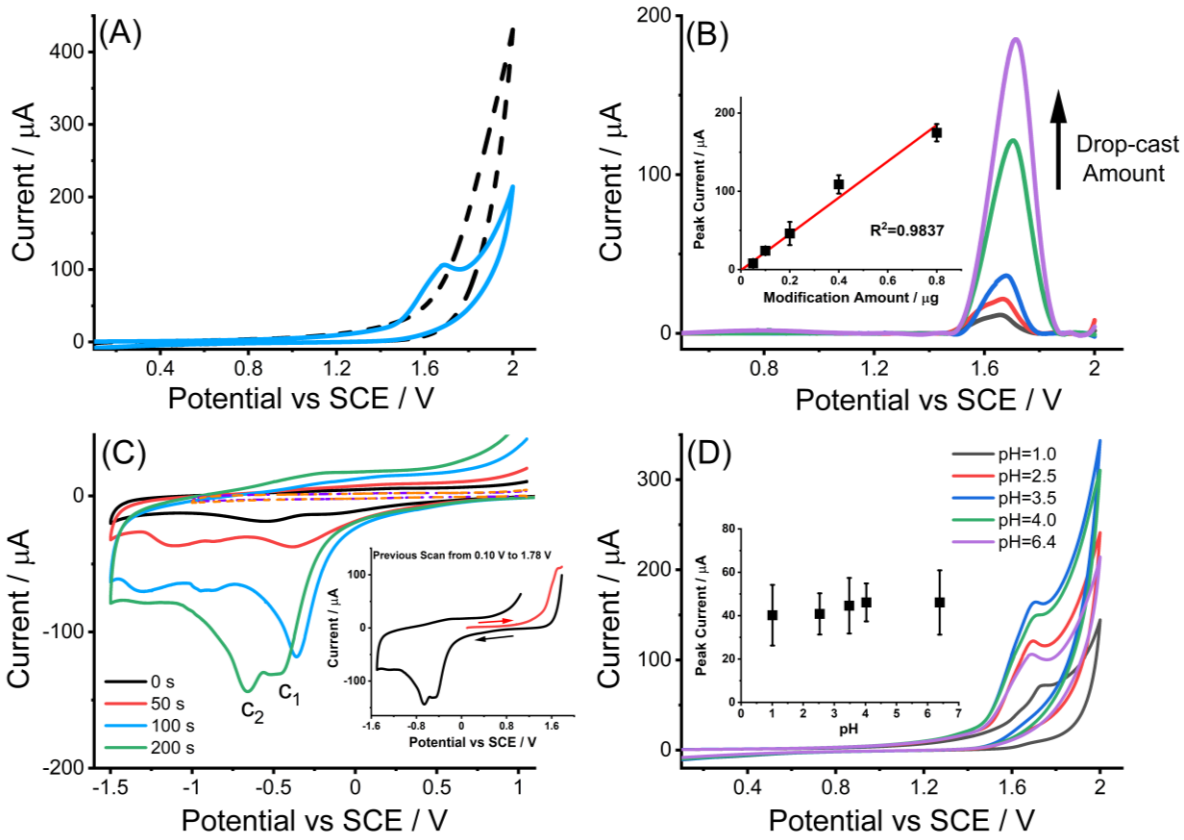


Figure.5.1(A) Cyclic voltammograms of a bare GC electrode (black dashed curve) and a MWCNTs modified GCE (blue solid curve) immersed in 0.1 M KNO_3 solution (pH = 6.4) by sweeping the potential from 0.1 V to 2.0 V vs SCE;(B) Voltammograms of MWCNTs modified GCEs with different modification amount of 0.05, 0.1, 0.2, 0.4 and 0.8 µg MWCNTs following background correction to the original cyclic voltammogram scanned in 0.1 M KNO_3 (pH=6.4) (Inlay: plot of oxidative peak current versus MWCNTs modification amount on the polished GCE); (C) Cyclic voltammograms of MWCNTs modified GCE recorded with a sweep from +1.0 V to -1.5 V after previous scan from 0.10 V to 1.78 V interrupted at a potential of 1.78 V for different durations of 0 s - 200 s in 0.1 M KNO_3 (pH=6.4) (Inlay: the

cyclic voltammograms scanned across the full range from 1.78 V to -1.50 V when the duration of the fixed potential oxidation was 200 s) (D) Cyclic voltammograms of a MWCNTs modified GCE immersed in 0.1 M HNO_3 (pH=1.0) and 0.1 M KNO_3 solutions at different pH values of 2.5, 3.5, 4.0 and 6.4 (Inlay: pH variable study of oxidative peak current obtained from MWCNTs modified GCEs using CV after background subtraction as described in experimental section). All voltammograms were conducted at a scan rate of 50 mVs^{-1}.

5.3.2 Electro-oxidation of MWCNTs: Nano-impact experiments

Nano impact experiments were conducted to probe the electro-oxidation of MWCNTs via the collision of individual MWCNTs particles with a microelectrode held at different potentials. A freshly polished carbon micro-disc electrode (diameter 33 μm) was first inserted into a suspension of 0.01g L^{-1} MWCNTs supported by 0.1M KNO_3 with a pH of 6.4, as described in the experimental section and separately for comparison into a blank solution without particles. As seen in Fig.5.2(A), at an applied potential of 1.90 V vs SCE, clear current steps and spikes were seen in the presence of MWCNTs (black line) whereas no spikes or steps were observed in the absence of MWCNTs (red line). The average spike height (current) at 1.90 V was calculated to be 0.64 ± 0.06 nA and the average step height (current) at 1.90 V were measured as 0.25 ± 0.04 nA. Based on the frequency of spikes and steps in each chronoamperogram curve, the appearance ratio of spikes to steps is calculated to be 1.8 ± 0.7.

Further, impacts for the electro-oxidation of MWCNTs were observed at various potentials from 1.4 V to 2.0 V vs SCE in the same solution. It was found that clear current spikes were observed in the chronoamperograms upon particle collisions with the electrode held at oxidizing potentials (1.7 - 2.0 V) and the current steps were observed in the chronoamperograms upon particle collisions with the electrode held at oxidizing potentials (1.6 - 2.0 V) (Fig.5.3 (A)-(D)). The rise times of the steps at high potentials may in part be controlled by the charging of the double layer associated with the CNTs. At and below 1.50 V, no impact signals were detected

(See Fig.A5.2). It is speculated that the steps are primarily associated with CNT catalysis of the solvent decomposition leading to the sustained currents seen for the impact duration. On the basis of the cyclic voltammetry reported above these will also be associated, to a smaller extent, by the oxidation of the nanotubes themselves forming surface functionality such as quinones. These may further enhance the catalysis of the solvent decomposition[44] corresponding to the oxidation of water to oxygen. The mean impact frequencies and duration of impact signals as a function of potential are plotted in Fig.A5.3 (A) - (B) respectively, the frequency of spikes and steps were found to only slightly increase while each average duration stayed nearly the same from which over the potential range of 1.7 to 2.0 V. The step features require a sustained electrical contact between the tube and the electrode of average duration 4.6 ± 0.9 s (43 measurements). In contrast the spike features require a much shorter contact time (of average length 12 ± 1 ms from 53 measurements) and may reflect simply the end of a tube contacting the electrode. In this case, given the known greater susceptibility of tube ends to electrochemical reaction[45, 46], these may be associated with the oxidation of the CNTs to oxygenated functionality. Fig.5.4 shows a schematic view of the possible different collisions associated with the spikes and steps.

The average charges of the individual spikes and steps from the collision of MWCNTs were measured as a function of the applied potential and the results are shown in Fig.5.2(B) and Fig.5.2(C) where the turn on of the electro-oxidation is consistent with the cyclic voltammogram of MWCNTs modified GCEs in the same solution. A plateau of ca. 0.41 pC per spike was seen when the potential exceeded 1.90 V, but no spikes were observed at the potential more negative than 1.70 V, indicating that those spikes are a result of MWCNTs oxidation. The same condition occurred in the steps when the potential was more positive than 1.60 V, the average charge was seen to increase gradually and reached a constant level around ca. 0.50 nC but no steps were observed at the potential more negative than 1.60 V. The small difference in

onset potentials might be speculated to indicate a different extent of the solvent oxidation as compared to oxidation of the CNT. The average impact step current plotted against the applied potential (Fig. 5.2(D)) indicated an upward trend over a potential range from 1.60 V consistent with the predominant process being water oxidation.

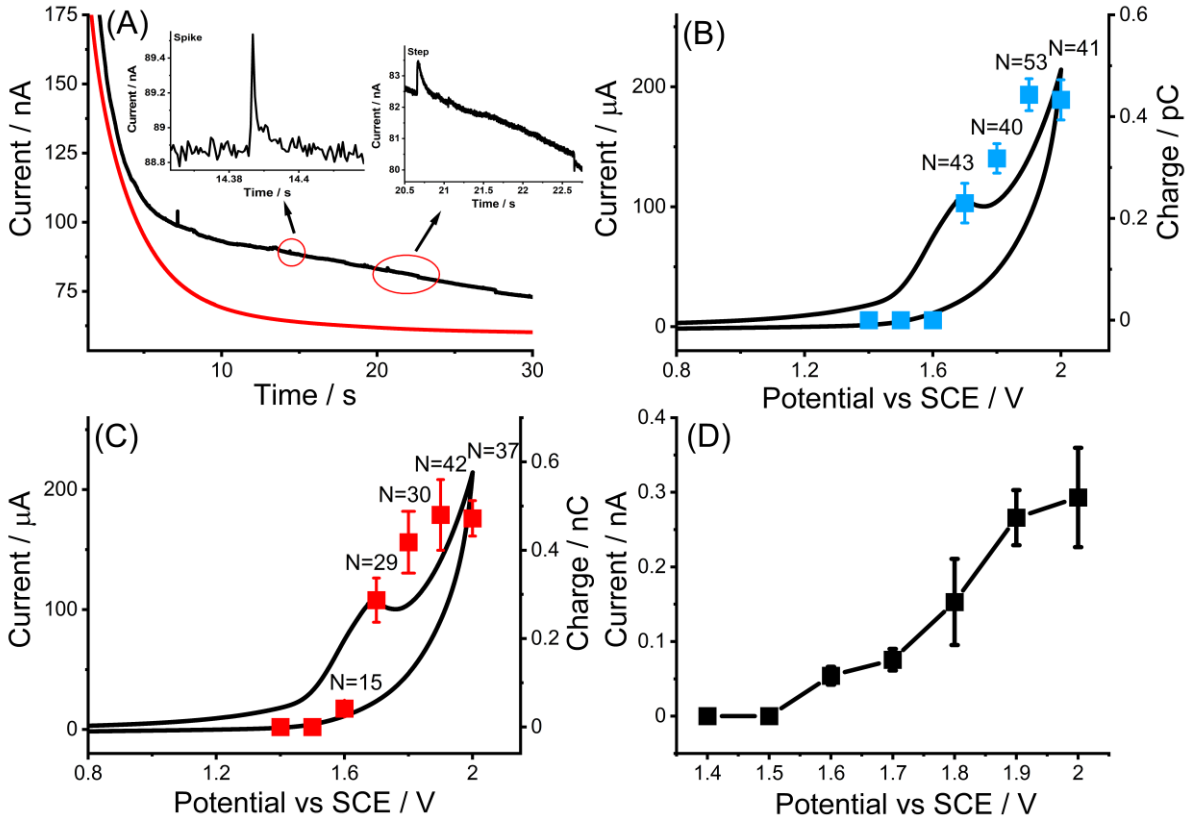


Figure.5.2(A) Chronoamperograms of a carbon micro-disc electrode (d=33 µm) immersed in a 0.1M KNO_3 (pH=6.4) solution containing 0.01 gL^{-1} MWCNTs (black line) or not (red line) at a potential of 1.90 V vs SCE. The inset is an enlarged view of impact spike and step at 1.90 V; Overlay of the plot of average impact spike charge (B) and step charge (C) as a function of applied potentials with the cyclic voltammogram (black line) of MWCNTs modified GCE; (D) Average step currents observed as a function of applied potential in 0.1M KNO_3 (pH=6.4) containing 0.01 g L^{-1} MWCNTs (The error bars are derived from $SD/(n)^{1/2}$, where SD is the standard deviation and n is the number of the spikes or steps).

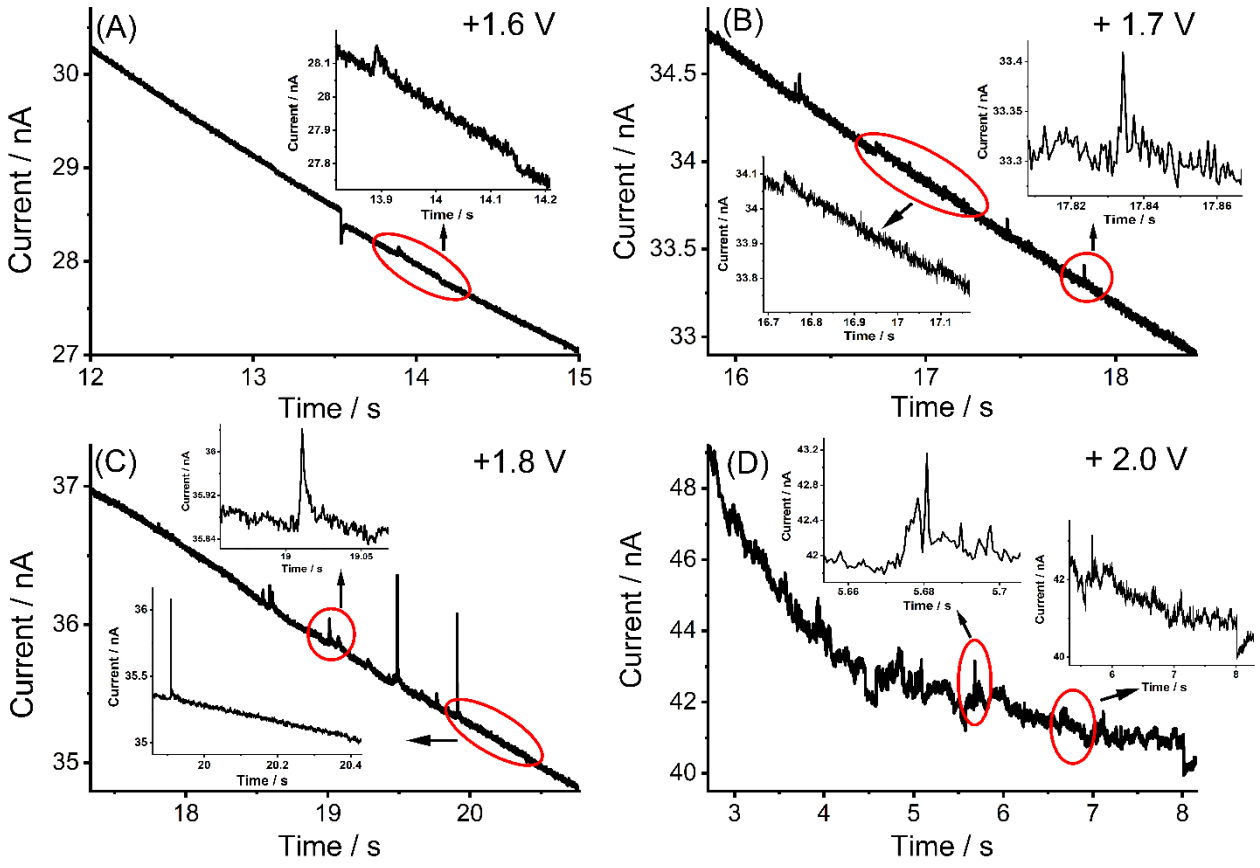


Figure.5.3(A)-(D) Examples of representative chronoamperometric profiles of nano-impact at different potentials (1.60, 1.70, 1.80 and 2.00) in a 0.1 M KNO_3 (pH=6.4) solution containing 0.01 gL^{-1} MWCNTs. No spikes or steps were detected below/at 1.50 V.

The insensitivity of the impacts (spikes and steps) to pH was demonstrated via an experiment carried out at a potential of 1.90 V in 0.1 M HNO_3 (pH=1.0) containing 0.01 gL^{-1} MWCNTs suspension. Concerning the spikes, these had an average charge of 0.40 ± 0.03 pC as measured from 48 current spikes consistent with the average charge from the oxidative spikes obtained in 0.1 M KNO_3 at pH=6.4 as reported above 0.43 ± 0.05 pC (the charge distribution is seen in Fig.A5.4 (A)-(B) respectively). The oxidative impact responses of MWCNTs particle have an average frequency of 0.053 ± 0.019 s^{-1}, consistent with the 0.051 ± 0.012 s^{-1} frequency of the spikes observed in chronoamperograms in 0.01 gL^{-1} MWCNTs + 0.1M KNO_3 (pH = 6.4).

As for the steps which appear in 0.1 M HNO_3 (pH=1.0) in the presence of MWCNTs, an average charge of 0.47 ± 0.05 nC as measured from 52 current steps. Compared with the average

charge from the oxidative steps obtained in 0.1 M KNO_3 at pH=6.4 (0.48 ± 0.07 nC) (the charge distribution is seen in Fig.A5.4 (C)-(D) respectively). The oxidative impact responses of MWCNTs particle have an average frequency of 0.044 ± 0.008 s^{-1}, consistent with the 0.040 ± 0.007 s^{-1} frequency of the steps observed in chronoamperograms in 0.01 g L^{-1} MWCNTs + 0.1 M KNO_3 (pH = 6.4). The result from the single electrochemistry of MWCNTs again indicates that the extent of the reaction of the electro-oxidation of pure MWCNTs is not controlled by solution pH.

The much larger charges resulting from the sustained currents seen in the steps are consistent with the assignment of these features to CNT catalysed solvent decomposition. Moreover, the charges passed in the impact steps (0.48± 0.07 nC) are comparable in magnitude to those seen in the cyclic voltammetry when measured on a per nanotube basis (0.46 nC, see Section A5.5 for details). This suggests that the peak seen in the cyclic voltammogram is not due to the formation of a finite number of oxygenated functionalities, as also suggested by the relative size of the reductive CV features discussed above, but rather might be attributed to the porous nature of the CNT layer on the electrode surface (~ at least 13 layers, see Section A 5.6) which can trap the protons released in the oxidation of the water leading to a local build-up of acidity. However, the above data indicates that the currents resulting from CNT catalysis of the solvent oxidation are insensitive to the value of the pH and hence the inhibition of the CNT catalysed solvent decomposition resulting in a voltammetric peak may result from excessive electro-oxidation of the CNTs, consistent with the data in Fig.5.1(C) showing not only progressively increasing oxygen functionality resulting from sustained electro-oxidation but also a change in the reductive voltammetric signal.

We next consider the origin of the spike currents where the charge is typically passed for ca 12 ± 1 ms before terminating. These may reflect different types of CNT-electrode collision than occur during the step features. Since the latter persist with a steady current for tens of

seconds, we suggest that the steps require electrical contact between the micro-disc electrode and CNT via the sides of the tubes, see Fig.5.4. The spikes may reflect electrical contacts between the tube ends and the electrodes with the short, finite duration controlled either by the nature of the collision or, possibly, by the formation of insulating functionality via oxidation of the tube ends. The latter possibility is discounted by the calculation (see Section A5.7) that the average charge per spike results in rather more functional groups than could be accommodated at the end of a nanotube.

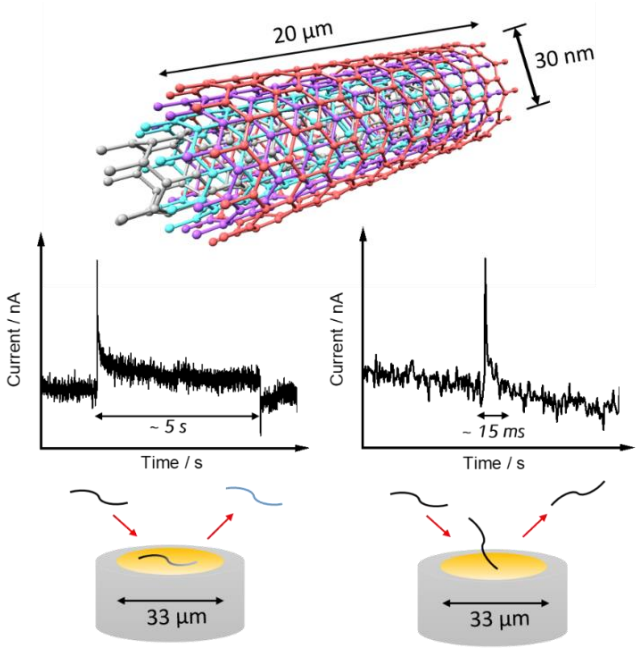


Figure.5.4 A schematic view of the possible different collisions of a single MWCNT on the micro-disc electrode (d = 33 µm) associated with the spikes and steps.

5.3.3 Cyclic Voltammetry (CV) of MWCNTs-NH_2

Next the electrochemical behaviour of MWCNTs-NH_2 was explored by applying cyclic voltammetry first in 0.1 M KNO_3 (pH=6.4) at a scan rate of 50 mVs^{-1}. The potential range was chosen to be from 0.1 V to 2.0 V as shown in Fig.5.5(A). In comparison with the MWCNTs modified GCE, a larger oxidative peak appeared with a peak potential of ca 1.72 V vs SCE under similar modification conditions. A good linear relationship between the height of the peak current and the amount of MWCNTs-NH_2 drop-cast was observed as shown in Fig.5.5(B).

Analogous experiments to those conducted for MWCNTs were made to investigate the reductive voltammetric behavior following electro-oxidation of the MWCNTs-NH_2 at 1.78 V, focusing on the potential range from +1.0 V to -1.5 V. As seen in Fig.5.5(C), two cathodic peaks appeared at -0.40 ± 0.05 V (c'_1) and -0.78 ± 0.14 V (c'_2) similar to what was seen in the cyclic voltametric behavior of MWCNTs again suggesting that a small amount of the oxidative current is used to introduce oxygen containing functionality but that most of the current is CNT catalyzed solvent oxidation.

Cyclic voltammograms were recorded at different scan rates in the range of 25 - 400 mVs^{-1} in 0.1 M HNO_3 (pH=1.0) and 0.1 M KNO_3 (pH=6.4). Polynomial fitting curves were used to infer the charge passed on a MWCNTs-NH_2 modified GCE as a function of scan rate (Fig.A5.8). Extrapolation of the reciprocal charge against scan rate to zero scan rate gave the average charge of 6.0 mC in 0.1 M HNO_3 (pH=1.0), which is approximately consistent with the charge passed at a MWCNTs modified GCE (7.0 mC) representing a similar extent of solvent oxidation and functional group formation in both types of CNT since the mass drop cast was the same in both cases and the individual tubes have similar surface areas (see Table 2.1 in Chapter 2). However, a clear difference was noticed for the average charge passed on a MWCNTs-NH_2 modified GCE in 0.1 M KNO_3 (pH=6.4) which was markedly larger than that at pH 1 and calculated to be 9.5 mC, suggesting that the presence or not of deprotonated -NH_2 groups is greatly possible factor whereby the amine groups are deprotonated at high pH but protonated at pH 1 such that they are easily electro-oxidized at the higher pH but not at the lower pH.

To explore this possibility, the variation of the magnitude of the oxidative peak as a function of solution pH was measured in the range from 0.3 to 6.4. Fig.5.5(D) shows an overlay of cyclic voltammograms for the oxidation of MWCNTs-NH_2 modified GCEs in various electrolytes: (a) 1.0 M HNO_3, (b) 0.1 M HNO_3 and (c) 0.1 M KNO_3 of different pH as controlled by small additions of 0.1 M HNO_3 or 0.5 M KOH assuming no ion pairing between nitrate and

amino-groups on the CNTs [47-49]. In this way the pH ranges from 0.3 to 6.4 was studied. The potential of the irreversible oxidative peak was unchanged with variation in pH with an average value of 1.73 ± 0.03 V. However, the plot of oxidative peak currents against pH value (Inlay of Fig.5.5(D)) shows an obvious pH-dependence in contrast to the MWCNTs modified GCEs. Specifically, the peak current was essentially pH independent between pH values of 0.3 to 2.5, then between pH 2.5 and 3.5, the height of oxidative peak current rose sharply as the pH was increased. Finally, at pH above 4.0, the oxidative peak current again remained stable. Overall a characteristic sigmoid-like 'titration curve' curve was seen. The magnitude of the current seen in the lowest pH range is of the same order of magnitude to that recorded for unmodified MWCNTs (albeit of different radius and length to the MWCNTs), suggesting that the same electrocatalytic solvent oxidation reaction as noted above for MWCNTs is also seen in MWCNTs-NH_2 and occurs at essentially the same potential in both types of CNT. It is inferred that the oxidation potential of the unprotonated -NH_2 groups approximately coincides with that of the electro-oxidation of the solvent. It is worthwhile to mention that the rate limiting step for the solvent oxidation and amino groups on the MWCNTs are inferred in each case to be the electron transfer prior to any proton release as reflected in the independence of the corresponding oxidation potentials on pH.

The additional current observed at higher pH is attributed to the oxidation of unprotonated -NH_2 groups where further follow up chemistry is probable, on the basis of electro-oxidation mechanism of aromatic amines proposed by Weinberg[50], considering that aromatic amines usually have an analogous hexatomic ring structure as is present in CNTs and generically show a single oxidative peak at a potential above 1.0 V vs SCE when oxidized at a carbon working electrode under acidic conditions [51, 52]. This possible mechanism also provides a reasonable explanation for the formation of the sigmoid-like 'titration' curve of oxidative peak height versus pH value. However, it is noted that the oxidation of the -NH_2 groups results in the release

and build-up of protons so changing the local pH and extent of solvent oxidation. This precludes quantitative analysis of the CVs by subtraction of the 'blank' responses. Owing to the acid-base characteristics of the $-NH_2/-NH_3^+$ pair, the electro-oxidation extent of electro-active $-NH_2$ decreases when the solution became more acidic as the generation of the protonated species.

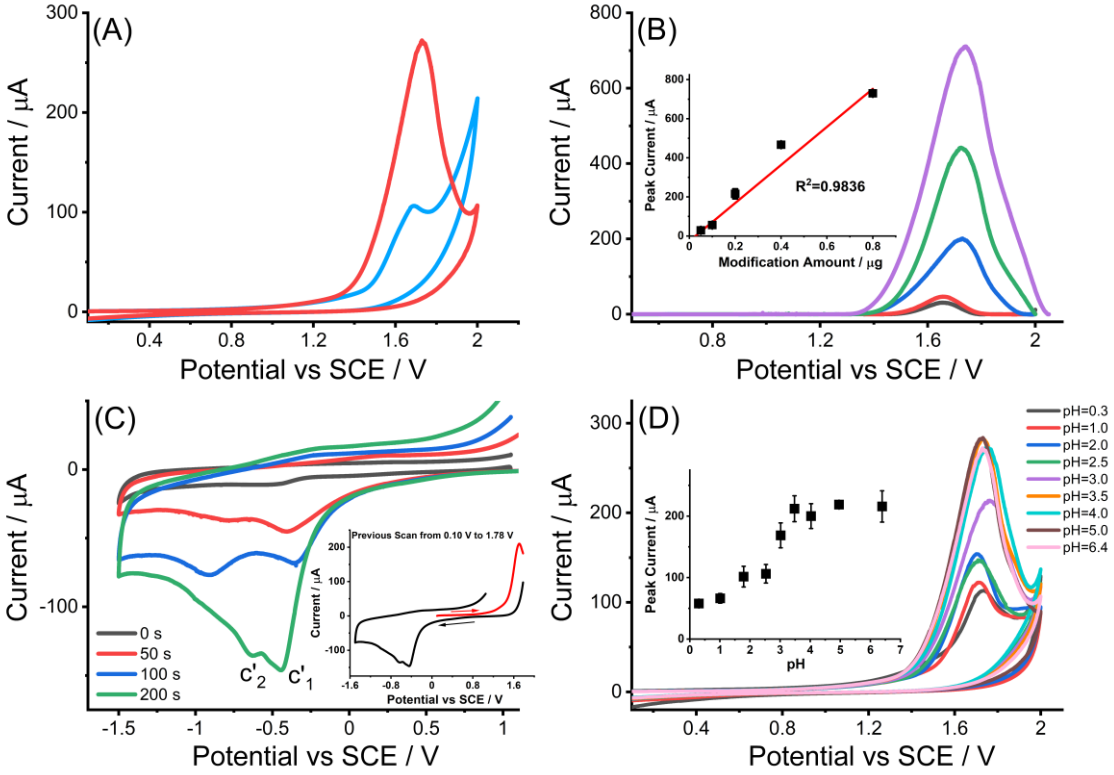


Figure.5.5 (A) Cyclic voltammograms of MWCNTs modified GCE (blue curve) and MWCNTs-NH_2 modified GCE (red curve) immersed in 0.1 M KNO_3 solution (pH = 6.4); (B) Voltammograms of MWCNTs-NH_2 modified GCEs with different modification amount of 0.05, 0.1, 0.2, 0.4 and 0.8 μg MWCNTs-NH_2 following background correction to the original cyclic voltammogram scanned in 0.1M KNO_3 (pH=6.4) (Inlay: plot of oxidative peak current versus MWCNTs-NH_2 modification amount on the polished GCE); (C) Cyclic voltammograms of MWCNTs-NH_2 modified GCE recorded at +1.0 V to -1.5 V after previous scan from 0.10 V to 1.78 V with a hold at a potential of 1.78 V for different duration of 0 s - 200 s in 0.1 M KNO_3 (pH=6.4) (Inlay: the cyclic voltammograms scanned across the full range from 1.78 V to -1.50 V when the held time was 200 s) ; (D) Cyclic voltammograms of

MWCNTs-NH_2 modified GCE immersed in 1.0 M HNO_3 (pH=0.3), 0.1 M HNO_3 (pH=1.0) and 0.1 M KNO_3 solutions at different pH of 2.0, 2.5, 3.0, 3.5, 4.0, 5.0 and 6.4. All the voltammetry were conducted by using sweep potential from 0.10 V to 2.0 V vs SCE at a scan rate of 50 mVs^{-1} (Inlay: pH variable study of oxidative peak current obtained from MWCNTs-NH_2 modified GCE using CV).

5.3.4 Single Particle Electrochemistry of MWCNTs-NH_2

Analogous nano-impacts experiments of MWCNTs-NH_2 to those made for MWCNTs were conducted in 0.1 M KNO_3 (pH=6.4) containing 0.01 g L^{-1} MWCNTs-NH_2 at a freshly polished carbon micro-disc electrode. At a fixed potential of 1.90 V vs SCE, clear impact signals (steps and spikes) as with MWCNTs were observed (Fig.5.6).

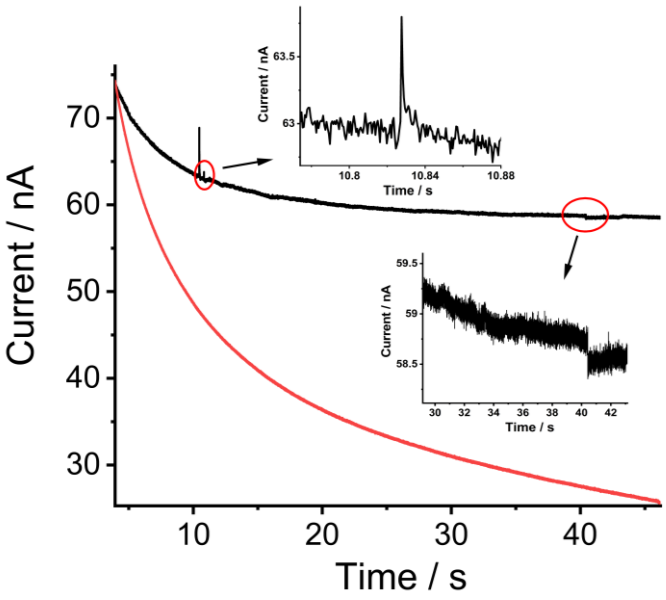


Figure.5.6 Chronoamperograms of a carbon micro-disc electrode (d=33 µm) immersed in a 0.1 M KNO_3 (pH=6.4) solution containing MWCNTs-NH_2 (black line) or not (red line) at a potential of 1.90 V vs SCE. The inset is an enlarged view of impact spike and step at 1.90 V in the presence of MWCNTs-NH_2.

Analysis of the step data showed that in terms of average current, duration and frequency, it was essentially indistinguishable from that recorded for MWCNTs using solutions of varying pH from 1.0 to 6.4 (representative chronoamperograms are shown in Fig. A5.9 (A)-(E)). The

average step current seen only in the presence of MWCNTs-NH_2 fluctuated at 0.26 ± 0.06 nA which is close to the value (0.27 ± 0.04 nA) obtained from 0.1 M KNO_3 (pH=6.4) containing MWCNTs and was pH independent (Fig.A5.9(F)). The corresponding oxidative step frequency under different pH condition (Fig.A5.10 (A)) stay nearly constant with a mean value of 0.039 ± 0.005 s^{-1}, close to the frequency (0.037 ± 0.008 s^{-1}) of the steps observed in 0.1 M KNO_3 (pH = 6.4) containing 0.01 gL^{-1} MWCNTs (albeit of different radius and length). The step duration was found to be steady at 4.8 ± 1.0 s (Fig.A5.10 (B)) again consistent with what is seen in the presence of non-functionalized MWCNTs (4.7 ± 0.9 s).

The spike data however showed interesting contrasts with those seen for MWCNTs. The average charge from 89 spikes (the charge distribution is shown in Fig.A5.11) for MWCNTs-NH_2 at 1.90 V (0.62 ± 0.02 pC) was higher than the value (0.43± 0.05 pC) obtained from the collision of MWCNTs particle in 0.1 M KNO_3 (pH = 6.4), suggesting the oxidation of unprotonated -NH_2 groups bonded to MWCNTs.

To investigate the oxidative charge variation of MWCNTs-NH_2 as a function of pH, current-time transients were recorded in solutions varying pH from 0.3 to 6.4 (Fig.5.7 (A)). The average charges of the individual spikes from the collision of MWCNTs-NH_2 were measured as a function of the pH and the results (Fig.5.11(B)) show two plateaus one at high (>3.7) and the other at low (<1.8) pH, which agree well with the variation of the oxidative peak current against pH variation observed in CV and again can be attributed to the different extents of amino group oxidation reflecting whether the amine groups are protonated or not. The corresponding oxidative spike frequency under different pH condition (Fig.A5.10 (A)) stay nearly the same with a mean value of 0.048 ± 0.010 s^{-1}, close to the frequency (0.051 ± 0.012 s^{-1}) of the spikes observed in 0.1 M KNO_3 (pH = 6.4) containing 0.01 gL^{-1} MWCNTs (albeit of different radius and length but similar area). While the spike duration was found to be unchanged at 15 ± 2 ms (Fig.A5.10 (B)) that is only slightly higher than that in the presence of

non-functionalized MWCNTs (12 ± 1 ms). All the results evidenced that transient electrocatalysis of solvent oxidation and oxidation of the deprotonated amino groups on the MWCNTs jointly contributed to the electro-oxidative spikes see for MWCNTs-NH_2 but the latter resulted in a titration-like curve based on the experimental data from single and ensemble electrochemical behavior.

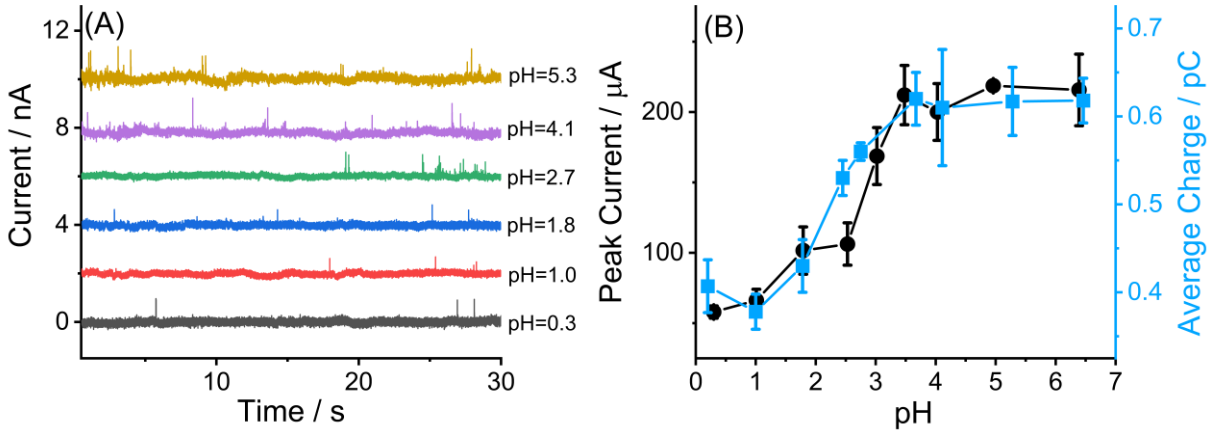


Figure.5.7 (A) Representative chronoamperograms of a carbon micro-disc electrode immersed in a 1.0 M (pH =0.3) and 0.1 M HNO_3 (pH=1.0) and 0.1 M KNO_3 solutions at different pH values of 1.8, 2.7, 4.1 and 5.3 containing 0.01 gL^{-1} MWCNTs-NH_2 at a potential of 1.90 V vs SCE; (B) The comparison of oxidative peak current from CV (black dots) and average charge from oxidative spikes (blue dots) as a function of solution pH.

5.3.5 Determination of MWCNTs-NH_2 pK_a using cyclic voltammetry and nano impact data

The average pK_a of the amino groups in MWCNTs-NH_2 is defined by the equilibrium between protonated and unprotonated amino groups functionalized on the surface of carbon nanotubes:

$$\boldsymbol{MWCNTs - NH_2 + H^+ \rightleftharpoons MWCNTs - NH_3^+} \quad (5.1)$$

$$\boldsymbol{pH = pK_a + log_{10}(\frac{[MWCNTs - NH_2]}{[MWCNTs - NH_3^+]})} \quad (5.2)$$

In the following we estimate the pK_a from both the CV and impact data. First from the CV we assume that the difference in the peak current seen in acid (-NH_3^+ only present) and in near neutral condition (-NH_2 exclusively present) reflects the extent of the deprotonation inferred in solution of higher pH. Thus, the oxidative peak current (I_p) at a MWCNTs-NH_2 modified GCE reflects two parts: the deprotonated [MWCNTs-NH_2] and protonated [MWCNTs-NH_3^+], then I_p can be described as:

$$\boldsymbol{I_P = I_{-NH_2}\,[MWCNTs - NH_2] + I_{-NH_3^+}[MWCNTs - NH_3^+]} \quad (5.3)$$

Assuming the sum [MWCNTs-NH_2] + [MWCNTs-NH_3^+] is a constant, according to Eqs. (5.1) - (5.3), the following equation can be obtained Eq. (5.4):

$$\boldsymbol{pK_a = pH - log_{10}(\frac{I_{-NH_3^+} - I_{-NH_2}}{I_p - I_{-NH_2}} - 1)} \quad (5.4)$$

where I_{-NH2} and I_{-NH3+} can be determined by the average values at high pH (>4) and low pH (<2). As shown in Fig.5.12 (A), the black solid line is the simulated curve using Origin Pro 2020 non-linear fitting function based on Eq. (5.4) (R^2=0.9942), and pK_a of MWCNTs-NH_2 was determined by the incremental ratio (dI_P/d_{pH}) expressing the differential value from the simulated curve data. The first derivative calculated for points could help to identify the equivalence point of the "titration" from its maximum value. Therefore, from the differential curves (Fig.5.8 (A) red dotted line), the pK_a of MWCNTs-NH_2 was estimated to be 2.7 ± 0.1 based on the CV data.

For comparison, the pK_a of amino group in MWCNTs was also estimated using the experimental data from nano impact. Using the same assumptions as above, a non-linear curve was fitted (see Section A.5.12) to the average charge of oxidative spikes as a function of pH was plotted in Fig.5.8(B) (R^2=0.9656, black solid line). The differential curve (red dotted line)

reflected the change of incremental ratio (d_Q/d_{pH}) and the highest inflection point was estimated to be 2.3 ± 0.1 as the pK_a of amino groups on the MWCNTs, which is slightly smaller than that inferred using the CV method. The breadth of the transition from low to high pH in Fig.5.8 (A) and (B) are similar and may reflect the response of amino groups in different locations on the tube surface.

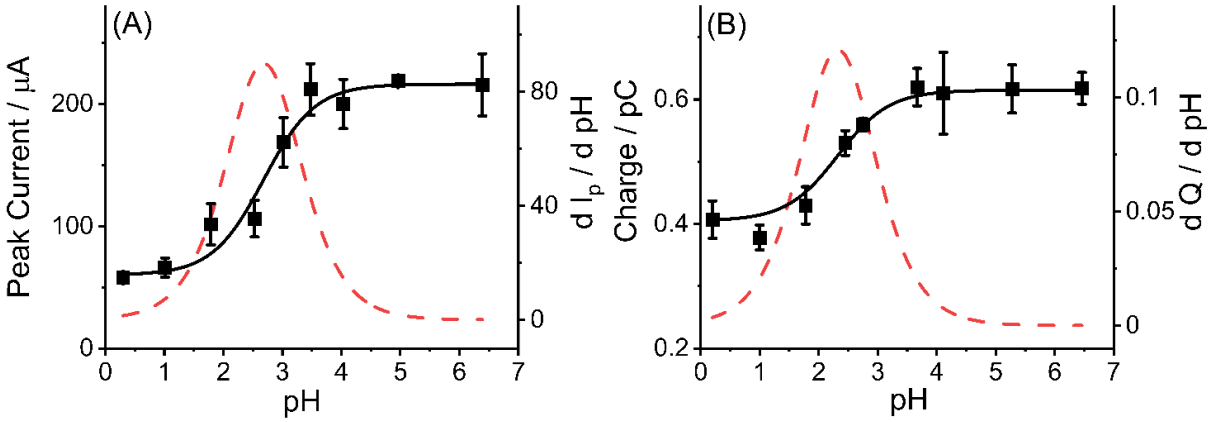


Figure.5.8 (A) Relationship between oxidative peak current of MWCNTs-NH_2 modified GCE and pH value of solution; (B) Relationship between average charge of oxidative spikes and pH value of solutions in the presence MWCNTs-NH_2 (black square: experimental data; black solid line: simulated curve, and red dotted line: differential curve of experimental data).

5.4 Conclusions

The electro-oxidations of MWCNTs and MWCNTs-NH_2 have been studied by single and ensemble electrochemistry respectively within the range of pH values from 0.3 to 6.4. The work opens up a new and generic approach to the study of the oxidation of entities made of carbon allotropes and of different forms of CNTs in particular. The MWCNTs-NH_2 and the MWCNTs at all pHs studied show catalysis of the solvent (water) decomposition together with the introduction of new surface functionality. The case of MWCNTs -NH_2 at higher pH shows excess oxidative charge in the case of impact spikes and peak current in the CV. The excess Faradaic component is attributed to the electro-oxidation of the amino group when deprotonated, a process which is inhibited when they exist in the -NH_3^+ form. Based on the pH variation of

oxidative peak current in MWCNTs-NH_2 modified GCE and the oxidative spike average charge of one single MWCNTs-NH_2 particle, the pK_a values of -NH_2 bonded to MWCNTs determined by two ways in our work are estimated to be around 2.5 at 298K. This study will assist in controlling and rationalizing the chemical reactivity of the -NH_2 groups bonded to carbonaceous material utilized as a catalyst or support composites. As for the study of the surface oxygen functional groups observed on both carbon nanotubes, we will discuss their catalytic effect on the oxygen reduction reaction in the next two chapters (**Chapter 6** and **7**).

Appendix

Section A5.1 Background subtraction of original cyclic voltammograms

Fig.A5.1 illustrates the background subtraction process for cyclic voltammograms, where a baseline spline (black curve) is fitted between the potentials at which the voltammetric wave (red curve) is judged to have started and ended, then subtracted from the peak to obtain the actual peak height (blue curve).

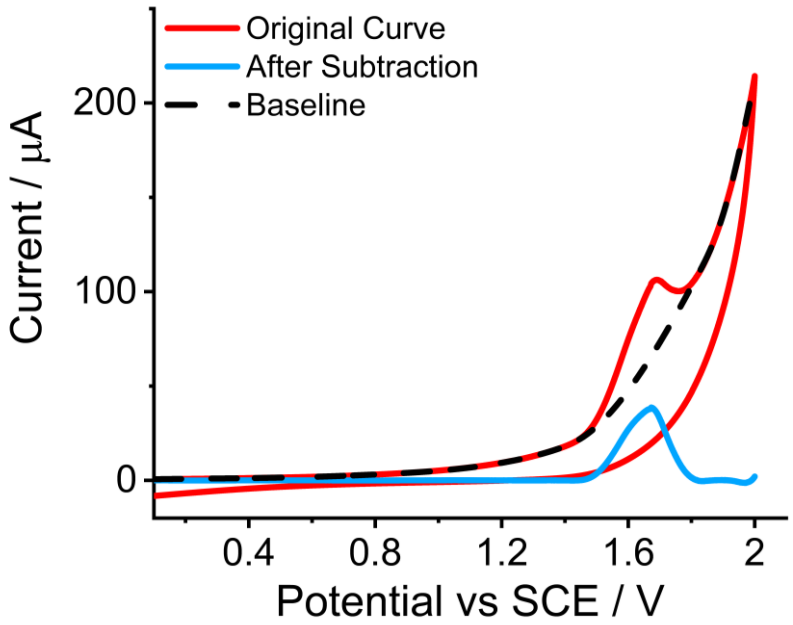


Figure.A5.1 Subtraction scheme for obtaining the peak height in cyclic voltammograms recorded at a MWCNTs modified GCEs in 0.1 M KNO_3 (pH = 6.4) at a scan rate of 50 mVs^{-1} via background correction to the original cyclic voltammogram: the original curve (red line), the baseline (black line) and subtracted curve (blue line).

Section A5.2: Chronoamperograms of a carbon micro-disc electrode at lower potentials

According to Fig. A5.2, No impacts for the electro-oxidation of MWCNTs were observed at potentials of 1.5 V and 1.4 V vs SCE in a suspension of 0.01 gL^{-1} MWCNTs particle containing 0.1 M KNO_3 (pH=6.4).

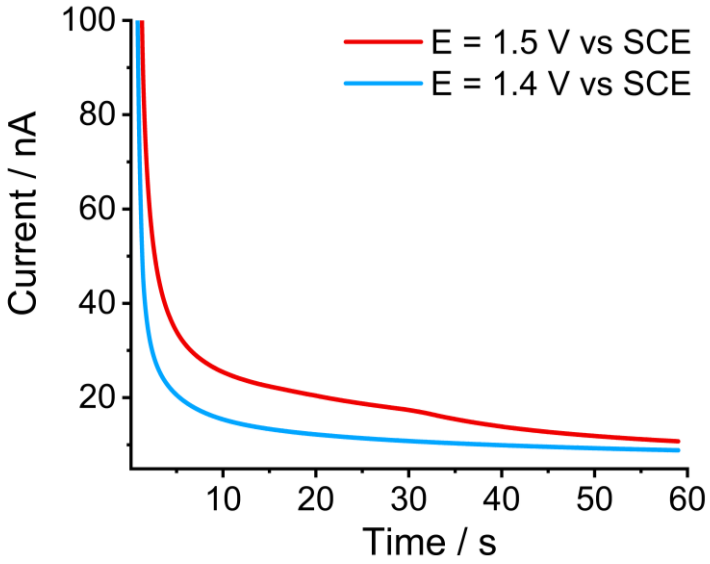


Figure.A5.2 Chronoamperograms of a carbon micro-disc electrode at 1.5 and 1.4 V vs SCE in a suspension of 0.01 gL^{-1} MWCNTs particle containing 0.1 M KNO_3 (pH=6.4).

Section A5.3: Potential variation of impact frequency and the average spike duration time in the presence of MWCNTs

The mean impact frequencies of the two types of impact signals as a function of potential are plotted in Fig.A5.3 (A). The frequency of spikes and steps were found to only slightly increase with the lifting applied potential. As for the residence time of impact signals versus potential as shown in Fig.A5.3 (B), each average duration stayed nearly the same from which over the potential range of 1.7 to 2.0 V. The step features show a sustained electrical contact between the tube and the electrode of average duration 4.6 ± 0.9 s (43 measurements). In contrast the spike features require a much shorter contact time (of average length 12 ± 1 ms from 53 measurements).

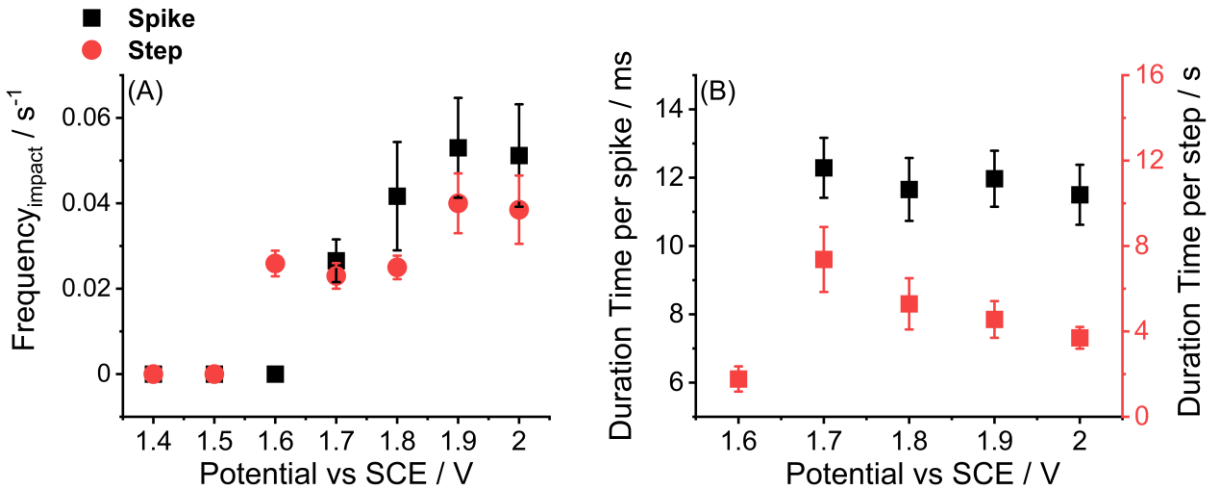


Figure.A5.3 (A) Impact frequency plot as a function of applied potentials from 1.4 V to 2.0 V vs SCE in the presence of 0.01 g L^{-1} MWCNTs; (B) Impact spike and step average duration time as a function of applied potentials from 1.6 V to 2.0 V in the presence of 0.01 g L^{-1} MWCNTs.

Section A5.4: The charge distribution of spikes in the presence of MWCNTs

Applying a fixed potential at + 1.90 V vs SCE, in 0.1 M KNO_3 at pH=1.0, the oxidative spikes in the presence of MWCNTs had an average charge of 0.40 ± 0.03 pC as measured from 48 current spikes consistent with the average charge from the oxidative spikes obtained in 0.1 M KNO_3 at pH=6.4 as reported 0.43 ± 0.05 pC from 53 current spikes (the charge distribution is seen in Fig.A5.4 (A)-(B) respectively).

The steps which appear in 0.1 M HNO_3 (pH=1.0) in the presence of MWCNTs, showed an average charge of 0.47 ± 0.05 nC was measured from 52 current steps consistent with the average charge of 0.48 ± 0.07 nC for the oxidative steps calculated from 42 current steps in 0.1 M KNO_3 at pH=6.4 (the charge distribution is seen in Fig.A5.4 (C)-(D) respectively).

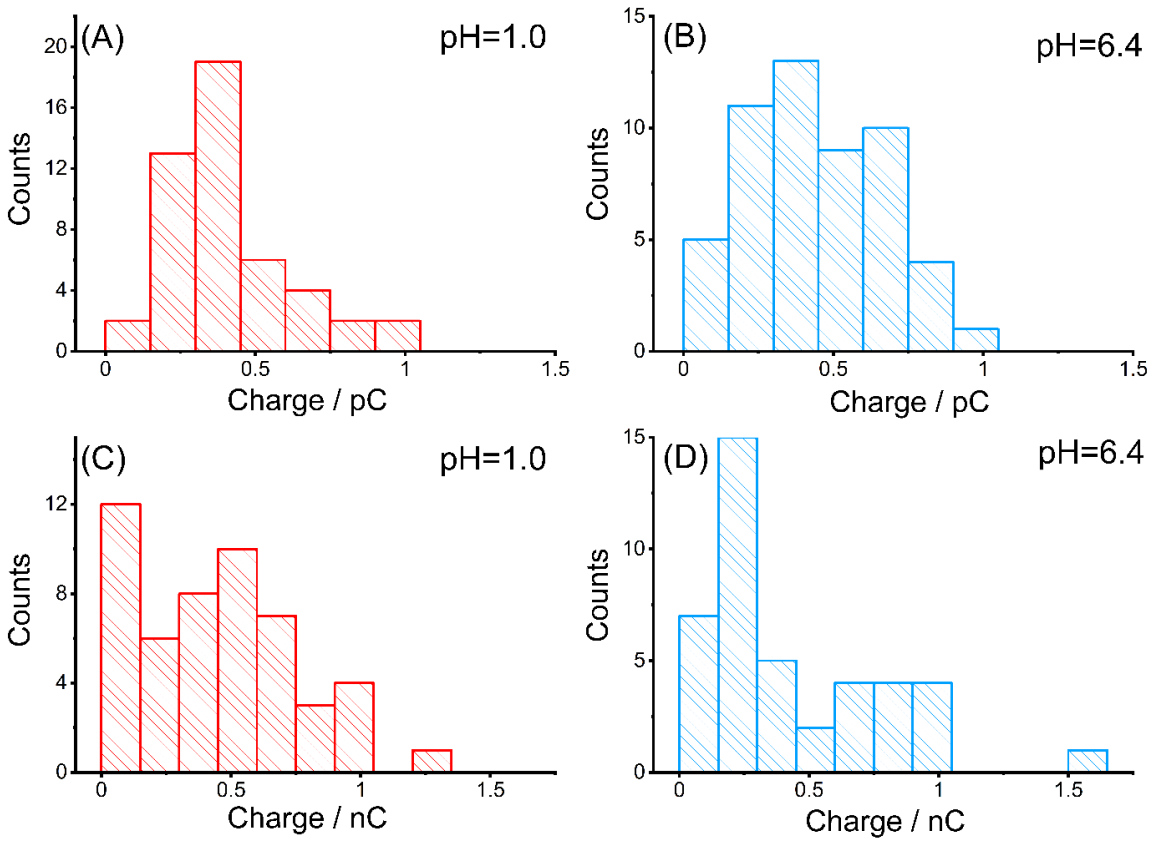


Figure A5.4 The charge distribution of 48 and 53 current spikes from the oxidation of MWCNTs in pH = 1.0 (A) and pH = 6.4 (B) solution respectively; The charge distribution of 52 and 43 current steps in the presence of 0.01 gL^{-1} MWCNTs in pH=1.0 (C) and pH=6.4 (D) solution respectively.

Section A5.5: The average functional group coverage on a single MWCNT based on ensemble electrochemistry

The area (S_h) of one hexagon composed of six carbon atoms (Fig.A5.5(A)) is

$S_h = 3\, d_{c\text{-}c}^2 \times \frac{\sqrt{3}}{2} = 5.2 \times 10^{-20}\ m^2$,

where $d_{c\text{-}c}$ (= 0.1421 nm) is the length of the C-C bond

The area (S_{mw}) of all the concentric tubes in one single MWCNT

$S_{mw} = l \times \pi d_{MWCNT} \times L = 9 \times \pi \times 3 \times 10^{-8}\ m \times 2.0 \times 10^{-5}\ m = 1.7 \times 10^{-11}\ m^2$,

where l (=9) is the number of concentric tubes within each MWCNT (Fig.A5.5 (B), supplied by NanoLab[40]), d_{MWCNT} (=30 nm) is the diameter of a carbon tube and L (=20 µm) is the length of each tube.

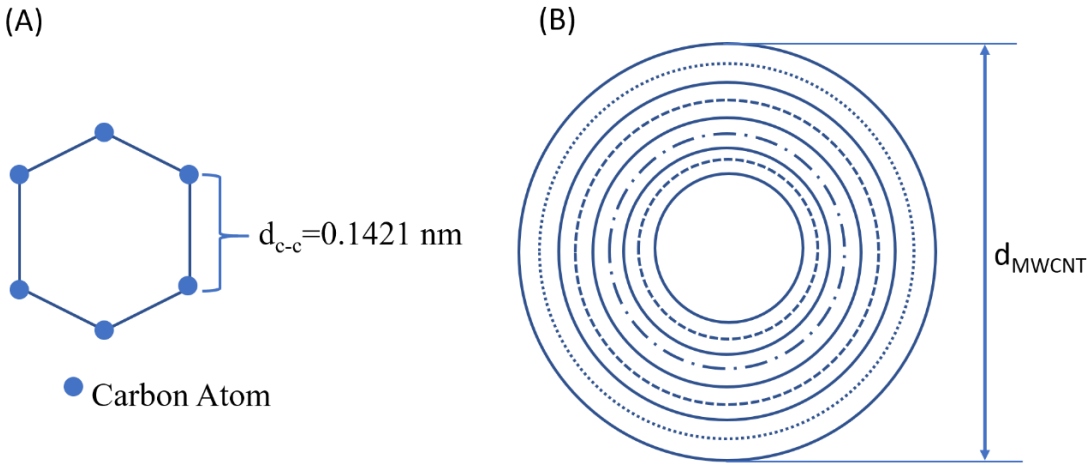


Figure.A5.5 Schematic representation of the arrangement of carbon atoms within the carbon nanotube layer (A) and an end on view of a multi-walled carbon nanotube made up of nine concentric shells (B).

The number of carbon atoms per tube $Nc = 2 \times S_{mw} / S_h = 2 \times 1.7 \times 10^{-11}\ m^2 / 5.2 \times 10^{-20}\ m^2 = 6.6 \times 10^8$

The mass per carbon tube $w_{mw} = 6.6 \times 10^8 \times 2 \times 10^{-23}\ g = 1.3 \times 10^{-14}\ g$

(one Carbon atom mass $w_c = 2 \times 10^{-23}\ g$)

Therefore, the number of carbon tubes present on the surface of a modified GCE (N_{MWCNT}) is

$N_{MWCNT} = 2 \times 10^{-7}\ g / 1.3 \times 10^{-14}\ g = 1.5 \times 10^7$

The cyclic voltammograms at different scan rates in the range of 25–400 mVs^{-1} in 0.1M KNO_3 (pH=6.4) (Fig.A5.6) were recorded, the peak shape gradually became better defined as the scan rate was decreased. The charge was estimated as a function of scan rate with an increased charge being observed at lower scan rates corresponding to a greater proportion of the drop cast layer being oxidized. Extrapolation of the reciprocal charge against scan rate to zero scan rate gave a charge $Q_{MWCNT\text{-}ensemble}$ of 7 mC averaged over five measurements.

The charge of oxidized groups (q_1) on each MWCNTs particle via electro-oxidation can be estimated to be $q_1 = Q_{MWCNT\text{-}ensemble} / N_{MWCNT} = 7\times10^{-3}$ C / $1.5\times10^{7} = 4.6\times10^{-10}$ C,

where $Q_{MWCNT\text{-}ensemble}$ is the average charge passed at MWCNTs modified GCE from CV in 0.1 M KNO_3 (pH=6.4) based on the polynomial fitting curve shown in Fig A5.6.

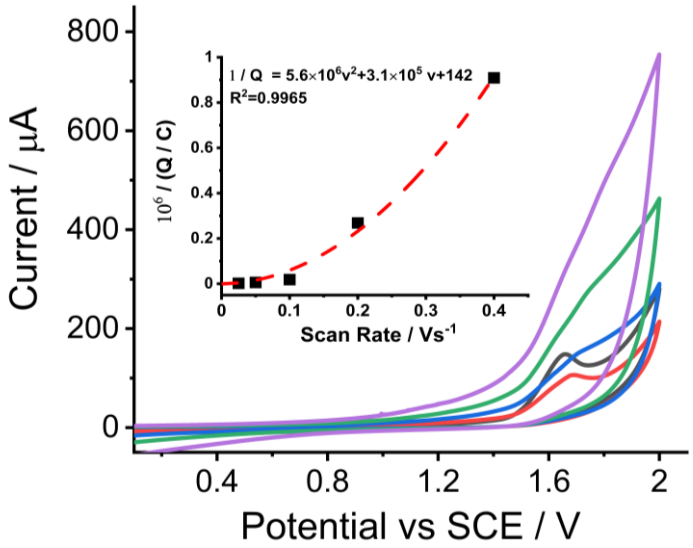


Figure.A5.6 Cyclic voltammograms of a MWCNTs modified GCE in 0.1 M KNO_3 (pH = 6.4) at varying scan rates of 25 mVs^{-1}, 50 mVs^{-1}, 100 mVs^{-1}, 200 mVs^{-1} and 400 mVs^{-1} (Inlay: Plot of 1/Q versus scan rate from 25 mVs^{-1} to 50 mVs^{-1}, 100 mVs^{-1}, 200 mVs^{-1} and 400 mVs^{-1} where Q is the average charge passed at MWCNTs modified GCE).

Section A5.6: Estimation of the number of layers of MWCNTs drop-casted on the GC electrodes

To estimate a minimum number of MWCNT monolayers on the bare GC electrode, we assume a closed pack arrangement of the MWCNT is laid uniformly across the whole GC surface. This gives a lower limit estimate for the number of layers.

The diameter and length of the bamboo-like multiwalled carbon nanotubes (purchased from NanoLab, USA) is ca. 30 nm and ca. 20 µm respectively.

Assuming the MWCNTs contact at the GC surface to be rectangular when arranged in a closed pack manner, the area covered by one MWCNT is 6×10^{-8} cm^2.

2 μL 0.1 gL^{-1} MWCNTs was drop cast on the bare GC electro, the number of MWCNTs modified on the surface of modified GCE ($N_{MWCNT)}$ (calculated in Section A5.5) is $N_{MWCNT}=1.5\times10^{7}$

Hence, the total area covered by 1.5×10^{7} MWCNTs is 0.9 cm^2

The diameter of GC electrode is 3.02 +/- 0.005 mm, the area is $A = (\pi D^2) / 4 = 7.07\times10^{-2}$ cm^2

The number of monolayers of MWCNTs for 2 μL 0.1 gL^{-1} MWCNTs drop cast

$$N_{layer} = \frac{Total\ area\ covered\ by\ MWCNTs}{Total\ surface\ area\ of\ GC\ electrode} = 0.9\ cm^2 / 0.07\ cm^2 \approx 13$$

Section A5.7: Estimation of the number of functional groups possibly created by electro-oxidation on a single MWCNT

The number of functional groups (N_{ox}) introduced into a single MWCNTs particle via electro-oxidation can be estimated from nano-impact experiments to be

$N_{ox}=Q_{MWCNT\text{-}single}/n_1e=4.3\times10^{-13}$ C / $(4\times1.6\times10^{-19}$ C) $=6.7\times10^{5}$

where $Q_{MWCNT\text{-}single}$ is the average charge from the oxidative spike current, n_1 is the number of electrons transferred, which is estimated to be equal to four corresponding to hypothetical quinone formation.

The circumferences of the one end of a single MWCNT has a total length of

$l_{end} = \pi d_{MWCNT} = \pi\times3\times10^{-8}$ m $= 9.5\times10^{-8}$ m

where d_{MWCNT} (=30 nm) is the diameter of carbon tube

The distance between each functional group oxidized at the end of carbon nanotube (d_1)

$d_1 = l_{end} / N_2 = 9.5\times10^{-8}$ m / $(6.7\times10^{5}) = 1.4\times10^{-13}$ m $=1.4\times10^{-3}$ Å

This extremely low value suggests that far more functionality is introduced than can possibly be accommodated on a single tube end. Hence the likely interpretation of the short timescale of

the spikes lies in the dynamics of the collision rather than the finite extent of the part of the CNT available for oxidation to quinones.

Section A5.8: The calculation of the average charge passed at a MWCNT-NH_2 modified GCE

The cyclic voltammograms of MWCNTs-NH_2 modified GCE at different scan rates in the range of 25–400 mVs^{-1} in 0.1M KNO_3 of different pH (pH=1.0 or 6.4) (Fig.A5.7) were recorded. The peak shape gradually became better defined as the scan rate was decreased. The charge was estimated as a function of scan rate with an increased charge being observed at lower scan rates corresponding to a greater proportion of the drop cast layer being oxidized. Polynomial fitting curves were used to infer the charge passed on a MWCNTs-NH_2 modified GCE as a function of scan rate (Fig.A5.8). Extrapolation of the reciprocal charge against scan rate to zero scan rate gave the average charge of 6.0 mC and 9.5 mC in 0.1 M HNO_3 with pH=1.0 or pH=6.4 respectively.

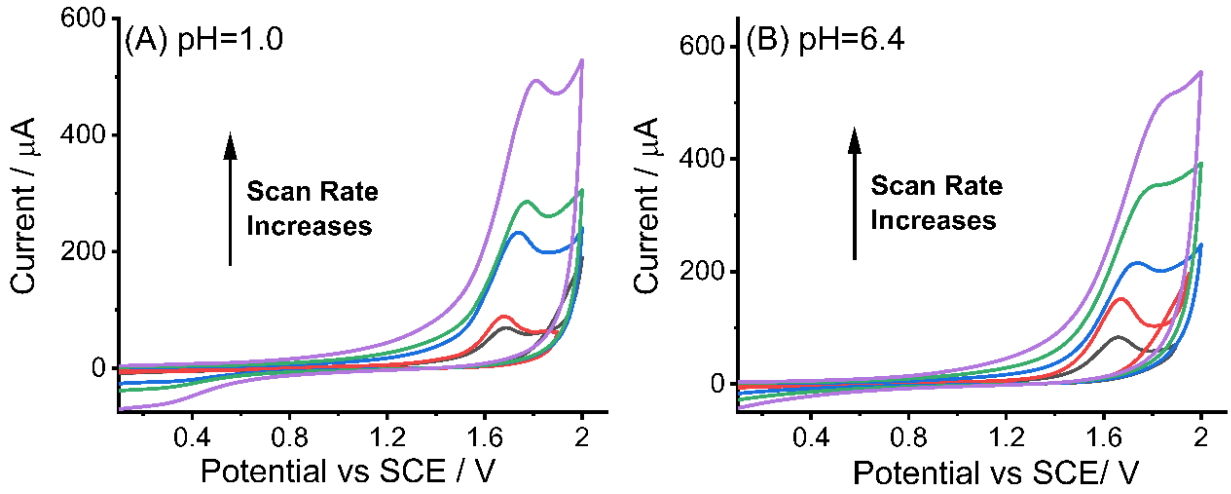


Figure. A5.7 Cyclic voltammograms of MWCNTs-NH_2 modified GCE immersed in 0.1 M KNO_3 solution of pH = 1.0 (A) and pH = 6.4 (4) at different scan rates from 25 mVs^{-1} to 50, 100 and 200 mVs^{-1}.

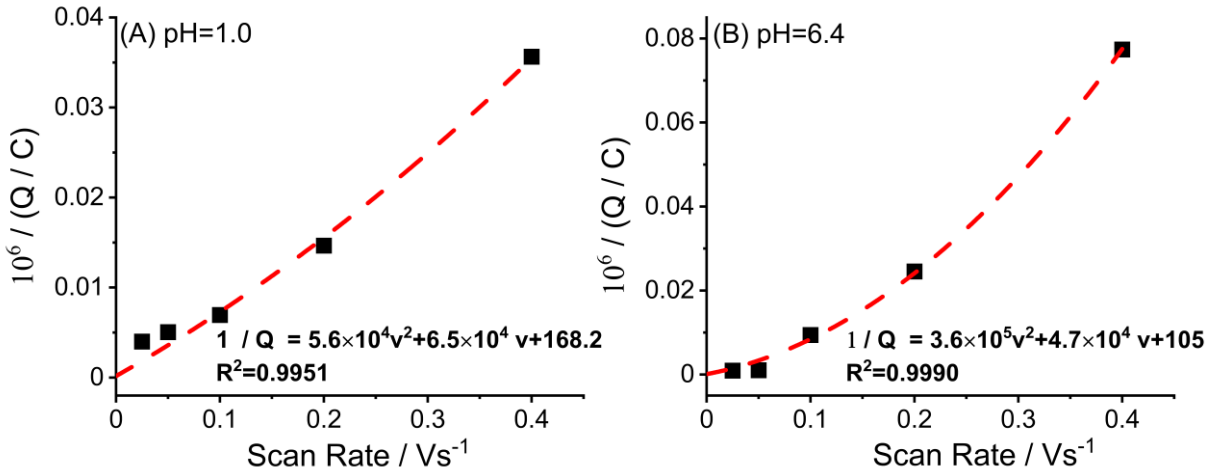


Figure. A5.8 Plot of 1/Q versus scan rate from 25 mVs^{-1} to 50, 100 and 200 mVs^{-1} where Q is the average charge passed at MWCNTs-NH_2 modified GCE in pH = 1.0 (A) and pH = 6.4 (B) solution.

Section A5.9: Representative chronoamperograms showing impacts of MWCNTs-NH_2

As shown in Fig. A5.9 (A)-(E)), the representative chronoamperograms for the oxidation of single MWCNTs-NH_2 particle using solutions of varying pH from 1 to 1.8, 2.7, 4.1 and 5.3 were recorded. Fig.A5.9(F) suggests that the average step current seen in the presence of MWCNTs-NH_2 fluctuated at 0.26 ± 0.06 nA as a function of solution pH from 0.3 to 6.4 demonstrating their pH independency.

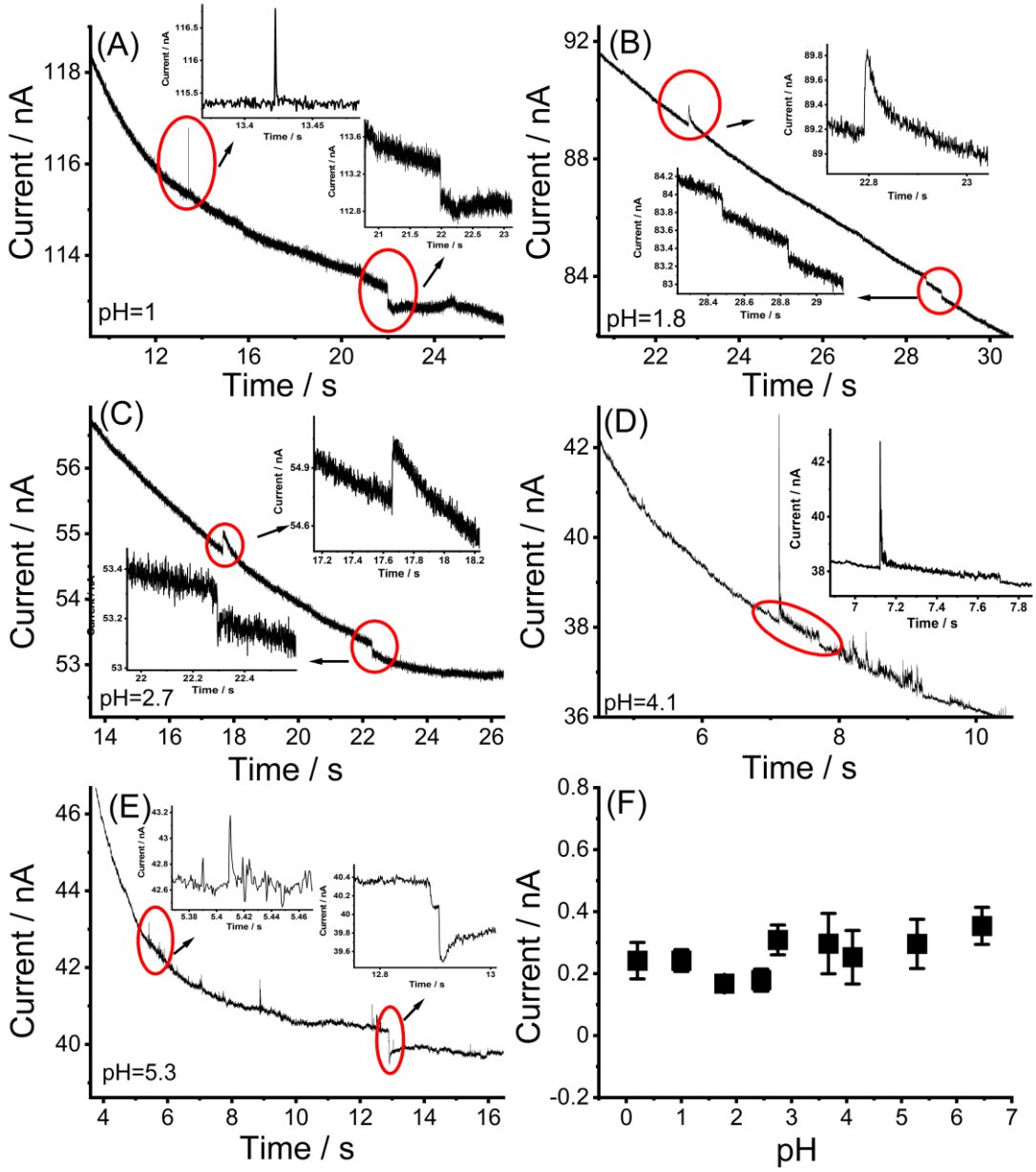


Figure A5.9 (A)-(E) Representative chronoamperograms of a carbon micro-disc electrode immersed in a 0.1 M HNO_3 (pH = 1.0) and 0.1 M KNO_3 solutions at different pH values of 1.8, 2.7, 4.1 and 5.3 containing 0.01 gL^{-1} MWCNTs-NH_2 at a potential of 1.90 V vs SCE; (F) The plot of average step current as a function of solution pH.

Section A5.10: pH variation of impact frequency and average duration time of spikes and steps in impacts of MWCNTs-NH_2

The oxidative step frequency in the presence of MWCNTs-NH_2 under different pH condition (Fig.A5.10 (A)) stay nearly constant with a mean value of 0.039 ± 0.005 s^{-1}. The step duration was found to be steady at 4.8 ± 1.0 s (Fig.A5.10(B)).

As for the oxidative spike in the presence of MWCNTs-NH_2, the corresponding frequency under different pH condition (Fig.A5.10(A)) stay nearly the same with a mean value of 0.048 ± 0.010 s^{-1}. While the spike duration was found to be unchanged at 15 ± 2 ms (Fig.A5.10(B)).

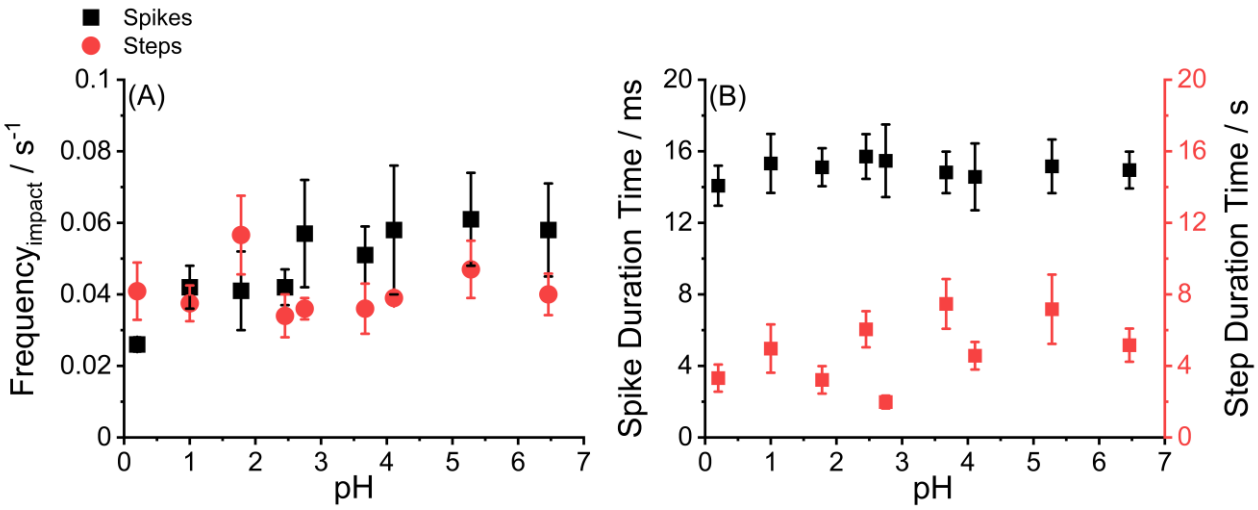


Figure.A5.10 (A) Impact frequency plot as a function of pH from 0.3 to 6.4 in the presence of 0.01 g L^{-1} MWCNTs-NH_2; (B) Impact spike and step average duration time as a function of pH from 0.3 to 6.4 in the presence of 0.01 g L^{-1} MWCNTs-NH_2.

Section A5.11: The charge distribution of spikes from impacts of MWCNTs-NH_2

The average charge from 89 spikes for MWCNTs-NH_2 at 1.90 V in 0.1 M KNO_3 (pH=6.4) solution was calculated to be 0.62 ± 0.02 pC, and its charge distribution is shown in Fig.A5.11.

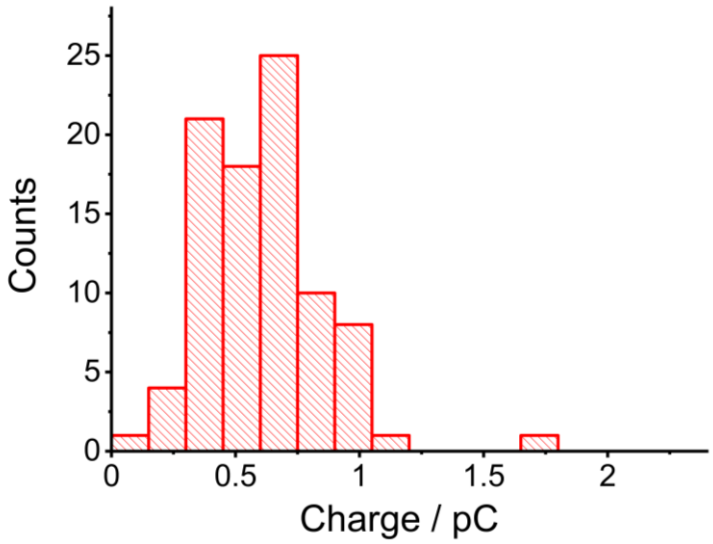


Figure A5.11 The charge distribution of 89 current spikes from the oxidation of MWCNTs-NH_2 particle in 0.1 M KNO_3 (pH = 6.4) solution.

Section A5.12: The fitting of the relationship between average charge of oxidative spikes and pH value

The oxidative spike average charge (q) is given by:

$$q = q_{\text{-NH}_2}[\text{MWCNTs-NH}_2] + q_{\text{-NH}_3^+}[\text{MWCNTs-NH}_3^+] \qquad \text{(A5.1)}$$

where $q_{\text{-NH}_2}$ and $q_{\text{-NH}_3^+}$ can be determined from the average spike charge at high pH >4 (0.61 nC) and low pH <2 (0.40 nC) where the difference between the two charges represents q-NH_2 and the value at low pH gives q-NH_3^+

Combined with $pH = pK_a + \log_{10}\left[\frac{[MWCNTs-NH_2]}{[MWCNTs-NH_3^+]}\right]$ (A5.2)

And assuming the sum [MWCNTs-NH_2] + [MWCNTs-NH_3^+] is a constant, the following equation Eq. (A5.3) can be obtained:

$$pK_a = pH - \log_{10}\left(\frac{q_{-NH_3^+} - q_{-NH_2}}{q - q_{-NH_2}} - 1\right) \qquad \text{(A5.3)}$$

Using the Origin Pro2020 non-linear fitting function, the Fitting Function Formula is input by simplifying the Eq. (A5.3) as:

$$q = 0.61 - \frac{0.21}{10^{pH-pK_a+1}} \quad \text{(A5.4)}$$

Setting the initial value of pK_a to be around 2.5, the fitting curve was then generated automatically ($R^2 = 0.9656$).

References

1. Y. Lu, X. Li and R. G. Compton, *Chemical Science*, 2022.
2. J. H. Lehman, M. Terrones, E. Mansfield, K. E. Hurst and V. Meunier, *Carbon*, 2011, **49**, 2581-2602.
3. Y. Ando, X. Zhao, H. Shimoyama, G. Sakai and K. Kaneto, *International journal of inorganic materials*, 1999, **1**, 77-82.
4. A. Rawal and V. Kumar, *Applied Physics Letters*, 2013, **103**.
5. Y. Chen, C. Liu, F. Li and H.-M. Cheng, *Journal of Porous Materials*, 2006, **13**, 141-146.
6. L. Fu, Y. Q. Liu, Z. M. Liu, B. X. Han, L. C. Cao, D. C. Wei, G. Yu and D. B. Zhu, *Advanced Materials*, 2006, **18**, 181-185.
7. P. K. Brahman, L. Suresh, V. Lokesh and S. Nizamuddin, *Anal Chim Acta*, 2016, **917**, 107-116.
8. Shereen M. Azab and A. M. Fekry, *RSC Advances*, 2017, **7**, 1118-1126.
9. C. Jiajia, J. Xin, S. Qiujie, W. Chong, Z. Qian, Z. Ming-sen and D. Quan-feng, *Electrochimica Acta*, 2010, **55**, 8062-8066.
10. R. Shu, W. Li, Y. Wu, J. Zhang and G. Zhang, *Chemical Engineering Journal*, 2019, **362**, 513-524.
11. Q. Shu, W. Zou, J. He, H. Lesmana, C. Zhang, L. Zou and Y. Wang, *Renewable Energy*, 2019, **135**, 836-845.
12. N. Gupta, S. M. Gupta and S. K. Sharma, *Carbon Letters*, 2019, **29**, 419-447.
13. K. Balasubramanian and M. Burghard, *Small*, 2005, **1**, 180-192.
14. Y. Liu, L. Gao, J. Sun and Y. Wang, *J Ceram Process Res*, 2010, **11**, 120-122.
15. T. I. T. Okpalugo, P. Papakonstantinou, H. Murphy, J. McLaughlin and N. M. D. Brown, *Carbon*, 2005, **43**, 153-161.

16. J. Shen, W. Huang, L. Wu, Y. Hu and M. Ye, *Materials Science and Engineering: A*, 2007, **464**, 151-156.
17. M. Soleimani, M. Ghahraman Afshar and A. Sedghi, *ISRN Nanotechnology*, 2013, **2013**, 1-8.
18. G. Yang, X. Chen, Q. Pan, W. Liu and F. Zhao, *International Journal of Electrochemical Science*, 2017, **12**, 7272-7286.
19. Y. Sugano, S. Kuittinen, O. Turunen and A. Pappinen, *Bioinspir Biomim*, 2019, **14**, 036007.
20. X. Ma, D. Deng, N. Xia, Y. Hao and L. Liu, *J Nanomaterials*, 2021, **11**, 1757.
21. S. Shahzad, L. Karadurmus, B. Dogan-Topal, T. Taskin-Tok, A. Shah and S. A. Ozkan, *Electroanalysis*, 2019, **32**, 912-922.
22. A. V. Velasco, J. R. Romo and H. E. Duran, *Journal of Physics: Conference Series*, 2019, **1159**, 12003.
23. M. Garrido, L. Gualandi, S. Di Noja, G. Filippini, S. Bosi and M. Prato, *Chem Commun (Camb)*, 2020, **56**, 12698-12716.
24. G. Vuković, A. Marinković, M. Obradović, V. Radmilović, M. Čolić, R. Aleksić and P. S. Uskoković, *Applied Surface Science*, 2009, **255**, 8067-8075.
25. G. Papp, G. Olveti, H. Horvath, A. Katho and F. Joo, *Dalton Trans*, 2016, **45**, 14516-14519.
26. H. Gong, S.-T. Kim, J. D. Lee and S. Yim, *Applied Surface Science*, 2013, **266**, 219-224.
27. Z. Zhang, L. Pfefferle and G. L. Haller, *Catalysis Today*, 2015, **249**, 23-29.
28. P. Abiman, A. Crossley, G. G. Wildgoose, J. H. Jones and R. G. Compton, *Langmuir*, 2007, **23**, 7847-7852.
29. W. N. Olmstead, Z. Margolin and F. G. Bordwell, *The Journal of Organic Chemistry*, 1980, **45**, 3295-3299.
30. Y. Zeng, X. Chen, D. Zhao, H. Li, Y. Zhang and X. Xiao, *Fluid Phase Equilibria*, 2012, **313**, 148-155.
31. M. D. Liptak, K. C. Gross, P. G. Seybold, S. Feldgus and G. C. Shields, *Journal of the American Chemical Society*, 2002, **124**, 6421-6427.
32. P. Abiman, G. G. Wildgoose, A. Crossley, J. H. Jones and R. G. Compton, *Chemistry*, 2007, **13**, 9663-9667.
33. R. Barhdadi, M. Troupel, C. Comminges, M. Laurent and A. Doherty, *J Phys Chem B*, 2012, **116**, 277-282.
34. N. V. Rees, *Electrochemistry Communications*, 2014, **43**, 83-86.

35. W. Cheng and R. G. Compton, *TrAC Trends in Analytical Chemistry*, 2014, **58**, 79-89.
36. P. H. Robbs and N. V. Rees, *Physical Chemistry Chemical Physics*, 2016, **18**, 24812-24819.
37. J. Ye, X. Liu, H. F. Cui, W. Zhang, F. Sheu and T. M. Lim, *Electrochemistry Communications*, 2005, **7**, 249-255.
38. A. Doepke, C. Han, T. Back, W. Cho, D. D. Dionysiou, V. Shanov, H. B. Halsall and W. R. Heineman, *Electroanalysis*, 2012, **24**, 1501-1508.
39. J. Ellison, K. Tschulik, E. J. Stuart, K. Jurkschat, D. Omanovic, M. Uhlemann, A. Crossley and R. G. Compton, *ChemistryOpen*, 2013, **2**, 69-75.
40. N. Inc, Multiwall Carbon Nanotubes (Bamboo Structure), can be found at https://www.nano-lab.com/bamboopowderd30l520.html).
41. T. L. d. A. Montanheiro, F. H. Cristóvan, J. P. B. Machado, D. B. Tada, N. Durán and A. P. Lemes, *Journal of Materials Research*, 2014, **30**, 55-65.
42. R. Sadri, M. Hosseini, S. N. Kazi, S. Bagheri, N. Zubir, K. H. Solangi, T. Zaharinie and A. Badarudin, *J Colloid Interface Sci*, 2017, **504**, 115-123.
43. B. R. Eggins and J. Q. Chambers, *Journal of The Electrochemical Society*, 1970, **117**, 186.
44. C. A. Little, R. Xie, C. Batchelor-McAuley, E. Katelhon, X. Li, N. P. Young and R. G. Compton, *Phys Chem Chem Phys*, 2018, **20**, 13537-13546.
45. M. Pumera, *Chemistry–A European Journal*, 2009, **15**, 4970-4978.
46. C. E. Banks, T. J. Davies, G. G. Wildgoose and R. G. Compton, *Chem Commun (Camb)*, 2005, 829-841.
47. L. Pederson and S. Bryan, *Assessment of the potential for ammonium nitrate formation and reaction in Tank 241-SY-101*, Pacific Northwest Lab., Richland, WA (United States), 1994.
48. J. Glazer, E. Hughes, C. Ingold, A. James, G. Jones and E. Roberts, *Journal of the Chemical Society (Resumed)*, 1950, 2657-2678.
49. J. B. Tingle and F. Blanck, *Journal of the American Chemical Society*, 1908, **30**, 1395-1412.
50. N. Weinberg and H. J. C. R. Weinberg, 1968, **68**, 449-523.
51. L. Sharma, A. Manchanda, G. Singh and R. S. Verma, *J Electrochimica Acta*, 1982, **27**, 223-233.
52. M. Masui and S. Ozaki, *Chemical and Pharmaceutical Bulletin*, 1978, **26**, 2153-2159.

Chapter 6

The Oxygen Reduction Reaction at Single Entity Multiwalled Carbon Nanotubes

Chapter 6 reports the electrocatalysis of the oxygen reduction reaction (ORR) in aqueous base (0.1M KOH) by multiwalled carbon nanotubes (MWCNTs) at the single entity level. Electroactive surface functionality is shown to facilitate significant electrocatalysis leading to peroxide formation which is seen to occur at lower potentials as compared to the voltammetric responses obtained at bare carbon macroelectrodes and at such electrodes modified with layers of carbon nanotubes.

Considering that the ORR holds a special place in many fuel cell devices, the electrocatalysis of the reaction has been widely explored at the macroscale but not previously the intrinsic ORR activity at the single nanotube level. This work develops a new approach to the study of the kinetics of the ORR catalytic reaction.

The work of **Chapter 6** has been published in the journal *The Journal of Physical Chemistry Letters* [1], and was carried out under the supervision of Prof. Richard G.Compton (University of Oxford) and in collaboration with Dr. Xiuting Li (Shenzhen University) who helped with the interpretation of the experimental results.

6.1 Introduction

Rapid advances in fuel cells facilitate renewable energy generation and give optimism for a sustainable future[2, 3]. As a core cathodic reaction in fuel cell technology, the oxygen reduction reaction, ORR, has been extensively investigated in the field of electrocatalysis [4, 5]. Depending on the electrode material, the ORR is found to occur through one of two pathways in alkaline solutions [6, 7]: a direct four-electron pathway from oxygen to hydroxyl ion (OH^-) or a stepwise pathway which involves oxygen reduced to hydrogen peroxide anion (HO_2^-) first, then followed

by further reduction to OH^- as the final product. On the basis of voltammetric studies, it has been concluded that the ORR at bulk carbon electrodes predominantly proceeds via the formation of hydrogen peroxide and the initial possible formation of a superoxide anion intermediate indirectly inferred ($O_2^{\cdot-}$) [8, 9] although peroxide is thought to be the likely product in aqueous base [10].

Multiwalled carbon nanotubes, MWCNTs, have attracted considerable attention as possible electrocatalysts for the ORR reaction in both acid [11, 12] and alkaline [13-15] conditions, encouraged by the high surface area and the possibility of a multiplicity of active sites [16, 17] including edge plane like defects and oxygen functionality such as quinones where the latter are particularly suggested to play a role at high pH[18, 19]. Such investigations rely on voltammetry and hence the study of layers of carbon nanotubes immobilized on a substrate electrode. As such the complexity of the mass transport of reactants, intermediates and products can mask the intrinsic electrocatalytic response of single nanotubes. In the following, we compare the electrocatalytic behaviour of MWCNTs for the ORR in aqueous base using ensemble and single entity electrochemistry techniques. As introduced in the previous chapter the study of electrochemistry at single carbon nanotubes has recently been shown to be possible [20-22] via collisions of MWCNTs at the individual nanotube level by using carbon microelectrodes, where random collisions of the CNTs suspended in aqueous solution leads to transient electrical contact between the electrode and the impacting CNT for periods of up to tens of seconds in favourable cases facilitating electrochemical measurement, in the present case, of dissolved oxygen. If the CNT has greater electrocatalytic character than the impacted microelectrode, this is revealed via currents flowing at potentials which are inert except for the duration of the impact and are clearly signalled by current steps corresponding to the arrival and departure of the CNT from the electrode surface (Fig.6.1).

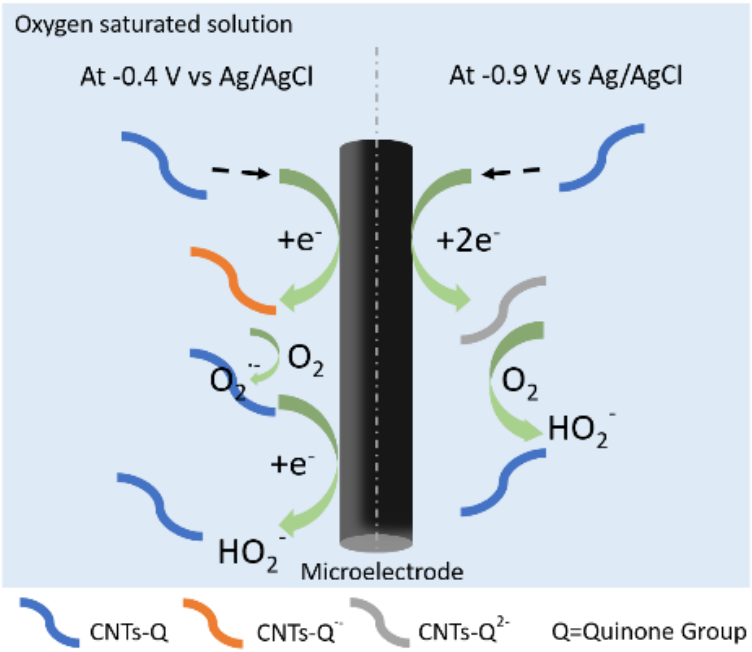


Figure.6.1 A schemic diagram for the oxygen reduction reaction studied at the single entity level in the presence of MWCNTs at different applied potentials of -0.4 V and -0.9 V vs Ag/AgCl. (where Q refers to the quinone group on the surface of MWCNTs)

6.2 Experimental

Details of the characterisation of the MWCNTs are presented in Section 2.1.

Cyclic Voltammetry of the Oxygen Reduction Reaction (ORR)

A suspension of 0.05 g L^{-1} MWCNTs was prepared by adding 0.5 mg of MWCNTs to 10 mL ethanol. The suspension was then sonicated for 30 min in a Fisher Scientific FB15050 ultrasonic bath to get a well-dispersed solution. The freshly polished GCE was modified by drop-casting a 2 µL (0.1 µg of MWCNTs) suspension of MWCNTs and left to dry under vacuum.

To investigate possible surface oxygen functional groups on the MWCNTs, CVs were recorded using MWCNTs modified GCE in 0.1 M KOH by sweeping the potential from 0 V to –1.0 V under degassed conditions. The voltammograms were recorded at scan rates varying from 10 mVs^{-1} to 25, 50, 100 and 200 mVs^{-1}.

For the cyclic voltammetric behavior of oxygen reduction, the MWCNTs modified GCE were immersed in 0.1 M KOH (measured pH=13.3). Prior to the measurements, the solution was bubbled with pure oxygen gas (O_2, BOC Gases plc, Guildford, UK) for 15 mins. The potential window was chosen to be 0 to -1.4 V and the voltammograms were conducted at different scan rates from 10 to 25, 50, 100 and 200 mVs^{-1}. A control experiment was also performed in the same solution but on a bare GCE.

Nano-impact Experiments of MWCNTs

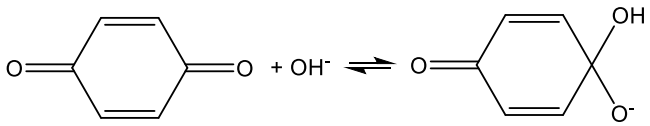
The measurements of current for the ORR on single carbon nanotube were based on the general method reported [20, 21] previously and in Chapter 5. At various potentials in the range from 0.1 V to -1.0 V vs Ag/AgCl, chronoamperometry were performed using carbon micro-wire electrode (diameter = 7 μm) on 10 mL 0.1 M KOH aqueous solution after bubbling with N_2 or O_2 for 15 minutes. The fabrication of method of carbon fibre micro-wire electrodes is described in Section 2.2. A 0.001 g L^{-1} suspension of dispersed MWCNTs was added after the outgassing reach a steady-state. The data analysis program "Signal Counter" (Centre for Marine and Environmental Research, Zagreb, Croatia) [23] and OriginPro 2020 were employed for impact signal identification and analysis.

6.3 Results and Discussion

6.3.1 Cyclic Voltammetry (CV) of MWCNTs in the absence of oxygen

Voltammetry was first carried out to study the cyclic voltammetry (CV) behaviour of MWCNTs modified glassy carbon macro electrodes (MWCNTs/GCE) in 0.1M KOH under nitrogen degassed conditions. The MWCNT layer on the electrode surface was estimated to be at least ca 0.7 layers (see Section A6.1), but probably much more from drop-casting 0.1 μg MWCNTs on to a freshly polished GCE. As shown in Fig.6.2(A), for a sweep potential from 0 V to -1.0 V vs Ag/AgCl, no voltammetric signal was seen at the bare GCE but a well-defined reductive peak at -0.35 V was observed at the MWCNTs/GCE (red curve). The reductive peak

current had a linear scan rate dependence as shown in Fig. 6.2 (B) and also increased linearly with the amount of MWCNTs drop cast (Fig. A6.2), which was attributed to the reduction of surface-bound oxygen-containing groups (for example quinone-like groups) from MWCNTs as reported in the literature[11, 24]. By holding the electrode potential at 0.5V for a period of minutes with a previous scan from 0 V to 0.5 V, the reductive signals were reduced or eliminated after 5 minutes (see Fig. A6.3) suggesting that the quinone groups on the surface of MWCNTs may be irreversibly oxidized to carboxylic or other groups [25]. The oxidation may be facilitated by the presence of the high concentrations for hydroxide ions since, at least in the case of benzoquinone in solution these form an adduct when the pH is above ca 12 [26, 27]:



(6.1)

Last, we note that a single peak is observed in the reductive voltammetry of the MWCNTs and this is chemically irreversible and the reductive peak is absent in subsequent scans if multiple CV cycles in the potential range of Fig.6.2(A) are made (see Fig. A6.4) as will be discussed further below.

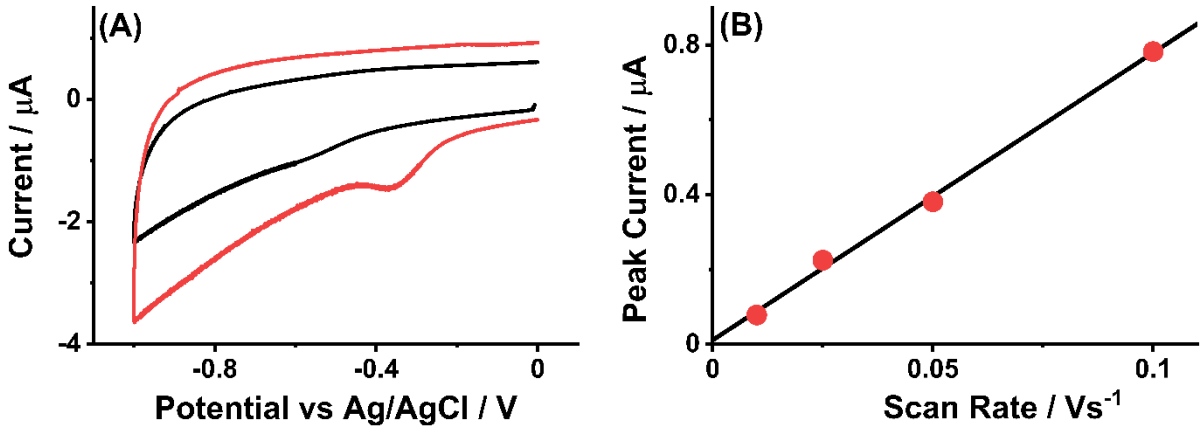


Figure.6.2 (A) A comparison of cyclic voltammograms measured at a bare GCE (black line) of surface area 7.1×10^{-2} cm^2 and the same GCE modified with 0.1 µg MWCNTs (red line) in the potential window from 0 V to -1.0 V at a scan rate of 50 mVs^{-1}; (B) Plot of reductive peak current observed at a MWCNTs/GCE in the presence of oxygen (red line in A) versus

scan rate from 10 mVs^{-1} to 25, 50 and 100 mVs^{-1} after baseline subtraction (as shown in Fig.A6.1).

6.3.2 Nano-impact experiments of single MWCNT particles in the absence of oxygen

Nano impact experiments were conducted to further probe the redox behaviour of MWCNTs surface functionality via the collision of individual MWCNTs particles with a carbon fiber microwire electrode in a N_2-saturated solution containing 0.1 M KOH and 0.001 g L^{-1} MWCNTs. Chronoamperometric scans were made at variable potentials in the range 0 to -1.0 V giving clear reductive impacts as shown in Fig. 6.3(A) for the example case of -0.4 V. The average impact duration was 22 ± 2 ms with individual impacts ranging from 11 to 78 ms (at least 40 samples for each potential, see Fig. A6.6(A)) The frequency of reductive impact responses maintained a value of 0.068 ± 0.011 s^{-1} over the potential range from -1.0 V to -0.2 V (Fig. A6.7 (A)) and the potential dependency of the average current and charge is shown in Fig.6.3(B). It shows two current plateaus: the first plateau has an average current height of ca. -0.32 ± 0.03 nA with an average of ca. 1.9 ± 0.3 pC passed when the potential is between -0.4 V and -0.7 V, and the second appeared at potentials negative than -0.9 V with ca. -0.55 ± 0.03 nA with an average of ca. 3.6 ± 0.5 pC passed. The halfwave potentials of the two current-potential waves in Fig.6.3(B) is ca -0.20 ± 0.05 V and -0.80 ± 0.05 V vs Ag/AgCl respectively. No reductive impacts were observed for potentials more positive than – 0.1 V or in the absence of CNTs. The magnitude of the charge passed in the reductive impacts are consistent with 3.2×10^{14} molecules per cm^2 of CNT external surface assuming a two-electron process (Section A6.3), which corresponds to an unrealistically high fraction (1 in 6 for quinone groups to C_6 hexagons on the tube surface) suggesting the possibility that some aggregates of MWCNTs are involved in the collision process.

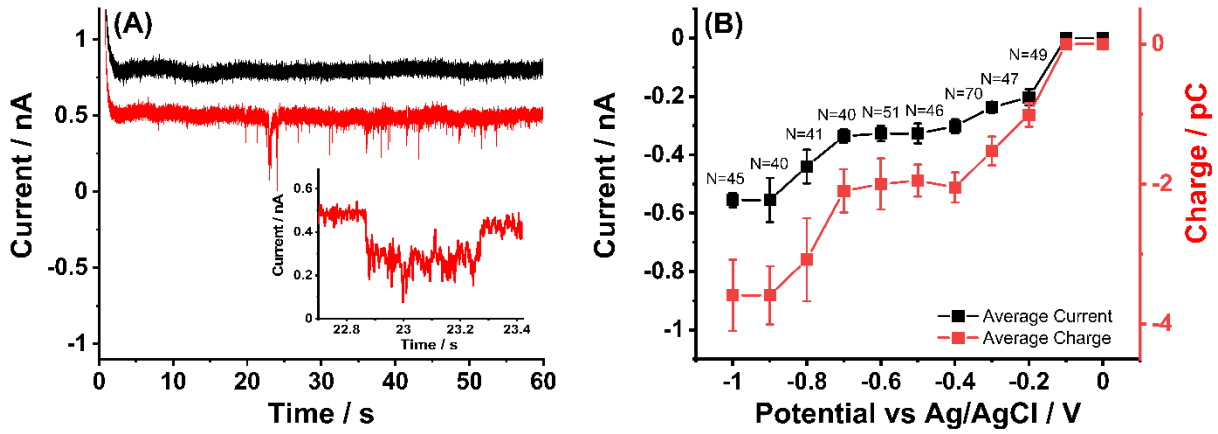


Figure.6.3 (A) Chronoamperometric profiles showing reductive single CNT impact signals at -0.4 V vs Ag/AgCl (C) vs Ag/AgCl in the presence (black line) or absence of 0.001 gL^{-1}MWCNTs (red line). The inset shows enlargements of individual impact; (B) Plot of average impact current (black dots) and impact average charge (red dots) as a function of potential from 0 to -1.0 V (The error bars represent the average of at least 40 separate impacts at a carbon microwire electrode for each potential). All the experiments were conducted in nitrogen degassed 0.1M KOH.

It is interesting that two features are seen in the single entity current-voltage response whereas just one appears in the CV recorded for the drop casted GCE. The first single entity 'wave' occurs at a similar potential seen for the single feature in the CV, whilst the absence of a second wave in the latter is consistent with the inferred chemical irreversibility of the former so that the surface feature has been consumed at higher potentials. The observation of two peaks of similar magnitude in the impact responses is again possibly suggestive of the presence of quinones since in aqueous solution a single two-electron CV wave for ensembles is typically seen in the accessible pH range [28, 29] including in strong alkaline media [18, 30]. Whilst in the hydrophobic environments of non-aqueous solutions, two voltammetric features are seen corresponding to the generation of surface semi-quinones ($Q^{\cdot -}$) and di-anions (Q^{2-}) in separate one electron processes [31-33]:

$$\boldsymbol{Q + e^- \rightleftharpoons Q^{\cdot -}} \quad (6.2)$$

$$\boldsymbol{Q^{\cdot -} + e^- \rightleftharpoons Q^{2-}} \quad (6.3)$$

where Q denotes a quinone group on the CNT. The surface of the CNTs are thought, as with basal plane graphite, to have a hydrophobic nature [34, 35] so we accordingly tentatively suggest the two features seen possibly have their origin in the two one-electron reductions of surface quinones. Anodic impacts were observed at positive potentials as reported in the Section A6.4. Last, we note that the shape of individual impact transient has been used to infer the possible collision dynamics in the case of graphene nanoplatelets [36]. This may also be possible in the case of MWCNTs but is beyond the scope of this letter.

6.3.3 Cyclic voltammetry of the oxygen reduction reaction at MWCNTs

Next, we explored the ORR at MWCNTs. For comparison, cyclic voltammograms were scanned at a freshly polished GCE and a MWCNTs/GCE in 0.1M KOH in the absence and presence of O_2 over the potential range 0 V to -1.4 V; no signals were seen in the absence of oxygen (Fig.6.4(A)). The dominant features seen in the bare GCE voltammograms are the peak at -0.56 V ($Peak_1$) and a much smaller peak at -0.76 V ($Peak_2$) as shown in Fig.6.4(A). Voltammetric analysis of the two peaks is described in the Section A6.5. Note that both peaks are associated with overall reduction to peroxide as fully discussed in previous literature [10], where the role of surface adsorbed species, is identified in bringing about a two-electron reduction at high pH, in contrast to the solution phase only mechanism at pH < 10 where, counter to thermodynamic expectations, the reduction appears at less cathodic potentials at high pH (0.1 M KOH). Note that the reported quasi-reversible formal potential for the $O_2/O_2^{\cdot -}$ couple is -0.39 V vs Ag/AgCl [37] so that an overall simple one electron process can be discounted. The literature [10] indicates that the likely surface chemistry involves the formation of adsorbed hydroperoxide species at the electrode surface with subsequent loss of peroxide ions, HO_2^-, in

basic but not under neutral conditions where the hydroperoxide is protonated and remains on the surface.

Fig.6.4(A) also shows the corresponding voltammetry recorded at the same GCE after modification with a drop casted layer of 0.1 µg of MWCNTs. The corresponding scan rate dependence is shown in Fig.6.4(B), from which the peak potentials of both peaks shift cathodically with scan rate, suggesting some degree of electrochemical irreversibility whilst the current of $Peak_1$ increases relative to $Peak_2$. Fig.A6.9 shows that if the amount of MWCNT drop cast on the surface increases, then $Peak_1$ also increases approximately linearly with the coverage, suggesting the role of thin layer effects on the voltammetric response [38-40]. Comparison of the response of the bare and MWCNTs modified GCE indicated that the currents are slightly higher for both peaks on the MWCNTs modified GCE but otherwise the voltammograms are rather similar except at higher coverages reflected by the increase in $Peak_1$ (Fig.A6.9). The possible causes for differences include changed electrode kinetics between the glassy carbon and the CNTs, altered numbers of sites for adsorption of intermediates, changed diffusion to and from the electrode with the porous layer promoting thin-layer like response as reported in refs [38, 39], and altered homogeneous chemical reactivity of the superoxide and other species within the porous layer.

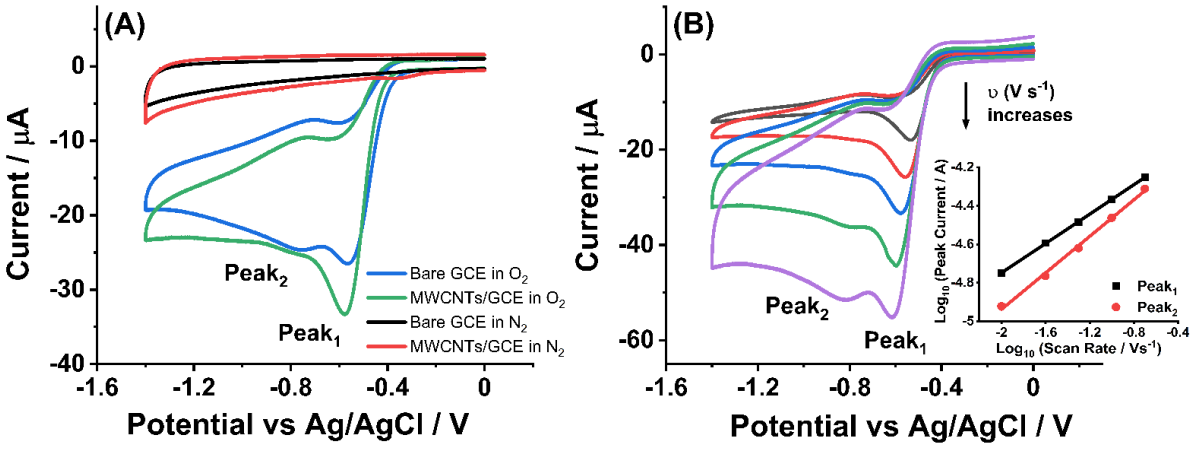


Figure.6.4 (A) Voltammograms of bare GCE and the same GCE modified with 0.1 µg MWCNTs in 0.1 M KOH in the presence or absence of O_2 at a scan rate of 50 mVs^{-1}; (B)

Voltammograms at the 0.1 µg MWCNTs modified GCE in 0.1 M KOH with saturated O_2 as a function of scan rate (Inlay: Plot of peak currents versus scan rates in a log-log form for Peak$_1$ (R^2=0.99, Slope=0.38) and Peak$_2$ (R^2=0.99, Slope=0.47)).

6.3.4 Single Particle Electrochemistry of the ORR at MWCNTs

Having tentatively inferred a *possible* catalytic effect of MWCNTs towards the ORR from ensemble electrochemistry, single entity electrochemistry was then conducted at the single MWCNTs entity level with the anticipation of establishing a clear catalytic effect or otherwise. A carbon fiber micro-wire electrode was inserted into a suspension of 0.001g L^{-1} MWCNTs in a 0.1M KOH solution with saturated O_2, and then chronoamperograms were recorded at -0.6 V vs Ag/AgCl (red line in Fig. 6.5 (A)), for more examples see Fig. A6.10. Clear reductive current steps were seen whilst no impact signals were detected in the absence of MWCNTs (black line in Fig. 6.5 (A)). A steady state ORR reduction wave was observed on the carbon wire electrode in the absence of MWCNTs with a halfwave potential at -0.49 V and a quasi-limiting current at -0.8 µA (Fig.A6.11). The wave is 'drawn out' probably reflecting the merging of the two peaks seen at the GCE. This is discussed further below.

A potential variation study was conducted for the micro-wire electrode at a series of applied potentials from 0.1 V to -1.0 V, Fig. 6.5 (B) shows the average current height of the impact features as a function of potential. Two steps are seen in which the halfwave potentials in the single entity 'voltammograms' are -0.28 V and -0.71 V. The limiting current of the first wave is 3.7 nA and of the second wave is 8.6 nA. The average residence time was independent of potential with an average value of 68 ± 15 ms (based on at least 30 samples for each potential, see Fig. A6.12). The potential of the first wave is anodic of the reversible oxygen/superoxide couple but occurs at a similar potential to that seen for the reduction of the CNTs in the absence of oxygen. Similarly, the second wave occurs at potentials consistent with those required for the observation of the second wave seen in the absence of oxygen. The much greater currents

flowing when oxygen is present revealed by the reductive impacts with similar average frequency ($0.060 \pm 0.013\ s^{-1}$, Fig.A6.13) indicates that the features suggested above to be related to the two one-electron reductions of surface quinone on the CNTs are responsible for catalytic oxygen reduction (see Fig. A6.14).

Fig. A6.11 shows that impact signals are seen at potentials less negative than required for the ORR at the microwire electrode. The magnitude of the impact signal is ca two order of magnitude lower than that for the steady ORR signal seen at the microwire electrode with absence of CNTs. The reason that impact signals are also apparent even at high negative potentials and appear superimposed on the underlying ORR current at the microwire electrode is that we suppose the CNT to make electrical contact via its end or side and since the tube has a larger length than the substrate electrode radius, the CNT extends beyond the diffusion layer near the electrode. Thus, the partial depletion of oxygen at the microwire electrode does not stop impact signals being seen. At the same time distinctive ORR impacts signals are seen at potentials where no current flows on the underlying microwire electrode. The diffusion controlled limited current for the reduction of oxygen at a single MWCNT tube is estimated to be ~ 8 nA assuming a two-electron process and that the diffusion is to a micro cylindrical electrode with a radius of 15 nm and a length of 20 μm (Section A6.11) [41, 42]. Comparison of Fig.6.3 (B) and 6.5 (B) suggests that the first step can be ascribed to a kinetically controlled reduction of oxygen by the inferred semi-quinone whilst the doubly reduced quinone mediates a full two electron electrocatalytic reduction of oxygen under diffusion control. Previous work has shown the reliability of estimating diffusion-controlled currents to single CNTs on this basis. In summary, we suggest the following electrochemistry:

First wave:

$$\boldsymbol{Q} + \boldsymbol{e^-} \rightarrow \boldsymbol{Q^{\cdot -}} \quad (6.4)$$

$$\boldsymbol{Q^{\cdot -}} + \boldsymbol{O_2}\,(\boldsymbol{aq}) \rightarrow \boldsymbol{Q \cdot O_2^{\cdot -}} \quad (6.5)$$

$$\boldsymbol{Q \cdot O_2^{\cdot -}} + \boldsymbol{H_2O} + \boldsymbol{e^-} \rightarrow \boldsymbol{Q} + \boldsymbol{HO_2^-} + \boldsymbol{OH^-} \quad (6.6)$$

Second wave:

$$\boldsymbol{Q} + \boldsymbol{2e^-} \rightarrow \boldsymbol{Q^{2-}} \quad (6.7)$$

$$\boldsymbol{Q^{2-}} + \boldsymbol{O_2} + \boldsymbol{H_2O} \rightarrow \boldsymbol{Q} + \boldsymbol{HO_2^-} + \boldsymbol{OH^-} \quad (6.8)$$

where the catalysis is sufficiently strong to allow the near diffusion-controlled reduction of oxygen at the single CNTs by the quinone di-anions (Q^{2-}). This is consistent with earlier speculations [43, 44] about the role of quinones (or other oxygen functionality) in the ORR at carbon electrodes. The magnitude of the current seen for the second wave in the single entity current-voltage plot suggest a two-electron process. It is interesting to reflect on the fact that the reduction of oxygen occurs at a less negative potential at the single nanotubes than seen at the drop-casted CNT electrode as apparent on Fig.6.5(B). Specifically, the question arises as to why oxygen electroreduction is seen at more anodic potentials than for ensembles of nanotubes. The origin likely lies in the fact that in the single entity experiments each point in the current-voltage curve is an average of measurements lasting only tens of milliseconds on fresh entities newly arrived at the electrode surface. In contrast, in the CV experiments, the potential is swept and the recording of the signal occurs over a period of seconds. As shown above the surface CV signal inferred to be the first reduction of a quinone leads to the irreversible destruction of the signal; we infer that in CV mode the quinones are destroyed in preference to undergoing electrocatalytic reaction with oxygen.

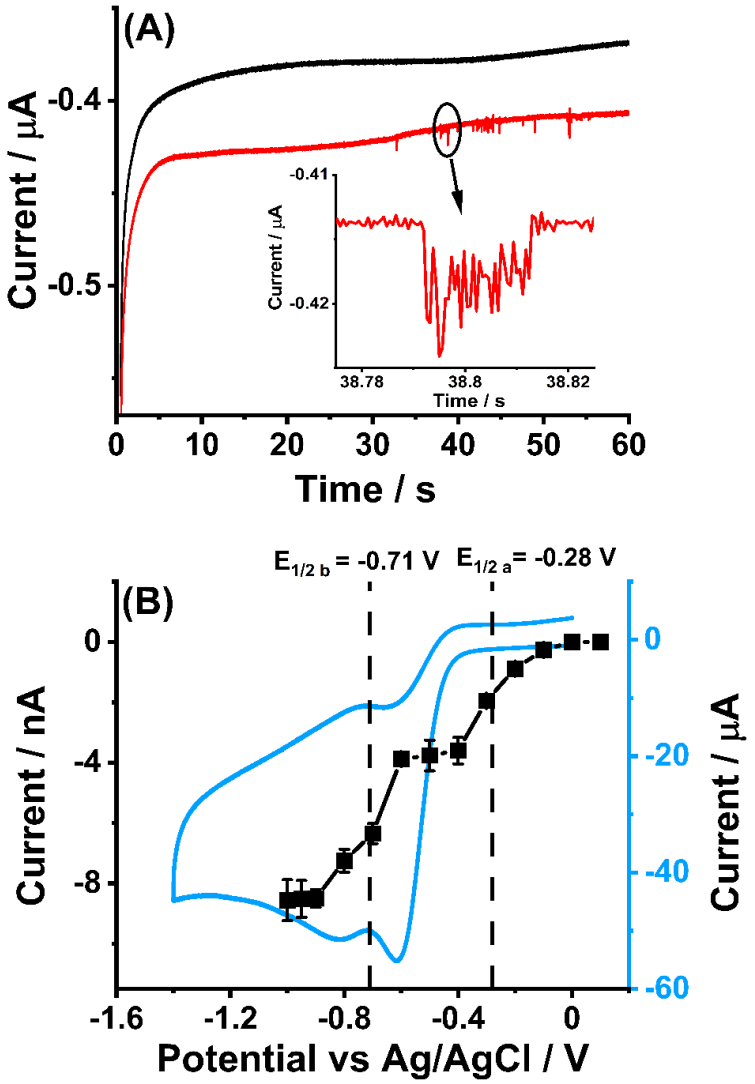


Figure.6.5 (A) Representative chronoamperometric profiles showing impact signals in oxygen-saturated 0.1M KOH at −0.6 V vs Ag/AgCl using a carbon wire electrode with presence of 0.001 gL^{-1} MWCNTs (black line) or not (red line) (Inlay: the enlarged impact signals); (B) Potential dependence of the average impact currents for oxygen reduction reaction catalyzed by MWCNTs using carbon wire, shown for comparison is a CV recorded at a MWCNTs modified GCE for ORR at a scan rate of 200mVs^{-1}. Vertical dashed lines represent the half-wave potential ($E_{1/2}$) at each step.

6.4 Conclusions

To conclude, we have shown the role of surface functionality on carbon nanotubes at both the single entity and ensemble level and the conditions under which electrocatalysis takes place characterized. At single entity level, the nano-impact signals with the random collisions of individual MWCNT particle corresponding to the reduction from oxygen to peroxide are found at lower potentials in the form of current steps, relative to the potential location of reductive peak supported by cyclic voltammetry (CV). Comparison with the ensemble behaviour of MWCNTs, the greater electrocatalytic character of MWCNTs at single electrochemistry level can be attributed to the surface functionality on carbon nanotubes, which is also explored by observing the voltammetric features in CV and impact signals for the redox behaviour of oxygen-containing groups. The generic approach developed in this chapter suggests the merits of using joint single entity and ensemble measurements for exploring electrocatalysis in general and the ORR in particular and can be applied to wide range of nano-entities. In the next chapter, we explore MWCNTs with amino group functionalization in the next chapter and compare catalytic effect between the two types of carbon nanotubes.

Appendix

Section A6.1：Estimation of the number of layers of MWCNTs drop-casted on the GC electrodes

To estimate the minimum number of MWCNT monolayers on the bare GC electrode, we assume a closed pack arrangement of the MWCNT is laid uniformly across the whole GC surface. This gives a lower limit estimate for the number of layers.

The diameter and length of the bamboo-like multiwalled carbon nanotubes (purchased from NanoLab, USA) is ca. 30 nm and ca. 20 μm respectively.

Assuming the MWCNTs contact at the GC surface to be rectangular when arranged in a closed pack manner,

The area covered by one MWCNT:

$S_{CNT} = 6 \times 10^{-9}$ cm^2,

The modification amount of MWCNTs (2 μL 0.05 gL^{-1}) on the bare GC electrode:

$m_{CNT} = 1 \times 10^{-7}$ g

The number of MWCNTs modified on the surface of modified GCE

$N_{MWCNT} = 1 \times 10^{-7}$ g / 1.3×10^{-14} g = 7.7×10^6 (the mass per carbon tube is 1.3×10^{-14} g [22])

Hence, the total area covered by 7.7×10^6 MWCNTs

$S_{total} = 6 \times 10^{-9}$ cm^2 × 7.7×10^6 = 0.046 cm^2

The surface area of GC electrode

$A = (\pi D^2) / 4 = 7.1 \times 10^{-2}$ cm^2 (the diameter of GC electrode is 3.02 ± 0.005 mm)

The number of monolayers of MWCNTs for 2 μL 0.05 gL^{-1} MWCNTs drop cast

$N_{layer} = \frac{S_{total}}{A} = 0.046$ cm^2 / 0.07 cm^2 ≈ 0.65

Section A6.2: CV of MWCNTs/GCE in the absence of oxygen

All cyclic voltammograms of MWCNTs/GCE recorded in the absence of oxygen in 0.1 M KOH were baseline subtracted to obtain the reported values of reductive peak currents as illustrated in Fig.A6.1. The background correction for the raw cyclic voltammograms were conducted by using OriginPro 2020, a baseline was fitted between the potentials at which the surface bound voltammetric wave was judged to have started and ended, then subtracted from the peak.

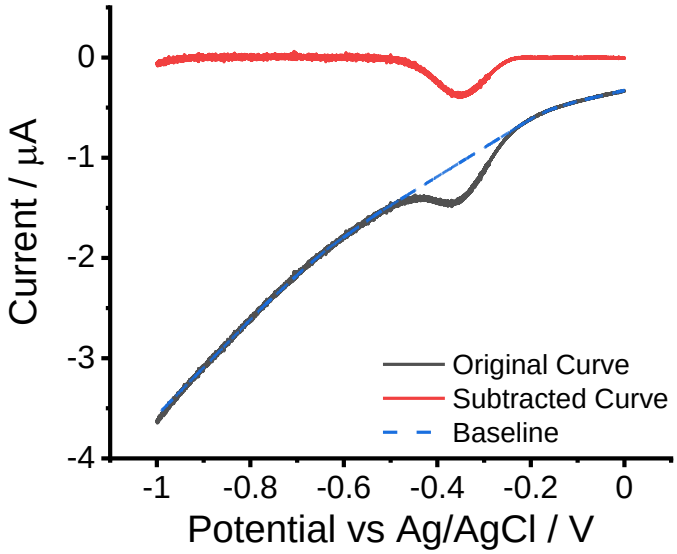


Figure.A6.1 the baseline subtraction process for cyclic voltammograms of 0.1 µg MWCNTs modified GCE swept forward to -1.0 V at a scan rate of 50 mV s^{-1}.

The freshly polished GCEs were modified with different amount of MWCNTs from 0.05 µg to 0.1, 0.2, 0.4, and 0.8 µg respectively, then by scanning cyclic voltammgrams of each modified electrode in degassed 0.1 M KOH, the enhanced reductive peak height was found with the increasing modification amount. After baseline subtraction according to Fig.A6.1, the subtracted cyclic voltammograms were shown in Fig.A6.2 (A). This reductive peak current had a linear scan rate dependence as shown in Fig. A6.2 (B) and also increased linearly with the amount of MWCNTs dropcast.

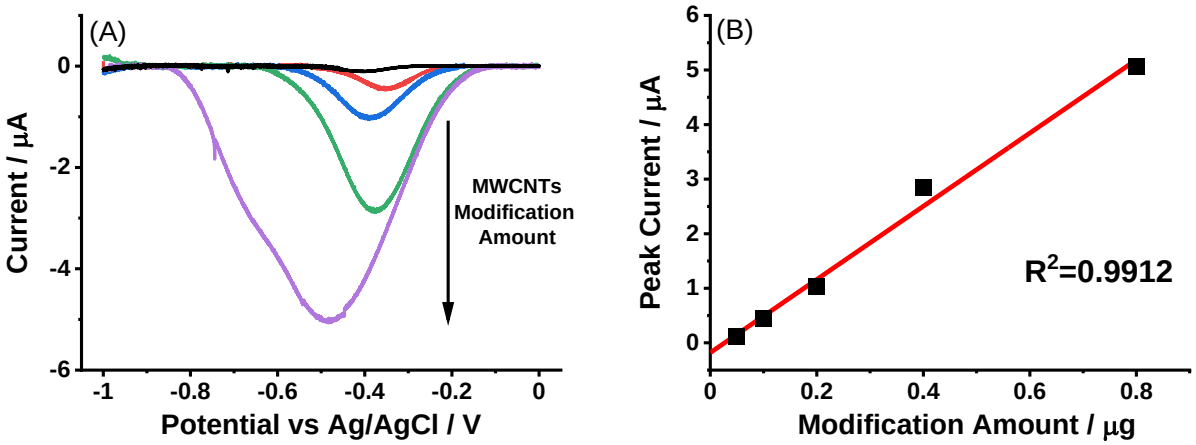


Figure. A6.2 (A) Cyclic voltammograms of polished GCE in degassed 0.1 M KOH solution with different modification amount of MWCNTs from 0.05 µg to 0.1, 0.2, 0.4, and 0.8 µg swept forward to -1.0 V at a scan rate of 50 mVs^{-1} after baseline correction; (B) The linear relationship between reductive peak current and MWCNTs modification amount.

CVs were recorded at a MWCNTs/GCE in degassed 0.1 M KOH by scanning first from 0 V to 0.5 V and holding the potential at 0.5 V before making the cathodic scan. Under these conditions the reductive peak appearing at -0.35 V decreased in size compared with the CV recorded directly from 0 V to -1 V (Fig.A6.3(A)). Furthermore, as the holding time at + 0.5 V was extended to 1, 3 and 5 mins, the reductive peak gradually decayed until disappeared (Fig.6.3(B)). It was inferred that the surface oxygen groups on MWCNTs may be irreversibly converted to carboxylic or other electro-inactive groups under potential control at + 0.5V.

Voltammetry was scanned three times successively using the same MWCNTs modified electrode in 0.1M KOH under nitrogen degassed condition. As shown in Fig.A6.4, the reductive peak was found to decay in subsequent scans after first scan.

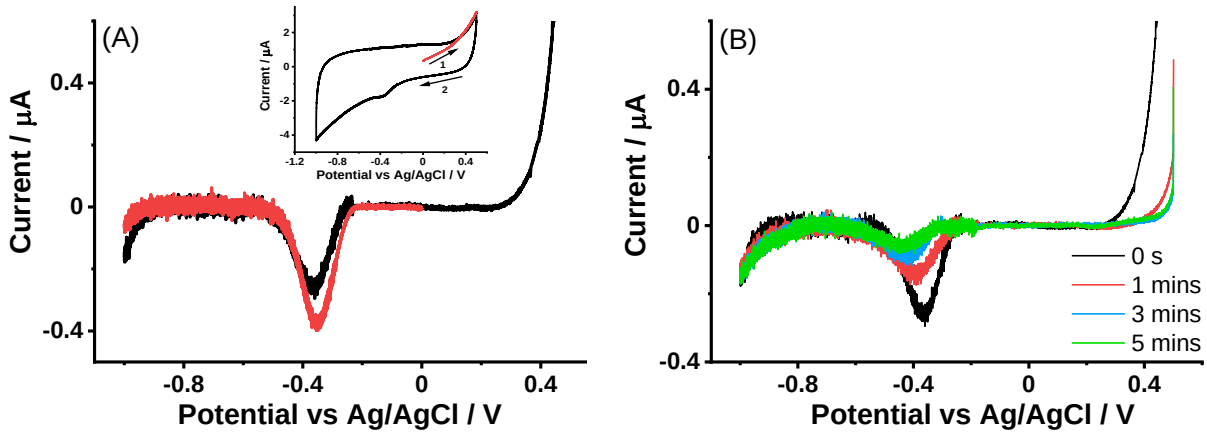


Figure.A6.3(A) A comparison of cyclic voltammograms measured by 0.1 µg MWCNTs modified GCE in the potential window from 0 V to -1.0 V with a previous scan from 0 V to 0.5 V (black line) or not, inlay: the detailed scan process from 0 V to 0.5 V then back to -1 V; (B) Cyclic voltammograms of 0.1 µg MWCNTs/GCE in the forward scan from 0.5 V to -1.0 V with a previous potential sweep from 0 to 0.5 V then hold at 0.5 V for 0, 1 mins, 3 mins and 5 mins. All the voltammograms were at a scan rate of 50 mV s^{-1} and after baseline correction.

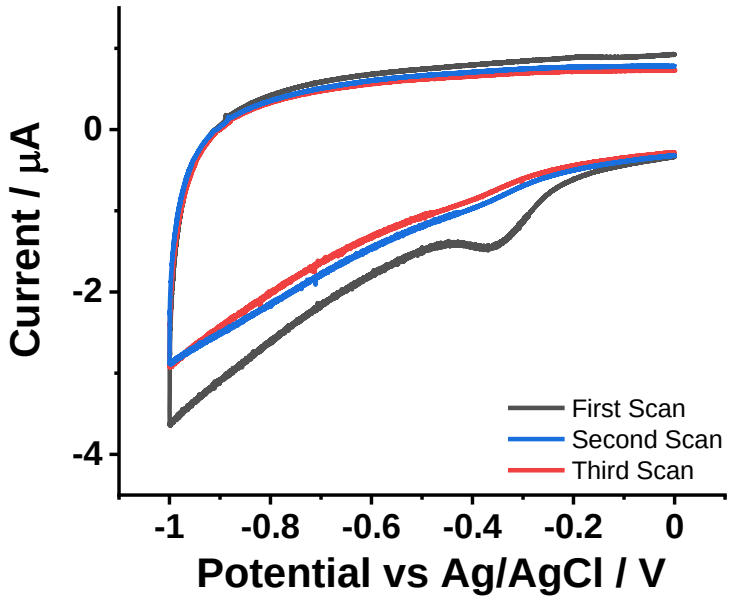


Fig.A6.4 Cyclic voltammograms of 0.1 µg MWCNTs modified GCE in degassed 0.1 M KOH solution at a scan rate of 50 mVs^{-1} swept from 0 V to -1 V in three successive scans.

Section A6.3: Estimation of the surface coverage of quinones at a single CNT

Here, we compare the number of quinones with the number of hexagonal C_6 rings on the external surface of the MWCNTs:

The external area (S_{mw}) of one single MWCNT

$S_{mw}= \pi d_{MWCNT} \times L = \pi \times 3 \times 10^{-8}$ m $\times 2.0 \times 10^{-5}$ m $= 1.9 \times 10^{-12}$ m^2,

where d_{MWCNT} (=30 nm) is the diameter of a carbon tube and L (=20 μm) is the length of each tube.

The number of quinone groups (N_q) introduced into a single MWCNTs particle via electro-reduction can be estimated from nano-impact experiments to be

$N_q = Q_{MWCNT\text{-}single}/ne = 1.9 \times 10^{-12}$ C / $(2 \times 1.6 \times 10^{-19}$ C) $= 6 \times 10^6$

where $Q_{MWCNT\text{-}single}$ is the average charge from the reductive spike current when the potential was between -0.4 V and -0.7 V, n is the number of electrons transferred (n=2, assuming a complete two-electron quinone reduction process here).

Therefore, the coverage (Γ) of quinone groups on a single MWCNTs particle is

$\Gamma = N_q / S_{mw} = 6 \times 10^6 / 1.9 \times 10^{-8}$ cm^2 = **3.2×10^{14} molecules per cm^2 of external surface area**

The area (S_h) of one C_6 hexagon composed of six carbon atoms is

$S_h = 3\, d_{c\text{-}c}^2 \times \frac{\sqrt{3}}{2} = 5.2 \times 10^{-20}$ m^2, where $d_{c\text{-}c}$ (= 0.1421 nm) is the length of the C-C bond

The number of hexagons (N_h) on the external surface of a single MWCNTs particle is

$N_h = S_{mw} / S_h = 1.9 \times 10^{-12}$ m^2 / 5.2×10^{-20} m^2 = 3.6×10^7

The amount ratio between quinone groups and hexagons is N_q / N_h = 1:6.

Section A6.4: Nano-impact experiment of MWCNTs in the absence of oxygen

Single entity measurements were conducted at oxidizing potentials. Extending the applied potential positive than 0.2 V, oxidative impacts appeared as shown in Fig.A6.5(A) and demonstrated a potential dependency for the impact current height and charge as shown in Fig.A6.5(B). Compared with the average impact duration (22 ± 2 ms, at least 40 samples for each potential) in the potential range of -0.2 to -1.0 V vs Ag/AgCl (see Fig. A6.6(A)), at the more positive potentials the impacts with an average frequency of 0.066 ± 0.015 s^{-1} (Fig.A6.7(B)) show a slightly longer average impact time of length 42 ± 13 ms (see Fig.6.6(B)). Over the potential range of 0.6 V to 0.8 V, the average current and charge reached a constant level around ca. 0.73 ± 0.09 nA and 35 ± 10 pC. The oxidative impacts are, in the light of the CV experiments mentioned above assigned to the further oxidation of the CNTs, possibly at edge planes and at pre-existing oxygen functionality such as the quinone functionality inferred from the reductive electrochemistry.

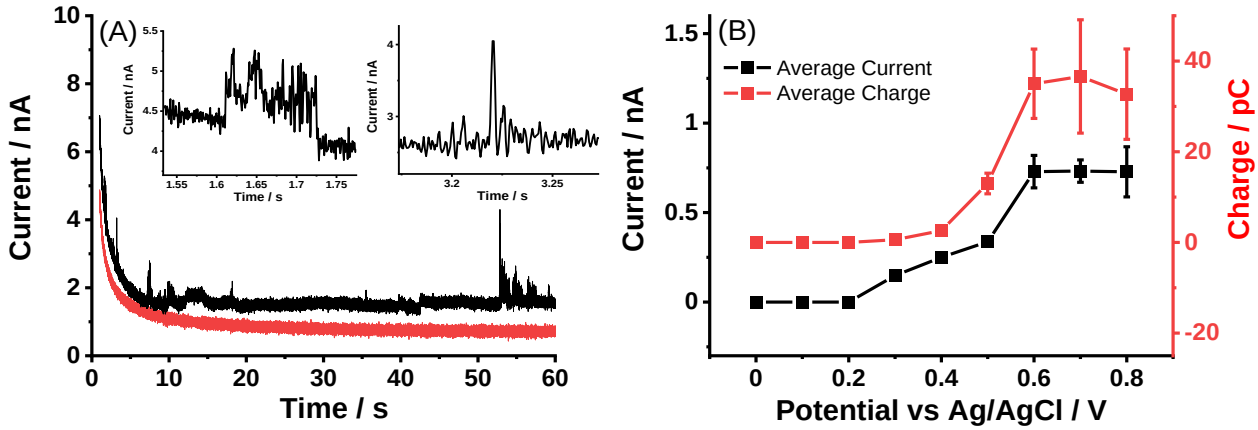


Fig.A6.5 (A) Chronoamperometric profiles showing oxidative impact signal at 0.5 V vs Ag/AgCl with presence of 0.001 g L^{-1} MWCNTs (black line) or not (red line), the inset is the enlarged impacts with short or long duration; (B) Plot of average impact current (black dots) and impact average charge (red dots) as a function of potential from 0 to 0.8 V. All the experiments were conducted in degassed 0.1 M KOH using a carbon fiber microwire electrode.

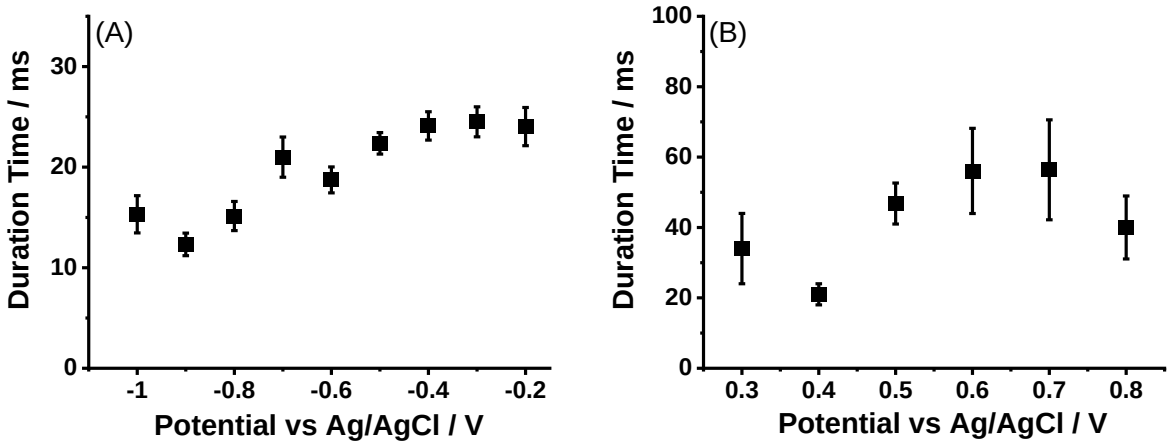


Fig.A6.6 Plot of average duration time of reductive and oxidative impacts as a function of potential from -0.2 V to -1.0 V (A) and 0.3 V to 0.8 V (B) respectively in the presence of 0.001 g L^{-1} MWCNTs.

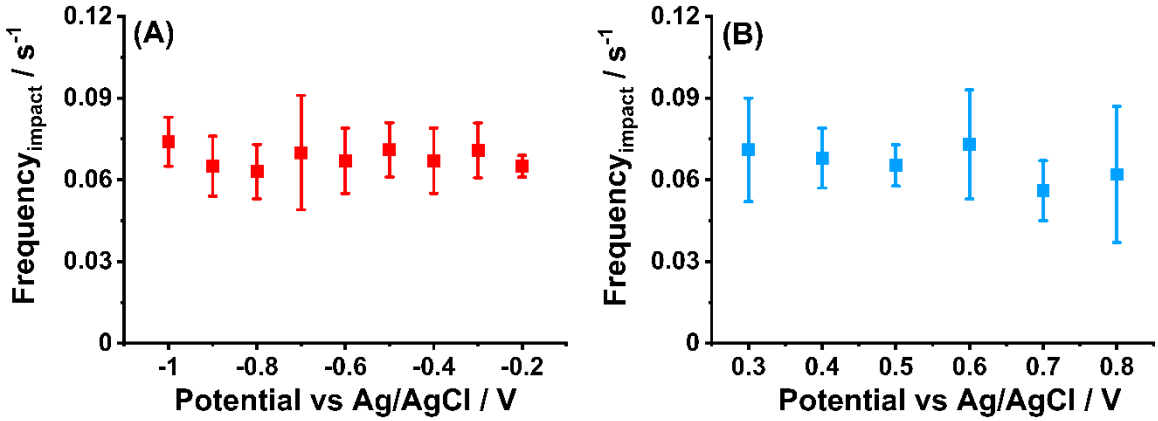


Figure. A6.7 Impact frequency plot as a function of potential from -0.2 V to -1.0 V (A) and 0.2 V to 0.8 V (B) vs Ag/AgCl in the presence of 0.001 g L^{-1} MWCNTs in nitrogen degassed 0.1 M KOH.

Section A6.5: Voltammetry at unmodified carbon electrodes in the presence of oxygen

To investigate the ORR performed on a bare GCE in 0.1 M KOH, CVs were scanned for scan rates varying from 10 mVs^{-1} to 200 mVs^{-1} on a bare GCE first from 0 V to -1.4 V vs Ag/AgCl respectively, as shown in Fig. A6.8 (A). The inset shows dependence of the peak current on the square root of voltage scan rate hinting at probable diffusion control and the formation of peroxide via a two-electron process as outlined in reference [10]. The Tafel slope is found to vary as a function of scan rate and the calculated cathodic transfer coefficients α_c decreases from 0.79 to 0.48 as scan rate increases (Fig. A6.8(B)) according to Eq. (A6.1) defined by the International Union of Pure and Applied Chemistry (IUPAC) [45] as follows:

$$-\frac{RT}{F}\frac{dln|I_c|}{dE} = \alpha_c \qquad \text{(A6.1)}$$

where I_c is the experimentally measured cathodic current (in the range of 20 % - 30 %), E is the potential of the working electrode, F is the Faraday constant (96485 C mol^{-1}), R is the Gas Constant (8.314 J mol^{-1} K^{-1}) and T is the experimental temperature (298 K). The interpretation of these data has been given elsewhere [10] where the formation of peroxide species is confirmed and the role of surface adsorbed species is emphasized.

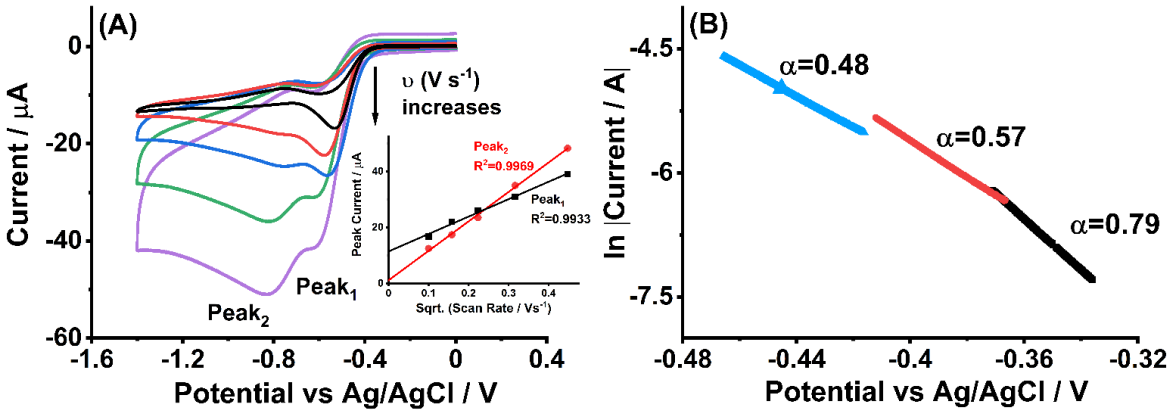


Fig. A6.8 (A) Voltammograms of bare GCE in oxygen saturated 0.1 M KOH solution at different scan rates from 10 mVs^{-1} to 25, 50, 100 and 200 mVs^{-1} (Inlay: Plot of the peak current-with square root of scan rate for $Peak_1$(black line) and $Peak_2$ (red line)); (B) The Tafel analysis for 10 mVs^{-1} (black), 50 mVs^{-1} (red) and 200 mVs^{-1} (blue).

Section A6.6: Voltammetric behavior of MWCNTs/GCE with different amounts (g) of modification

Freshly polished GCEs were modified with different amount of MWCNTs from 0.02 to 0.1, 0.2, 0.4, 0.8 and 1.6 µg respectively, then by scanning cyclic voltammgrams of each modified electrode in oxygen saturated 0.1 M KOH, the height of $Peak_1$ at -0.56 V was observed to increase with the increasing modification amount (Fig.A6.9 (A)). This reductive peak current had a linear scan rate dependence as shown in Fig. A6.9 (B) and also increased linearly with the amount of MWCNTs dropcast.

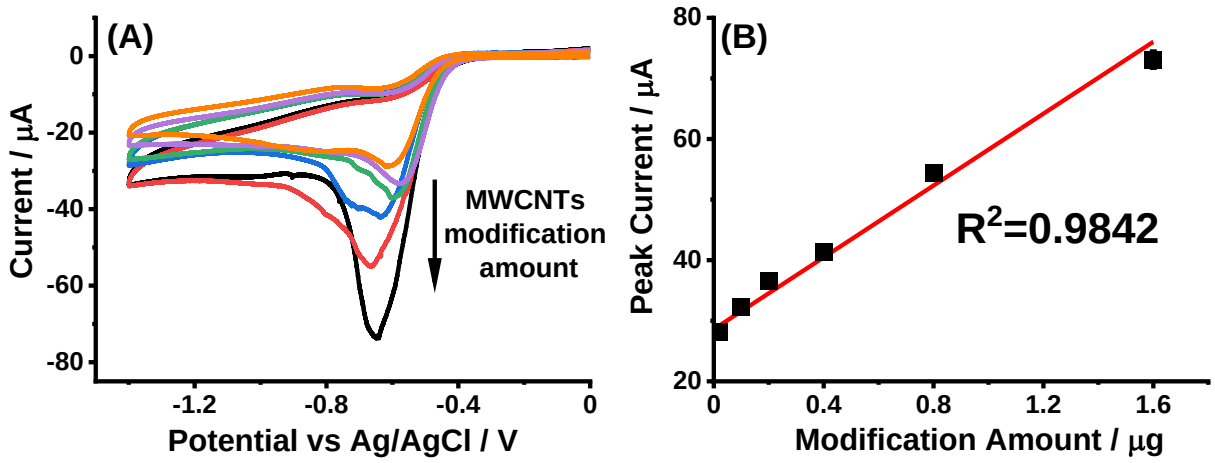


Figure.A6.9 (A) Cyclic voltammograms of GCE in oxygen saturated 0.1 M KOH solution with different modification amount of MWCNTs from 0.02 to 0.1, 0.2, 0.4, 0.8 and 1.6 µg at a scan rate of 50 mVs^{-1}; (B) The linear relationship between peak current of $Peak_1$ and MWCNTs modification amount.

Section A6.7: Representative Impact samples in the presence of MWCNTs

Fig. A6.10 demonstrated more examples of chronoamperograms recorded at -0.6 V vs Ag/AgCl. Clear reductive current steps with an average current height ranging from 4 nA to 10 nA were seen in each figure.

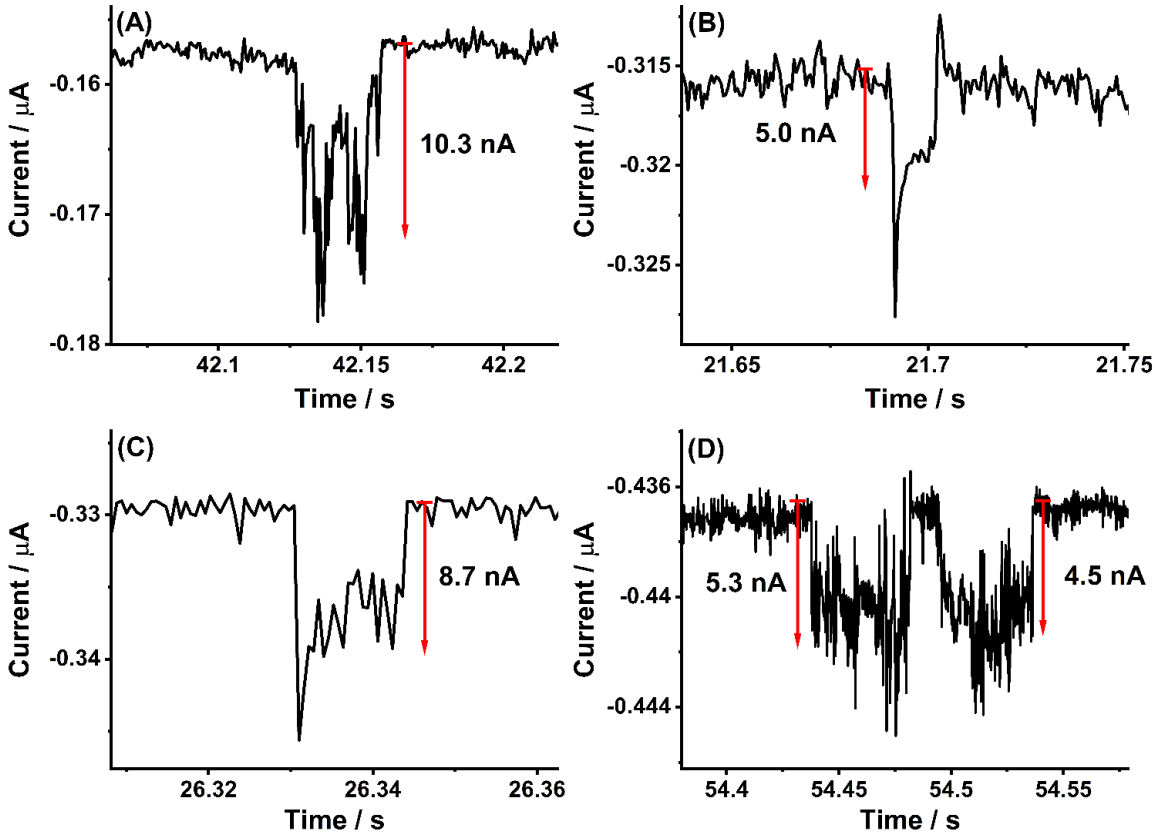


Figure.A6.10 Representative impact signals in oxygen-saturated 0.1 M KOH at -0.6 V vs Ag/AgCl using a carbon wire electrode with presence of 0.001 g L^{-1} MWCNTs.

Section A6.8: The cyclic voltammograms at the carbon microwire electrode towards ORR

At different scan rates from 5 mVs^{-1} to 10, 20 and 40 mVs^{-1}, a steady state ORR reduction wave was observed on the carbon wire electrode in the absence of MWCNTs with a halfwave potential at -0.49 V and a quasi-limiting current at -0.8 µA (Fig. A6.11). The impact signals are seen at potentials less negative than required for the ORR at the microwire electrode.

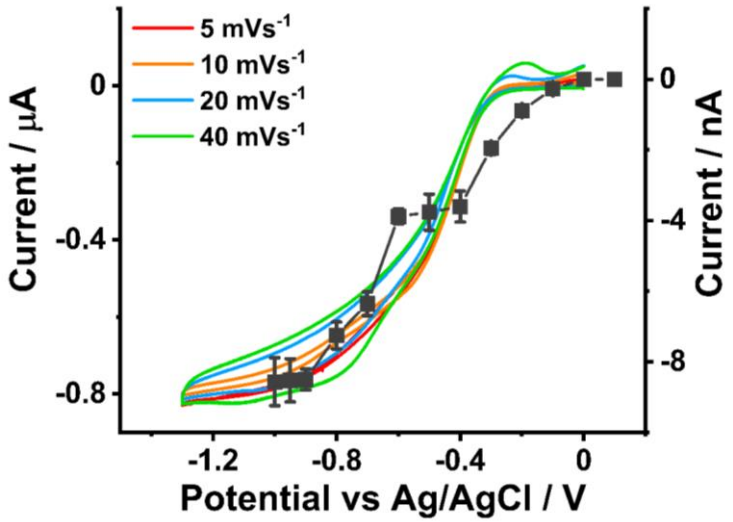


Figure.A6.11 Cyclic voltammograms of carbon microwire electrode in 0.1 M KOH with presence of saturated oxygen in the potential range from 0 V to -1.3 V at different scan rates in comparison with impact currents as a function of potential (orange dots).

Section A6.9: The average duration time per impact in the presence of oxygen as a function of potential

Over the applied potential range of -0.1 V and -1.0 V vs Ag/AgCl, the residence time per impact step was independent of potential with an average value of 68 ± 15 ms (based on at least 30 samples for each potential, see Fig. A6.12). The average frequency at each potential fluctuated at 0.060 ± 0.013 s^{-1} (Fig. A6.13).

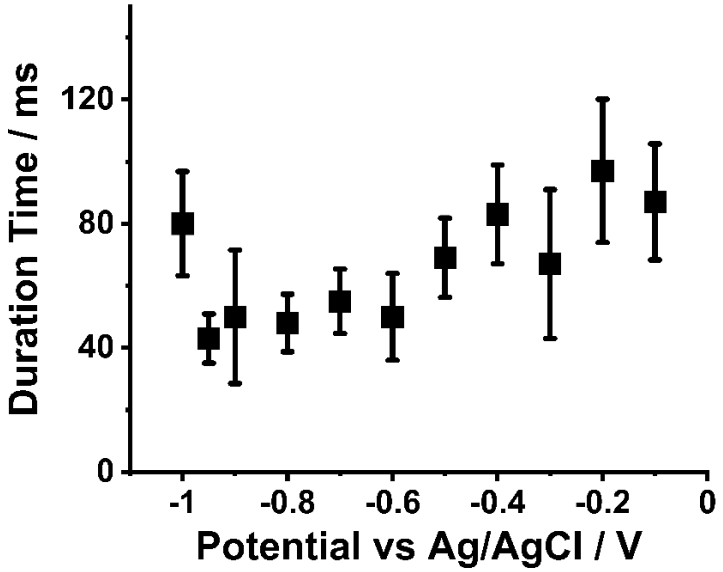


Figure.A6.12 Impact step average duration time as a function of applied potentials from -0.1 V to -1.0 V vs Ag/AgCl in the presence of 0.001 g L^{-1} MWCNTs.

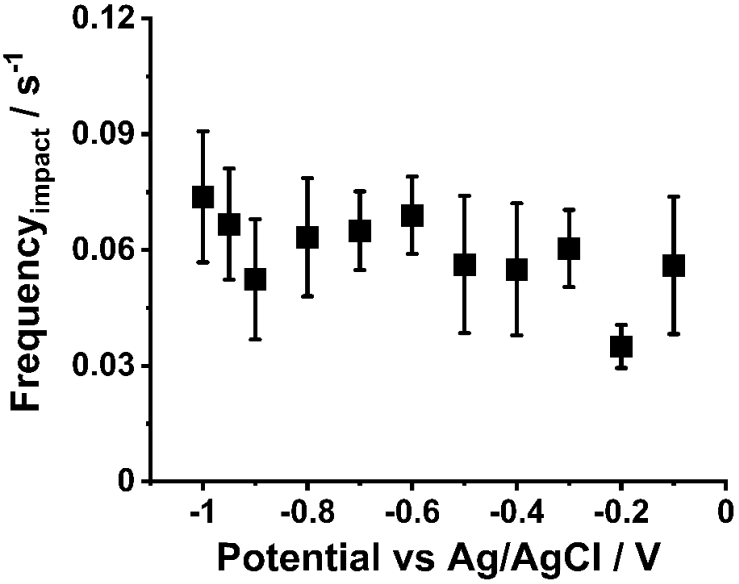


Figure.A6.13 Impact frequency plot as a function of potential from -0.1 V to -1.0 V vs Ag/AgCl in the presence of 0.001 g L^{-1} MWCNTs in oxygen saturated 0.1 M KOH.

Section A6.10: The comparison of potential dependence of impacts in the presence and absence of oxygen

Fig.A6.14 overlays average current of impacts observed in 0.1 M KOH including 0.001 gL^{-1} MWCNTs with the presence (black dots) and absence of oxygen (red dots) as a function of potential from 0.1 V to -1.0 V. The much greater currents flowing when oxygen is present indicates that the features suggested above to be related to the two one-electron reductions of surface quinones on the CNTs are responsible for catalytic oxygen reduction.

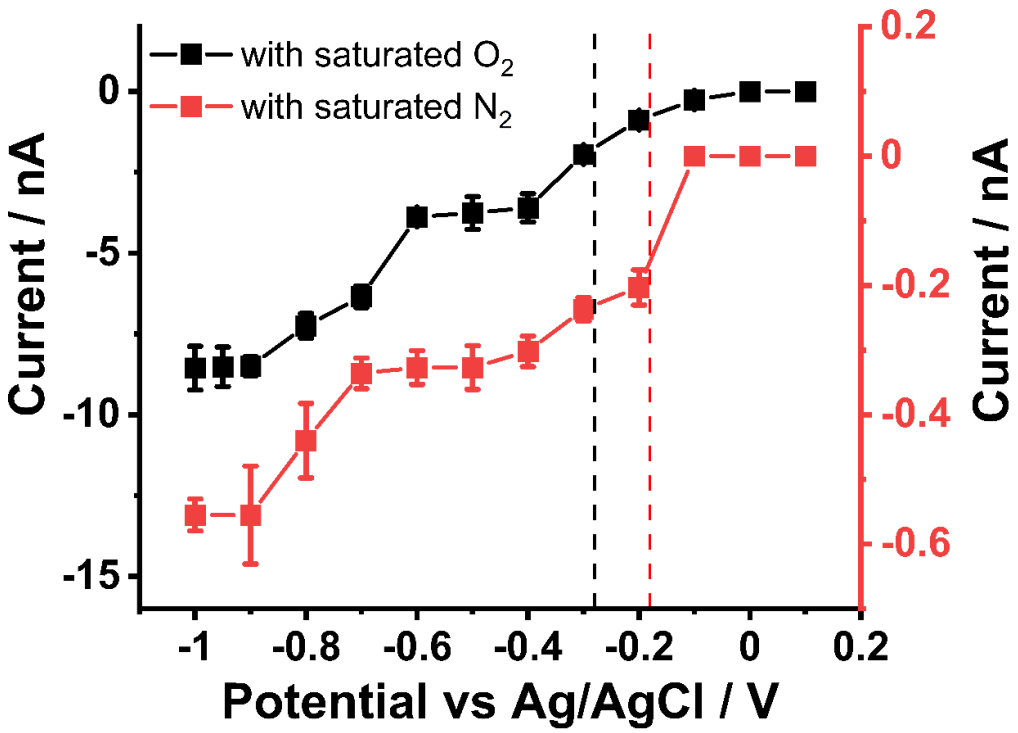


Fig.A6.14 Potential dependence of the average impact currents in the presence of 0.001 g L^{-1} MWCNTs in a 0.1 M KOH solution with saturated N_2 or O_2. The vertical dashed lines represent the half-wave potential for quinone reduction (red) and oxygen reduction (black) respectively.

Section A6.11: Calculation of the transport limited current for single carbon nanotubes

To interpret the single nano-imapct events we approximately view the impacted MWCNT as a cylindrical electrode with uniform diffusional access to its surface to which the transport limited current is given by Szabo et al.[41]:

$$I_{lim} = (2\pi nFD_0C_0l) \times f(\tau) \quad \text{(A6.2)}$$

with

$$f(\tau) = \frac{2e^{-\sqrt{\pi\tau}/20}}{\sqrt{\pi\tau}} + \frac{1}{\ln[(e^{-\gamma}\tau)^{0.5} + e^{5/3}}$$

$$\tau = \frac{4D_0 t}{r_0^2}$$

where n is the number of electrons transferred, F is the Faraday constant (96485 C mol^{-1}), D_0 is the diffusion coefficient (1.9×10^{-9} $m^2 \cdot s^{-1}$ [46]) for O_2 in 0.1 M KOH (298K), C_0 is the saturated concentration of O_2 in 0.1 M KOH (1.21 mM [46]) and *l* is the CNT length (20 μm) and r_0 is the CNT radius (15 nm), t is the average step or spike duration time (s), γ = 0.5772156.

Assuming a two-electron reduction process occurring on a single nanotube (n=2), the limiting current (I_{lim}) is derived to be 8.1 nA based on the average duration time (t) of 0.065 s.

References

1. Y. Lu, X. Li and R. G. Compton, *The Journal of Physical Chemistry Letters*, 2022, **13**, 3748-3753.
2. A. Ajanovic and R. Haas, *Energy Policy*, 2018, **123**, 280-288.
3. S. Chu, Y. Cui and N. Liu, *Nature materials*, 2017, **16**, 16-22.
4. A. Kulkarni, S. Siahrostami, A. Patel and J. K. Norskov, *Chem Rev*, 2018, **118**, 2302-2312.
5. Z. W. Seh, J. Kibsgaard, C. F. Dickens, I. Chorkendorff, J. K. Nørskov and T. F. J. S. Jaramillo, *Science*, 2017, **355**, 4998.
6. E. Yeager, *Electrochimica acta*, 1984, **29**, 1527-1537.

7. J. Masa, W. Xia, M. Muhler and W. Schuhmann, *Angewandte Chemie International Edition*, 2015, **54**, 10102-10120.
8. R. Taylor and A. Humffray, *J Electroanal Chem Interfac Electrochem*, 1975, **64**, 63-84.
9. H. S. Wroblowa and G. Razumney, *J Electroanal Chem Interfac Electrochem*, 1976, **69**, 195-201.
10. H. Zhang, C. Lin, L. Sepunaru, C. Batchelor-McAuley and R. G. Compton, *Journal of Electroanalytical Chemistry*, 2017, **799**, 53-60.
11. S. Shanmugam and A. Gedanken, *J Phys Chem B*, 2006, **110**, 2037-2044.
12. P. J. Britto, K. S. Santhanam, A. Rubio, J. A. Alonso and P. M. Ajayan, *Adv Mater*, 1999, **11**, 154-157.
13. K. Gong, F. Du, Z. Xia, M. Durstock and L. Dai, *science*, 2009, **323**, 760-764.
14. Y. J. Sa, C. Park, H. Y. Jeong, S. H. Park, Z. Lee, K. T. Kim, G. G. Park and S. H. Joo, *Angewandte Chemie*, 2014, **126**, 4186-4190.
15. B. H. Suryanto, S. Chen, J. Duan and C. Zhao, *ACS Appl Mater Inter*, 2016, **8**, 35513-35522.
16. C. Hu and L. Dai, *Angewandte Chemie International Edition*, 2016, **55**, 11736-11758.
17. M. Pumera, *Chemistry*, 2009, **15**, 4970-4978.
18. K. Tammeveski, K. Kontturi, R. J. Nichols, R. J. Potter and D. J. Schiffrin, *Journal of Electroanalytical Chemistry*, 2001, **515**, 101-112.
19. L. M. Gilbertson, D. G. Goodwin Jr, A. D. Taylor, L. Pfefferle and J. B. Zimmerman, *Environ Sci Technol*, 2014, **48**, 5938-5945.
20. X. Li, C. Batchelor-McAuley, S. A. Whitby, K. Tschulik, L. Shao and R. G. Compton, *Angew Chem Int Ed Engl*, 2016, **55**, 4296-4299.
21. X. Li, C. Lin, C. Batchelor-McAuley, E. Laborda, L. Shao and R. G. Compton, *J Phys Chem Lett*, 2016, **7**, 1554-1558.
22. Y. Lu, X. Li and R. G. Compton, *Chemical Science*, 2022, **13**, 1355-1366.
23. J. Ellison, K. Tschulik, E. J. Stuart, K. Jurkschat, D. Omanovic, M. Uhlemann, A. Crossley and R. G. Compton, *ChemistryOpen*, 2013, **2**, 69-75.
24. G. Jürmann and K. Tammeveski, *Journal of Electroanalytical Chemistry*, 2006, **597**, 119-126.
25. J. Koehne, H. Chen, J. Li, A. M. Cassell, Q. Ye, H. T. Ng, J. Han and M. Meyyappan, *Nanotechnology*, 2003, **14**, 1239.
26. C. Bishop and L. Tong, *Tetrahedron lett*, 1964, **5**, 3043-3048.
27. C. Bishop and L. Tong, *J Am Chem Soc*, 1965, **87**, 501-505.

28. S. I. Bailey and I. M. Ritchie, *Electrochimica Acta*, 1985, **30**, 3-12.
29. M. Quan, D. Sanchez, M. F. Wasylkiw and D. K. Smith, *J Am Chem Soc*, 2007, **129**, 12847-12856.
30. K. Lin, Q. Chen, M. R. Gerhardt, L. Tong, S. B. Kim, L. Eisenach, A. W. Valle, D. Hardee, R. G. Gordon and M. J. Aziz, *science*, 2015, **349**, 1529-1532.
31. Y. O. Kim, Y. M. Jung, S. B. Kim and S. M. Park, *Anal Chem*, 2004, **76**, 5236-5240.
32. X. Zhao, H. Imahori, C. Zhan, Y. Sakata, S. Iwata and T. Kitagawa, *J Phys Chem A*, 1997, **101**, 622-631.
33. M. Gómez, F. J. González and I. González, *Electroanalysis*, 2003, **15**, 635-645.
34. R. T. Kachoosangi, G. G. Wildgoose and R. G. Compton, *Anal Chim Acta*, 2008, **618**, 54-60.
35. A. T. Masheter, P. Abiman, G. G. Wildgoose, E. Wong, L. Xiao, N. V. Rees, R. Taylor, G. A. Attard, R. Baron, A. Crossley, J. H. Jones and R. G. Compton, *Journal of Materials Chemistry*, 2007, **17**.
36. A. D. Pendergast, C. Renault and J. E. Dick, *Anal Chem*, 2021, **93**, 2898-2906.
37. J. Baxendale, M. Ward and P. Wardman, *Trans Faraday Soc*, 1971, **67**, 2532-2537.
38. I. Streeter, G. G. Wildgoose, L. Shao and R. G. Compton, *Sensors and Actuators B: Chemical*, 2008, **133**, 462-466.
39. G. P. Keeley and M. E. Lyons, *Int. J. Electrochem. Sci*, 2009, **4**, 794-809.
40. M. J. Sims, N. V. Rees, E. J. Dickinson and R. G. Compton, *Sensor Actuat B-Chem*, 2010, **144**, 153-158.
41. A. Szabo, D. K. Cope, D. E. Tallman, P. M. Kovach and R. M. Wightman, *J Electroanal Chem Interfac Electrochem*, 1987, **217**, 417-423.
42. J. Ellison, C. Batchelor-McAuley, K. Tschulik and R. G. Compton, *Sensors and Actuators B: Chemical*, 2014, **200**, 47-52.
43. I. Kruusenberg, N. Alexeyeva and K. Tammeveski, *Carbon*, 2009, **47**, 651-658.
44. K. Tammeveski, K. Kontturi, R. J. Nichols, R. J. Potter and D. J. Schiffrin, *J Electroanal Chem*, 2001, **515**, 101-112.
45. R. Guidelli, R. G. Compton, J. M. Feliu, E. Gileadi, J. Lipkowski, W. Schmickler and S. Trasatti, *Pure and Applied Chemistry*, 2014, **86**, 245-258.
46. R. E. Davis, G. L. Horvath and C. W. Tobias, *Electrochimica Acta*, 1967, **12**, 287-297.

Chapter 7

Does Nitrogen Doping Enhance the Electrocatalysis of the Oxygen Reduction Reaction by Multiwalled Carbon Nanotubes?

Chapter 7 reports the oxygen reduction reaction (ORR) from the perspective of electrocatalysis by multiwalled carbon nanotubes (MWCNTs) and amino-functionalized multiwalled carbon nanotubes (MWCNTs-NH_2) at the single entity level under alkaline conditions. As introduced in **Chapter 6**, the study of electrocatalytic ORR at single carbon nanotubes has been shown to be feasible via the single entity approach.

It is often believed that doping with Nitrogen (N) can improve the catalytic performance of carbon nanotubes (CNTs) for the ORR. Therefore, the main purpose of this work is to clarify whether the introduction of N is helpful for CNT-based ORR catalysts. For this purpose, single entity measurements are used to avoid the ambiguities of using composites as in previous reports which came to conflicting conclusions [1]. It is found that the surface quinone groups in both types of CNTs are responsible for promoting the reduction from oxygen to hydrogen peroxide and the key difference between the two types of CNTs is that catalytic behaviour more reflects the relative quinone populations on the two types of tube rather than the N content.

The work of **Chapter 7** has been accepted by *ACS Catalysis* and was carried out in collaboration with Dr. Xiuting Li (Shenzhen University) and Archana Kaliyaraj Selva Kumar (University of Oxford). Dr. Xiuting Li helped with the interpretation of the experimental results and Archana Kaliyaraj Selva Kumar conducted the scanning electron microscopy analysis.

7.1 Introduction

The oxygen reduction reaction (ORR) plays an essential role in achieving a desirable performance at the cathode of fuel cells [2] and metal-air batteries [3]. The ORR can proceed either through a highly efficient four-electron process to form H_2O/OH^- directly or a less efficient

two-step, two-electron pathway involving the formation of H_2O_2/HO_2^- as an intermediate in acidic or alkaline conditions respectively [4]. In the past several decades, Platinum (Pt)-based catalysts have been utilized to improve the reaction kinetics of the ORR [5, 6]. However, considering the great expense, short durability [7] and susceptibility to deactivation [8] of Pt, the study of low-cost carbon-based metal-free materials as ORR electrocatalysts to replace Pt in fuel cells has grown worldwide [9].

Among these carbon based materials, carbon nanotubes (CNTs) have become interesting due to their high specific surface area, chemical stability [10, 11] , and often abundant active sites [12, 13] including edge plane like defects and oxygen functionality such as quinones that are involved in the reduction of oxygen forming peroxide [14, 15]. Impactfully, Dai et.al [16] reported that nitrogen-doped carbon nanotube arrays demonstrated superior electrocatalytic activity than Pt for the ORR in alkaline media and there has been suggestions that the ORR electrochemical activity mostly comes from doped impurities such as nitrogen (N) [17], sulphur (S) [18], phosphate (P) [19] and not from the pristine carbon material. This issue has been partly revolved by the defect mechanism of carbons proposed by Zhao et.al [20] that the removal of N atoms from graphene could create catalytically active defects contributing to the higher ORR activity. On the other hand, similar catalytic voltammetric responses for the ORR at non-doped and N-doped carbon nanofiber (CNF) electrodes under alkaline conditions (pH > 10) was observed. It was inferred that the N-doped CNFs hindered the superoxide radical anion ($O_2^{\cdot-}$) adsorption process so as to limit the rate of in-situ hydrogen peroxide (HO_2^-) generation [21]. Composites of the CNTs, either undoped or doped were used in previous studies. The complexity of unscrambling mechanistic detail from such porous layers is well documented [22, 23]. So to better clarify the benefits, if any of N doping of CNTs for promoting carbon based materials for the ORR, multiwalled carbon nanotubes (MWCNTs) and amino-functionalized multiwalled carbon

nanotubes (MWCNTs-NH_2) were studied as catalysts for the ORR at the single entity level [24, 25] in this paper.

In previous studies as reported in Chapter 6, the electrocatalytic behaviour of MWCNTs for the ORR in aqueous base using single entity electrochemistry techniques has been shown to be feasible [26, 27]. These experiments employed a microelectrode in a suspension of CNTs which by virtue of their Brownian motion impact the electrode randomly allowing voltammetric interrogation of the single tube in the medium of interest during the period, often just 10s of milliseconds, in which the tube is in electrical contact with the electrode. In the following, we used the nano-impact experiment to compare the electrocatalytic behaviour of MWCNTs and MWCNTs-NH_2 towards ORR to seek clear evidence about the role of N substitution in promoting, or otherwise, the ORR (Fig.7.1).

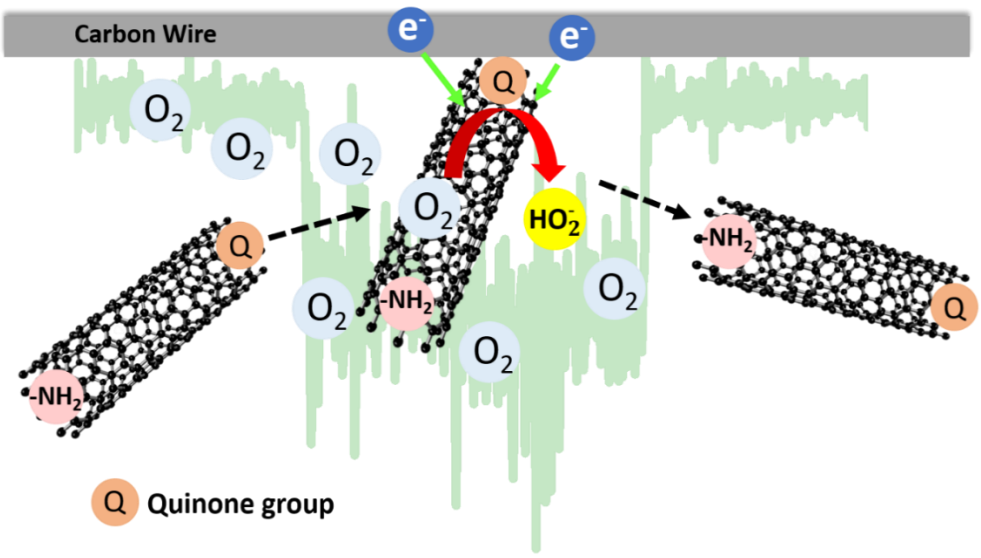


Figure.7.1 A schemic diagram for the oxygen reduction reaction studied at the single entity level in the presence of MWCNTs-NH_2.

7.2 Experimental

Details of the characterisation of the MWCNTs and MWCNTs-NH_2 are presented in Section 2.1. The scanning electron microscopy images (SEM) of the samples MWCNTs and MWCNTs-NH_2 are shown in Fig.7.2. Note that the two types of CNTs have similar external

surface areas per tube (~2×10^{-12} m^2) facilitating comparisons discussed below whilst the MWCNTs are formed of 9 concentric tubes [28], the MWCNTs-NH_2 are comprised of 6 [29].

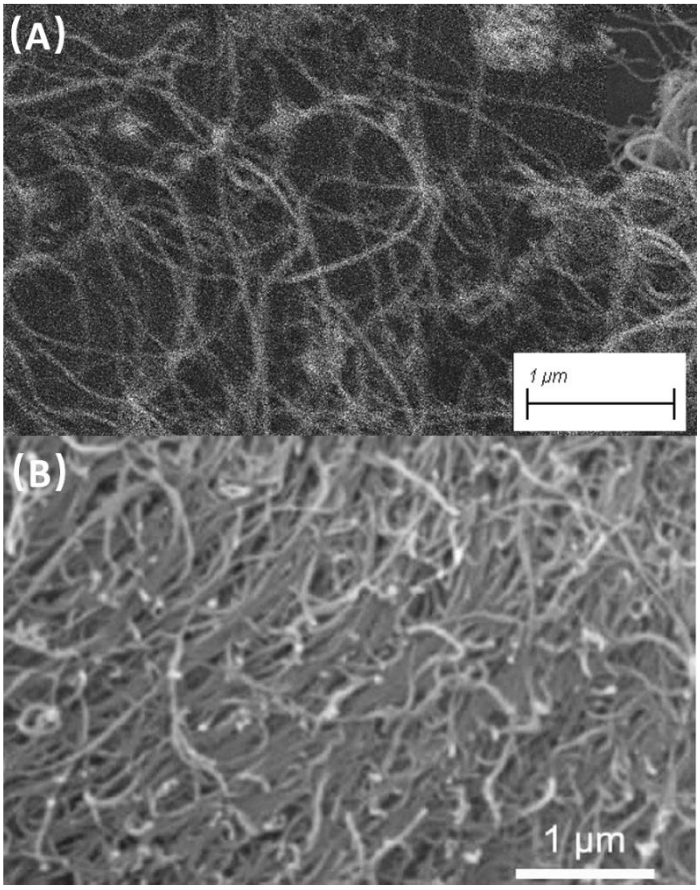


Figure.7.2 The scanning electron microscopy images of a typical single MWCNT [28] ***(A) and MWCNT-NH_2*** [29] ***(B).***

Cyclic voltammetry of MWCNTs or MWCNTs-NH_2 modified GCEs

By adding 0.5 mg of MWCNTs to 10 mL ethanol, a suspension of 0.05 g L^{-1} MWCNTs was prepared was prepared and then sonicated for 30 min in a Fisher Scientific FB15050 ultrasonic bath to get a well-dispersed solution. The freshly polished GCE was modified by drop-casting a 2 μL (0.1 μg of MWCNTs) suspension of MWCNTs and left to dry under vacuum. A similar procedure was used to prepare MWCNTs-NH_2 modified GCEs again with 0.1 μg of MWCNTs-NH_2 via drop casting.

Under degassed conditions, CVs were conducted using MWCNTs or MWCNTs-NH_2 modified GCE in 0.1 M KOH (pH=13.3) by sweeping the potential from 0 V to - 1.0 V to investigate possible surface functional groups on the MWCNTs and MWCNTs-NH_2. The voltammograms were recorded at scan rates varing from 10 to 25, 50, 100 and 200 mVs^{-1}.

For the cyclic voltammetric behavior of oxygen reduction, the as-prepared MWCNTs modified GCE or MWCNTs-NH_2 modified GCE were immersed in 0.1 M KOH. Prior to the measurements, the solution was bubbled with pure oxygen gas (O_2, BOC Gases plc, Guildford, UK) for 15 mins. The potential window was chosen to be 0 to -1.4 V and the voltammograms were conducted at different scan rates from 10 to 25, 50, 100 and 200 mVs^{-1}. A control experiment was also performed in the same solution but on a bare GCE.

Nano-impact experiments of MWCNTs or MWCNTs-NH_2

For single impact electrochemistry measurements of impact currents at various potentials in the range from 0.8 V to -1.0 V vs Ag/AgCl ("chronoamperometry") were made using a carbon micro-wire electrode (diameter = 7 μm, length = 1 mm) in 10 mL 0.1M KOH with 0.001 g L^{-1} dispersed MWCNTs after degassing with nitrogen for 15 minutes. The fabrication of method of carbon fibre micro-wire electrodes is described in Section 2.2. An atmosphere of nitrogen was maintained during the experiments.

The measurements of current for the ORR on single carbon nanotube were based on the general method reported [31, 32] previously. At various potentials in the range from 0.1 V to -1.0 V vs Ag/AgCl, chronoamperometry were performed using carbon micro-wire electrode on 0.1 M KOH aqueous solution after bubbling with O_2 for 15 minutes. Then 0.001 g L^{-1} solution dispersed MWCNTs were added. Control experiments were conducted in the presence of a MWCNTs-NH_2 suspension of the same concentration. The data analysis program "Signal Counter" (Centre for Marine and Environmental Research, Zagreb, Croatia)[33] and Origin Pro 2020 were employed for impact signal identification and analysis.

7.3 Results and Discussion

7.3.1 Cyclic Voltammetry (CV) of MWCNTs or MWCNTs-NH_2 in the absence of oxygen

The electrochemical reductions of MWCNTs and MWCNTs-NH_2 in degassed 0.1 M KOH aqueous solution (pH=13.3) were explored using cyclic voltammetry (CV) at a freshly polished glassy carbon electrode (GCE) modified with 0.1 μg MWCNTs or MWCNTs-NH_2 respectively. The coverages used correspond to *ca.* monolayer coverage assuming the CNTs to be uniformly spread and arranged in a closed pack manner (see Section A7.1); in reality the CNTs will aggregate, distribute heterogeneously [34] and locally form thicker and randomly oriented layers (Fig.A7.1). The voltammetry is illustrated in Fig.7.3(A). A single reductive peak appeared at -0.38 ± 0.03 V and -0.37 ± 0.01 V vs Ag/AgCl ($[Cl^-]$= 3.5 M) for the MWCNTs modified GCE (red line) and MWCNTs-NH_2 modified GCE (blue line), while which is not observed at bare GCE (black line) at a scan rate of 50 mVs^{-1}. The reduction is assigned to surface quinones (and/or possibly other oxygen functionality) present in the CNTs as previously reported [35]. Meanwhile the reductive peak currents for both types of CNT showed a linear scan rate dependence as shown in Fig.7.3(B) consistent with the voltammetry of a surface immobilised entity. The peak from the MWCNTs modified GCE displays obviously larger cathodic currents compared to that from MWCNTs-NH_2 modified GCE, suggesting a greater quantity of quinones on the drop-casted MWCNTs since comparable numbers of CNTs are drop-casted in each case (7.7×10^6 MWCNTs and 1.8×10^7 MWCNTs-NH_2 covered on the electrode surface separately, see Section A7.1). The reductive voltammetry at both types of modified GCE is chemically irreversible (Fig.A7.3), especially for MWCNTs-NH_2, where the quinone signal was completely eliminated in subsequent scans.

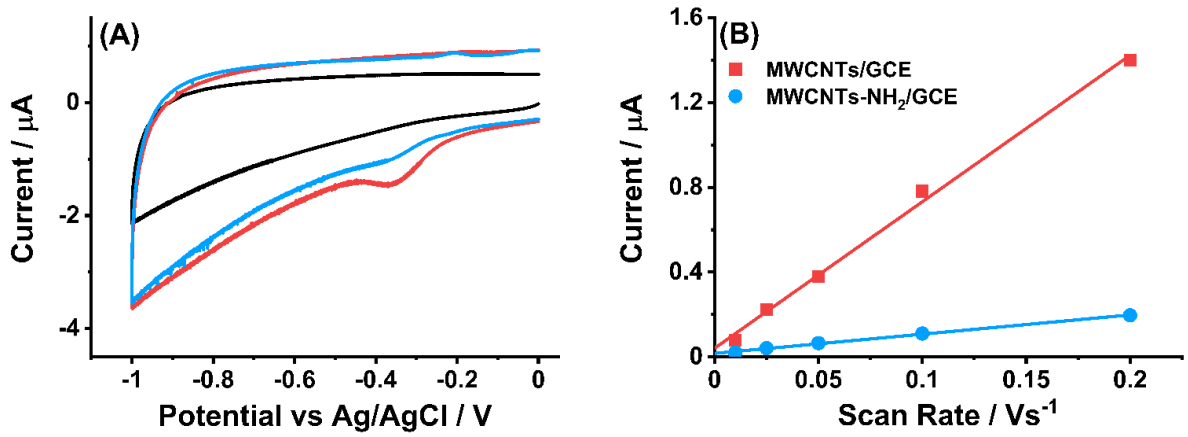


Figure.7.3 (A) Cyclic voltammograms measured at a bare GCE (black line) and polished GCE modified with 0.1 µg MWCNTs (red line) or 0.1 µg MWCNTs-NH_2 (blue line) in the potential window from 0 V to -1.0 V at a scan rate of 50 mVs^{-1} in nitrogen saturated 0.1 M KOH solution; (B) A comparison of the reductive peak current observed at MWCNTs/GCE and MWCNTs-NH_2/GCE as a function of scan rate at 10, 25, 50, 100 and 200 mVs^{-1} (The cyclic voltammograms of MWCNTs/GCE and MWCNTs-NH_2/GCE at various scan rates are shown in Fig.A7.2 respectively and the baseline subtraction process is shown in Fig.A7.4).

7.3.2 Nano-impact experiments of single CNTs in the absence of oxygen

The electro-reduction kinetics of MWCNTs and MWCNTs-NH_2 was further studied using single entity electrochemistry with a carbon wire microelectrode. To analyse the average current height of the impact signal as a function of potential in the presence of 0.001 g L^{-1} MWCNTs or MWCNTs-NH_2 in a nitrogen-saturated 0.1 M KOH solution, at least 10 chronoamperometric scans were run to record the clear impact steps for each applied potential within the range from 0 to -1.0 V. As shown in Fig.7.4 (A), the appearance of the reductive step features in the representative case shown for - 0.4 V reflected the random arrival and loss of the MWCNT particles at the electrode surface with an average residence time of 0.024 ± 0.005 s. Analogous nano-impact experiments towards MWCNTs-NH_2 also demonstrated clear reductive steps at the same potential but with a similar duration time (0.020 ± 0.005 s) (Fig.7.4(B)). In the absence of both CNTs, the chronoamperometric current showed no impact

signals, only a monotonic decay first and levelled off gradually as an indicative of the capacitive charging of the electrode (black line in Fig.7.4 (A) and (B)).

The average impact current at different potentials for both MWCNTs and MWCNTs-NH_2 were calculated from at least 40 samples per potential and plotted against the applied potential (Fig. 7.4(C)). For potentials more positive than -0.1 V, no reductive impacts were seen. Two current plateaus on both types of CNTs are observed, the first in the potential range from -0.4 V to -0.6 V and the second at potentials more negative than -0.9 V. The comparison of average current heights for the MWCNTs and MWCNTs-NH_2 at those plateaus are obvious: for MWCNTs, an average reductive current height of *ca*. 0.32 ± 0.03 nA at the first plateau and *ca*. 0.55 ± 0.03 nA at the second plateau was estimated; while for MWCNTs-NH_2, two relatively smaller values of *ca*. 0.17 ± 0.02 nA and *ca*. 0.45 ± 0.06 nA respectively reflected the current response at two plateaus respectively. An enhanced number of reductive quinone groups ~3.3×10^{14} molecules per cm^2 of MWCNTs external surface was calculated from its average impact charge (2.0 ± 0.3 pC) in the first wave relative to the value (~ 2.4×10^{14} molecules per cm^2) for single MWCNTs-NH_2 (see Section A7.3) assuming a two-electron process, supporting the difference in peak height from CV for ensembles of MWCNTs and MWCNTs-NH_2. Note that the high approximate coverages inferred indicate a contribution to the signal from some CNT aggregates. Also, it is interesting to observe that only the first single entity 'wave' appears as the single reductive peak in the CV of the modified GCEs, the absence of the second reductive peak in the CV likely results from depletion of active surface bound species as a result of the chemical irreversibility of the first reduction (see above). As inferred from both ensemble and single entity electrochemistry above, and building on earlier literature [36], the two-step features in the nano-impact experiments are suggested to relate to the formation of semi-quinones ($Q^{\cdot -}$) and quinone di-anions (Q^{2-}):

First reduction:

$$Q + e^- \rightleftharpoons Q^{\cdot -} \tag{7.1}$$

Second reduction:

$$Q + 2e^- \rightarrow Q^{2-} \tag{7.2}$$

Overall the single entity data in the absence of oxygen suggests the presence of greater surface oxygen functionality on the MWCNTs than that present on the corresponding amino functionalised analogues. We next turn to the single entity response in the presence of oxygen.

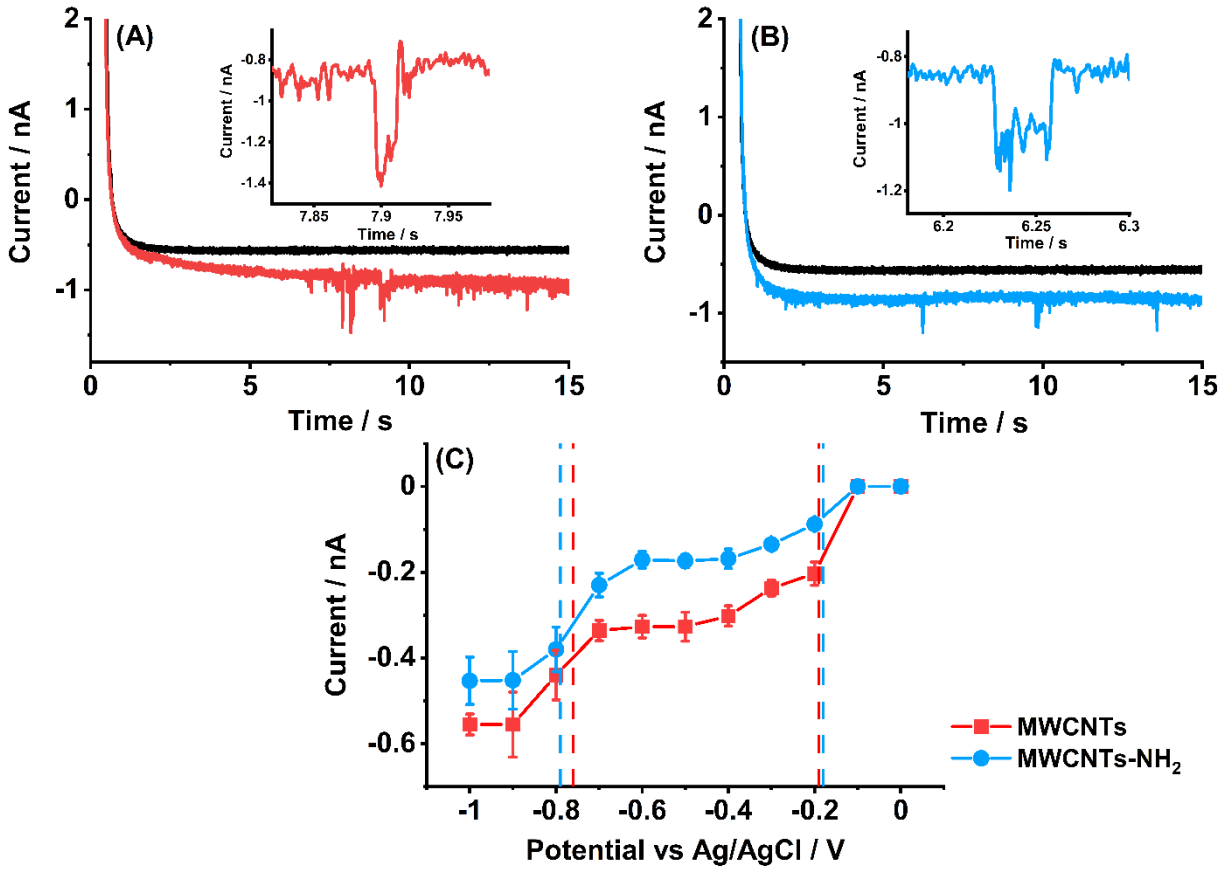


Figure.7.4 Representative chronoamperometric curves presenting reductive step signals at -0.4 V vs Ag/AgCl in nitrogen degassed 0.1M KOH in the presence of 0.001 gL^{-1}MWCNTs (A, red line), 0.001 gL^{-1}MWCNTs-NH$_2$ (B, blue line) and absence of both CNTs (black line). The inset shows enlargements of individual step; (C) Plot of corresponding average step current produced by the collision of MWCNTs or MWCNTs-NH$_2$ on the carbon microwire electrode against the applied potential from 0 to -1.0 V (The error bars represent the average of at least

40 separate impacts for each potential). Vertical lines represent the half-wave potential ($E_{1/2}$) at each step in the presence of MWCNTs (red dotted line) or MWCNTs-NH_2 (blue dotted line).

7.3.3 CV of the ORR at MWCNTs and MWCNTs-NH_2

Next, the investigation of the ORR at the MWCNTs and MWCNTs-NH_2 was conducted by drop-casting two types of material with an amount of 0.1 µg onto a freshly polished GCE. As shown in Fig 7.5, in oxygen-saturated 0.1 M KOH, similar voltammetric features were observed on all three electrodes: a bare GCE, MWCNTs or MWCNTs-NH_2 modified GCEs recorded in the potential window from 0 V to -1.4 V vs Ag/AgCl were two reductive peaks at -0.58 ± 0.01 V ($Peak_1$) and -0.82 ± 0.05 V ($Peak_2$). The voltammetric behaviour of both peaks on bare GCE reflects an overall two-electron reduction from oxygen to peroxide due to the formation of surface adsorbed hydroperoxide species at high pH as described in previous studies [37, 38]. Compared with bare GCE, the CV response of two modified GCEs demonstrated higher currents for $Peak_1$, with the MWCNTs modified GCE showing the largest current for both peaks. The peak current of $Peak_1$ and $Peak_2$ obtained from MWCNTs/GCE and MWCNTs-NH_2/GCE were respectively studied as a function of scan rate where both magnitudes were found to scale linearly with the scan rate in a logarithmic scale (Fig. A7.5) as an indicative of diffusional responses. Therefore, the observations for the enhanced peaks may be caused by the change in diffusion from semi-infinite at the bare electrode to thin-layer with the porous layer formed by drop-casting carbon nanotubes on the electrode surface. Focusing on $Peak_1$ by narrowing the sweeping potential range to -0.7 V, as shown in the inlay of Fig.7.5, the signal at the MWCNTs/GCE showed a slightly lower peak potential (E_{c1} =-0.50 ± 0.01 V) than seen at the MWCNTs-NH_2/GCE (E_{c2}= -0.56 V± 0.04 V), suggesting a possibly enhanced catalytic ability of MWCNTs.

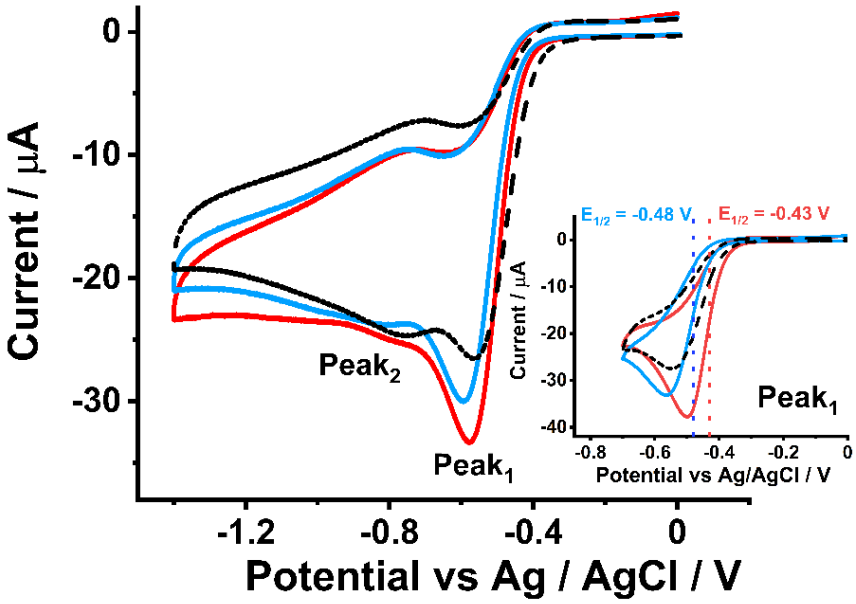


Figure.7.5 Cyclic voltammograms of the bare GCE (black dotted line), MWCNTs modified GCE (red dashed line) and MWCNTs-NH_2 (blue dashed line) in oxygen-saturated 0.1 M KOH, scan rate = 50 mVs^{-1}. Inset: the CV scanned from 0 to -0.7 V, vertical dotted line represents the half-wave ($E_{1/2}$) for the ORR in the presence of MWCNTs (red) or MWCNTs-NH_2 (blue).

7.3.4 Single Particle Electrochemistry of the ORR at MWCNTs or MWCNTs-NH_2

Having compared the catalytic ability of the MWCNTs and MWCNTs-NH_2 towards ORR in the ensemble electrochemistry, single entity experiments were then conducted to investigate this catalysis on both types of individual CNT particles. A clean carbon fibre microwire electrode (diameter ca.7 μm and length ca. 1mm) was inserted into oxygen-saturated 0.1 M KOH solution containing 0.001 g L^{-1} MWCNTs or MWCNTs-NH_2, then applying the chronoamperometric scans at -0.4 V vs Ag/AgCl, clear reductive steps were seen and associated with the ORR catalysed by a single MWCNT (orange line in Fig.7.6(A)) or MWCNT-NH_2 (green line in Fig.7.6(A)) randomly impacting on the electrode surface with different average residence time of 0.083 ± 0.016 s and 0.043 ± 0.015 s respectively. The average impact current (3.6 ± 0.4 nA from 43 impacts) for the MWCNTs particle was higher than the value (1.8 ± 0.2

nA from 40 impacts) for the MWCNTs-NH_2 particle. In the absence of any CNT particles, only capacitive charging of the underlying microwire electrode was observed (Fig.A6.6).

Further, impacts for the ORR facilitated by the MWCNTs or MWCNTs-NH_2 were explored at various potentials from 0.1 V to -1.0 V. The representative chronoamperometric curves recorded at -1.0 V for MWCNTs and MWCNTs-NH_2 are shown in Fig.A7.6(B). Plotting the measured average Faradaic current for each CNT against the corresponding applied potential (Fig.A7.7), two plateaus were seen reflecting the current-potential characteristics for the ORR at either MWCNTs or MWCNTs-NH_2. The average currents at the two plateaus were 3.7 nA and 8.6 nA for MWCNTs whilst lower values were seen at single MWCNTs-NH_2 namely 2.7 nA and 7.2 nA. A cylindrical electrode geometry was used to approximate the diffusion limiting current flowing on a single CNT tube for the ORR. Assuming an overall two-electron process, this value was estimated to be ~8 nA for MWCNTs and ~ 18 nA for MWCNTs-NH_2 (Section A7.6) with the chemistry assumed to be [38]

First reduction:

$$\boldsymbol{Q + e^- \rightleftharpoons Q^{\cdot -}} \tag{7.3}$$

$$\boldsymbol{Q^{\cdot -} + O_2\,(aq) \rightarrow Q \cdot O_2^{\cdot -}} \tag{7.4}$$

$$\boldsymbol{Q \cdot O_2^{\cdot -} + H_2O + e^- \rightarrow Q + HO_2^- + OH^-} \tag{7.5}$$

Second reduction:

$$\boldsymbol{Q + 2e^- \rightarrow Q^{2-}} \tag{7.6}$$

$$\boldsymbol{Q^{2-} + O_2 + H_2O \rightarrow Q + HO_2^- + OH^-} \tag{7.7}$$

The values of the plateau currents suggest that reduction via the di-anion route brings about the ORR at a rate which is close to the diffusion-controlled reduction of oxygen. In contrast, the amino derivatised CNTs are less effective; as discussed above, the latter contain less quinone functionality. Meanwhile in the single entity 'voltammograms', the halfwave potentials for the first wave were -0.28 ± 0.02 V and -0.36 ± 0.005 V for MWCNTs and MWCNTs-NH_2 which

are cathodic of the consistent values of -0.19 ± 0.01 V seen in the absence of oxygen. The cathodic shift in the presence of oxygen suggests that the oxygen complexes with the quinone before the electrochemically reversible electron transfer. The more anodic value seen for the MWCNTs compared to the MWCNTs-NH_2 is consistent with the greater catalytic activity of the former. Based on the analysis of the reductive signals from both the ensemble and the single entity data in the presence of oxygen, all results evidenced that the addition of N contents to carbon nanotubes played little role in improving ORR activity which mainly depended on the oxygen functionality at carbon materials.

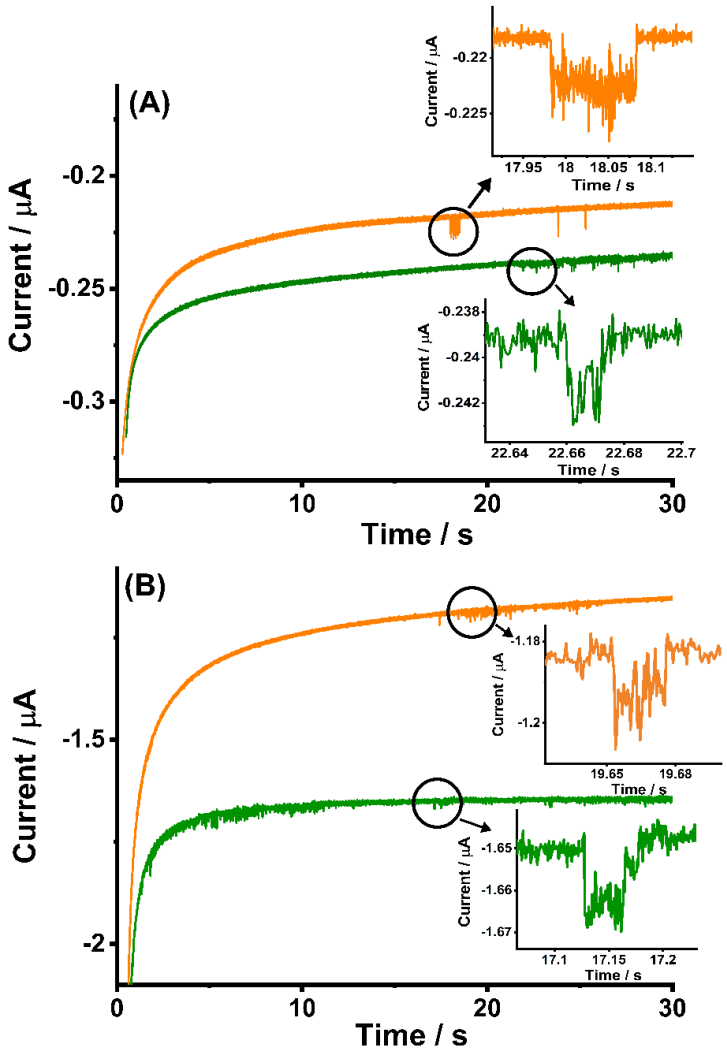


Figure.7.6 Representative Chronoamperometric profiles showing impact signals in oxygen-saturated 0.1 M KOH at -0.4 V (A) or -1.0 V vs Ag/AgCl with presence of 0.001 g MWCNTs (orange line) or MWCNTs-NH_2 (blue line) (Inlay: corresponding enlarged impact steps).

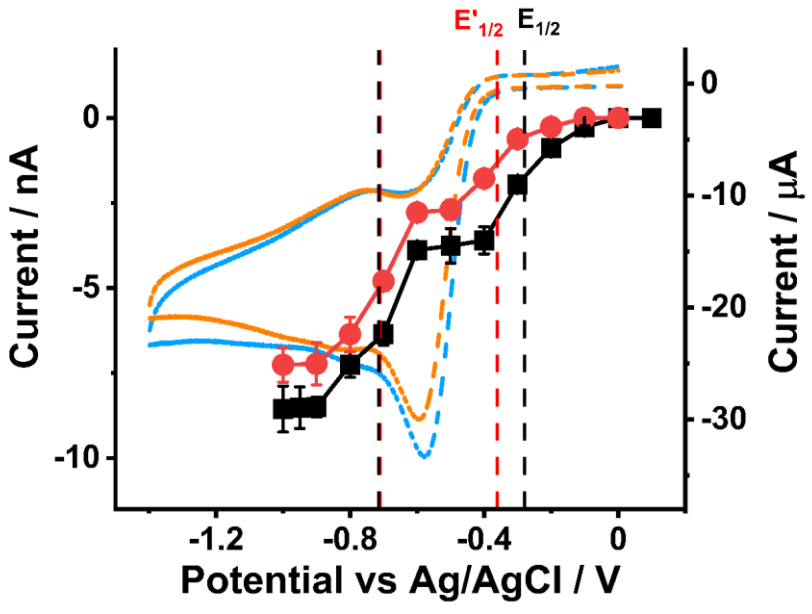


Figure.7.7 Potential dependence of the average impact currents for oxygen reduction reaction catalysed by MWCNTs (black dots) or MWCNTs-NH_2 (red dots) using carbon wire, shown for comparison is a CV recorded at a MWCNTs modified GCE (blue line) and MWCNTs-NH_2 modified GCE (orange line) for ORR at a scan rate of 50 mVs^{-1}. Vertical dashed lines represent the half-wave potential ($E_{1/2}$) at each step in the presence of MWCNTs (black dotted line) or MWCNTs-NH_2 (red dotted line).

7.4 Conclusions

In this chapter, the electrocatalysis of the ORR by virtue of MWCNTs or MWCNTs-NH_2 has been compared using single entity and ensemble electrochemistry, showing the role of surface oxygen functionality to facilate peroxide formation from oxygen in alkaline media.. MWCNTs are an often considered electrocatalyst for the ORR which is important as the basis of the cathodic reaction in many energy transformation devices based on their abundant active sites including structural defects and oxygen functionality. Although the doping of Nitrogen content was reported to be able to improve the catalytic performance of CNTs for the ORR, the work in this chapter shows that the functionalization with surface amino groups is less important than the presence of quinone groups for ORR electrocatalysis.

Appendix

Section A7.1：Estimation of minimum number of layers of MWCNTs or MWCNTs-NH2 drop-casted on the GC electrodes

The minimum numbers of layers of MWCNT and MWCNTs-NH_2 drop-casted on the bare GC electrode were estimated assuming the rectangular-shape carbon nanotubes to be laid uniformly across the whole GC surface in a closed pack manner. According to the parameters (diameter and length) of MWCNTs and MWCNTs-NH_2 provided in Section 2.1:

For MWCNTs:

The area covered by one MWCNT (S_{CNT}):

$S_{CNT} = 3\times10^{-6} \times 2\times10^{-3} = 6 \times10^{-9}$ cm^2,

where the diameter and length of MWCNTs is ca. 30 nm and ca. 20 μm respectively.

The modification mass (m_{CNT}) of 2 μL 0.05 gL^{-1} MWCNTs on the bare GC electrode:

$m_{CNT} = 2\times10^{-6}\times0.05 = 1\times10^{-7}$ g

The number of MWCNTs (N_{MWCNT}) modified on the surface of modified GCE:

$N_{MWCNT}=1\times10^{-7}$ g / 1.3×10^{-14} g = 7.7×10^{6}

(the mass per carbon tube is 1.3×10^{-14} g [39] with 9 concentric tubes inside)

Hence, the total area (S_{total}) covered by 7.7×10^{6} MWCNTs:

$S_{total} = 6 \times10^{-9}$ $cm^2 \times 7.7\times10^{6} = 0.046$ cm^2

The surface area of GC electrode (A):

$A = (\pi D^2) / 4 = 7.1\times10^{-2}$ cm^2

where the diameter of GC electrode (D) is 3.02 ± 0.005 mm

The number of monolayers of MWCNTs for 2 μL 0.05 gL^{-1} MWCNTs drop cast

$N_{layer} = \frac{S_{total}}{A} = 0.046$ cm^2 / 0.07 $cm^2 \approx 0.65$

For MWCNTs-NH_2:

The area covered by one MWCNT-NH_2 ($S_{CNT\text{-}NH2}$):

$S_{CNT\text{-}NH2} = 1.5\times10^{-6} \times 5\times10^{-3} = 7.5 \times10^{-9}$ cm^2,

where the diameter and length of MWCNTs-NH_2 is ca. 15 nm and ca. 50 μm respectively.

The area (S_h) of one hexagon composed of six carbon atoms is

$S_h = 3\, d_{c\text{-}c}^{\,2} \times \frac{\sqrt{3}}{2} = 5.2 \times 10^{-16}$ cm^2,

where $d_{c\text{-}c}$ (= 0.1421 nm) is the length of the C-C bond

The area ($S_{total\text{-}NH2}$) in one single MWCNT-NH_2 with 6 concentric tubes [29]

$S_{total\text{-}NH2} = 6\times\pi\times1.5\times10^{-6} \times5\times10^{-3} = 1.4\times10^{-7}$ cm^2,

The number of carbon atoms per tube (N_C):

$N_C = 1.4 \times10^{-7}$ cm^2 / 5.2×10^{-16} cm^2 = 2.7×10^{8}

The mass per carbon tube ($w_{MWCNT\text{-}NH2}$):

$w_{MWCNT\text{-}NH2} = 2.7\times10^{8} \times2\times10^{-23}$ g = 5.4×10^{-15} g, where one Carbon atom mass $w_c = 2\times10^{-23}$ g

The modification mass ($m_{CNT\text{-}NH2}$) of 2 μL 0.05 gL^{-1} MWCNTs-NH_2 on the bare GC electrode:

$m_{CNT\text{-}NH2} = 2\times10^{-6}\times0.05 = 1\times10^{-7}$ g

The number of MWCNTs-NH_2 ($N_{MWCNT\text{-}NH2}$) modified on the surface of modified GCE:

$N_{MWCNT\text{-}NH2} = 1\times10^{-7}$ g / 5.4×10^{-15} g = 1.8×10^{7}

Hence, the total area (S'_{total}) covered by 1.8×10^{7} MWCNTs-NH_2:

$S'_{total} = 7.5 \times10^{-9}$ cm$^2\times 1.8\times10^{7} = 0.13$ cm^2

The number of monolayers of MWCNTs for 2 μL 0.05 gL^{-1} MWCNTs drop cast

$N'_{layer} = \frac{S'_{total}}{A} = 0.13$ cm^2 / 0.07 cm^2 ≈ 1.8



Figure.A7.1 Optical microscopy image of 0.1 µg MWCNT modified GCE.

Section A7.2: CV of MWCNTs or MWCNTs-NH_2 modified GCE under degassed conditions

Fig.A7.2 (A) and (B) demonstrated cyclic voltammograms of MWCNTs modified GCE and MWCNTs-NH_2 modified GCE at different scan rates from 10 to 25, 50, 100 and 200 mVs^{-1}. The reductive peak currents after baseline subtraction (Fig.A7.4) were found to have a linear relationship with scan rates as shown in Fig.7.3.

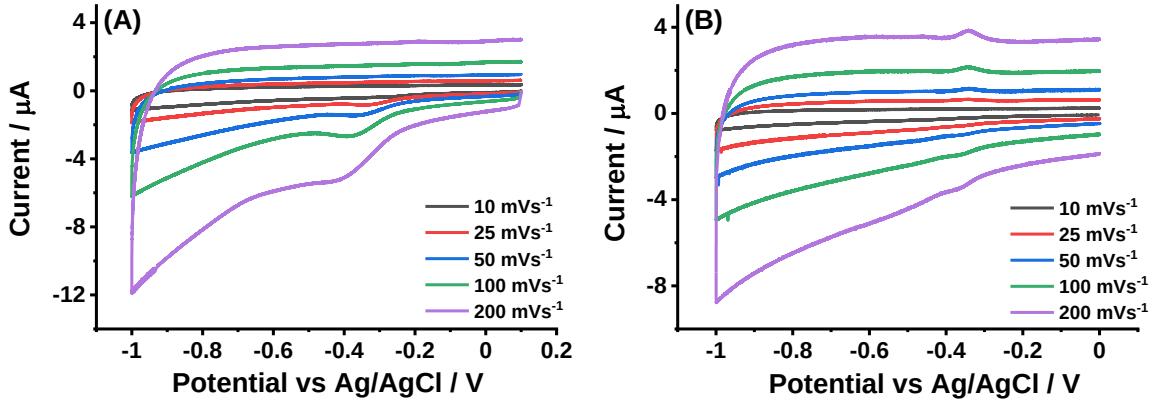


Figure.A7.2 Cyclic voltammograms of MWCNTs modified GCE (A) and MWCNTs-NH_2 modified GCE (B) at different scan rates from 10 to 25, 50, 100 and 200 mVs^{-1} in degassed 0.1 M KOH solution.

Voltammetry was scanned three times successively using the same MWCNTs or MWCNTs-NH_2 modified electrode in 0.1M KOH under nitrogen degassed condition. As shown

in Fig.A7.3 (A) and (B), each reductive peak was found to decay in subsequent scans after first scan.

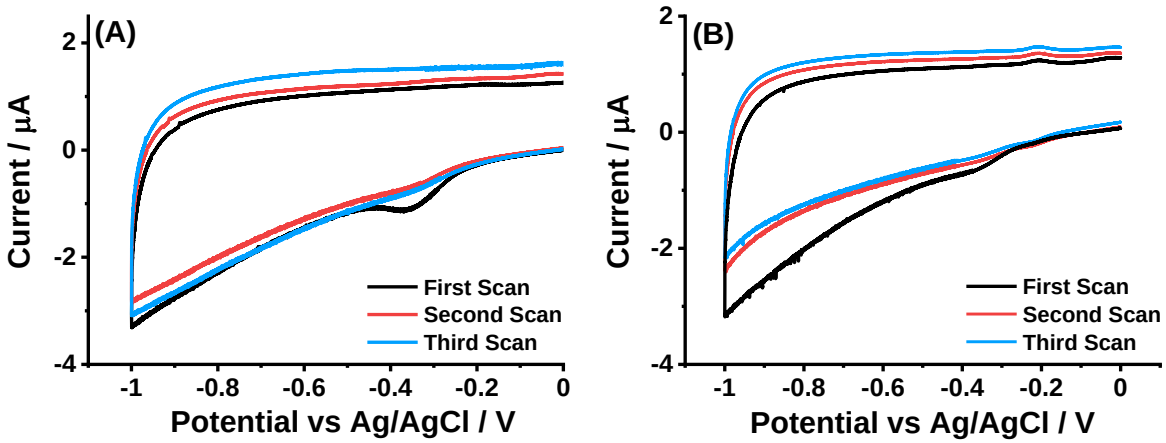


Figure.A7.3 Cyclic voltammograms of 0.1 µg MWCNTs or MWCNTs-NH_2 modified GCE in degassed 0.1 M KOH solution at a scan rate of 50 mVs^{-1} swept from 0 V to -1.0 V in three successive scans.

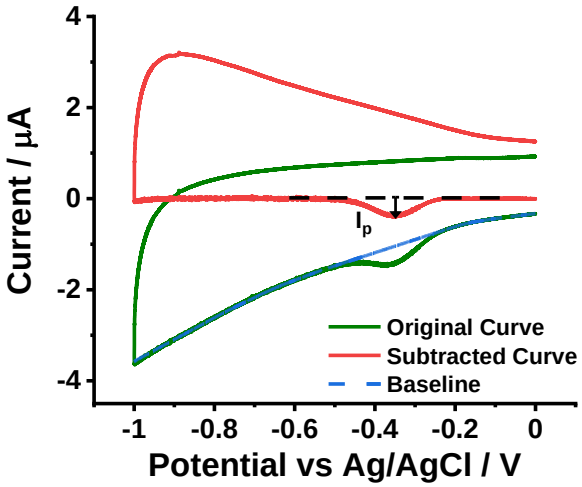


Figure.A7.4 the baseline subtraction process for cyclic voltammograms of 0.1 µg MWCNTs modified GCE swept forward to -1.0 V under degassed condition at a scan rate of 50 mV s^{-1}.

All cyclic voltammograms of MWCNTs/GCE or MWCNTs-NH_2/GCE recorded in the absence of oxygen in 0.1 M KOH were baseline subtracted to obtain the reported values of reductive peak currents as illustrated in Fig.A7.4. The background correction for the raw cyclic voltammograms were conducted by using OriginPro 2020, a baseline was fitted between the potentials at which the surface bound voltammetric wave was judged to have started and ended, then subtracted from the peak.

Section A7.3: Estimation of the number of quinones on a single CNT

Here, we compare the number of quinones at a single MWCNTs or MWCNTs-NH_2 based on the experimental data from nano-impact experiments:

For MWCNTs:

The number of quinone groups (N_{q1}) introduced into a single MWCNTs particle via electro-reduction can be estimated from nano-impact experiments to be

$N_{q1}=Q_{MWCNT\text{-}single}/ne=2\times10^{-12}$ C / $(2\times1.6\times10^{-19}$ C) $=6.3\times10^{6}$

where $Q_{MWCNT\text{-}single}$ is the average charge from the reductive step current when the potential was between -0.4 V and -0.6 V, n is the number of electrons transferred (n=2, assuming a complete two-electron quinone reduction process here).

Therefore, the coverage (Γ_{single}) of quinone groups on a single MWCNTs particle is

$\Gamma_{single}= N_{q1} / S_{mw} =6.3\times10^{6} / 1.9\times10^{-8}$ cm^2 = **3.3×10^{14} molecules per cm^2 of external surface area**

For MWCNTs-NH_2:

The number of quinone groups (N_{q2}) introduced into a single MWCNTs-NH_2 particle via electro-reduction can be estimated from nano-impact experiments to be

$N_{q2}=Q_{MWCNT\text{-}NH2\text{-}single}/ne=1.8\times10^{-12}$ C / $(2\times1.6\times10^{-19}$ C) $=5.6\times10^{6}$

where $Q_{MWCNT\text{-}NH2\text{-}single}$ is the average charge from the reductive spike current when the potential was between -0.4 V and -0.6 V

Therefore, the coverage (Γ_{single}') of quinone groups on a single MWCNTs-NH_2 particle is

$\Gamma_{single}'= N_{q2} / S_{mw\text{-}NH2} =5.6\times10^{6} / 2.3\times10^{-8}$ cm^2 = **2.4×10^{14} molecules per cm^2 of external surface area**

Given that the C=O bond lengths in a quinone moiety are ~ 1.4 Å [40, 41], the coverages above are too high to be realistic for a single CNT so we infer that the impact signals likely contain a significant component from aggregated CNTs.

Section A7.4: CV of MWCNTs or MWCNTs-NH_2 modified GCE in the presence of oxygen

To investigate the ORR performed on a MWCNTs or MWCNTs-NH_2 modified GCE in 0.1 M KOH, CVs were scanned for scan rates varying from 10 mVs^{-1} to 200 mVs^{-1} on each modified GCE from 0 V to -1.4 V vs Ag/AgCl respectively, as shown in Fig. A7.5 (A) and (C). Fig.A7.5 (B) and (D) show dependence of the peak current on the voltage scan rate in a logarithmic scale indicating a diffusion control process to form peroxide via a two-electron process as inferred in Chapter 6.

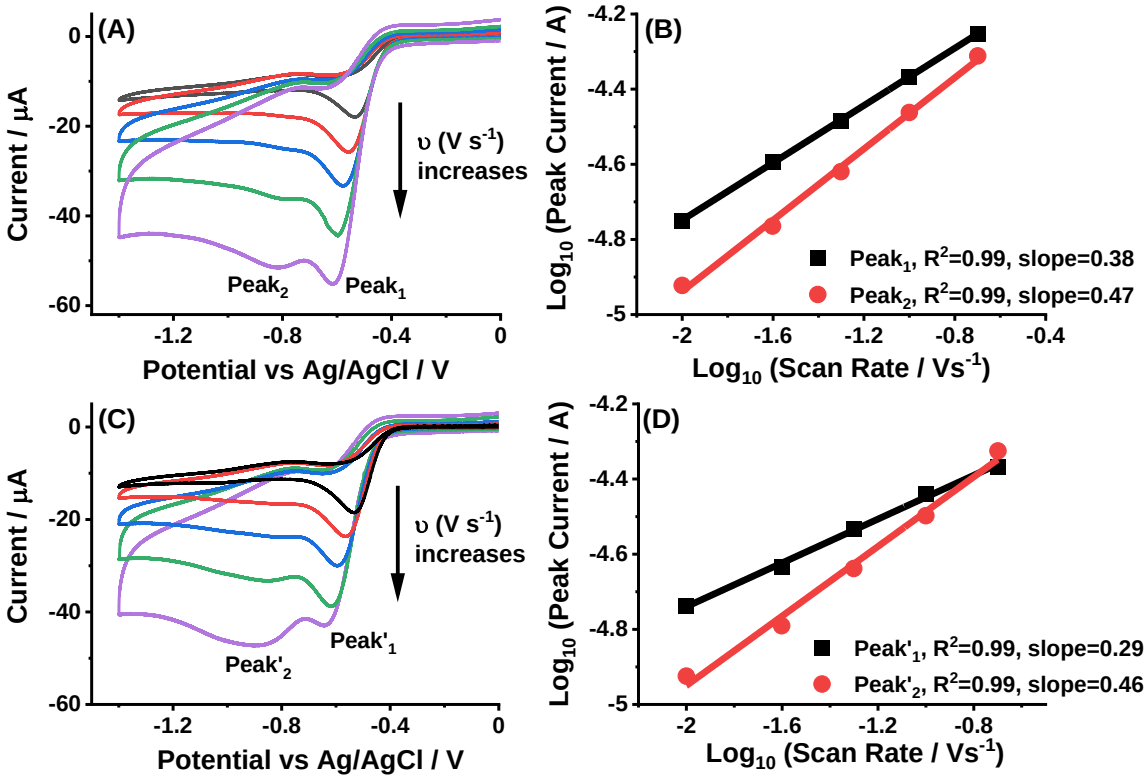


Figure.A7.5 Voltammograms at the 0.1 µg MWCNTs (A) or MWCNTs-NH_2 (C) modified GCE in 0.1 M KOH with saturated O_2 as a function of scan rate and their corresponding plot of peak currents versus scan rates in a log-log form for $Peak_1$ and $Peak_2$ (MWCNTs/GCE (B) and MWCNTs-NH_2/GCE (D)).

Section A7.5: Chronoamperogram of a carbon microwire electrode in the absence of CNTs

Fig.A7.6 showed only capacitive charging of the underlying microwire electrode was observed in the absence of any CNT particles at -0.4 V vs Ag/AgCl in oxygen-satured 0.1 M KOH.

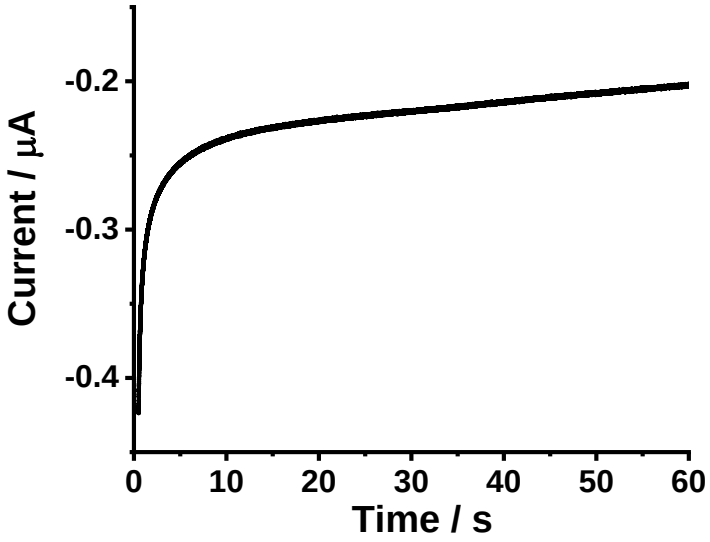


Figure.A7.6 Chronoamperogram of a carbon microwire electrode at -0.4 V vs Ag/AgCl in oxygen-saturated 0.1 M KOH with absence of CNTs.

Section A7.6: Calculation of the transport limited current for single carbon nanotubes

To calculate the transport limited current through a single impacted CNT under uniform diffusion-controlled, we viewed a carbon nanotube as a microcylindrical electrode. According to the equation by Szabo et al.[42]:

$$I_{lim} = (2\pi n F D_0 C_0 l) \times f(\tau) \qquad \text{(A7.1)}$$

with

$$f(\tau) = \frac{2e^{-\sqrt{\pi\tau}/20}}{\sqrt{\pi\tau}} + \frac{1}{\ln[(e^{-\gamma\tau})^{0.5} + e^{5/3}}$$

$$\tau = \frac{4D_0 t}{r_0^2}$$

where n is the number of electrons transferred, F is the Faraday constant (96485 C mol^{-1}), D_0 is the diffusion coefficient (1.9×10^{-9} $m^2 \cdot s^{-1}$ [43]) for O_2 in 0.1 M KOH (298K), C_0 is the saturated concentration of O_2 in 0.1 M KOH (1.21 mM [43]), *l* is the CNT length, r_0 is the CNT radius, t is the average step duration time (s), γ = 0.5772156.

Assuming a two-electron reduction process occurring on a single nanotube (n=2),

For MWCNTs:

l =20 μm, r_0 =15 nm, t=0.065 s

$I_{lim} \approx 8.1$ nA

For MWCNTs-NH_2:

l' =50 μm, r_0' =7.5 nm, t'=0.064 s

$I'_{lim} \approx 18.3$ nA

References

1. A. Yaghoubi and A. Ramazani, *Current Organic Chemistry*, 2018, **22**, 1505-1522.
2. B. C. H. Steele and A. Heinzel, *Nature*, 2001, **414**, 345-352.
3. Z. Chen, A. Yu, D. Higgins, H. Li, H. Wang and Z. Chen, *Nano Lett*, 2012, **12**, 1946-1952.
4. J. Duan, S. Chen, M. Jaroniec and S. Z. Qiao, *ACS Catalysis*, 2015, **5**, 5207-5234.
5. J. Zhang, K. Sasaki, E. Sutter and R. R. Adzic, *science*, 2007, **315**, 220-222.
6. J. Greeley, I. E. L. Stephens, A. S. Bondarenko, T. P. Johansson, H. A. Hansen, T. F. Jaramillo, J. Rossmeisl, I. Chorkendorff and J. K. Nørskov, *Nature Chemistry*, 2009, **1**, 552-556.
7. K. Sasaki, M. Shao and R. Adzic, *Polymer electrolyte fuel cell durability*, 2009, 7-27.
8. Y. Zheng, Y. Jiao, M. Jaroniec, Y. Jin and S. Z. Qiao, *Small*, 2012, **8**, 3550-3566.
9. J. C. Li, P. X. Hou and C. Liu, *Small*, 2017, **13**.
10. H. Dai, *Surface Science*, 2002, **500**, 218-241.
11. M. S. Dresselhaus, A. Jorio, M. Hofmann, G. Dresselhaus and R. Saito, *Nano Lett*, 2010, **10**, 751-758.

12. C. Hu and L. Dai, *Angewandte Chemie International Edition*, 2016, **55**, 11736-11758.
13. M. Pumera, *Chemistry*, 2009, **15**, 4970-4978.
14. K. Tammeveski, K. Kontturi, R. J. Nichols, R. J. Potter and D. J. Schiffrin, *Journal of Electroanalytical Chemistry*, 2001, **515**, 101-112.
15. E. Yeager, *Electrochim Acta*, 1984, **29**, 1527-1537.
16. K. Gong, F. Du, Z. Xia, M. Durstock and L. Dai, *science*, 2009, **323**, 760-764.
17. S. Kundu, T. C. Nagaiah, W. Xia, Y. Wang, S. V. Dommele, J. H. Bitter, M. Santa, G. Grundmeier, M. Bron and W. Schuhmann, *The Journal of Physical Chemistry C*, 2009, **113**, 14302-14310.
18. I. M. Patil, V. Reddy, M. Lokanathan and B. Kakade, *Applied Surface Science*, 2018, **449**, 697-704.
19. L. Chen, J. Ren and Z. Yuan, *ACS Sustainable Chemistry & Engineering*, 2021, **9**, 1856-1866.
20. H. Zhao, C. Sun, Z. Jin, D.-W. Wang, X. Yan, Z. Chen, G. Zhu and X. Yao, *Journal of Materials Chemistry A*, 2015, **3**, 11736-11739.
21. S. Maldonado and K. J. Stevenson, *The Journal of Physical Chemistry B*, 2005, **109**, 4707-4716.
22. E. Kätelhön and R. G. Compton, *Applied Materials Today*, 2020, **18**, 100514.
23. L. Chen, E. Kätelhön and R. G. Compton, *Applied Materials Today*, 2020, **18**, 100480.
24. X. Li, C. Batchelor-McAuley, S. A. I. Whitby, K. Tschulik, L. Shao and R. G. Compton, *Angew Chem Int Edit*, 2016, **55**, 4296-4299.
25. W. Cheng and R. G. Compton, *TrAC Trends in Analytical Chemistry*, 2014, **58**, 79-89.
26. X. Li, C. Lin, C. Batchelor-McAuley, E. Laborda, L. Shao and R. G. Compton, *The Journal of Physical Chemistry Letters*, 2016, **7**, 1554-1558.
27. Y. Lu, X. Li and R. G. Compton, *The Journal of Physical Chemistry Letters*, 2022, **13**, 3748-3753.
28. N. Inc, Multiwall Carbon Nanotubes (Bamboo Structure), can be found at https://www.nano-lab.com/bamboopowderd30l520.html).
29. X. N. A. M. Supplier, Amino Modified Multiwall Carbon Nanotubes, can be found at https://en.xfnano.com/product/pro223.aspx).
30. J. Ellison, C. Batchelor-McAuley, K. Tschulik and R. G. Compton, *Sensors and Actuators B: Chemical*, 2014, **200**, 47-52.
31. X. Li, C. Lin, C. Batchelor-McAuley, E. Laborda, L. Shao and R. G. Compton, *J Phys Chem Lett*, 2016, **7**, 1554-1558.

32. X. Li, C. Batchelor-McAuley, S. A. Whitby, K. Tschulik, L. Shao and R. G. Compton, *Angew Chem Int Ed Engl*, 2016, **55**, 4296-4299.
33. J. Ellison, K. Tschulik, E. J. Stuart, K. Jurkschat, D. Omanovic, M. Uhlemann, A. Crossley and R. G. Compton, *ChemistryOpen*, 2013, **2**, 69-75.
34. A. Kaliyaraj Selva Kumar, Y. Zhang, D. Li and R. G. Compton, *Electrochemistry communications*, 2020, **121**, 106867.
35. P. S. Guin, S. Das and P. Mandal, *International Journal of Electrochemistry*, 2011, **2011**.
36. K. Tammeveski, K. Kontturi, R. J. Nichols, R. J. Potter and D. J. Schiffrin, *J Electroanal Chem*, 2001, **515**, 101-112.
37. H. Zhang, C. Lin, L. Sepunaru, C. Batchelor-McAuley and R. G. Compton, *J Electroanal Chem*, 2017, **799**, 53-60.
38. Y. Lu, X. Li and R. G. Compton, *The Journal of Physical Chemistry Letters*, 2022, 3748-3753.
39. Y. Lu, X. Li and R. G. Compton, *Chemical Science*, 2022, **13**, 1355-1366.
40. B. Kim, G. Storch, G. Banerjee, B. Q. Mercado, J. Castillo-Lora, G. W. Brudvig, J. M. Mayer and S. J. Miller, *Journal of the American Chemical Society*, 2017, **139**, 15239-15244.
41. S. Saxena, S. Panchagnula, M. E. Sanz, C. Pérez, L. Evangelisti and B. H. Pate, *ChemPhysChem*, 2020, **21**, 2579-2584.
42. A. Szabo, D. K. Cope, D. E. Tallman, P. M. Kovach and R. M. Wightman, *J Electroanal Chem Interfac Electrochem*, 1987, **217**, 417-423.
43. R. E. Davis, G. L. Horvath and C. W. Tobias, *Electrochimica Acta*, 1967, **12**, 287-297.

Conclusions

In this thesis, we employed electrochemical methods including cyclic voltammetry, square wave voltammetry, chronoamperometry and nano-impacts to explore electron transfer kinetics and reaction mechanisms under different electroactive surface. The key electrochemical studies inside benefit the development of applications from sensors to fuel cells. The following conclusions have been drawn:

1. The electrochemical detection of phosphate in aqueous solutions at an ammonium molybdate tetrahydrate (AMT)-chitosan modified glassy carbon macro electrode (AMT-CS-GCE) was investigated using cyclic voltammetry (CV) and square wave voltammetry (SWV). In synergy with knowledge about the speciation of molybdate (Mo (VI)), phosphate (P) and related complex species in aqueous solution as a function of concentration and pH, the enhancement of the observed Mo reduction peaks seen in the presence of phosphate indicated an electrocatalytic mechanism. Meanwhile, SWV effectively improved detection sensitivity to 4.4 ± 0.1 μA/μM and this developed sensor was shown to be valuable as a reagent free sensor for quantifying phosphate concentration in real water samples. Attempts to immobilise the AMT system on carbon nanotubes were unsuccessful but led to the following studies on the nanotubes themselves.

2.The electrochemical oxidative behaviour of MWCNTs-NH_2 was studied in the pH range from 0.3 to 6.4 using quantitative CV and single entity electrochemistry measurements, allowing comparison with non-functionalized MWCNTs. The ensemble electrochemistry of MWCNTs-NH_2 reflected the variable amount of deprotonated amino groups present as a function of pH in addition to the similar catalytic behaviour for the solvent (water) decomposition and irreversible electro-oxidation forming surface oxygen functionality on both carbon MWCNTs. Nano-impact experiments conducted at the single particle level further confirmed the oxidation of

both types of MWCNTs, showing agreement with the CV. The pK_a of the amino groups in MWCNTs was determined via both electrochemical methods giving consistent values of ca 2.5.

3. The electrocatalysis of the oxygen reduction reaction (ORR) by MWCNTs was explored in aqueous base at the single entity level, complementing the cyclic voltammetric responses obtained at bare carbon macroelectrodes and such electrodes modified with layers of MWCNTs. It was found that the nano-impact signals reflecting the electrocatalytic reduction from oxygen to peroxide by virtue of electroactive surface oxygen functionality of MWCNTs were observed at lower potentials relative to the location of reductive peak from CV. The joint study between single entity and ensemble electrochemical measurements emphasised the likely role of surface quinones in electrocatalysis in general but the ORR in particular as then further explored in respect of N doping.

4. The catalytic effect from the doping of Nitrogen into CNTs on the ORR was investigated by comparing the electrocatalytic behaviour of MWCNTs and MWCNTs with amino group functionalization at single entity and ensemble level. In the absence of oxygen, the results implied, as above, the formation of semi-quinones and quinone dianions from reduction of quinone groups on the surface of MWCNTs. Followed by the experiments in the presence of oxygen, all evidence showed the surface oxygen functionality facilitated the formation of peroxide from reduction of oxygen while the addition of nitrogen groups did not play any role in this process.

Future prospects

The conclusions above give an overall perspective of the work reported in this thesis, however, based on the current electrochemical experiments and analysis, there are still some areas for clarification with scope for further improvement and exploration as summarised below.

1. In Chapter 3 and 4, the thesis reported a type of AMT-CS-GCE electrochemical sensor applied in aqueous solution. For the assignment of the observed five voltammetric reduction peaks in the presence of phosphate, we drew clear inferences about the underlying chemistry based on electrochemical data. It may be helpful to use other characterization techniques like Ion Chromatography [1,2] to do confirmatory further analysis so that the future experiments can more conveniently obtain the mass balance among all the existing ions in the solution. As for the actual application, in addition to the two most important interfering substances (NO_3^- and Cl^-) reported in Chapter 4, the interference caused by other organic and inorganic impurities [3] might also be usefully considered in authentic water samples. Beyond the experiments as mainly conducted in the laboratory, how to realize the integration of water sample collection and testing as an in-situ measurement technology [4] will be a further major technological challenge in the future operation process.

2. The emergence of nano-impact techniques allows the clear clarify of functional features on the electrochemical reactions from the nanomaterial itself and provides an understanding of the connection between the properties of individual particles and their ensembles to obtain the more accurate kinetics of associated electrochemical reactions. In Chapters 5, 6 and 7, it is reported the electrochemical redox behaviour at two different types of single MWCNTs particle. Here it raises a question concerning how the MWCNT will approach and attach (or detach) the microelectrode. Accordingly, the shape of individual impact transient might possibly be studied to infer the likely collision dynamics. From another perspective, because carbon supports are quite popular as diverse catalytic substrates [5,6], it will be more useful to know how this identified

approach can be reliably used with other allotropic forms of carbon like graphenes, graphene quantum dots, fullerenes and that family of compounds, and (reduced) graphene oxide.

3. Single entity electrochemical technique was originally designed to characterize physical and chemical properties of the corresponding single nanoparticles. But now, its application should be further extended in the field of energy, biology and environment. For example, in Chapters 6 and 7, we only proved the surface oxygen functional groups at MWCNTs play an important role in electrocatalyzing the first step of ORR from oxygen to hydrogen peroxide. Meanwhile, because of the limitation of self-fabricated carbon wire electrodes which easily break at very positive or negative potentials, the studied potential cannot be extended further. In this case, to study the second reduction step of ORR from hydrogen peroxide to water, we could find out another material to prepare the microwire electrode as working electrode. By investigating the whole kinetics of the ORR catalytic process, the MWCNTs will be of great potential to become a new commercial material in fuel cell as a type of suitable replacement for platinum materials.

References

1. M. Bello and A. G. Gonzalez, *Journal of chemical education*, 1996, **73**, 1174.
2. Y. Nakashima, Y. Inoue, T. Yamamoto, W. Kamichatani, S. Kagaya and A. Yamamoto, *Analytical Sciences*, 2012, **28**, 1113-1116.
3. M. Kumar, P. Borah and P. Devi, in *Inorganic Pollutants in Water*, Elsevier, 2020, 33-49.
4. M. P. Mahmud, F. Ejeian, S. Azadi, M. Myers, B. Pejcic, R. Abbassi, A. Razmjou and M. Asadnia, *Chemosphere*, 2020, **259**, 127492.
5. X. Chen, W.D. Oh and T.T. Lim, *Chemical Engineering Journal*, 2018, **354**, 941-976.
6. W. Liu, M. Li, G. Jiang, G. Li, J. Zhu, M. Xiao, Y. Zhu, R. Gao, A. Yu and M. Feng, *Advanced Energy Materials*, 2020, **10**, 2001275.